Spin dynamics and spatially resolved spin transport phenomena in GaAs based structures

Dissertation

zur Erlangung des Doktorgrades
der Naturwissenschaften (Dr. rer. nat.)
der Fakultät für Physik
der Universität Regensburg

vorgelegt von

Roland Völkl

aus Weiden i.d.OPf.

Oktober 2013

Promotionsgesuch eingereicht am 25.09.2013
Die Arbeit wurde von Prof. Dr. Christian Schüller angeleitet.

Prüfungsausschuß:	Vorsitzender:	Prof. Dr. Jaroslav Fabian
	1. Gutachter:	Prof. Dr. Christian Schüller
	2. Gutachter:	Prof. Dr. Sergey D. Ganichev
	Weiterer Prüfer:	Prof. Dr. Dieter Weiss

"Don't dream your life, but live your dream."

Mark Twain

Contents

Chapter 1

Introduction

Despite W. Paulis statement that "One should not work on semiconductors. They are a mess. Who knows whether semiconductors exist at all." [1] semiconductor technologies have become the foundation of modern information technology. At Bell Laboratories, the first step in developing this technology that is indispensable today was done, by implementing a transistor based on Germanium [Bar48] [2]. W. Shockleys proposal of a field effect transistor [Sho52] and J. S. Kilbys invention of the integrated circuit [Kil63; Kil76] then laid the foundation of today's electronics. Advances in the fabrication of semiconductor structures for instance Metal-Organic-Vapor-Phase Epitaxy (MOVPE) [Man68] and Molecular-Beam Epitaxy (MBE) [Art68; Cho71], allowed the development of low-dimensional structures such as quantum wells (2D), quantum wires (1D), and quantum dots (0D). Quantization effects become apparent when the movement of carriers is restricted in one or more degrees of freedom on a scale comparable to their de Broglie wavelength $\lambda_{dB} = h/p$. Quantum mechanical effects, such as the quantum Hall effect [Kli80] or the Aharonov-Bohm-effect (electron interference) [Aha59; Web85] could be observed in those structures. Furthermore, the possibility to fabricate heterojunctions resulted in structures with high carrier mobilities, utilized for example in high-electron-mobility transistors (HEMT) [Mim80], and the proposal of semiconductor lasers [Kro63; Kro01; Hal62] [3]. Since the first works of Kilby computing hardware has developed enormously. The well-known Moore's law reflects this evolution, and it states that the amount of transistors on an integrated circuit doubles approximately every 18 months [Moo65]. Eventually, this minimization creates problems when the size approaches an atomic scale and quantum mechanical effects gain impact. Moreover, parasitic capacitances, and leakage currents create problems in the low-scale planar electronics [Tho06]. The development of new technologies is therefore inevitable.

To improve the efficiency of electronic devices and to enrich them with new functionalities is the goal of spintronics, where the intrinsic spin replaces the charge in the elements of modern information manipulation (logic, storage, and communication). Metal-based spintronics already enjoyed great success in the proposal of the giant magneto resistance (GMR) [Bai88; Bin89] [4], which became a basis in developing modern storage devices. Modern hard disk read heads, as well as non-volatile memory, such as the magnetoresistive random access memory (MRAM), are developed on this basis.

[1] From a letter of Wolfgang Pauli to Rudolph Peierls, 1931.

[2] Awarded with the Nobel Prize in Physics 1956 to W. B. Shockley, J. Bardeen, W. H. Brattain.

[3] The Nobel Prize in Physics 2000 was awarded to Z. I. Alferov, H Kroemer and J. S. Kilby for basic work on information and communication technology.

[4] A. Fert and P. Grünberg received the Nobel Prize in Physics in 2007 for the GMR concept.

After Johnson and Silsbee's observation of the injection of spin-polarized electrons from a ferromagnet into a metal [Joh85; Joh88], the proposal of a spin field effect transistor (sFET) drew a lot of attention and boosted the research efforts in semiconductor spintronics. In this concept, as well as in the experiments presented here, the spin-orbit interaction (SOI), which is strong in semiconductors compared to a free electron, plays a central role. The influence of SOI is essential in various transport experiments. Prominent examples are weak (anti) localization effect [Ber84a; Has97], spin photocurrents [Gan04; Gan03], and beatings in the Shubnikov-de Haas oscillations [Das90; Sil94; Nit97]. The interplay of carrier drift and SOI generates a spin polarization in a material, due to current-induced spin polarization [Aro91; Ede90; Gan06; Sih05; Ste06] and the spin Hall effect [Dya71b; Dya71a; Kat04b]. A further development of the spin Hall effect is the quantum spin Hall effect (QSHE), whose revealing enhanced the research efforts on the so-called topological insulators [Kan05; Ber06c; Ber06b; Has10]. Although the conventional quantum Hall effect shows spin-polarized charge transport for odd filling factors and especially for filling factor 1, there is still an external magnetic field required [Eis90; Buh11]. The QSHE shows spin-polarized conducting edge channels in the bulk insulating regime in materials with high SOI.

In contrast, the spin orientation is not conserved due to the influence of the SOI, and it relaxes into thermal equilibrium after a certain spin relaxation time. The most important spin relaxation mechanism in non-centrosymmetric semiconductors, such as GaAs, was proposed by M.I. Dyakonov [Dya71c; Dya86]. The symmetry of the crystal and the heterostructure give rise to the SOI, which can be assumed as an effective magnetic field, which causes spin precession [Dre55; Byc84b; Byc84a]. In 2D systems, symmetry and direction of this effective field depend on the orientation of the substrate. Interference effects between the contributions to this effective field, as well as certain growth directions, particularly growth on a (110)-oriented GaAs substrate, induce anisotropies in the spin dephasing [Ave99; Dya86; Bel08].

In the concept of the sFET, spin-polarized electrons are injected into a semiconductor through a ferromagnetic source contact and move ballistically towards a ferromagnetic drain contact. A spin precession is induced with an applied gate voltage, and the transmitted current through the drain contact then depends on the relative orientation of the magnetization in the contact and the electron spin. This concept has been realized by Koo et al. recently [Koo09]. It is, however, quite unsuitable for practical use, since the ballistic transport requires low temperatures, and it lacks scalability [5]. The proposal by Schliemann et al. developed the idea of Datta and Das further. In their concept, ballistic transport is no longer necessary, which is achieved due to a special interplay between Dresselhaus and Rashba coupling [Sch03b]. Further variations of the sFET concept rely on varying the spin lifetime in the semiconductor by a gate [Car03; Hal03a]. A promising approach is the spin complementary field effect transistor [Kun12], which is based on gate controlled persistent spin helix states. Such states arise with a special symmetry of the spin orbit fields, which yields that the spin polarization of a helical mode is preserved [Ber06a; Kor09; Wal12]. In contrast, Betthausen et al. proposed a spin transistor concept which does not rely on SOI. It rather relies on tunable Landau-Zener transitions [Bet12].

The use of spin instead of charge is playing an important role in quantum computing. Here, the conventional logic is replaced by quantum mechanical phenomena, such as superposition and entanglement. This allows the development of new algorithms, with whom faster and more efficient operations are possible [DiV95; Los98; Ben00; Häg01].

[5] The spin-precession length depends on the strength of the SOI parameters. For example in InGaAs, which has a strong SOI, it is about 1 μm. Compared to the actual Si-based CMOS transistors, whose size approaches tens of nanometers [Tho06], this size is no improvement.

Very long spin lifetimes, such as those found in nitrogen vacancy centers in diamond (350 μs) [Gae06], and the possibility of coherent manipulation of electron spins, which allows for short gate times [Pet05], could lead to the realization of an efficient quantum computing system.

Recently, it was shown that applications combining optics and semiconductor spintronics can enhance the performance of lasers for communications and signal processing. By optically pumping spin-polarized electrons in the gain medium, the laser threshold is effectively reduced by up to 50% compared to conventional semiconductor lasers [Rud03; Rud05; Hol07]. Employing spin-polarized electrons also allows for fast amplitude modulation of the laser emission [Lee10; Ger11]. Furthermore, a giant photoinduced Faraday rotation caused by the spin-polarized electron gas in a n-GaAs microcavity was reported, which might find an application in fast light modulation devices [Gir12].

Besides the task of spin injection, the knowledge of how long a spin orientation exists and how far spin information can be transported is crucial for spintronics applications. This work addresses these topics in the case of GaAs based structures. As a direct-gap semiconductor, GaAs is ideal for optical orientation and detection. In bulk GaAs, spin lifetimes exceeding 100 ns have been found at low temperatures [Dzh02; Kik98] and tens of ps at room temperature [Kim01; Hoh06; Kik98]. Spin diffusion lengths of a few μm have been observed [Häg98; Fur07; Cio09], whereas in an electric field a spin coherence was transported over a distance exceeding 100 μm [Kik99].

Electrical spin injection from a metallic ferromagnet into a semiconductor, as required in the previously discussed sFET, faces the problem of the huge difference in the conductivity of the two materials, which results in very low spin injection efficiencies. One solution to this problem is to use the diluted magnetic semiconductor gallium manganese arsenide (Ga,Mn)As as a ferromagnetic contact [Ohn99a; Koh01; JH02; VD04]. One part of the experimental results presented in this work is investigating such a structure. Spin dynamics and spin transport phenomena are examined employing the Hanle-MOKE technique. Similar samples have already been investigated with different detection methods and geometries: Ciorga et al. demonstrated an all-electrical spin injection and detection method [Cio09; Cio10; Cio11; Ein09], and Endres et al. used cross-sectional imaging of the spin polarization on the cleaved edge of the GaAs channel [End11; End12]. Together with these works, the results presented here give a more complete description of this kind of samples.

In the second part of this work, two-dimensional electron systems embedded in GaAs/AlGaAs quantum wells grown on a (110)-oriented substrate are investigated. The special symmetry of (110)-grown quantum wells promises long spin lifetimes [Ohn99b; Ada01; Döh04; Mül08]. Due to the use of very sophisticated growth schemes [Uma09], exceptionally high electron mobilities are present in the samples examined here. Spin lifetimes of up to 248 ns at low temperatures were observed, employing RSA-measurements in one of the utilized samples [Gri12a; Gri12b]. Besides studying the spin dynamics under the influence of external parameters such as temperature, carrier density and excitation density, spin transport phenomena such as spin diffusion and spin drift are also examined. The Hanle-MOKE method and photoluminescence measurements are the means for these investigations. Furthermore, current-induced spin polarization is demonstrated in the samples. This method of generating a spin orientation was already successfully demonstrated at room temperature in n-type ZnSe epilayers [Ste06]. Under the condition that the spin polarization can be made large enough, this method has the potential to become an efficient tool to generate spin orientations in non-magnetic semiconductors.

The structure of this work is as follows:

Chapter 2 outlines the fundamental theory. It starts with the material properties of GaAs, GaAs heterostructures, and the ferromagnetism in (Ga,Mn)As. Afterward, the

concepts of generating a spin imbalance in a semiconductor are elucidated, in particular electrical spin injection and optical spin orientation. Then this chapter discusses spin-orbit interaction in connection with crystal symmetries and the various spin dephasing mechanisms. Next subject are the transport phenomena such as diffusion and drift, which are discussed in regard to carrier and spin. The chapter closes by giving attention to dynamic nuclear polarization.

Chapter 3 explains the measurement techniques and the experimental setup. First, it illustrates the magneto-optic Kerr/Faraday effect and its combination with the Hanle effect, the technique most employed in this work to determine spin lifetimes and spin polarization. Then, this chapter discusses photoluminescence spectroscopy and the possibilities of changing the carrier density by gating optically as well as electrically.

Chapter 4 describes the experiments, in which a p^+ (Ga,Mn)As/ n^+ GaAs Esaki Zener diode structure is used to inject a spin polarization into GaAs bulk. First, the sample structure is described and characterized in terms of I-V characteristics and the dependence of the magnetization of the electrode on an external field. The spin lifetime in the sample is then investigated utilizing an all-optical method in comparison to the results from electrical injection. Then, the chapter focuses on the sign of the spin polarization depending on the applied bias at the electrode. By moving the detection laser spot on the sample relative to the spin injecting contact, spin diffusion and spin drift profiles are revealed. Finally, this chapter introduces a technique, where electrical and optical spin injection are combined in order to observe dynamic nuclear polarization effects.

Chapter 5 presents first the complex sample structure of the high-mobility (110)-grown quantum wells. For a complete description of the spin dynamics, knowledge of the carrier dynamics depending on the external parameters is essential. Therefore, this chapter introduces photoluminescence measurements as well as time-resolved photoluminescence measurements. Then the spin dynamics for three samples, which differ in terms of quantum well width and carrier density, is examined in regard to the external parameters temperature excitation density and carrier density (modulated by above-barrier illumination). Hereby, spin-resolved PL measurements support the results of the Hanle-MOKE technique. Spin diffusion is investigated when varying the relative distance between injection point and detection point. The spin diffusion is monitored depending on an external gate voltage as well. In (110)-grown quantum wells, the symmetry of the Dresselhaus field together with an electron drift, yields an out-of-plane spin polarization, owing to current-induced spin polarization. After this effect is examined the chapter focuses on further effects of electron drift, such as the reduction of the spin lifetime. Finally, dynamic nuclear polarization in this system is discussed briefly.

Chapter 6 presents the summary of the results.

Chapter 2

Basics

The materials subject to investigation in this work are based on gallium arsenide and aluminium gallium arsenide, which have drawn quite some attention in semiconductor physics in the past decades. Constant developments in fabrication now provide very pure crystal structures, allowing the observation of quantum effects, and give rise to very high carrier mobilities. A full understanding of the spin dynamics requires knowledge of the fundamental material properties as well. This chapter starts therefore with a brief discussion on the material characteristics and the fabrication of such semiconductor structures. This introduction contains as well the diluted ferromagnetic semiconductor gallium manganese arsenide, which is used as a source of spin injection in chapter 4. Thereafter essential fundamentals of electron spin physics in semiconductors are outlined (chapter 2.2). This discussion starts with possibilities to generate a spin polarization in semiconductors, emphasizing the two mechanisms this work uses, optical and electrical spin injection. A crucial point in understanding spin dephasing, which is the relaxation of a spin imbalance into its thermal equilibrium, is to understand the interaction of the orbital motion of an electron and its spin. After discussing the most prominent spin dephasing mechanisms in GaAs based heterostructures, the spin dynamics, particularly in the investigated types, GaAs bulk and (110)-grown GaAs / $Al_xGa_{1-x}As$, are illustrated. Besides the spin dynamics, the spin transport is studied as well here. This chapter outlines, therefore, the transport phenomena diffusion and drift with regard to carrier transport, as well as spin transport. The chapter closes with the influence and interplay of nuclear and electron spins.

2.1 Material properties

In this section the basic properties of gallium arsenide and aluminium gallium arsenide (GaAs / $Al_xGa_{1-x}As$) are introduced, starting by addressing the crystal growth, and continuing by giving attention to the electronic band structure in the GaAs crystal. Thereafter the formation of heterostructures as well as the possibility of doping is dealt with. Finally, the ferromagnetism in the diluted magnetic semiconductor (Ga,Mn)As is addressed.

2.1.1 GaAs / AlGaAs structures

The III-V semiconductors gallium arsenide (GaAs) and aluminium arsenide (AlAs) are the basic materials for the structures examined in this work. An effective spin transport entails high carrier mobilities, which can be achieved by producing high purity

crystal structures. The Molecular-Beam Epitaxy (MBE) [1] is a method to fabricate such materials. A basic setup of a MBE chamber is depicted in figure 2.1 (a). Here, pure materials evaporate from effusion cells, which are set in a ultra-high vacuum (UHV 10^{-9} Pa) chamber. Due to the UHV, which is supported by cryogenic cooling shields (to freeze out impurity atoms), the molecules do not interact with each other until they eventually condense on a heated and rotating substrate. The slow deposition rate this method provides, allows epitaxial growth. This means the deposited layer is congruent to the substrate (assuming matching physical properties of substrate and the evaporated materials). Mechanical shutters control the relative fluxes out of the effusion cells, and the growth is monitored with the RHEED technique (reflection high energy electron diffraction). In a nutshell, MBE provides crystal structures with sharp layer boundaries, and negligible thickness variations of the layer [Cho81].

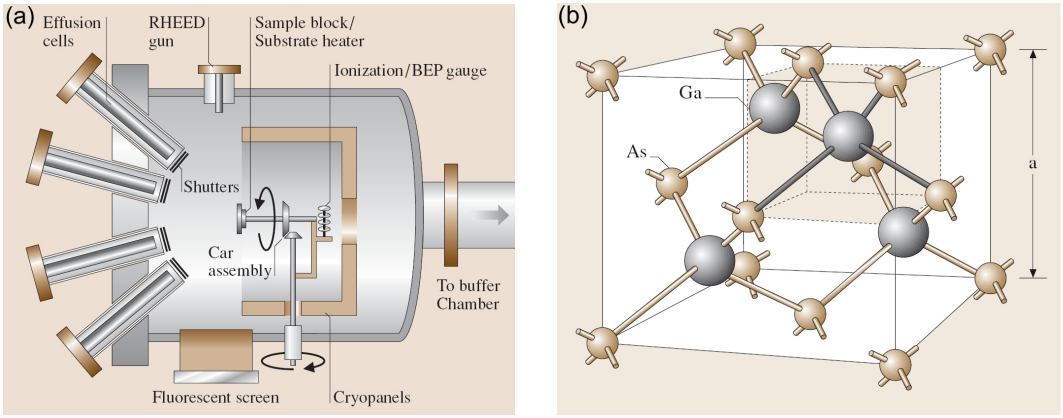

Figure 2.1: ***(a)*** *Schematic layout of a MBE chamber. Taken from [Kas06].* ***(b)*** *The GaAs zincblende structure consists of two fcc lattices (Ga,As) shifted by* $(1/4, 1/4, 1/4)$ *a (lattice constant) along the space diagonal. Taken from [Kas06].*

The crystal structure of the compound semiconductor GaAs consists of tetrahedral covalent bonds by each Ga (As) atom formed with four As (Ga) atoms [2] [3]. Hence, the two interpenetrating fcc (face centered cubic) lattices of the two atom types are forming a zincblende crystal as figure 2.1 (b) depicts. The space group symmetry of this crystal is symorphic and labeled T_d^2 [Dre55], with a space group number two, and a point group symmetry T_d (similar to the methane molecule (CH_4)). T_d contains 24 symmetry operations: the identity, eight C_3 operations (rotation by 120°, two C_2 operations (rotation by 180°), six S_4 operations (rotation followed by a reflection perpendicular to the rotation axis), and six σ operations (reflection with respect to a plane) [4].

The energy of an electron moving in a crystal can only have certain energy values. An exact calculation of this energy bands is quite complex, since the electron lattice interactions create a many-body problem. Thus, approximative models are necessary to determine the **band structure**. One of these is the intuitive tight-binding picture, where the valence orbitals of neighboring atoms hybridize (sp^3 hybridisation) and form bonding and antibonding composite orbitals. Those composite orbitals broaden into bands because of the overlap of the orbitals in the crystal. On the one hand the s-antibonding orbitals (the angular momentum of the electrons is $l = 0$) form the lowest conduction band (CB), and on the other hand, the p-bonding orbitals (the angular

[1] Invented at Bell Laboratories [Art68; Cho71].

[2] In the particular case of GaAs where two atom types are involved, additionally ionic bonding is present, resulting in a increased bond strength.

[3] Standard textbooks [Ash76; Kit96] describe the basic principles of chemical bonds.

[4] A detailed discussion of the symmetry groups may be found in [Yu05].

momentum of the electrons is $l = 1$) constitute the highest valence band (VB). Due to its s-like ($l = 0$) character the conduction band is double degenerate (spin degeneracy $s = \pm 1/2$), whereas the valence band has a six-fold degeneracy because of its p-like character. Furthermore, this degeneracy splits into a four-fold (heavy-hole HH and light-hole LH) and a two-fold degenerate band (split-off-band) as a result of the spin-orbit interaction (SOI)(see chapter 2.2.2). The terms heavy-hole and light-hole band are derived from their different **effective masses** which correspond to the curvature of the bands $\left(\frac{1}{m^*}\right)_{i,j} = \frac{1}{\hbar^2}\frac{\partial^2 E_n(\boldsymbol{k})}{\partial k_i \partial k_j}$. For bulk GaAs those two bands are degenerate at the Γ-point ($\boldsymbol{k} = 0$), in heterostructures however this degeneracy is lifted (see chapter 2.1.1). Figure 2.2 (a) exhibits the band structure of bulk GaAs close to the Γ-point, where an approximately parabolic behavior is assumed (effective mass approximation). The bands are occupied according to the product of the density of states and a distribution function, typically the Fermi-Dirac distribution. In that case the energy of the highest occupied state is called Fermi energy (E_F). The position of the Fermi energy depends on factors such as doping concentration and the temperature [5]. In 3D it may be expressed as: $E_F = [\hbar^2/(2m^*)](3\pi^2 n)^{2/3}$ and in 2D as: $E_F = \hbar^2 \pi n/m^*$ [Gru06]. A couple of important expressions are derived from the Fermi energy: The Fermi temperature T_F is defined as: $T_F = E_F/k_B$, the Fermi velocity v_F is given by: $v_F = \sqrt{2E_F/m^*}$, and the Fermi wave vector k_F is defined as: $k_F = (3\pi^2 n)^{1/3}$ in 3D, and $k_F = \sqrt{2\pi n}$ in 2D.

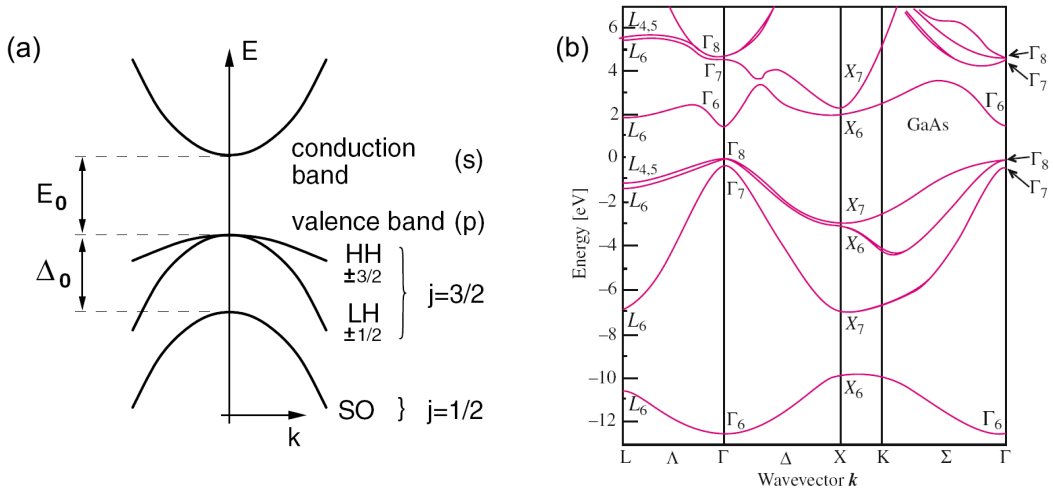

Figure 2.2: ***(a)*** *Band structure close to the Γ-point according to effective mass approximation. Due to SOI the VB states split into states with total angular momentum $j = 3/2$ (HH-band, LH-band) and $j = 1/2$ (split-off band, SO-band). The difference between the CB minimum and the VB maximum is the band gap energy E_g . The energy gap Δ_0 is called the spin-orbit gap (SO-gap). Taken from [Win03].* ***(b)*** *Band structure for GaAs. The top of the filled VB is set to zero energy. Taken from [Yu05].*

A conceptually different approach to obtain the band structure is the quasi-free particle approximation. Here nearly free valence electrons are considered, moving in a periodic potential of the ions and core electrons. In order to solve the one electron Schrödinger equation in such a periodic potential, Bloch's theorem is used. The electron wave function then has the form $\psi_{n,k}(\boldsymbol{r}) = u_{n,k}(\boldsymbol{r}) \exp[i\boldsymbol{k} \cdot \boldsymbol{r}]$, with a periodic function $u_{n,k}(\boldsymbol{r})$ and an envelope function $\exp[i\boldsymbol{k} \cdot \boldsymbol{r}]$ [6]. Nowadays very sophisticated methods are deployed to calculate band structures, such as the $k \cdot p$-method. This

[5] Providing an undoped sample, the VB is fully occupied at zero temperature $T = 0$, whereas the CB is not occupied at all. The Fermi energy is then located midmost between CB and VB.

[6] A detailed discussion may be found in standard textbooks like [Ash76; Kit96].

approach is based on the fact that the Bloch-function ansatz yields a coupling term $\vec{k} \cdot \vec{p}$ in the Hamiltonian. Treating this $k \cdot p$-term as a perturbation, the energy band structure is calculated. Considering the degeneracy of the VB, however, spin orbit interaction must be included, and the incorporation of higher order perturbation terms are necessary. Usually it is sufficient for an effective calculation to consider the bands Γ_6,Γ_8 and Γ_7. This is called the Kane model [7]. A further approach is the pseudopotential method, where the strong Coulomb potential of the nucleus and the core electrons are replaced by an effective ionic potential acting on the valence electrons. The band structure displayed in figure 2.2 (b) is a result of pseudopotential calculations. Detailed discussions on such methods may be found in [Win03; Yu05]. It is often sufficient to consider only the states close to the Fermi energy or at the minimum of the conduction band. For small $\boldsymbol{k}$, the band around the minimum can be approximated as parabolic. Using a Taylor expansion up to second order and assigning the second derivative to an inverse effective mass ($m^*_{e,h}$) allows the use of a semiclassical model of transport. Corrections due to high order effects may invoke non-parabolicity though. Since each band has a unique curvature that is reflected in the effective mass, this approximation is called effective mass approximation (figure 2.2 (a)). Strictly speaking, holes in the Γ_8-band cannot be described by such an effective mass approximation since they are highly anisotropic and nonparabolic.[Win03].

Heterostructures

Crystal growth techniques, like the MBE method, allow the fabrication of ternary alloys such as $Al_xGa_{1-x}As$. In such structures one of the two above mentioned fcc-lattices consists of As atoms and the other is statistically occupied by Ga and Al atoms. Because AlAs has a larger bandgap than GaAs, the band gap of the alloy may be designed, by changing the portion of Al_x ($E_g = 1.424 + 1.247x$ [eV] at room temperature [Lev99]). Since the emission/absorption lies in the near IR to red spectral range, this material is quite interesting for optoelectronic applications. However, only in the range $0 < x < 0.45$ $Al_xGa_{1-x}As$ has a **direct band gap**, i.e., the maximum of the highest valence band and the minimum of the lowest conduction band are at the Γ-point (k=0), see figure 2.2. For $0.45 < x < 1$ the conduction band minimum can be found at the X-point, yielding an indirect band gap, see also chapter 2.2.1. The width of the band gap depends on the temperature as well, since an increase in temperature causes an expansion of the lattice, due to a rising amplitude of atomic vibrations [8]. According to the Varshni formula the maximal band gap energy E_g at $T = 0$ K decreases first quadratically ($T \ll \Theta_D$ [9]) and changes into a linear decline for higher T [Var67]:

$$E_g(T) = E_g(T = 0) - \alpha_v T^2/(T + \beta_v). \tag{2.1}$$

Here α_v represents the volume coefficient of thermal expansion and β_v the volume compressibility. Thus, in the direct band gap regime, the band gap energy of $Al_xGa_{1-x}As$ for low temperatures, is given by [Lev99]:

$$E_g = 1.519 + 1.155x + 0.37x^2 \text{ [eV]}. \tag{2.2}$$

Standard textbooks and publications such as [Ada85; Kas06; Lev99] also include further fundamental material properties.

The nearly identical lattice constants of GaAs and AlAs ($a = 5.6533 + 0.0078x$ [Å] allow a strain-less growth of relatively thick $Al_xGa_{1-x}As$ layers. One may create heterostructures with various potential landscapes, like a potential well, by stacking such

[7] There exists also an extended Kane model which includes 12 bands.

[8] Strictly speaking only due to the anharmonic potential.

[9] Θ_D Debye temperature.

layers with different band gaps. The structures this work uses are categorized as type I, where the higher VB edge and the lower CB edge are both in the material with the smaller bandgap. These offsets of CB and VB are calculated from the difference of the electron affinities (χ) in the materials[10] (see figure 2.3). In the case the de Broglie wavelength is comparable with the layer thickness d [11], the electron and hole states along the growth direction z [12] are quantized in so-called subbands (see figure 2.3). The

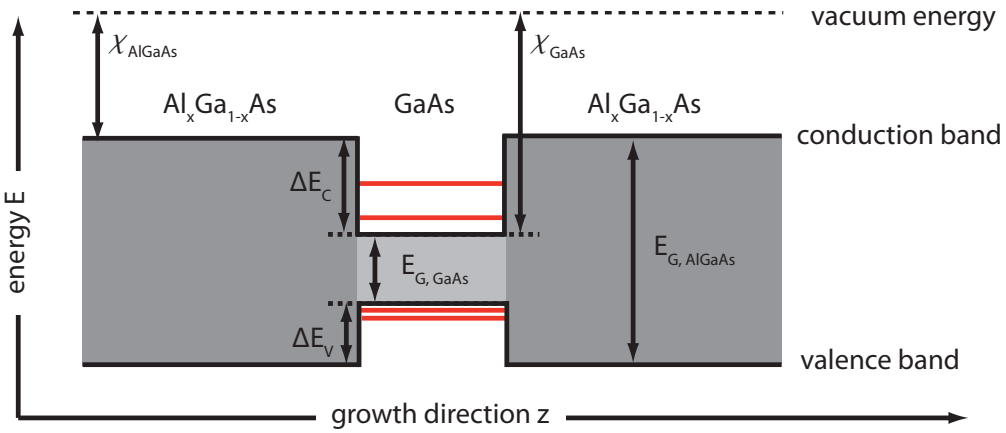

Figure 2.3: *Type-I heterostructure. The CB and VB discontinuities are given by* $\Delta E_C = \chi_{AlGaAs} - \chi_{GaAs}$ *and* $\Delta E_V = (\chi_{AlGaAs} + E_{G,AlGaAs}) - (\chi_{GaAs} + E_{G,GaAs})$ *are given. Taken from [Gri12b].*

electron/ hole states are stationary in this direction, along the in-plane axis the Bloch wave character remains though. In such a 2D-electron-system (2DES) the density of states is now a step function (in 3D it is proportional to $E^{1/2}$). One speaks of a quantum well (QW) in the case of confinement in a single direction, whereas for two (three) confinement directions a quantum wire (quantum dot) is present. A further consequence of the confinement of electrons and holes is the increase of the radiative recombination probability. In order to estimate the confinement energy, it is often sufficient to consider a model of a potential well with infinite high barriers, where the allowed electron wave vectors in z direction are given by $k_{z,n'} = n'\pi/d$, and the electron energy is given by:

$$E_{n',k} = E_{n',k_z} + E_{n',k_\parallel} = \frac{\hbar^2}{2m^*_{e,h}} \left[\left(\frac{n'\pi}{d} \right)^2 + k_x^2 + k_y^2 \right]. \tag{2.3}$$

Here n' is the subband index, $k_\parallel$ the in-plane component of the $\boldsymbol{k}$-vector, d the QW width and $m^*_{e,h}$ the electron/hole effective mass. Assuming a finite potential barrier height allows the electrons to tunnel into the barrier. The electron wave function decays exponentially in the barrier, and the eigen-energies are reduced compared to those of the infinitely deep well [13]. Within the well, the electron wave functions are approximately sinusoidal and have parities of $(-1)^{n'+1}$ ($n' = 1, 2, ...$ subband index).

The envelope function approximation, which is based on the $k \cdot p$-method, is often used to calculate the band structure of heterostructures [Bas81]. Herein the wave functions

[10] This so-called Anderson rule may, however, only be considered as a qualitative approximation [Bau83].

[11] $\lambda_{dB} = h/\sqrt{2\pi m k_B T}$. For an estimate, one can consider for an electron in GaAs an effective mass of $m^* = 0.067 m_e (k = 0)$ [Ada85]. Hence at $T = 4$ K a layer thickness of 144 nm would be sufficient to see quantized effects.

[12] In the following a cartesian coordinate system x,y,z is used with z being the growth direction

[13] Examples may be found in [Bas81; Bas85; Yu05].

are a product of fast oscillating Bloch functions and a slowly varying envelope function in the corresponding region of the heterostructure. Such calculations show that in 2D the size quantization lifts the degeneracy for the HH and LH bands at the Γ-point. Moreover, the HH and LH bands have a reversed correlation in the plane than along the quantization axis, yielding a coupling between HH and LH states for $k \gg 0$. This HH-LH mixing gives rise to a repulsive behavior of the two bands, the so-called HH-LH **anticrossing**, where the light hole and heavy hole character (band curvature) are exchanged (see figure 2.4).

In addition to the band structure theory, the interaction of free carriers is important in semiconductors. Due to the Coulomb interaction between electrons and holes, a bound state, a so called neutral **exciton**, is formed [14]. Excitons may be described analogously to a hydrogen model with discrete states below the bandgap energy, leading to an optical absorption below the bandgap, for more details see [Gru06; Yu05; Dya08]. In quantum wells, electron and hole wave functions overlap more because of the spatial confinement, yielding an increased binding energy for excitons compared to the bulk. For large electron densities, these excitons are not stable though, because the screening effects reduce binding energy.

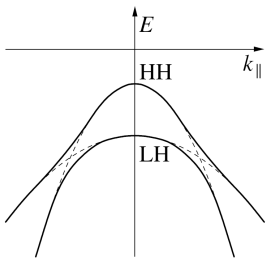

Figure 2.4: *Scematic picture of HH-LH anticrossing [Win03].*

Doping

The occupation of the bands is defined by the product of the density of states and the step-like Fermi-Dirac distribution: $f_e(E) = 1/\left(\exp\left[\left(E - E_F\right)/k_B T\right] + 1\right)$ with E_F the Fermi energy. For $E - E_F >> k_B T$ this function can be approximated by the Boltzmann distribution: $f_e(E) = 1/\left(\exp\left[\left(E - E_F\right)/k_B T\right]\right)$. In this case, the system is called nondegenerate (high T or small carrier density), otherwise the system is called degenerate (small T or high carrier density). If the Fermi level is within the band, the system is highly degenerate [Gru06]. In order to increase electrical properties, such as conductivity, the carrier concentration (electrons or holes) is intentionally increased by introducing impurities. III-V semiconductors are usually doped with materials of the IV group, typically C, Si. The temperature of the effusion cells in the MBE controls in which sublattice the doping atom is integrated and thereby whether the atom acts as donor or acceptor. Low-doped semiconductors obey nondegenerate statistics, whereas highly-doped semiconductors follow degenerate statistics (like metals).

Additionally to its effect on spin dephasing (discussed in section 2.2.4), the doping concentration has a strong influence on the optical absorption edge (see also section 2.2.1). On the one hand, because of the resident electrons in the CB owing to n-doping, higher energies are required to lift an electron from the VB into an unoccupied state in the CB. This shift in the absorption energy is called the **Burstein-Moss shift** Δ_{BM} [Mos54; Bur54]. On the the other hand, exchange and Coulomb interactions between the additional electrons as well as electron impurity scattering, lead to a reduction of the band gap, which is called **band gap renormalization** Δ_{RN} [Wal08; DS90; Kle85b]. Hence, the net change in the bandgap energy ΔE_g is $\Delta E_g = \Delta_{BM} - \Delta_{RN}$.

Although large carrier densities are essential for high mobilities, the ionized impurity atoms induce scattering, which reduces the carrier mobility. Heterostructures, however, provide the possibility to integrate the doping into the barriers (remote doping). The carriers diffuse into the energetically favored quantum well, and due to the spatial separation, scattering of electrons and doping atoms is reduced. Nevertheless, remote donor scattering (scattering via Coulomb interaction) still exists, which needs to be

[14] If an additional electron or hole is involved one speaks of a negatively or positively charged exciton.

suppressed by the incorporation of an additional undoped layer. Such a procedure is called modulation doping [Din78; Dru81]. The ionized donor concentration in the wide bandgap material and the electron concentration adjacent to the heterointerface introduce a built-in electric field (through Poisson's equation $\boldsymbol{\mathcal{E}} = -\nabla\phi$ with ϕ the electrostatic potential). This dipole layer gives rise to an equilibrium band bending. A single-sided doping (ssd) causes therefore the electron wave function to shift towards the doped layer and to penetrate deeper into the low mobility barrier material, which reduces the total mobility [15]. Thus, in order to achieve high electron mobilities double-sided doping (dsd) is employed. Using highly sophisticated growth schemes [Uma09] may achieve further enhancement, see also chapter 5.1 for more details. Additionally, a symmetric band profile is also essential for long spin lifetimes (see chapter 2.2).

2.1.2 Ferromagnetism in Gallium manganese arsenide

For the electrical spin injection discussed in chapter 4, a ferromagnetic contact composed of gallium manganese arsenide (Ga,Mn)As, introduces a spin polarization into GaAs bulk. Such an all-semiconductor device bears some advantages (described in chapter 2.2.1) compared to a combination of a ferromagnetic metal with a semiconductor. In a typical semiconductor like GaAs no magnetic order is present (diamagnetism may still exist). Furdya et al., however, proposed the doping of semiconductors with magnetic transition metals, yielding so-called diluted magnetic semiconductors (DMS) [Fur88]. DMS are an alloy between nonmagnetic and magnetic semiconductors [16] where the magnetic moments are randomly distributed in the host. (Ga,Mn)As [17], a DMS on the basis of the widely used semiconductor GaAs, was introduced by Ohno et al. [Ohn96; Ohn98]. In this material, the Mn atoms substitute ideally a Ga atom in the lattice. Although less likely, the Mn atoms may also be incorporated interstitially, meaning the Mn atom sits between the atom sites in the lattice. There are different possibilities for a Mn atom to incorporate into the lattice: two tetrahedral positions between four As/Ga atoms (T_{As4}, T_{Ga4}) or hexagonal positions between three As/Ga atoms. Yet T_{As4} is energetically favored [Maŝ04; Hol06]. The crystal structure of (Ga,Mn)As with both (substitutional, interstitial) incorporation cases is depicted in Figure 2.5 (a). In the crystal, substitutional manganese acts as an acceptor, since Mn has an electron less than Ga in the 4p shell (Mn = [Ar] $3d^5 4s^2$, Ga = [Ar] $3d^{10} 4s^2 4p^1$). This acceptor behavior, however may be compensated partially (even fully), due to interstitial Mn impurities, which act as double donors, owing to the two $4s^2$ electrons. The 3d shell of a Mn atom is only half occupied, yielding a magnetic moment of $5/2\,\mu_B$ according to Hund's rules [Lan77]. Since these electrons are not involved in the atomic bonding, the magnetic moment is conserved in the macroscopic material, bearing ferromagnetic behavior. Typically, the MBE growth temperature for GaAs is high ($\sim 600°$ C), to ensure a pure crystal growth. The low solubility of Mn in GaAs, however, would cause segregation at this high temperature, yielding a Mn accumulation on the surface. Therefore, low temperatures are necessary on the one hand to incorporate the Mn atoms, but on the other hand, are giving rise to the implementation of defects. Eventually, the combination of growth temperature and the Mn concentration determines the state of the alloy. The phase transitions of the alloy depending on growth temperature and Mn concentration are depicted in figure 2.5(b). At low temperatures a transition from

[15] Typically one distinguishes in ssd heterostructures on which side of the GaAs layer the doping is introduced. In a normal heterostructure the doping is on top of the GaAs layer. Is this on the contrary the other way around one speaks of a inverted heterostructure. Although an inverted structure allows a better formation of an ohmic contact, the electron mobility is lower due to dopant migration in growth direction [Sht88].

[16] Magnetic semiconductors like MnAs contain a sublattice with magnetic elements.

[17] The notation according to section 2.1.1 $Ga_{1-x}Mn_xAs$ is also often used.

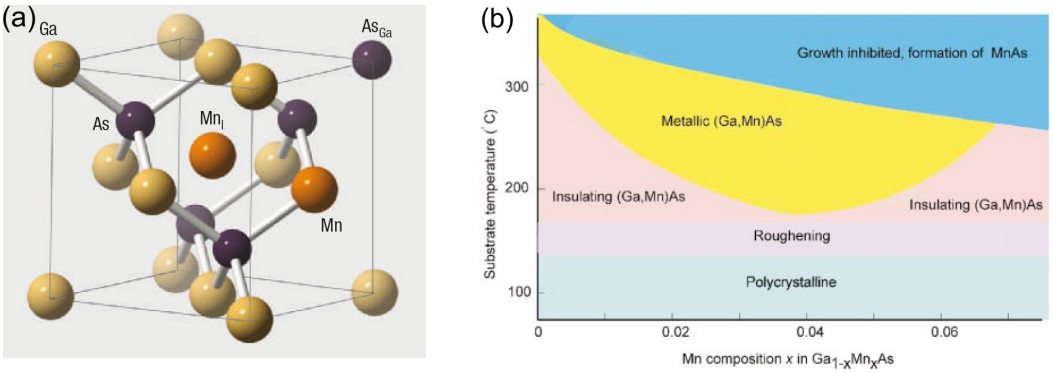

Figure 2.5: ***(a)*** *Crystal structure of (Ga,Mn)As. Defects in the crystal structure are for example As anti-sites As_{Ga}. Mn_I represents a Mn interstitial. Taken from [Mac05].* ***(b)*** *Schematic phase diagram showing the properties of (Ga,Mn)As, grown by MBE, depending on substrate temperature and Mn concentration. Taken from [Ohn98].*

the insulating to the metallic phase happens with rising Mn concentration, whereas for very high temperatures and high Mn concentrations (metallic) MnAs crystallizes in a NiAs-structure [Ohn98]. The growth of the desired metallic (Ga,Mn)As requires low temperatures ($\sim$ 230° C to $\sim$ 260° C) and a Mn concentration of 2% to 6%. The drawback of the low temperature growth is the inclusion of further impurities like Ga vacancies (not occupied Ga site, acts as acceptor) or As antisites (As on a Ga site, acts as double donor, As_{Ga}) in the crystal.

Below the Curie temperature (T_C) ferromagnetic materials have a nonvanishing spontaneous magnetization $\boldsymbol{M}$, even in the absence of an external magnetic field. In this regime the magnetic moments are oriented parallel within domains, and an external magnetic field may align the magnetization directions of the domains macroscopically. Above T_C on the contrary, the magnetic moments are randomly oriented in the paramagnetic phase. In a phenomenological description of ferromagnetism, the magnetic moments align in such a way that the total energy consisting of the exchange energy and the kinetic energy is minimized, yielding an energy splitting in the density of states of the two spin orientations, see figure 2.6. A simple model to describe ferromagnetism is the Heisenberg model. In this approach the two nearest neighbor spins couple (anti)ferromagnetically according to the Heisenberg Hamiltonian:

$$\hat{H}_H = -\sum_{i,j} \tilde{J}_{i,j} \boldsymbol{S_i} \cdot \boldsymbol{S_j}, \qquad (2.4)$$

where $\boldsymbol{S}_{i,j}$ are two nearest neighbor spins and $\tilde{J}_{i,j}$ is the exchange integral [18]. There are various kinds of exchange interactions. In the common 3 d transition metals for example, the ferromagnetism is based on the direct exchange interaction, which is an interplay between the Coulomb interaction and the Pauli principle [19]. In (Ga,Mn)As, due to the dilute incorporation, the average distance of magnetic moments is too large to allow for a direct exchange coupling, since the overlap of the wave functions of the involved spins is

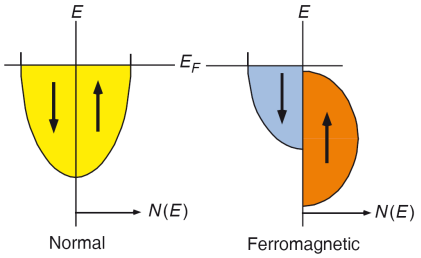

Figure 2.6: *The density of states for the two spin orientations is split in the energy for a ferromagnet. Taken from [Pri98].*

[18] The sign of $\tilde{J}_{i,j}$ defines the type of the coupling: $\tilde{J}_{i,j} < 0$ means antiferromagnetic and $\tilde{J}_{i,j} > 0$ means ferromagnetic coupling

[19] [Blu01; Stö06] for example, include a detailed discussion of ferromagnetism.

too small. Nevertheless, Ohno et al. observed a ferromagnetic order in (Ga,Mn)As for Mn concentrations higher than 1% [Ohn96; Ohn98], indicating that the ferromagnetism in (Ga,Mn)As is caused by an indirect exchange interaction, the so-called RKKY (Rudermann, Kittel, Kasuya, Yosida [Rud54; Kas59; Yos57; Blu01; Stö06]) interaction based on itinerant holes. A magnetic impurity within a metallic material is screened by the itinerant carriers. In this process, the carriers get spin polarized and can couple with other close-by magnetic moments [20]. The resulting exchange integral in equation 2.4, in the case of RKKY interaction, has an oscillatory behavior: $\tilde{J}_{i,j} \propto cos(k_F r_{i,j})/r_{i,j}^3$ with k_F the Fermi wave vector and $r_{i,j}$ the distance between the two coupled magnetic moments.

For the metallic (Ga,Mn)As, with Mn concentrations of $1 - 12\%$, the distances are small enough to assume only antiferromagnetic coupling [Jun06]. Thus, the holes couple antiferromagnetically with the localized 3d electron spins (p-d interaction), yielding a local ferromagnetic coupling between two Mn magnetic moments. In the case the hole concentration is large enough, the hole impurity band merges with the GaAs valence band, and the holes, that are now freely propagating, align the Mn spins all over the sample. Dietl et al. [Die00; Die01] developed a mean-field Zener model to describe the ferromagnetism in (Ga,Mn)As in detail. In this approach the p-d interaction is considered as an effective magnetic field which causes a spin splitting in the valence band. Below the Curie temperature, it is energetically more favorable to align the Mn spins than to redistribute the holes. The expression found for the Curie temperature is:

$$T_C \propto x_i n_h^{1/3}, \tag{2.5}$$

with n_h the hole concentration and x_i the effective Mn concentration [21]. Compared to the magnetic 3d materials, the Curie temperature in (Ga,Mn)As is lower, since the indirect exchange coupling is weaker than the direct exchange. A high Mn concentration, as well as a high hole concentration, is necessary in order to achieve high Curie temperatures. This, however, requires low growth temperatures, yielding the incorporation of impurities which again may compensate the p-doping, that is essential for the ferromagnetic coupling. The initial Curie temperatures of 60 K to 110 K [Mat98] could be topped by including post-growth annealing processes [22] [Hay01; Edm02; Pot01], and Curie temperatures up to 173 K were reported [Wan05a; Jun05]. Recently it was shown that (Ga,Mn)As nanostructures may have a Curie temperature of up to 200 K [Che11]. Maccherozzi et al. found a robust magnetic coupling between a thin Fe film epitaxial grown on top of an undoped (Ga, Mn)As (100) layer. Thus, in the paramagnetic (Ga, Mn)As, ferromagnetic proximity polarization induces ferromagnetic order. This approach could produce a stack of Fe/(Ga, Mn)As thin layers with a Curie temperature up to room temperature.

2.2 Spin in Semiconductors

Electrons carry an intrinsic form of angular momentum called spin [Uhl26]. Although such a spin can point in any direction, according to the uncertainty relation, only one component can be measured at a time, giving two possible eigen-values $s_i = \pm\hbar/2$ ($i = \{x, y, z\}$). The associated magnetic moment $\bar{\mu}_i = -g_0\mu_B s_i/\hbar$ is antiparallel to the spin angular momentum. Hence, the ratio of the spin angular momentum and the magnetic moment (also gyromagnetic ratio) is characterized by the Bohr magneton $\mu_B = e\hbar/2m_e$

[20] An equivalent phenomenon based on electric charges in metals are the Friedel oscillations [Fri54].

[21] A review of further properties of (Ga,Mn)As may be found in [Jun05].

[22] After the MBE growth the sample is heated. Thus, the weakly bound defects like As antisites or Mn interstitials are thermally activated and diffuse to the surface, leading to a purer crystal structure.

and a dimensionless quantity, the so called g-factor g_0, also called gyromagnetic factor or Landé factor. From the Dirac equation a value of $g_0 = 2$ for a free electron is derived. Quantum electrodynamics, however, provides a correction of $g_0 = 2\,(1 + \alpha'/2\pi + ...) \approx 2.0023$ (with $\alpha' = e^2/\,(4\pi\epsilon_0)\,\hbar c$ fine structure constant) [Sch00b; Sch48; Odo06]. In a semiconductor crystal the electron g-factor may deviate from the vacuum value due to the influence of the spin-orbit interaction, see chapter 2.2.2 for a detailed discussion. The quantum state of a spin-1/2 particle is described by a normalized two-component vector (spinor) in Hilbert space, and the corresponding spin operators are represented by 2×2 matrices, the Pauli matrices $\hat{s}_i = (\hbar/2)\,\hat{\sigma}_i$. In a nonmagnetic semiconductor at equilibrium the spins are statistically oriented. Various methods discussed in section 2.2.1 can be applied to create a surplus of one "spin kind". Such a degree of spin polarization is given by:

$$P = \frac{n_\uparrow - n_\downarrow}{n_\uparrow + n_\downarrow}, \tag{2.6}$$

where $n_{\uparrow\downarrow}$ represents the carrier density of the two spin types. One distinguishes the degree of spin polarization from the spin polarization, which is defined as oriented non equilibrium spins per area in a 2D system or spins per volume in bulk:

$$P_S = P \cdot n, \tag{2.7}$$

with n the carrier density, which is the number of spins per area N/A or per volume $N/\tilde{V}$.

In the following, means to induce such a spin imbalance in a semiconductor are presented, succeeded by the introduction of spin-orbit interaction (SOI) 2.2.2. SOI not only has an impact on the magnetic moment and the electron g-factor, but is also responsible, with the crystal symmetry, for breaking the spin-degeneracy. After establishing the general terms of spin dynamics, spin relaxation and spin dephasing in section 2.2.3, the spin dephasing mechanisms important for this work are presented in section 2.2.4. This chapter closes with a discussion on the special case of (110)-grown quantum wells 2.2.6.

2.2.1 Generation of a spin polarization

In a nonmagnetic semiconductor the spins are statistically oriented, in a way that spin up and spin down orientations are balanced. Finding an effective manner to create a spin imbalance has been a great effort in science recently. In this work, the spin injection is done optically with a circularly polarized laser, and electrically using a ferromagnetic (Ga,Mn)As electrode. Both methods are introduced in the following. There are, however, other means to create a spin imbalance. One example is the Spin Seebeck effect, where spin imbalance arises due to a thermal gradient [Uch08]. Another viable method is the Spin Hall effect, which is based on the fact that an electrical current driven through a material with a strong spin-orbit interaction yields a spin imbalance at the edges of the conducting channel [Dya71b; Dya71a; Kat04b].

Optical spin injection

The interaction of light with a semiconductor crystal may be described similar to the interaction of light with a single atom, providing a symmetry, that is high enough for an isotropic momentum distribution of electrons and holes. Typically, the transition probabilities between two states are given by Fermi's golden rule, which is derived by solving the time-dependent Schrödinger equation [Sch00b]:

$$\tilde{T}_{i\to f} = \frac{2\pi}{\hbar} \sum_f \left|\langle f\,|V_{fi}|\,i\rangle\right|^2 \delta\left(E_f - E_i \pm \hbar\omega\right), \tag{2.8}$$

with $\langle i|$ and $|f\rangle$ the initial and final states and V_{fi} the perturbation operator. The delta function term indicates the conservation of energy, where an incident photon creates an electron-hole pair in conduction and valence band for $\hbar\omega \geq E_g$. Since the momentum of the photon is evanescently small compared to the electron momentum, the momentum transfer due to the conservation of momentum is neglected ($p_e - p_h = h/\lambda \approx 0$), implicating a vertical transition in $\boldsymbol{k}$-space ($k_e \approx k_h$). In first order, V_{fi} is approximated by an electrical dipole potential. The possible transitions are constrained by selection rules obtained in first order through the electric dipole approximation. In the limit of weak SOI, the electric dipole operator does not depend on the spin. Hence, the conservation of angular momentum in interband transitions leads to selection rules for the total angular momentum $J = 0, \pm 1$ and its projection on the quantization axis (magnetic quantum number) $m_J = \pm 1$ [23]. These selection rules are satisfied by left (σ^+) or right (σ^-) circularly polarized photons incident along the quantization axis, since they carry an angular momentum $s = 1$ with $m_{ph} = \pm 1$. The relative transition probabilities, for $\sigma^{\pm}$-light, are derived from the matrix element in equation 2.8, and are depicted in figure 2.7 (a), for σ^+-light in the case of GaAs-bulk. An excitation from all three valence bands would therefore imply no spin polarization. A spectrally narrow excitation, leaving out the split-off band, however, results in a spin polarization of 50% according to equation 2.6 ($P = (3-1)/(3+1) = 0.5$). As discussed in chapter 2.1.1, the spatial confinement in a quantum well lifts the degeneracy of the HH and LH-bands. In the case that the spectral width of the excitation is small enough, and only electrons from the HH-band are excited, a spin polarization of 100% is achieved (figure 2.7 (b)). According to the conservation of angular momentum, for incident light along the quantization axis, the generated spin imbalance is oriented along the sample normal. Certainly, these selection rules are valid for emission as well, see chapter 3.3.

In (modulation) doped quantum wells, resident electrons occupy the states up to the

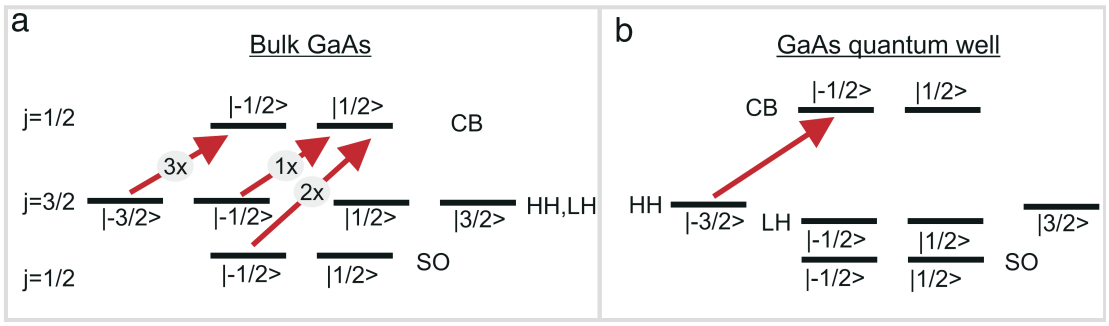

Figure 2.7: ***(a)*** *Transition probabilities for σ^+-light, in GaAs-bulk at the Γ-point. As shown in chapter 2.1.1, GaAs has a direct bandgap with a Γ_6 conduction band and a Γ_8 valence band.* ***(b)*** *In a Quantum well, spectral narrow excitation can produce full spin polarization, due to the HH-LH splitting. Taken from [Kor10].*

Fermi energy, which is in a 2DES represented by a Fermi disc in $\boldsymbol{k}$-space. Optical excitation is only possible for wave vectors around the Fermi disc (see figure 2.8). The admixture of HH and LH states in the VB for $\boldsymbol{k} > 0$ (chapter 2.1.1) results in excitation of both spin orientations, yielding reduced net spin polarization [Pfa05]. Thus, equation 2.6 is modified to [Kor10]:

$$P_{red} = \frac{n_{opt}}{n_e + n_{opt}^{tot}}, \tag{2.9}$$

[23] In quantum wells, the different parity of the envelope function implicates the selection rule $\Delta n' = 0$ in case of infinite barrier height, otherwise $\Delta n' = 0, 2, 4, ...$ with n' the subband index. This condition can be lifted due to asymmetries, e.g. the different effective masses of electrons and holes cause a not equal penetration of the wave functions into the barrier materials.

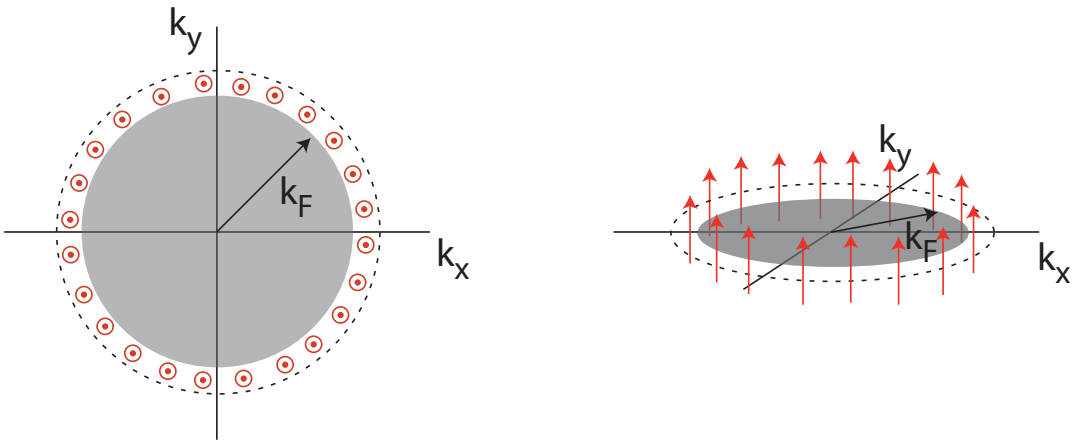

Figure 2.8: *Optical orientation in a 2DES. In doped quantum wells, resident electron occupy states up to the Fermi wave vector k_F. Optically excited states are around the Fermi disc. The spin polarization is parallel to the quantization axis. Taken from [Gri12b].*

with n_{opt}^{tot} is the total optically created electron density, n_e the density of the resident electron and $n_{opt} = \xi \cdot n_{opt}^{tot}$ the spin polarized portion of n_{opt}^{tot}. Because of the admixture of HH and LH band and the scattering between them, the spin polarization of the optically created holes dephases very quickly. Usually, this dephasing takes place on the scale of the momentum scattering time, which is below the photocarrier recombination time. Therefore, the holes recombine as well with background electrons leaving a spin polarization in the resident electrons. The optically created electron density within the laser spot can then be approximated as follows:

$$n_{opt}^{tot} = \frac{0.86}{\pi r^2} \cdot \tilde{\alpha}_{ab} \cdot \left(\bar{P}\lambda/hc\right) \cdot \tau_{ph}. \tag{2.10}$$

The first term describes the effective illuminated area of a gaussian beam profile. $\tilde{\alpha}_{ab}$ is the absorption coefficient. The third term describes the photon number per second with $\bar{P}$ average laser power and λ the laser wavelength. τ_{ph} is the photocarrier lifetime. An asymmetry in the quantum well reduces the absorption energy due to the quantum confined Stark effect, and the overlap of the electron and hole wave function is decreased causing a lowering of the recombination efficiency[Mil84].

Electrical spin injection

The concept of a spin field effect transistor (sFET) Datta and Das proposed [Dat90] raised great research interest in how to inject a spin polarization electrically, from a ferromagnet into a semiconductor. The discussion in this section starts by examining the spin polarization in the ferromagnetic contact and at the interface with a semiconductor in general, and continues focusing on the case of the p^+ (Ga, Mn)As/ n^+ GaAs Esaki Zener diode structure, which is used as a spin injection device in chapter 4.

In a ferromagnetic material the two spin subbands are split in energy, because of an exchange interaction, as described in section 2.1.2. Therefore, the densities of states (DOS) at the Fermi energy differ for the two spin orientations, yielding a strong impact on the mobility μ (see chapter 2.3.1) for those two spin kinds, since the scattering takes place at values around the Fermi energy. The total current through a ferromagnet can be described by the two current model proposed by N.F. Mott [Mot64; Fer68], where the two spin species are described by independent currents with different mobilities.

Thus, the current spin polarization P_j, caused by the split in the Fermi energies, can be described analogously to equation 2.6. In general this value is different from the density spin polarization P degree though. For a homogenous nonmagnetic semiconductor, the relation between P_j and P is given by[Yu02b]:

$$P_j(x) = \frac{j^{\uparrow} - j^{\downarrow}}{j^{\uparrow} + j^{\downarrow}} = P(x) + \frac{D}{\mu\mathcal{E}} \cdot \frac{dP}{dx}, \tag{2.11}$$

with D the diffusion constant, μ the mobility, and $\mathcal{E}$ the electric field. Moreover, a current density can be defined in the ferromagnet F and in the non magnetic material N by:

$$j_{F,N} = \tilde{\beta}_{F,N} j^{\uparrow}_{F,N} + \left(1 - \tilde{\beta}_{F,N}\right) j^{\downarrow}_{F,N}. \tag{2.12}$$

The parameter $\tilde{\beta}_{F,N}$ is a dimensionless parameter indicating the asymmetry of the current (in equilibrium: $\tilde{\beta}_N = 0.5$). P_j at a ferromagnet/nonmagnet interface (F/N) is often called spin injection efficiency, and is given by: $P_j = 2\tilde{\beta} - 1$ [Stö06]. Since charge neutrality requires a constant current density across the F/N interface, the different current densities on each side adjust to the interface value. The electrochemical potential $\tilde{\mu}$ [24] splits, therefore, for up and down spins at the interface. Hereby spin flips are induced (majority spins transform into minority spins) and a spin accumulation at the interface occurs $\tilde{\mu}_s = \tilde{\mu}^{\uparrow} - \tilde{\mu}^{\downarrow}$ [Val93; Cha07b], which implicates a nonequilibrium magnetization in the nonmagnetic material, see figure 2.9. Such a spin accumulation $\tilde{\mu}_s$ obeys a spin diffusion equation $\nabla^2\tilde{\mu}_s = \tilde{\mu}_s / L_s^2$ [Son87; Val93; Fer01; Žut04], where the spin diffusion length $L_s^{F,N}$ depends on the spin relaxation rate (described in chapter 2.2.4) of both the ferromagnet and the non magnetic material. In case of a transparent contact, meaning without an interface resistance, the spin accumulation is equal on both sides of the interface and decays exponentially [Fer01; Jaf02].

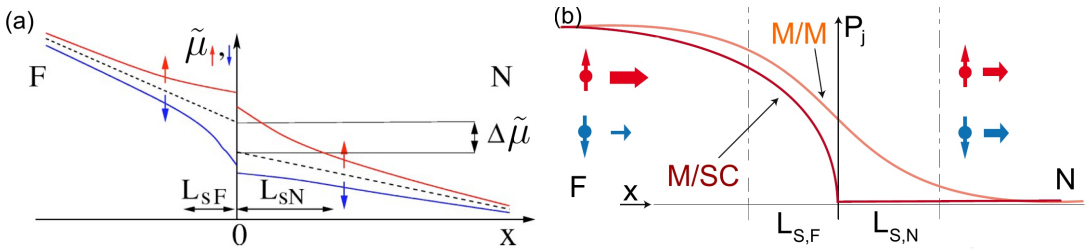

Figure 2.9: ***(a)*** *Interface between ferromagnet and nonmagnet. The chemical potentials $\tilde{\mu}^{\uparrow,\downarrow}$ for spin up and spin down are discontinuous in the case of a small interface resistance. This allows for an efficient spin injection. In the case of a transparent interface, on the contrary, $\tilde{\mu}^{\uparrow,\downarrow}$ would be continuous and the two diffusion lengths $L_{sF,N}$ are equal, and for a common spin polarization of a ferromagnet no effective spin injection is possible. The discontinuity of the averaged chemical potentials is called the spin accumulation voltage $\Delta\tilde{\mu}$. Taken from [Žut04].* ***(b)*** *The width of the zone of the spin accumulation is determined by the spin diffusion length $L_{sF,N}$. The spin polarization P_j decreases continuously from the ferromagnet to the nonmagnet. The huge difference in the conductance between metal (M) and semiconductor (SC) causes almost the whole spin polarization to relax before the interface. Adapted from [Cha07b].*

[24] The electrochemical potential is defined as the change in the energy in a thermodynamical system if an additional particle is added. For $T = 0$ it is identical to the Fermi energy, and even at room temperature the Fermi energy is a good approximation for the chemical potential. A general expression is: $\tilde{\mu} = E_F\left[1 - (\pi^2/12) \cdot (k_B T/E_F)^2\right]$. The current densities can be expressed in terms of the electrochemical potential with Ohms law: $j^{\uparrow,\downarrow} = \tilde{\sigma}\nabla\tilde{\mu}^{\uparrow,\downarrow}$ (with $\tilde{\sigma}$ the conductivity) [Stö06].

The first experiments of spin injection in semiconductors showed very poor injection efficiency [Ham99; Lee99]. The reason is the so-called **conductivity mismatch** [Sch00a]. In the ferromagnet, the density of states (DOS) is several orders of magnitude higher than the DOS in a semiconductor [Fer01]. In order to adjust the continuity conditions at the interface, the spin polarization almost completely relaxes through spin flip on the ferromagnetic side (see figure 2.9 (b)). An efficient spin injection, however, requires a spin polarization at the interface of almost 100% [Sch00a]. The spin polarization at the interface ($\beta_N = \beta_F$) follows from equation 2.11, with the definition of the resistivity for a spin channel as $\rho_F^{\uparrow(\downarrow)} = 2\left[1 - (+)\beta_F\right]\rho_F$ and $\rho_N^{\uparrow(\downarrow)} = 2\rho_N$, by Fert et al. [Fer01]:

$$P_{interface} = \frac{\beta}{1 + r_N/r_F}. \tag{2.13}$$

$r_{F,N} = \rho_{F,N} \cdot L_s^{F,N}$ is the effective resistance for spin polarized transport. The ratio r_N/r_F is about a factor 10^6, which results in a vanishing spin polarization at the interface [25] [Fer01]. A solution for the conductivity mismatch problem is introducing a spin-dependent interface resistance [Fil00; Ras00; Fer01]. Equation 2.13 is then modified to:

$$P_{interface} = \frac{\beta r_F + \tilde{\gamma} r_b}{r_F + r_N + r_b}, \tag{2.14}$$

where r_b is the interface resistance, and $\tilde{\gamma}$ is an asymmetry parameter. For $r_b \gg r_N, r_F$ the interface resistivity dominates, and the effect of r_N/r_F is neglected. Additionally, the chemical potentials $\tilde{\mu}^{\uparrow,\downarrow}$ are not continuous at the interface anymore, yielding a much higher spin accumulation μ_s on the nonmagnetic side than in the ferromagnetic side. This implies a more balanced spin flip rate in both materials [Fer01]. Eventually, the spin accumulation in the semiconductor is then given by [Fab07]:

$$\mu_s = P_j \cdot j r_N, \tag{2.15}$$

The difference of the averaged chemical potentials at the interface $\Delta\tilde{\mu}$ is called the spin accumulation voltage. This voltage includes drift as well as diffusion effects and causes a movement against the applied voltage, which results in an additional resistance called spin bottleneck effect [Joh91; Fab07].

One possibility for the realization of such an interface resistance is the introduction of a **tunnel barrier** between ferromagnet and semiconductor. According to Juliere's model, the spin is conserved during tunneling and the conductance of a particular spin kind is the product of the density of states on both sides. Therefore, the resistivity for majority spins is lower than for minority spins [Jul75]. The spin accumulation expressed in equation 2.15 is then depending on the polarization $P_{j,tunnel}$ at the tunnel barrier. So far various kinds of tunnel barriers have been proposed, starting with Alvaro et al., who showed spin injection from a ferromagnetic STM tip, where the tunnel barrier is vacuum, with an efficiency up to 30% [Alv92]. Another possibility is the use of a Schottky barrier. The mismatch of the Fermi energies at a metal/semiconductor interface causes a band bending. Most metal semiconductor combinations form a depletion zone at the interface, called Schottky barrier (see e.g. [Gru06] for details). Zhu et al., Hanbicki et al., and Adelmann et al. used an iron contact on a GaAs-based structure and detected the spin polarization by analyzing the polarization of the electroluminescence in a LED structure, a so-called spin-LED [Zhu01; Han03; Ade05]. Crooker et al. utilized a similar combination for the spin injection. The detection method in this case, however, was

[25] For example Co has $\rho_{Co} = 7.5 \cdot 10^{-8}$ Ωm, $L_{sf}^{Co} = 59$ nm, $\tilde{\beta}_{Co} = 0,46$. This results in $r_{Co} = 4.5 \cdot 10^{-15}$ Ωm^2. For GaAs the values are: $\rho_{GaAs} = 2.4 \cdot 10^{-3}$ Ωm, $L_{sf}^{GaAs} = 1.83$ μm and $r_{GaAs} = 4.4 \cdot 10^{-9}$ Ωm^2 [Fer01].

Kerr microscopy [Cro05b; Cro05a; Cro07; Fur07]. Kotissek et al. also used a Schottky tunnel barrier of FeCo contact on GaAs. Furthermore they could apply Kerr microscopy on the cleaved edge of the sample. Another way to create a tunnel barrier is by inserting an isolating material between the ferromagnetic contact and the semiconductor. The advantage here is the physical separation between injector and semiconductor which increases the chemical stability of the interface. Jiang et al used MgO as insulator and as injector Co/Fe on top of a GaAs-based spin LED structure [Jia05]. In a similar structure Motsnyi et al. used Al_2O_3 as insulating material [Mot02].

A different approach to avoid the conductivity mismatch, is to use an all-semiconductor device, which has the advantage of an integrated epitaxial growth. First, Ohno et al. realized the injection of spin-polarized holes from the ferromagnetic p-doped (Ga,Mn)As into n-GaAs [Ohn99a]. They detected the spin polarization with a spin-LED structure. Electron spin injection, however, is preferable, due to the small hole spin lifetimes in GaAs, caused by the high SOI in the VB (see chapter 2.2.4). A way to realize such spin-polarized electron injection is a **p^+(Ga,Mn)As/ n^-GaAs Esaki Zener diode** structure, first shown by Khoda et al. [Koh01]. In further experiments, a spin polarization of up to 80% could be achieved [JH02; VD04]. The detection in these experiments was based on a spin LED structure as well. An all-electrical injection and detection scheme presented by Ciorga et al. exhibits a spin injection efficiency between 50% and 80% [Cio09; Cio11; Cio13]. The principle of an Esaki diode structure rests on a reverse biased p-n junction, consisting of two highly degenerate materials. In the case that the depletion zone is small enough, spin polarized electrons are tunneling from the VB of the p-doped side to the CB of the n-doped side because of an applied electric field [Esa58]. The (Ga,Mn)As and the GaAs are highly doped so that the Fermi energy lies in the VB in (Ga,Mn)As (p^+), and in the CB in GaAs (n^+). At a p-n junction the majority carriers diffuse into the adjacent layer, due to the gradient, which is caused by the doping. The remaining ion cores give rise to an electric field which induces minority carrier drift. In equilibrium both currents are equal. The diffusion process aligns the Fermi levels of the two layers which results in a band bending, see figure 2.10. Usually,

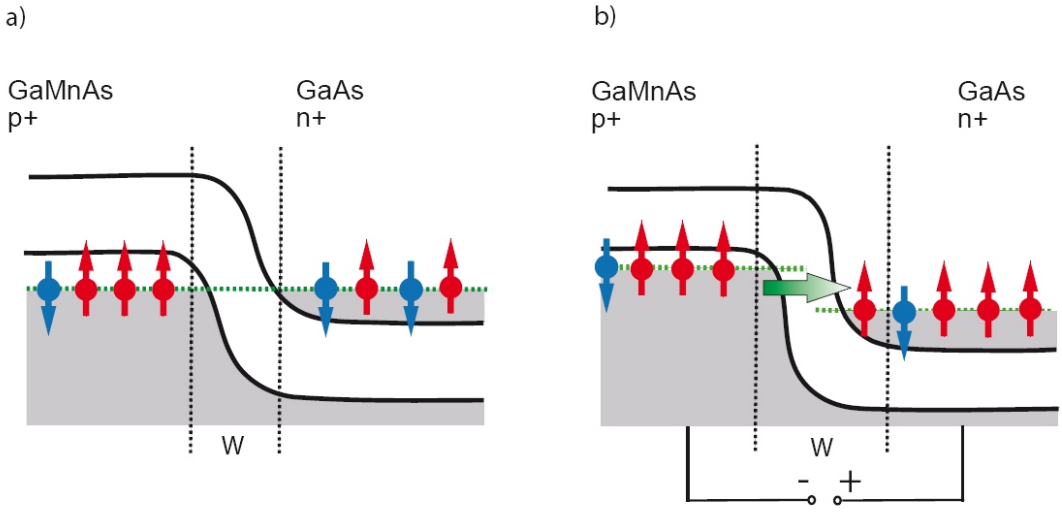

Figure 2.10: ***(a)*** *A p^+(Ga,Mn)As/ n^-GaAs Esaki Zener diode in equilibrium. The quasi Fermi niveaus arr due to the high doping in the Vb respectively the CB.* ***(b)*** *By applying a small reverse bias, the quasi Fermi niveaus are separated by $e \cdot V$ with V the applied bias. Hence spin polarized electrons tunnel from the VB of the ferromagnet into the CB of the semiconductor resulting in a spin polarization there.*

the difference of the two Fermi niveaus is of the order of the GaAs band gap [Utz12]. The samples used in this work have a Mn concentration of about 5.5%, which results in a hole concentration of 10^{20}cm^{-3} [Utz12], that is about four magnitudes higher than the doping concentration of the GaAs. Hence, the band bending on the GaAs side is more pronounced. The width W of the depletion zone is given by [Gru06; Sho49]:

$$W = \sqrt{\frac{2\varepsilon}{e} \cdot \frac{n_a + n_d}{n_d n_a} (V_{bi} - V)}, \tag{2.16}$$

where $n_{a,d}$ are the acceptor/donator doping densities, $\varepsilon = \varepsilon_0 \varepsilon_r$ is the permittivity and $V_{bi} = (k_B T/e)\, ln\left[\left(n_a n_d / n_i^2\right)\right]$ (n_i is the intrinsic carrier density) is the built-in voltage due to the ionized doping atoms, and V is the applied voltage. In case of high enough doping, the depletion zone is thin enough to allow tunneling. A small reverse bias applied on the Esaki diode [26], shown in figure 2.10, causes a shift in the quasi Fermi levels allowing spin polarized electrons to tunnel into the semiconductor. According to the standard model a forward bias yields an extraction of majority spins (higher conductance in the interface) leaving a measurable spin polarization of minority spins. This is not always the case as discussed in chapter 4.3.2.

For efficient spin-dependent tunneling the band structures of the involved materials need to be considered as well. Typically, a complex band structure is calculated, as depicted in figure 2.11, and the symmetry matching of the wave functions on the interface reveals the tunnel probabilities. At the interface, the wave vector splits into a component parallel to the interface $k_{\|}$, which is conserved in epitaxially grown structures because of the spatial symmetry. The perpendicular component contains an imaginary part $k_{\perp} = q + i\kappa$ describing the exponential decay of the wave function towards the surface, with κ the decay parameter [Mav00]. Inside the bandgap, the momentum is imaginary. Thus, in the tunneling process CB and VB are connected through imaginary trajectories in the E-k space. Figure 2.11 (a) shows such connecting loops for tunneling from states close to the Γ-point for low bias.

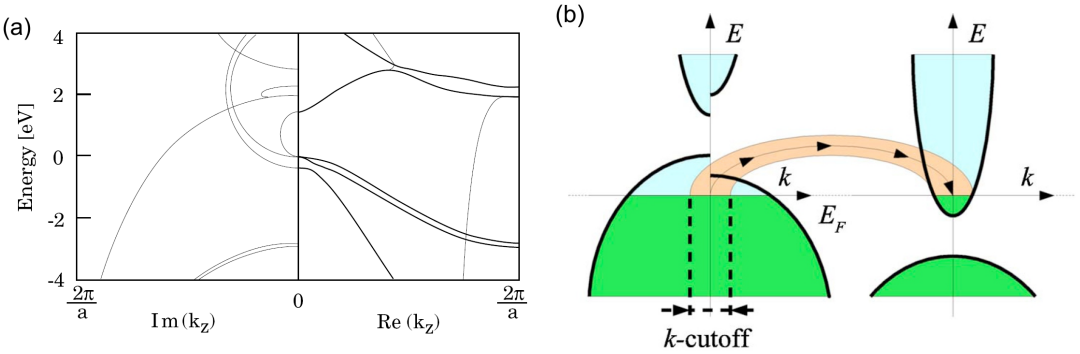

Figure 2.11: ***(a)*** *In the low-bias limit the LH states are connected with the CB minimum, the HH states are connected to higher states in the CB. Taken from [DC03].* ***(b)*** *Only states around the Γ-point participate in the tunneling, for low biases, since the* $\boldsymbol{k}_{\|}$ *vectors must match. Taken from [San07].*

Since the $k_{\|}$ components are preserved in tunneling, only states close to the Γ-point, with matching $k_{\|}$ components are involved in the tunneling. Such a k-cutoff is depicted in figure 2.11 (b). According to Sankowski et al. the spin polarization increases for larger $k_{\|}$ values [San07]. Hence, to rise the doping concentration in the GaAs would increase

[26] A reverse bias means that the (Ga, Mn)As contact is at a negative potential compared to the GaAs. The opposite case is forward biased.

the current spin polarization. Then again, the spin lifetime in the GaAs decreases for high doping concentrations (see chapter 2.2.5). Thus, a careful optimization of the parameters is essential. Because of the large Fermi energy, the tunneling electrons have a large-enough parallel component so that a significant spin polarization may be achieved by including HH states in the tunneling (to higher CB states due to the wave function symmetry). Sankowski et al. also showed that the spin polarization is maximal for $k_{\|}$ parallel to the magnetization M. The reason is that the heavy hole spin is polarized along $\boldsymbol{k}$ and the exchange splitting vanishes for $\boldsymbol{k} \perp \boldsymbol{M}$ [Die01]. Further calculations have proven an increase in the spin polarization for higher Mn content but a decrease for a higher hole concentration [San06]. To determine the actual injected spin polarization, the exact knowledge of the band structures and the transmission probabilities of the interface is required.

2.2.2 Spin-orbit interaction and symmetry

In a semiclassical picture, a moving electron senses any electrical field as magnetic field $\boldsymbol{B}$ ($\boldsymbol{B} = \boldsymbol{v} \times \boldsymbol{\mathcal{E}}/c^2$, with $\boldsymbol{v}$ electron velocity, c the speed of light) [Jac99] [27]. Considering an electron in a resting frame and the nucleus moving, the resulting current generates a magnetic field according to Biot-Savart's law [Jac99]. This magnetic field is called spin-orbit field, since it originates from the orbital motion and it is acting on the electron spin. A more sophisticated description of physics involving the spin of fermions, is the Dirac equation [Dir28]. This approach describes fermions quantum mechanically and considers also special relativity, in contrast to the Schrödinger equation. Reducing the four-component Dirac equation to two components, and keeping terms of the order $1/(mc)^2$ from the resulting power series, the spin-orbit interaction term can be derived as [Ell54; Sch00b]:

$$\hat{H}_{SO} = \frac{\hbar}{4m_0^2c^2}\hat{\boldsymbol{p}} \cdot (\hat{\boldsymbol{\sigma}} \times \nabla V(\boldsymbol{r}))\,, \tag{2.17}$$

where m_0 is the free electron mass, $\hat{\boldsymbol{\sigma}}$ is the vector of the Pauli matrices and $\hat{\boldsymbol{p}}$ is the linear momentum operator. In an isolated atom, $V(\boldsymbol{r})$ would be the Coulomb field of the nucleus and the core electrons. Here, it influences the splitting of atomic levels (fine structure), which increases for heavier atoms (large Z) [Dya08]. Concerning semiconductors, $V(\boldsymbol{r})$ represents the interaction of an electron spin with the average electric field consisting of the periodic lattice potential and other induced fields. In this case the SOI is enlarged by a factor m_0c^2/E_g relative to the vacuum case, under the condition that the gap energy and the spin-orbit splitting are of comparable magnitude ~ 1 eV [Ras06]. Hence, SOI is strong for narrow-bandgap semiconductors [Win03]. Of course, the influence of SOI on electrons in the CB, because of their s-like character ($l = 0$), is comparatively small to carriers in the VB ($l = 1$). Moreover, the SOI lifts the degeneracy in the VB (see chapter 2.1.1). Additionally, the magnetic dipole moment of an electron in a solid with SOI must consequently consist of an orbital and a spin contribution as well. The total magnetic moment is then $\bar{\mu}_J = -g\mu_B\boldsymbol{J}/\hbar$ (with $\boldsymbol{J} = \boldsymbol{S} + \boldsymbol{L}$ the total angular momentum).

The symmetry of a semiconductor structure has a strong influence on the SOI. An existing space inversion symmetry implicates that the energy for spin up and spin down are degenerate $\epsilon_\uparrow(\mathbf{k}) = \epsilon_\downarrow(\mathbf{k})$ [28]. This is the consequence of the time-reversal symmetry ($t \to -t : \epsilon_\uparrow(\mathbf{k}) = \epsilon_\downarrow(-\mathbf{k})$)[29] and the space-inversion symmetry ($r \to -r : \epsilon_\uparrow(\mathbf{k}) =$

[27] In this picture, a correction of a factor 1/2 is actually necessary, the so called Thomas correction [Tho26].

[28] For example in silicon (diamond structure).

[29] Kramers' theorem states, in the absence of an external magnetic field, for time reversal $k \to -k$ and $\sigma_\uparrow \to \sigma_\downarrow$.

$\epsilon_\uparrow(-\mathbf{k})$) [Dre55] [Fab07]. A break in the space inversion symmetry lifts the spin degeneracy ($\epsilon_\uparrow(\mathbf{k}) \neq \epsilon_\downarrow(\mathbf{k})$). Such a space inversion asymmetry can be caused by an electric field, resulting from the asymmetric charge distribution inside the semiconductor unit cell, or an electric field applied along a certain crystal axis. According to equation 2.17, through the potential gradient, this leads to a horizontal spin splitting of the parabolic CB in the $E(\boldsymbol{k})$-dispersion (The origin of parabola in Figure 2.2 (a) would be shifted along the k-axis by k_{SO}) in the absence of an external magnetic field, see figure 2.12. An external magnetic field $B_{ext} \neq 0$ would break the time inversion symmetry and therefore cause a Zeeman splitting vertical in $E(\boldsymbol{k})$ [Zee97]. The SO splitting may be considered equivalent to an intrinsic effective $\boldsymbol{k}$-dependent magnetic field ($\boldsymbol{B_{eff}(k)}$) in which an electron spin precesses with the Larmor frequency [30]. Consequently, equation 2.17 may be expressed with the Larmor precession vector $\boldsymbol{\Omega(k)} = (g\mu_B/\hbar)\,\boldsymbol{B_{eff}(k)}$ [31]:

$$\hat{H}_{SO} = \frac{\hbar}{2}\boldsymbol{\Omega(k)} \cdot \hat{\boldsymbol{\sigma}}. \tag{2.18}$$

The effective SO field must vanish at $k = 0$, since Kramer's theorem requires $\boldsymbol{\Omega(k)} = -\boldsymbol{\Omega(-k)}$. Consequently, there is no spin splitting at $\boldsymbol{k} = 0$, and for $\boldsymbol{k} \neq 0$ the splitting energy is $\Delta E_{SO} = 2\hbar\,|\boldsymbol{\Omega}\,(\boldsymbol{k})|$ (for those eigenstates parallel or antiparallel to $\boldsymbol{\Omega}\,(\boldsymbol{k})$), see figure 2.12.

One distinguishes several kinds of space inversion asymmetries: (i) the bulk inversion asymmetry BIA ; (ii) the structure inversion asymmetry SIA ; and (iii) the natural interface asymmetry NIA. BIA and SIA are essential for this work and will be discussed in detail below.

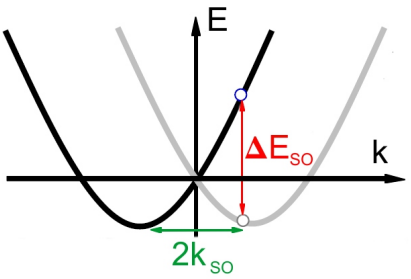

Figure 2.12: *The conduction band is split due to the SOI by $2k_{SO}$. ΔE_{SO} is the splitting energy.*

Heterostructure interfaces in which the adjoining layers share no common atom (e.g.InAs/GaSb) show NIA [Dya08] [Kre96] [Ivc96]. Since the anion As exists in a GaAs/AlGaAs structure, in the barrier as well as in the quantum well, NIA is absent here. Additionally, the quantum wells this work uses are grown in the (110)-direction. This growth scheme implicates an absence of NIA due to a symmetric interface potential, since the QW consists of planes with equal numbers of both anions and cations [Hal03b].

Furthermore, the SOI has a keen impact on the ***g*-factor** in solids (In the following the g-factor always refers to the electron g-factor since the hole g-factor can be quite different.). In most metals, electrons in the conduction band are quasi-free, the g-factor is therefore close to the vacuum value of about 2. Semiconductors, however, might have a quite large deviation from the vacuum value, depending on the strength of the SOI. In the narrow-bandgap semiconductor (large SOI) indium antimonide (InSb) for example, a g-factor of $g = -50$ [32] is found [Rot59], whereas silicon (Si, small SOI) has a g-factor of about 0.001 below the vacuum value [Fab07]. For GaAs a value of $g = -0.44$ at 4 K has been determined theoretically and experimentally for example by Oestreich et al. [Oes95; Oes96]. In those publications it is also shown that the g-factor strongly depends on temperature and doping concentration. By introducing a confinement, for instance in 2D structures, the space group symmetry T_d^2 is reduced. Thus, the g-factor

[30] In contrast to an applied external field, no macroscopic spin polarization is created by this internal field[Žut04].

[31] Hamiltonian for an applied B-field: $H = -\bar{\boldsymbol{\mu}} \cdot \boldsymbol{B}$. $\boldsymbol{\Omega(k)}$ must be an odd function in k.

[32] Per definition a negative electron g-factor means that spin angular momentum and the magnetic moment are parallel.

becomes anisotropic and has to be treated as a tensor. Symmetric (110)-grown QW, as well as (001)-grown QW (see chapter 2.2.6 for details) belong to the C_{2v} symmetry class. This implicates off-diagonal elements $g_{xy} = g_{yx}$ in the $\hat{\boldsymbol{g}}$-factor tensor [Eld11]. The $\boldsymbol{k} \cdot \boldsymbol{p}$ band calculations [Pfe06] with the extended Kane model [Hüb11] allow exact predictions in those systems. There exist different techniques to measure the g-factor in GaAs heterostructures, such as spin-flip Raman scattering [Sap92], spin quantum beat spectroscopy [Hüb11; Eld11; Yug07; Jeu97; Jeu97], or other techniques based on Kerr/Faraday rotation [Sne91; Gri12b; Bau94]. These publications show a dependence of the g-factor on temperature, electron density and quantum well width. A higher temperature, electron density or a larger confinement energy leads to an occupation of higher k-states where the conduction band cannot be considered parabolic anymore, resulting in a deviation in the g-factor. For narrower QW, the electron wave function penetrates more into the barrier material (AlGaAs: $g \approx +0.4$), which changes the percentage of the barrier contribution in the mixture of the two g-factors resulting in the total g-factor.

Bulk inversion asymmetry BIA

GaAs has a two-atomic basis (see chapter 2.1.1) and is referred to as a polar semiconductor. The lacking of an inversion center in, e.g., zincblende structure, gives rise to the bulk inversion asymmetry. G. Dresselhaus derived an expression for the spin splitting in this case, using general group-theoretical arguments [Dre55]. Accordingly, the Larmor precession vector $\boldsymbol{\Omega(k)}$ has, in the lowest order of perturbation theory, the form:

$$\boldsymbol{\Omega(k)}_{BIA} = \frac{\gamma}{\hbar}\left[k_x\left(k_y^2 - k_z^2\right), k_y\left(k_z^2 - k_x^2\right), k_z\left(k_x^2 - k_y^2\right)\right], \tag{2.19}$$

where $\hbar k_i$ are the momentum components in the principal cubic crystallographic directions: x=[100], y=[010] and z=[001]. This so-called Dresselhaus field is cubic in k. An intuitive interpretation is that the Dresselhaus SOI is induced by the electric field of the local GaAs dipole [Fab07]. The spin-splitting parameter γ can be expressed as [Dya71c; Dya86; Žut04]:

$$\gamma = \frac{\alpha_D \hbar^3}{m^* \sqrt{2 m^* E_g}}. \tag{2.20}$$

Thus, the magnitude of the Dresselhaus SOI depends on the material and is expressed in the dimensionless parameter α_D. A value of $\gamma \approx 24$ eVÅ^3 has been estimated using $\alpha_D = 0,07$ [Dya86; Pfe90a; Mar83]. There exist, however, several publications with deviating values in the range of $6.5 - 30$ eVÅ^3 [Kor09; Kri07; Cha06]. In the case of a 2DES, γ depends on the confinement energy in the QW due to the offsets of CB minimum and VB maximum from the the band gap energy. For rising confinement energy the value of γ decreases. Moreover, the penetration of the wave function in the barrier material also results in a change of the total parameter γ [Win03]. The sign of the parameter is determined by the used coordinate system. In case the cation (Ga) is place at the origin in a GaAs primitive cell and the anion (As) is located at $(1/4, 1/4, 1/4a)$ γ is negative [Stu10; Car88]. For a confinement energy of 25 meV (QW width of 15 nm) Studer et al. reported values in the range of $-5 - -8$ eVÅ^3 [Stu10], and for a confinement energy of 10 meV a $|\gamma|$ of 16.5 ± 3 eVÅ^3 [Jus95] . Leyland et al., using optical pump probe measurements, as well as Eldridge et al, employing spin-quantum beat spectroscopy reported values for $|\gamma|$ in the range of $12 - 4$ eVÅ^3 for confinement energies in the range of $10 - 100$ meV [Ley07b; Eld11].

The confinement of the electron wave function in 2D semiconductor systems, implicates a quantization of the momentum in growth (z-) direction. In first order perturbation theory, the terms k_z and k_z^2 in equation 2.19 may be replaced by their expectation

values. For rectangular QW, and occupation of the lowest subband, these values are $\langle k_z \rangle = 0$ [33] and $\langle k_z^2 \rangle = (\pi/d)^2$ (see equation 2.3 where $k_{z,n'} = n'\pi/d$) [34]. Shape and orientation of the Dresselhaus-field now depends on the direction of the quantization axis [Dya86; Žut04] . In the case of a [110]-grown QW follows with a coordinate system: $x \parallel [1\bar{1}0]$, $y \parallel [00\bar{1}]$, $z \parallel [110]$ [35]:

$$\mathbf{\Omega}_D^{(110)}(\boldsymbol{k}) = \frac{\gamma}{\hbar}\left[0, 0, k_x(\langle k_z^2 \rangle - (k_x^2 - 2k_y^2))\right]. \tag{2.21}$$

The resulting cubic terms may be neglected in narrow moderately doped quantum wells, since $\langle k_z^2 \rangle$ is much larger than the in-plane momentum $(k_\parallel)^2$ [Dya86; Has97]:

$$\mathbf{\Omega}_D^{(110)}(\boldsymbol{k}) = \frac{2\beta}{\hbar} \cdot [0, 0, k_x], \tag{2.22}$$

with

$$\beta = \gamma \langle k_z^2 \rangle = \gamma \left(\frac{\pi}{d}\right)^2. \tag{2.23}$$

β is called the Dresselhaus parameter. The fact that the Dresselhaus field points, in (110)-grown QW, for all allowed wave vectors along the growth direction (see figure 2.13) [Win04; Has97], leads to the suppression of the Dyakonov-Perel' spin dephasing mechanism (see chapter 2.2.4) [36].

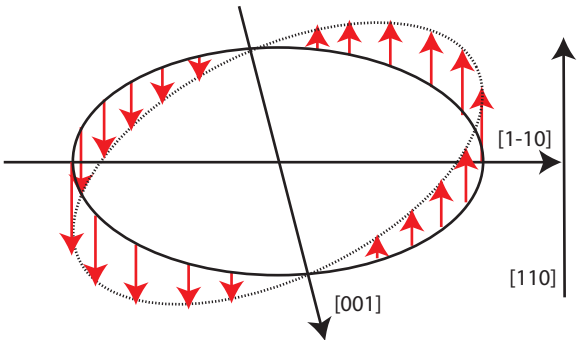

Figure 2.13: *The Dresselhaus-field in a (110)-grown quantum well is oriented along the growth axis. Taken from [Gri12b].*

D'yakonov and Kachorovskii derived a general formula for $\mathbf{\Omega}_D$ including the above mentioned approximations [Dya86]:

$$\mathbf{\Omega}_x(\boldsymbol{k}) = \frac{\gamma}{\hbar}\left[2n_x\left(n_y k_y - n_z k_z\right) + k_x\left(n_y^2 - n_z^2\right)\right]. \tag{2.24}$$

The other components are obtained by cyclic permutation of the indices. Besides (110)-grown systems, quantum wells grown in (001) and (111) direction are important for spintronics as well. The Dresselhaus fields for these directions are given by [Dya86; Žut04; Kor10; Car05]:

$$\mathbf{\Omega}_D^{(001)}(\boldsymbol{k}) = \frac{\beta}{\hbar} \cdot [-k_x, k_y, 0], \qquad \mathbf{\Omega}_D^{(111)}(\boldsymbol{k}) = \frac{2\beta}{\sqrt{3}\hbar} \cdot [k_y, -k_x, 0]. \tag{2.25}$$

[33] In case of the effective mass approximation with an z-independent mass, real electron wave functions $\xi(z)$, can be, without restriction assumed. With the hermitian (real eigen-values) momentum operator $\hat{\boldsymbol{p}} = -i\hbar\nabla$ follows $\langle k_z \rangle = -i \int dz \xi(z) \partial_z \xi(z) = 0$ [Kai03].

[34] For a triangular QW with a confinement potential eEz, $k_n \approx 0.7794(2m_0 E/\hbar^2)$ [Žut04].

[35] In the 3D case without the quantum mechanical substitution of the expectation value: $\mathbf{\Omega}(\boldsymbol{k})_{BIA}^{110} = \frac{\gamma}{\hbar}\left[4k_x k_y k_z, -k_x^2 k_z - 2k_y^2 k_z + k_z^3, -k_x k_z^2 - 2k_x k_y^2 + k_x^3\right]$.

[36] In chapter 2.2.6 the (110)-grown QW used in this work is discussed more in detail.

Structure inversion asymmetry SIA

In a quantum well, an external or internal (invoked by an asymmetry in the band edge profile [37]) electric field may break the space inversion symmetry [Byc84a; Byc84b]. Space charges can cause such an internal field, due to different alloy compositions in the barrier or single-sided modulation doping [38]. It can be shown that the resulting Bychkov-Rashba SOI is proportional to the average of the sum of the external and internal field [Wu10]. Moreover, the resulting confinement potential is described in first order by an electric field $\boldsymbol{\mathcal{E}}$ ($V_C(\boldsymbol{r}) = V_0 + e\boldsymbol{\mathcal{E}} \cdot \boldsymbol{r} + ...$) . Analog to the BIA, the contribution of the SIA to the Hamiltonian in equation 2.18, can be considered as an effective field, which is given in lowest order in $\boldsymbol{k}$ and $\boldsymbol{\mathcal{E}}$ [Win00; Win03]:

$$\boldsymbol{\Omega}_{BR}(\boldsymbol{k}) = \frac{2\alpha_0}{\hbar}\boldsymbol{k} \times \boldsymbol{\mathcal{E}}. \tag{2.26}$$

In the following, an electric field applied in the growth direction is assumed as $\boldsymbol{\mathcal{E}} = (0, 0, \mathcal{E}_z)$. α_0 is a material parameter and has been determined for GaAs with the extended Kane model to $\alpha_0 = 5,2$ eÅ^2 [Win03]. Typically, the electric field and the material parameter are averaged over barrier and quantum well. With $\alpha = 2\langle\alpha_0\mathcal{E}_z\rangle$ (the Rashba parameter) follows:

$$\boldsymbol{\Omega}_{BR}(\boldsymbol{k}) = \frac{\alpha}{\hbar} \cdot [k_y, -k_x, 0]\,. \tag{2.27}$$

The resulting spin splitting in the Γ_6-band, $\Delta E_{BR} = \alpha k_\parallel$ is linear in $k_\parallel = (k_x, k_y, 0)$ and $\mathcal{E}_z$ for small $k_\parallel$. Compared to the Dresselhaus field the Rashba field is not depending on the growth direction of the QW. Rather it is always oriented in the film plane and orthogonal to the electron in-plane $\boldsymbol{k}$-vector (see figure 2.14).

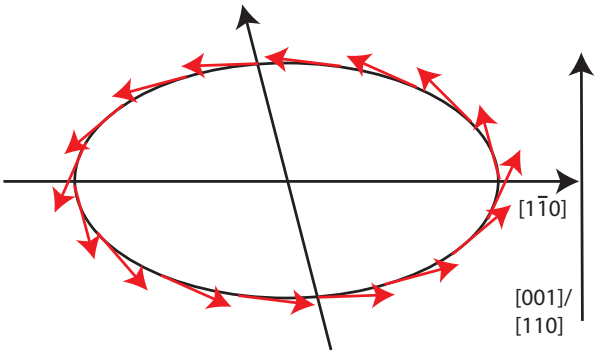

Figure 2.14: *The Bychkov-Rashba field (short Rashba field) is always oriented in-plane. Taken from [Gri12b].*

For large $k_\parallel$ the parabolic approximation of the bands does not hold anymore. As a consequence, the spin splitting converges towards a constant [Win00]. Furtermore, the more complex symmetry in the Γ_8 valence band demands a more complicated model to describe the spin splitting. In [Win03], a spin splitting of the HH-band cubic in $k_\parallel$ is demonstrated, whereas the LH-band spin splitting is linear in $k_\parallel$. Bernardes et al. derived from a 8×8-Kane model an additional SOI term for quantum wells with two occupied subbands. This inter-subband-induced term has a symmetry like the Rashba term and is nonzero in symmetric QW [Ber07]. Uniaxal stress along the $\langle 110\rangle$ (in-plane) axis in GaAs Bulk induces a $\boldsymbol{k}$-linear spin splitting as well, yielding an effective field with a symmetry similar to the Rashba field [Bir74; Mei84; Cro05a]. Chang et al.

[37] Strictly speaking the internal electric field due to the band profile must be called quasi electric, since it is possible that electrons and holes move in the same direction, or just one of them sees a force due to the internal field [Kro01].

[38] Using magnetogyrotropic photogalvanic effect (MPGE) in (110)-grown GaAs QW, Olbrich et al. showed that the SIA can be tuned to zero by symmetrically positioning of the δ-doping layers [Olb09].

showed that uniaxial or biaxial stress along the growth direction in [110] or [111] can compensate the k-linear Dresselhaus field [Cha05] and implies an enhancement of the spin lifetime.

The interplay of Rashba and Dresselhaus terms has drawn lots of attention in recent years. Averkiev et al. proposed a giant spin relaxation anisotropy in (001)-grown quantum wells. The resulting spin-orbit field for the in-plane directions [110] and $[1\bar{1}0]$ is minimal in [110]-direction and maximal in $[1\bar{1}0]$-direction [Ave99]. Various optical techniques are eligible for measuring such an anisotropy [Ave02; Sti07a; Eld11]. Ganichev et al. experimentally separated the Rashba and Dresselhaus contribution using photocurrent measurements (spin-galvanic effect) and deduced a ratio of Dresselhaus and Rashba field [Gan04]. Meier et al. could determine the absolute values for BIA and SIA using all-optical methods [Mei07]. Furthermore, the ratio of Rashba and Dresselhaus field can be controlled by an electric field [Lar08; Stu09]. Especially the case when $\alpha = \beta$ is interesting. For this case, Schliemann et al. proposed a non-ballistic spin-field-effect transistor due to $\boldsymbol{k}$-independent spin states leading to a fixed effective field and suppressed spin relaxation [Sch03b]. Bernevig et al. deduced further that the spin polarization of a helical mode is preserved because of a SU(2) symmetry. The spin rotation due to $\boldsymbol{\Omega}$ depends on the displacement but is independent of the path. A local spin excitation would expand into a helical spin wave with theoretically infinite lifetime, which is called the persistent spin helix PSH [Ber06a; Kor09; Wal12]. Kunihashi et al. proposed, on grounds of the PSH, a spin complementary field effect transistor [Kun12]. In (111)-grown structures the Dresselhaus field has the same symmetry as the Rashba field, by tuning the Rashba field a cancellation of the two may be achieved, resulting in long spin lifetimes [Car05; Bal11; Sun10].

2.2.3 Spin dynamics

The Bloch sphere is a common geometrical representation of a two-level state [Blo46]. A spin can be characterized as a point on a unit sphere by polar coordinates. On this basis, a set of differential equations may describe the spin dynamics in an external magnetic field $\boldsymbol{B} = (B_x, 0, 0)$, called the Bloch-Torrey equations [Blo46; Tor56]:

$$\frac{\partial S_x}{\partial t} = (\boldsymbol{S} \times \boldsymbol{\Omega})_x - \frac{S_x - S_x^0}{T_1} + D\nabla^2 S_x, \tag{2.28}$$

$$\frac{\partial S_y}{\partial t} = (\boldsymbol{S} \times \boldsymbol{\Omega})_y - \frac{S_y}{T_2} + D\nabla^2 S_y, \tag{2.29}$$

$$\frac{\partial S_z}{\partial t} = (\boldsymbol{S} \times \boldsymbol{\Omega})_z - \frac{S_z}{T_2} + D\nabla^2 S_z. \tag{2.30}$$

Here, the first term describes the Larmor precession with the Larmor precession vector $\boldsymbol{\Omega} = (\mu_B \hat{\boldsymbol{g}}/\hbar) \cdot \boldsymbol{B}$ (see chapter 2.2.2), the second term describes the loss of an initial spin polarization after a certain time, and the third term depicts a decay of spin polarization due to diffusion (with diffusion constant D). The time T_1 is called (longitudinal) **spin relaxation time** and represents the time in which a nonequilibrium spin polarization relaxes into the thermal equilibrium. Since the spin orientation is in this case parallel to an external magnetic field, an energy transfer from the spin system to the lattice is required [39] because of the Zeeman splitting. T_1 may, however, also denote relaxation in the absence of an external field. The time T_2 is called (transverse) **spin dephasing time**, and it characterizes the irreversible loss of coherence in a precessing spin system. Yet the experimentally determined relaxation time in most cases is the ensemble dephasing time T_2^*. It includes additional factors like inhomogeneous broadening due to g-factor

[39] The relaxation is typically via phonons.

fluctuations [40]. For localized spins, for instance in quantum dots, spin echo experiments can cancel this contribution [Žut04]. The spread of conduction electrons in solids yields an averaged contribution to the precession rate, thus the g-factor fluctuations can be neglected and $T_2 = T_2^*$ [Fab07]. Furthermore, it was shown that for isotropic systems $T_1 = T_2 = T_2^*$ because of short correlation times [Lü07]. Additionally, spin injection is always transversal to the external magnetic field in this work. Consequently, there is no distinction in the following between spin relaxation and spin dephasing, and the electron spin dephasing time is denoted by τ_s. If not explicitly stated, the external B-field is applied in x-direction. For bulk GaAs, the dephasing time is spatially isotropic, in contrast to the (110)-grown quantum wells, in which a strong anisotropy for the in-plane and the out-of-plane dephasing times is present (see chapter 2.2.6).

Although the Bloch sphere model clearly describes the spin dynamics phenomenologically, this description omits, however, the global phase factor, which also includes the geometric phase or Berry's phase [Ber84b]. A rotation of 2π on the Bloch sphere, for example, leads back to the initial state. Yet in the spinor formalism, a rotation of 4π is required to return to the initial state. Although the Berry phase can explain some quite interesting effects such as weak (anti) localization [41] [Kru11; Ber84a] it plays no important role in this work.

2.2.4 Spin dephasing mechanisms

A spin polarization in a nonmagnetic semiconductor returns into its thermal equilibrium within its spin dephasing time. Several mechanisms are responsible for this relaxation. In the following the ones most important for this work are described.

The Dyakonov-Perel' (DP) mechanism

A space inversion asymmetry, as described in section 2.2.2, evokes an effective internal magnetic field $\boldsymbol{\Omega}(\boldsymbol{k})$, whose magnitude and direction depend on the $\boldsymbol{k}$-vector and indirectly on the spin splitting in the conduction band. The $\boldsymbol{k}$-dependence of this effective magnetic field implicates the main dephasing mechanism in GaAs-bulk and heterostructures, called the Dyakonov-Perel' mechanism (DP mechanism). In an electron ensemble, the $\boldsymbol{k}$-values are distributed according to the effective statistics (Fermi, Boltzmann), and the electron spins precess in this effective spin-orbit field with a Larmor frequency $|\boldsymbol{\Omega}(\boldsymbol{k})|$ [Dya71c]. During each scattering event, however, the k-vector changes randomly for an individual electron, yielding a modification of $\boldsymbol{\Omega}(\boldsymbol{k})$. Eventually the ensemble spin polarization dephases between the scattering events (see figure 2.15).

Initially, it was believed that the microscopic scattering time τ_p contains only momentum relaxation processes. Later it was shown that electron-electron scattering, which does not affect the mobility, has an equal effect on the dephasing. Glazov et al. showed this using perturbation theory [Gla02; Gla03b; Gla04]. Additionally, Wu et al. conducted a fully microscopic study of the dephasing mechanism, and pointed out that only a many-body approach is sufficient to describe spin dephasing. Here the electron energy depends on the transition frequency between opposite spin states, resulting in inhomogeneous broadening of spin transitions. This inhomogeneous broadening may be caused by: energy-dependent g-factors, the momentum dependence of the effective field $\boldsymbol{\Omega}$, momentum-dependent spin diffusion along a spatial gradient or random Rashba fields via fluctuations of the remote donor densities. In the presence of this broadening, spin-conserving scattering such as Coulomb scattering may cause irreversible spin

[40] $(T_2^*)^{-1} = (T_2)^{-1} + (T_{2,inh})$ with $T_{2,inh} = \hbar/(\Delta g \mu_B B)$ for broadening due to g-factor fluctuations.

[41] Weak (anti) localization is a quantum mechanical correction to the classical resistance of a metal or semiconductor due to quantum interference.

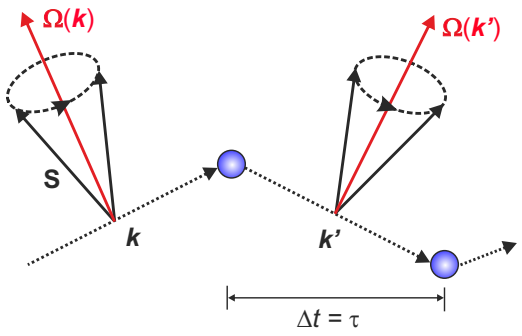

Figure 2.15: *The Dyakonov-Perel' spin dephasing mechanism: The electron spin S precesses around the precession axis* $\boldsymbol{\Omega(k)}$*, after the time* Δt *which corresponds with the microscopic scattering time* τ *the* $\boldsymbol{k}$*-vector changes to* $\boldsymbol{k'}$*, as well as the precession axis* $\boldsymbol{\Omega(k)} \rightarrow \boldsymbol{\Omega(k')}$*. Hence the ensemble spin polarization dephases.*

dephasing [Wu00; Wu02; Wen03; Zho07]. Leyland et al. confirmed the importance of electron-electron scattering in the dephasing experimentally, using pump-probe reflection techniques [Ley07a]. (For a detailed discussion on mobility and scattering times see chapter 2.3.1) In conclusion the scattering rate is given by:

$$\frac{1}{\tau} = \frac{1}{\tau_p} + \frac{1}{\tau_{ee}}, \tag{2.31}$$

with τ_p the momentum scattering time and τ_{ee} the electron-electron scattering time. The DP-mechanism is differentiated in two regimes, depending on the product of the scattering time and the average (over $\boldsymbol{k}$) precession frequency $\bar{\Omega}$, which is the number of precessions before the scattering event.

In the **weak scattering regime** $\tau\bar{\Omega} > 1$ the spin revolves more than once before the scattering. As previously mentioned, scattering entails irreversible spin dephasing. Consequently the spin relaxation time is proportional to the scattering time ($\tau_s \propto \tau$). In the absence of any scattering, the spins would relax reversibly because of the anisotropic distribution of the precession frequency $\boldsymbol{\Omega(k)}$, and the rate would then be proportional to the width of that distribution. The weak scattering regime dominates in very pure high-mobility structures at low temperatures. Moreover, it is possible to observe coherent damped oscillations of the spin ensemble caused by the spin orbit field, see [Sti07b; Ley07b; Gri09; Gri12b].

The other limit where $\tau\bar{\Omega} < 1$ is called the **motional-narrowing** or strong scattering regime. Here the electron spin does not fulfill a whole precession cycle before the scattering event, rather it only evolves up to a certain angle $\varphi = \tau\bar{\Omega}$. Applying a random walk model yields an estimate for the spin lifetime. The variance (expectation value of the square) of the angle φ, after the time t is then proportional to the number of random walk steps t/τ. Further, according to the definition of the spin dephasing time τ_s, the variance is one, after the time $t = \tau_s$: $\left\langle (\Delta\varphi)^2 \right\rangle \sim \bar{\Omega}^2\tau t \stackrel{!}{=} 1$ [42]. Hence, the relation for the spin dephasing time in the motional narrowing regime is given by:

$$\frac{1}{\tau_s} = \bar{\Omega}^2\tau. \tag{2.32}$$

Obviously, the more scattering occurs the longer the spin lifetime becomes. Thus a fluctuating spin-orbit field stabilizes the spin ensemble. The motional narrowing regime

[42] The expectation value of $\left\langle (\Delta\varphi)^2 \right\rangle$ after t/τ random walk steps is $\left(\bar{\Omega}\tau\right)^2 t/\tau$.

applies to all samples used in this work. Concerning the temperature dependence of the DP-mechanism one needs to consider on the one hand that higher $\boldsymbol{k}$-states are occupied, with increasing temperature. This results in a larger Fermi wave vector $\boldsymbol{k}_F = \sqrt{2\pi n}$ and therefore in a larger Larmor precession vector $\boldsymbol{\Omega}(\boldsymbol{k})$, implying shorter spin lifetimes. On the other hand, the temperature dependence of the dominating scattering mechanism (see chapter 2.3.1) needs to be accounted for to draw a conclusion about the temperature dependence of the spin lifetime. For GaAs bulk the temperature dependence is discussed in chapter 2.2.5, and the temperature dependence of the (110)-grown QW is discussed in chapters 2.2.6 and 5.2. By applying a longitudinal magnetic field, the DP-mechanism is suppressed. In this case the electrons perform a cyclotron motion, yielding a change of the $\boldsymbol{k}$-vector and therefore altering $\boldsymbol{\Omega}(\boldsymbol{k})$, which eventually involves a suppression of the spin relaxation [Ivc73; Tar09]. Additionally, the Zeeman interaction may also induce a Larmor precession, which slows down spin dephasing due to the interference of the Larmor frequencies [Wu10]. A special symmetry of the SO fields (e.g. (110)-grown QW) or their interplay as described in section 2.2.2, implicates strong anisotropies in the spin dephasing time.

The Bir-Aronov-Pikus (BAP) mechanism

Electron-hole exchange scattering can be another reason for spin dephasing [Bir75; Aro83]. This mechanism is important, especially in p-doped semiconductors at low temperatures [43] and in the case of optical spin generation, because of the increased hole density. The BAP-mechanism is based on the direct Coulomb exchange interaction between electrons and holes given by the following Hamiltonian [Žut04]:

$$\hat{H}_{BAP} = A_x \hat{\boldsymbol{S}} \cdot \hat{\boldsymbol{J}}_h \delta(\boldsymbol{r}) . \tag{2.33}$$

Here A_x is proportional to the matrix element of the Coulomb exchange interaction between conduction and valence band states. $\hat{\boldsymbol{S}}$ is the electron spin operator and $\hat{\boldsymbol{J}}_h$ is the operator of the total angular momentum of the hole. $\delta(\boldsymbol{r})$ depicts the relative position of the electron and the hole.

In a scattering event involving electrons and holes of opposite spin, this interaction entails a spin exchange during scattering. Such a spin flip, as a result of the long range interaction is possible because of SOI induced splitting of the valence (or conduction) band, since then the momentum matrix elements depend on the spin state [Bir75]. The spin-flip probability depends mainly on the state of the hole, i.e. free hole or acceptor-bound hole, degenerate or nondegenerate hole system (see chapter 2.1.1). On the grounds of the spin flip scattering, and in the presence of a non equilibrium electron spin polarization, a polarization is transferred to the hole system, and the electron polarization is reduced. Since the spin lifetimes of holes are quite short, the hole spin polarization decays fast. Hilton et al. measured heavy-hole spin lifetimes in GaAs of 110 fs [Hil02]. An explanation for this fast decay of hole spins is found in the mixing of HH and LH bands, which yield that the hole wave function is not a spin eigenfunction of the system, see chapter 2.1.1. Due to the degeneracy at the Γ-point of HH and LH states in GaAs bulk, each scattering event may change the character of the total wave function consisting of HH ($m_j = 3/2$) and LH ($m_j = 1/2$) parts.

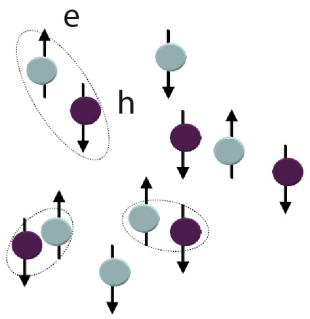

Figure 2.16: *BAP mechanism from [Völ09].*

The spin relaxation time resulting from the BAP-mechanism is derived by Fermi's golden rule [Wu10]. For a nondegenerate hole system, this expression can be reduced

[43] For higher temperatures, the DP-mechanism becomes more important in p-doped materials because electron states occupy higher $\boldsymbol{k}$-states, resulting in larger $\boldsymbol{\Omega}(\boldsymbol{k})$.

to [Aro83; Wu10]:

$$\frac{1}{\tau_{BAP}} = \frac{2}{\tau_0} n_h a_B^3 \frac{\langle v_k \rangle}{v_B}. \tag{2.34}$$

Here n_h is the hole density, $a_B \approx 114$ Å is the effective exciton Bohr radius, $\langle v_k \rangle$ is the effective electron velocity, $\tau_0 \approx 1 \cdot 10^{-8}$ s is an exchange splitting parameter and $v_B = \hbar/m^* a_B \approx 1.7 \cdot 10^7$ cm/s [Aro83]. For a degenerate hole system, the spin dephasing rate is given by [Wu10]:

$$\frac{1}{\tau_{BAP}} = \frac{3}{\tau_0} n_h a_B^3 \frac{\langle v_k \rangle}{v_B} \frac{k_B T}{E_F^h}, \tag{2.35}$$

with E_F^h the hole Fermi energy. Amo et al. and Zhou et al. pointed out that the Pauli blocking [44] inhibits spin flip scattering in fully occupied states. Since scattering takes place around the Fermi energy, it is suppressed by Pauli blocking for low temperatures [Amo07] [Zho08] [Zho09]. In the case of a suppressed DP-mechanism, e.g. in (110)-grown quantum wells, the BAP-mechanism dominates in n-doped 2D heterostructures with optical spin injection [Döh04; Mül08; Völ11], see also chapter 2.2.6. An essential fact there is that the BAP dephasing rate is proportional to the hole density ($\tau_{BAP}^{-1} \sim N_h$) which is proportional to the laser intensity in the case of optical spin injection.

The Elliot-Yafet (EY) mechanism

The spin-orbit interaction in a material (section 2.2.2, equation 2.17) gives rise to an admixture of electron states from the conduction band and the valence band with opposite spin. Consequently, these pseudospin states are not spin eigenstates to the spin operator $\hat{\boldsymbol{\sigma}}$ anymore. Such a Bloch state can be written as :

$$\psi_{\boldsymbol{k}n\uparrow}(\boldsymbol{r}) = \left[a_{\boldsymbol{k}} \left|\uparrow\right\rangle + b_{\boldsymbol{k}} \left|\downarrow\right\rangle\right] e^{i\boldsymbol{k}\cdot\boldsymbol{r}}, \tag{2.36}$$

$$\psi_{\boldsymbol{k'}n\downarrow}(\boldsymbol{r}) = \left[a^*_{-\boldsymbol{k'}} \left|\downarrow\right\rangle + b^*_{-\boldsymbol{k'}} \left|\uparrow\right\rangle\right] e^{i\boldsymbol{k'}\cdot\boldsymbol{r}}. \tag{2.37}$$

Here $a_{\boldsymbol{k}}$, $b_{\boldsymbol{k}}$ are the complex, lattice-periodic, envelope functions, which are connected by time and space inversion operators [Žut04; Wu10]. Typically, this admixture is rather small, so that $|a| \approx 1$ and $|b| = \Delta E_{SO}/E_g \ll 1$. On the grounds of this mixing, even spin-independent scattering does not conserve the spin state, so that, e.g., a predominantly spin up state flips to a spin down state during scattering. Elliot estimated this spin flip probability, on the order of b^2, using the Born approximation [Ell54]. Hereby, the actual scattering type is not relevant. Usually, there is electron-impurity scattering (dominant at low T), electron-phonon scattering (high T) [Ell54], and electron-electron scattering [Bog80]. Yafet showed an additional mechanism where the SOI induced by periodic lattice ions is modified by phonons, leading to a direct coupling of spin up and spin down states and thus invoking a spin flip [Yaf63; Žut04]. The spin relaxation rate for III-V bulk materials may be expressed for a conduction band electron with energy E_e by [Tac99; Fis77]:

$$\frac{1}{\tau_{EY}(E_e)} = \left(\frac{\Delta_0}{E_g + \Delta_0}\right)^2 \left(\frac{E_{CB}}{E_g}\right)^2 \frac{1}{\tau(E_e)}, \tag{2.38}$$

Here E_g is the bandgap energy, τ is the momentum scattering time and Δ_0 the spin-orbit splitting energy of the valence band (chapter 2.1.1). In the case of a degenerate system $E_e = E_F$ is valid, and for a nondegenerate $E_e = k_B T$. In a 2D system equation 2.35 must be modified [Ivc05; Tac99]:

$$\frac{1}{\tau_{EY}(E_e)} = \left(\frac{\Delta_0}{E_g + \Delta_0}\right)^2 \left(\frac{E_e E_{e1}}{E_g}\right) \frac{1}{\tau(E_e)} \tag{2.39}$$

[44] Pauli blocking is a consequence of the exclusion principle according to which two identical fermions can not occupy the same quantum state at once [Sch00b].

In this situation, the EY-mechanism is then proportional to the confinement energy E_{e1}. The EY becomes dominant for narrow-bandgap semiconductors, such as InSb, because of the strong SOI. In Si (weak SOI) at room temperature the phonon induced EY is dominant, see [Fab07]. In comparison with the DP-mechanism (motional narrowing regime) one finds that the relation of the dephasing rate to the momentum scattering time is opposite (DP: $\tau_s^{-1} \sim \tau_p$, EY: $\tau_s^{-1} \sim \tau_p^{-1}$). Additionally, in the EY the dephasing takes place during the scattering event, whereas in the DP-mechanism the dephasing is between the scattering events.

Further spin dephasing mechanisms

As previously mentioned in section 2.2.3, the g-factor may be inhomogeneous within the spin-polarized ensemble, which implies precession with different Larmor frequencies and, therefore, a spin dephasing of the ensemble. Spin dephasing may also occur via **hyperfine interaction (HFI)**. Since all the stable isotopes in GaAs have a nonzero nuclear magnetic moment ($I_n = 3/2$, see chapter 2.4 for details) a Fermi contact interaction between the nuclear spin ($\boldsymbol{I}_n$) and the spin of a localized electron ($\boldsymbol{S}$) is present: $\hat{H}_{HF} \sim A\,(\boldsymbol{I}_n \cdot \boldsymbol{S})$ where A is proportional to the probability density of the electron wave function at the position of the nucleus [45]. A spin exchange, that the interaction between localized electrons and the nuclei induced, implicates a dynamic nuclear polarization, resulting in a mean magnetic field of the nuclei, called the Overhauser field (chapter 2.4). The probability density of a localized electron is typically spread over $10^4 - 10^6$ lattice sites [Žut04]. Thus, aside from the mean hyperfine field, the electron is also influenced by a fluctuating field proportional to the square root of the nuclei quantity in the electron localization region [Dya08]. These temporal and spatial fluctuations [46] affect the Larmor frequency of individual electrons and cause dephasing of the spin ensemble [Dya73]. Dyakonov et al. [Dya74] and Berkovits et al. [Ber74] showed this for electrons bound in shallow donors. Furthermore, this mechanism is important in quantum dots where spin dephasing because of SOI is weak [Mer02; Pet05]. For free-moving electrons in bulk semiconductors or metals this dephasing is evanescently small, since their wave function overlaps with a great number of nuclei so that the fluctuations of the field are averaged out [Ove53a].

Döhrmann et al. proposed the **intersubband spin relaxation mechanism (ISR)** in (110)-grown quantum wells [Döh04]. Similar to the EY mechanism, the Dresselhaus term causes a mixing of states from different subbands with opposite spin. Without SOI a simultaneous intersubband and spin flip transition ($|\boldsymbol{k}, n=0, \uparrow\rangle \rightarrow |\boldsymbol{k}, n=1, \downarrow\rangle$) would be forbidden. The mixing $|\boldsymbol{k}, n=0, \uparrow\rangle\, \varepsilon_1\, |\boldsymbol{k}, n=1, \downarrow\rangle \rightarrow |\boldsymbol{k}, n=1, \downarrow\rangle\, \varepsilon_2\, |\boldsymbol{k}, n=1, \uparrow\rangle$) introduces a small probability of spinflip transitions. The dephasing rate of such a transition is then by a factor $\alpha_{ISR} = |\varepsilon_1|^2 + |\varepsilon_2|^2$ smaller than the rate of an allowed transition τ_{IB}. On this grounds, the spin dephasing time is given by: $\tau_s = \alpha_{ISR}^{-1} \tau_{IB}$. The ISR is more effective for higher temperatures > 120 K and wider quantum wells, due to the closer subband levels and stronger Dresselhaus field (see equations 2.22 and 2.23).

Kavokin et al. showed that localized electrons experience an effective field during tunneling, similar as in the DP-mechanism [Kav01; Dzh02]. As a result, the exchange interaction between two coupled electrons becomes anisotropic (due to SOI) [47], and does

[45] Applications using holes are in this context more favorable since holes have p-like wave functions and, therefore, the probability density at the nucleus is zero.

[46] The spatial fluctuations are due to the random orientation of the nuclear spins in the crystal. The temporal fluctuations are caused by hyperfine interaction and nuclear spin dipole-dipole interaction [Wu10].

[47] This asymmetric part is called Dzyaloshinskii-Moriya interaction.

not conserve spin along any direction, leading to spin dephasing of the ensemble. This spin dephasing due to **anisotropic exchange interaction (AEI)** is found in weakly doped semiconductors and in quantum dots.

2.2.5 Spin in GaAs bulk

Chapter 4 presents experiments, where spins are electrically injected into GaAs bulk. Therefore, spin dephasing in bulk GaAs is discussed here in more detail. Dzhioev et al. investigated the dependence of the spin lifetime on the doping density at low temperatures [48], using photoluminescence measurements, depicted in figure 2.17 (a) [Dzh02]. For low doping density n_D the majority of the electrons are localized. In this

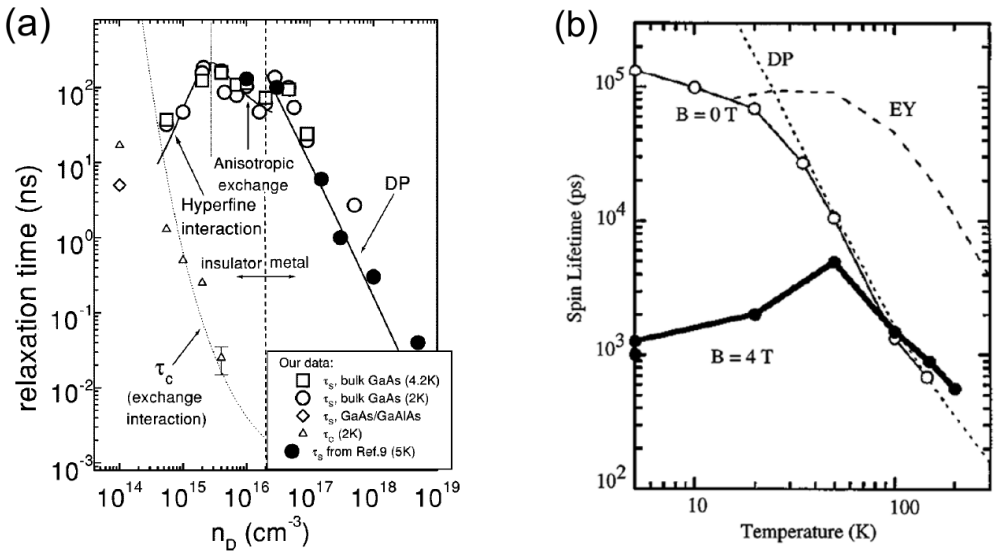

Figure 2.17: ***(a)*** *Spin lifertime depending on the doping density in GaAs bulk. Taken from [Dzh02].* ***(b)*** *Spin lifetime depending on the temperature in n-GaAs. The carrier density was* $1 \cdot 10^{16}$ cm^{-3} *for* $B = 0$. *Here, for temperatures below* 50 K *the sample is insulating and nondegenerate at high temperatures. The sample used at* 4 K *had a carrier density of* $2 \cdot 10^{14}$ cm^{-3} *Taken from [Kik98].*

insulating regime, spin dephasing due to the HFI dominates. With increasing density, the localization of the electrons decreases. Hence, the electrons interact with more nuclei, the fluctuation effect averages out, and the spin dephasing weakens. The spin lifetime reaches its first maximum of ~ 180 ns at $3 \cdot 10^{14}$ cm^{-3}. By further increasing the doping density, the tunnel probability of electrons between the doping sites rises and the spin dephasing because of AEI dominates, which yields a slight decrease of the spin relaxation time. At high doping densities, the wave functions of the donor electrons overlap and form an impurity conduction band. Thus the electron states delocalize and the semiconductor has a metallic character [Ros83]. At a doping density of $n_d \approx 2 \cdot 10^{16}$ cm^{-3} this metal-insulator transition (MIT) is found in GaAs. In this regime the DP-mechanism dominates. Close to this transition, a second maximum spin lifetime of about 150 ns was observed. The slight increase is owed to the increasing motional narrowing effect for increasing electron density. Above $n_d \approx 2 \cdot 10^{16}$ cm^{-3} the spin lifetime drops due to the interplay of both factors in equation 2.32. With increasing density, higher $\boldsymbol{k}$-states are occupied, resulting in a larger Fermi wave vector $\boldsymbol{k}_F =$

[48] At higher temperatures, the shallow donors would be ionized and the insulator state at low donor densities could not be achieved.

$\sqrt{2\pi n}$ and therefore in a larger cubic Dresselhaus term (equation 2.19), which yields shorter spin relaxation times. The scattering time, however, needs to be considered as well (see chapter 2.3.1). The most important types of electron scattering are with ionized impurities, phonons and electrons. In the metallic regime, the electron system is degenerate and the ionized impurity scattering dominates. According to the Brooks-Herring formula [Žut04], the scattering rate is given by $1/\tau_p \sim n_d E_F^{-3/2}$, which gives: $\tau_s \sim 1/n_d^2$.

Kikkawa et al. [Kik98] measured the temperature dependence of the spin dephasing time in GaAs below the MIT ($1 \cdot 10^{16}$ cm^{-3}) as figure 2.17 (b) depicts. Hohage et al. [Hoh06] and Römer et al. [Röm10] found similar results. At low temperatures, the spin lifetime is given by two interacting subsets of spins: the localized states, which dephase according to AEI and HFI, and the itinerant states, which dephase according to the DP-mechanism. For increasing temperature the localization decreases, and the spin dephasing is consistent with the DP-mechanism [Put04]. It can be shown that equation 2.32 may be transformed to $1/\tau_s \sim T^3\,\tau_p$ (for a nondegenerate system). The mobility of the ionized impurity scattering has a $T^{3/2}$ dependence (chapter 2.3.1), and with the Brooks-Herring formula follows $\tau \sim T^{3/2}\,n_d^{-1}$ and $\tau_s \sim T^{-9/2}\,n_d$ [Wu10]. Additionally, a similar argumentation as above is valid because of the occupation of higher $\boldsymbol{k}$ states. For the increase of the spin lifetime with magnetic field in the range up to 50 no satisfactory explanation has been provided so far [Žut04]. At room temperature spin lifetimes of 5 ps$< \tau_s <$ 10 ps for undoped GaAs and 15 ps$< \tau_s <$ 35 ps for heaviliy doped n-GaAs have been reported [Kim01].

2.2.6 Spin in (110)-grown GaAs quantum wells

In this section, the properties of (110)-grown GaAs quantum wells are discussed in more detail. As presented in section 2.2.2 the Larmor precession vector $\boldsymbol{\Omega}(\boldsymbol{k})$ consists of Rashba (equation 2.27) and Dresselhaus (equation 2.22) contributions [Tar09]:

$$\boldsymbol{\Omega}(\boldsymbol{k}) = \frac{2}{\hbar} \cdot [\alpha_1 k_y, -\alpha_2 k_x, \beta k_x]\,, \tag{2.40}$$

with a coordinate system as described in chapter 2.2.2 and in figure 2.18. In contrast to equation 2.27, where only one Rashba coefficient α is used, here a second coefficient α_2 is introduced. This is a higher-order contribution, which can be obtained by microscopic band structure calculations [Car06]. Figure 2.13 depicts the orientation of the Dresselhaus field and figure 2.14 of the Rashba field. For a symmetric QW, α_1 and α_2 are zero. Fluctuations of the dopant ion concentration on each side of the QW cause an electric field at each point in the QW, with random magnitude. Consequently a Rashba field is present with a zero spatial average [She03; Gla05; Gla10; Zho10; Pos13]. This Rashba contribution, however, is quite small and often neglected. Spins oriented perpendicular to the QW plane are then not affected by spin dephasing due to the DP-mechanism. In-plane oriented spins, on the contrary, dephase according to the DP-mechanism with a dephasing rate $\frac{1}{\tau_s} = \bar{\Omega}^2\tau$ (equation 2.32). As a consequence, there exists a huge anisotropy in the spin lifetimes for those spin orientations. Ohno et al. first observed this [Ohn99b]. They measured spin lifetimes of a few ns in undoped multiple quantum wells (MQW) at room temperature using time- and polarization-resolved transmission measurements. Adachi et al. found spin lifetimes up to 10 ns in doped MQW at room temperature [Ada01]. Döhrmann et al. [Döh04] obtained results in the same range for doped MQW in a temperature range from 4 K to 300 K, using time- and polarization-resolved photoluminescence (TRPL) techniques. Müller et al. [Mül08] measured spin lifetimes one order of magnitude higher in a doped MQW structure using spin noise spectroscopy. In this work spin lifetimes up to 100 ns are measured in a doped high

mobility single quantum well. According to Karimov et al. the spin lifetime may be modulated by a factor 10 by introducing a Rashba field via a gate voltage. They could demonstrate this with a MQW embedded in a p-i-n structure, at 170 K [Kar03], as well as Iba et al. [Iba10], at room temperature. Bel'kov et al. showed that the spin lifetime in a (110)-grown QW is maximal in the case the QW is symmetric. Using the photogalvanic effect they were able to probe the symmetry of the sample since a photocurrent is observed only for asymmetric structures. Using time-resolved Kerr rotation, then the spin lifetime could be determined and compared with the symmetry of the sample [Bel08].

The T_d^2 symmetry in bulk GaAs is reduced when a 2D confinement is introduced. A symmetric (110)-grown QW belongs to the C_{2v} symmetry group, which contains: the identity, a two fold rotational axis (180° rotation) and two mirror planes, see figure 2.18 (c). [49]. An asymmetric quantum well belongs then to the C_s symmetry group (figure 2.18 (b)), which only contains the identity and a mirror plane perpendicular to the film plane. The spin dynamics of a spin ensemble is described by a kinetic equation [Bro04]

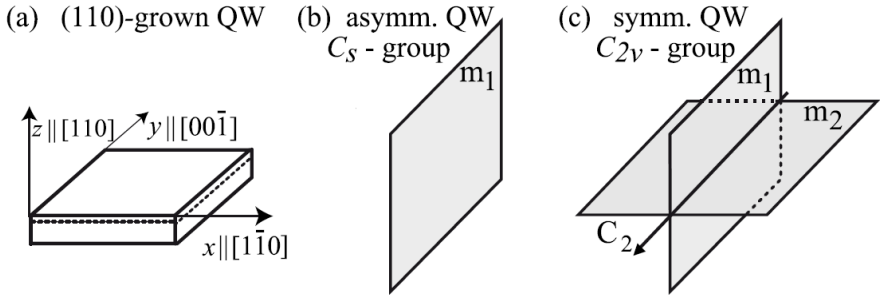

Figure 2.18: ***(a)*** *The coordinate system in (110)-grown quantum wells.* ***(b)*** *The C_s symmetry in asymmetric (110)-oriented QW.* ***(c)*** *The C_{2v} symmetry in (110)-grown QW. Taken from [Olb09].*

which is derived from the Bloch Torrey equations (2.28 to 2.30):

$$\frac{dS_\alpha}{dt} + [\boldsymbol{S} \times \boldsymbol{\Omega}]_\alpha = G_\alpha - \sum_\beta \Gamma_{\alpha\beta} S_\beta. \tag{2.41}$$

Here α and β stand for the cartesian coordinates. G is the spin generation rate, and $\Gamma_{\alpha\beta}$ are the components of the spin relaxation tensor. The form of this tensor depends on the spin relaxation mechanism and the point group symmetry [Tar09]. An applied magnetic field along the QW plane causes a Larmor precession of spins initially aligned perpendicular to the plane with the frequency $\boldsymbol{\Omega}$. Therefore, the spin vector has now an in-plane component, which dephases fast because of the DP-mechanism. Accordingly, the total spin lifetime reduces, which is typically an average of the two lifetimes [Wu02; Döh04; Völ11]. As previously discussed, for symmetric (110)-grown quantum wells the DP-mechanism is suppressed. Consequently the BAP mechanism is then dominating at low temperatures in the case of optical excitation [Döh04]. In chapter 5.2, the temperature dependence of the dephasing mechanisms will be discussed in detail. The

[49] An ideal (001)-grown QW would have D_{2d} symmetry (in the case the confining potential is inversion-symmetric). A practical QW, however, has nonsymmetric interfaces and the symmetry is reduced to C_{2v} (confining potential is inversion-asymmetric) [Che02] [Win03]. In contrast to the (110)QW, both mirror planes are perpendicular to the interface plane [Olb09]. D_{2d} contains C_{2v} plus inversion.

spin dephasing rate for a symmetric (110)-grown QW, considering only the out-of-plane component is given by:

$$\frac{1}{\tau_s} = \frac{1}{\tau_z^{lim}} + \gamma_z^{BAP} N_h + \gamma^r N_h. \tag{2.42}$$

τ_z^{lim} is the dephasing time in the limit of zero excitation. This rate includes the EY-mechanism and the DP-mechanism owing to fluctuating remote donor densities. $\gamma_z^{BAP} N_h$ denotes the dephasing because of the BAP mechanism, which is proportional to the hole density N_h. $\gamma^r N_h$ stands for the loss of spin polarization due to recombination. It is assumed that the recombination probability for an electron is proportional to the steady-state hole density N_h, which is usually valid for a nondegenerate hole gas in the absence of recombination centers [Völ11].

S.A. Tarasenko showed that because of the C_s symmetry in asymmetric QW the spin relaxation tensor has off-diagonal elements [Tar09]:

$$\hat{\Gamma} = \begin{pmatrix} \Gamma_{xx} & 0 & 0 \\ 0 & \Gamma_{yy} & \Gamma_{yz} \\ 0 & \Gamma_{zy} & \Gamma_{zz} \end{pmatrix}, \tag{2.43}$$

with:

$$\Gamma_{xx} = \left(\alpha_2^2 + \beta^2\right) C, \quad \Gamma_{yy} = \left(\alpha_1^2 + \beta^2\right) C, \quad \Gamma_{zz} = \left(\alpha_1^2 + \alpha_2^2\right) C, \quad \Gamma_{yz} = \Gamma_{zy} = \alpha_2 \beta C, \tag{2.44}$$

The parameter C depends on the microscopic scattering time (τ) and the Fermi wave vector ($\boldsymbol{k}_F$) and therefore on temperature and carrier density. When the high-order corrections on the Rashba parameter are neglected ($\alpha_1 = \alpha_2 = \alpha$), the off-diagonal elements are given by:

$$\Gamma_{yz} = \Gamma_{zy} = \pm \frac{1}{2} \sqrt{\Gamma_{zz}(2\Gamma_{yy} - \Gamma_{zz})}. \tag{2.45}$$

The existence of these off-diagonal components implies that the axes y and z are not principal axes of the relaxation tensor. It can be shown that as consequence, the relaxation of a spin polarization initially oriented along the growth direction S_z leads to a rotation of the spin in the (yz) plane resulting in a nonzero in-plane value of S_y and the spin does not point along the QW normal anymore. Both spin components relax with different rates and the total spin lifetime is characterized by two lifetimes. The spin lifetime according to equation 2.41 and equation 2.43 is given by (according to M. Glazov):

$$S_z(t) = S_0 e^{-t/\overline{\tau}} \left[\cos \tilde{\Omega} t + \frac{\Gamma_{yy} - \Gamma_{zz}}{2\tilde{\Omega}} \sin \tilde{\Omega} t \right], \tag{2.46}$$

with

$$\frac{1}{\overline{\tau}} = \frac{\Gamma_{yy} + \Gamma_{zz}}{2}, \qquad \tilde{\Omega} = \sqrt{\Omega^2 - \frac{\Gamma_{yy}^2}{4}}. \tag{2.47}$$

The spin ensemble oscillates for real values of $\tilde{\Omega}$ and decays exponentially for imaginary $\tilde{\Omega}$ values.

A furthermore important fact about (110)-grown QW concerns the VB structure. The average spacing between HH subbands is smaller in (110)-grown QW than in (001)-grown QW. Therefore, the two highest VB states at the Γ-point are HH bands followed by the first LH band. This can be explained by the fact that in GaAs bulk, the effective mass of the (110) direction is higher. The average effective mass in the QW plane, however, is smaller in (110)-grown QW than in (001)-grown QW [Win03].

2.3 Spin transport phenomena

In this section, first of all the various scattering times are discussed,which are important for not only the mobility and transport phenomena, but also for the already discussed spin dephasing mechanisms. The chapter continues with carrier transport phenomena, and ends with spin transport including many-body effects on spin diffusion.

2.3.1 Scattering time and mobility

Since an electron does not scatter according to the Bloch theorem in a perfect crystal (periodic potential), the conductivity would be infinite. In a real semiconductor, however, several scattering processes exist. The time between the scattering is called the microscopic scattering time τ. The empirical Matthiessen rule states that the total reciprocal scattering time is the sum of the individual reciprocal scattering times:

$$\frac{1}{\tau} = \sum_i \frac{1}{\tau_i}. \tag{2.48}$$

There is a detailed study of the different scattering mechanisms in standard textbooks like [Ash76; Gru06; Yu05]. In the following the most important scattering types are listed, including the temperature dependence of the individual scattering time:

(a) Scattering on impurities, which are neutral or ionized. In doped semiconductors, the ionized impurity scattering dominates because of the strong Coulomb interaction. The scattering may be treated classically like Rutherford scattering, known as the Conwell-Weisskopf approach [Con50], or quantum mechanically where the effect of screening the impurity potential by free carriers is considered, known as the Brooks-Herring approach [Cha81]. Here the scattering time is given by: $\tau_p \propto T^{3/2} n_{ion}^{-1}$.

(b) Acoustic phonons cause a deformation of the lattice which affects the position of the band edges. Electrons may scatter on such steps $\tau_p \propto T^{-3/2}$.

(c) In a polar semiconductor such as GaAs, a longitudinal acoustic phonon induces a variation of the local electric field which deflects the carriers. The corresponding scattering time is $\tau_p \propto T^{-1/2}$.

Figure 2.19 (a) shows the individual temperature dependencies and the combined dependence for GaAs according to Matthiessen's rule. The experiments in this work on GaAs bulk are conducted at low temperatures, so that the ionized impurity scattering is dominating.

The movement of carriers in a semiconductor can be described according to a random walk model. If no scattering is present, however, the transport is called ballistic. The kinetic energy of a carrier is without an external field given by the thermal energy. Hence, an average carrier velocity may be derived: $v_{th} = \sqrt{3k_B T/m^*}$ [Ash76] [50], which yields a mean free path of $l = v_{th}\tau_p$. The Drude model is a good approximation, when considering the carrier motion in an applied electrical field $\boldsymbol{\mathcal{E}}$ [Dru00; Ash76]. The average velocity of a carrier in an electric field is called drift velocity and defined as [51]:

$$\boldsymbol{v_{D,(e,h)}} = \frac{\mp e\tau}{m^*_{e,h}} \boldsymbol{\mathcal{E}} = \mp \mu_{e,h} \boldsymbol{\mathcal{E}}. \tag{2.49}$$

Here, $\mu_{e,h} = e\tau/m^*_{e,h}$ is the electron/hole mobility. Since electrons move opposite to the direction of the electric field and holes along it, there is a difference in the signs.

[50] There exist different definitions for the thermal velocity in the literature. Here the root mean square of the total velocity in 3D is used.

[51] The drift velocity is an average velocity and therefore much smaller than the actual thermal velocity. It actually means that the whole electron density moves with a constant average velocity due to a shift in the Fermi surface. Equation 2.49 may easily be derived from momentum conservation.

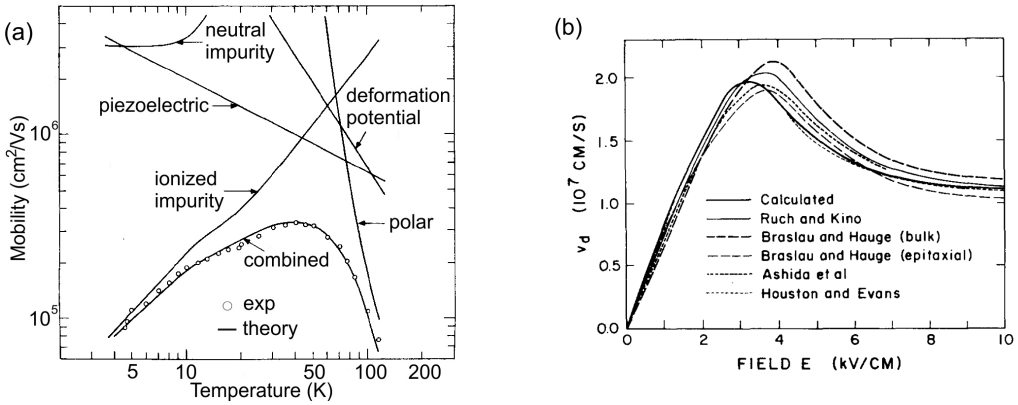

Figure 2.19: *(a) Dependence of the mobility on the temperature, in GaAs according to the individual scattering mechanism, as well as the combined dependence according to Matthiesens rule. Adapted from [Wol70].* ***(b)*** *Saturation of the drift velocity in high electric field, due to energy transfer to the lattice. Taken from [Bla82].*

The sign is, however, often neglected in mobility information. $q\mathcal{E}$ is the electrostatic force causing the drift, with Ohm's law $j = \tilde{\sigma}\boldsymbol{\mathcal{E}} = \mp n_{e,h}\, e\, \boldsymbol{v_{D,(e,h)}}$ the conductivity $\tilde{\sigma}$ is given by: $\tilde{\sigma} = e\,(n_e\mu_e + n_h\mu_h)$. So far the (elastic) scattering has been considered in the limit of low fields, where the drift velocity increases linearly with the electric field. In the case of high fields, the electron temperature is higher than the lattice temperature. Hence, there is an energy transfer from the electron system to the lattice by emission of optical phonons (LO). Through this transfer, the drift velocity is limited, resulting in a non-ohmic characteristic, see figure 2.19 right. The drift saturation velocity is given by [Gru06]:

$$v_D^s = \sqrt{\frac{8}{3\pi}\frac{\hbar\omega_{LO}}{m^*}}. \tag{2.50}$$

In modulation-doped heterostructures, the ionized doping scattering is absent since the dopands are physically separated from the 2DES. For high temperatures, the phonon scattering dominates, such as in the bulk case, and at low temperatures, the Coulomb scattering on remote ionized impurities dominates, which is independent of T for low temperatures [Wal84]. An increase of the spacer width would weaken this scattering mechanism but with a larger spacer width, the electron density in the QW decreases, which lowers the mobility. Thus, a spacer thickness optimization is necessary [Wal84; Uma09]. Further small scattering contributions are background impurity density scattering and interface roughness scattering events (only important if roughness length scale is comparable to the electron Fermi wave length). For high electron densities $\geq 7 \cdot 10^{11}\mathrm{cm}^2$ inter subband scattering exists as well.

The scattering times are not only important in the transport, but also for some spin dephasing mechanisms such as the DP or the EY mechanism (chapter 2.2.4). As previously mentioned in this chapter, electron-electron (e-e) scattering contributes to the spin dephasing. The mobility, however, is not influenced by this kind of scattering, due to conservation of the momentum in the ensemble. Nevertheless, electron-electron scattering has an influence on the spin transport properties, since it reduces the DP- spin dephasing mechanism in the motional narrowing regime [Kam11]. Obviously an extended spin lifetime causes a longer spin diffusion length, see chapter 2.3.2. Especially in the high-mobility samples, where at low temperatures the previously discussed scattering is small, the e-e scattering becomes important. In a degenerate 2DES ($T \ll T_F = E_F/k_B$ Fermi temperature) only the electrons at the Fermi edge are involved in scattering events. For a degenerate electron gas a scattering rate may be approximated in this

case as [Gla04; Ley07a]:

$$\frac{1}{\tau_{ee}} = H(\tilde{q})\left(\frac{\pi}{4}\right) ln\left(\frac{E_F}{k_B T_e}\right)\frac{E_F}{\hbar}\left(\frac{k_B T_e}{E_F}\right)^2 \approx 3.4\frac{E_F}{\hbar}\left(\frac{k_B T}{E_F}\right)^2. \tag{2.51}$$

Here, T_e the electron temperature is used, this temperature may be quite different from the lattice temperature in high-mobility QW [Rya84], see chapter 5.2. $H(\tilde{q})$ is a form factor taking into account a weaker electron-electron interaction in quasi-two-dimensional electron systems ($H(\tilde{q}) < 1$) [Gla03a]. $\tilde{q}$ is the transferred wave vector in a scattering event, assuming a strictly 2D system ($H(\tilde{q}) = 1$). The electron-electron scattering rate is then $\tau_{ee}^{-1} \sim T^2 n_e^{-1}$ since $E_F = \hbar^2 \pi m^{-1} n_e$. In the limit $T \to 0$ the e-e scattering time is absent due to the Pauli exclusion principle [Ley07a]. For a nondegenerate system ($T \gg T_F$) all electrons contribute to the scattering, and τ_{ee} is approximately [Gla04] [Ley07a]:

$$\frac{1}{\tau_{ee}} = 35.7\frac{e^4 n_e}{\hbar \boldsymbol{\kappa} k_B T_e}, \tag{2.52}$$

with $\boldsymbol{\kappa} = \boldsymbol{\Omega}\hbar/\gamma$ from equation 2.19. Hence, $\tau_{ee}^{-1} \sim n_e T^{-1}$. Photoluminescence measurements, as discussed in chapter 3.3, are a convenient way to determine the electron temperature. In the high mobility 2DES, even at liquid-Helium temperature τ_{ee} is significantly smaller than the momentum relaxation time, and provides therefore the upper limit for the microscopic scattering time τ.

2.3.2 Drift and diffusion

In the following section, the transport phenomena drift and diffusion are reviewed. The discussion is limited to the case of electrons, yet holes might be treated analog. Particles distribute in the volume according to Fick's law in the presence of a concentration gradient. For a semiconductor, the carrier diffusion flux can be written as: $J_F = -D\nabla n$. Thus, the total current density is then given by the sum of drift and diffusion [52]:

$$\boldsymbol{j}_e = n_e e \mu_e \boldsymbol{\mathcal{E}} + e D_e \nabla n_e, \tag{2.53}$$

D_e is the diffusion constant. So far the Drude model was used, however, this model relies on classical statistics and is therefore often not sufficient for treating carrier motion in semiconductors. A better approximation is the Boltzmann transport equation, where the temporal evolution of a certain distribution function (on the condition that the total number of carriers is constant in the time interval) is considered. Standard textbooks such as [Ash76; Yu05] provide a detailed introduction regarding this topic. In this context, a general term for the diffusion constant may be derived [Fla00] :

$$D_e = -\frac{\mu_e}{e}\frac{\int_0^\infty g_e(E) f_e(E)\, dE}{\int_0^\infty g_e(E)\frac{\partial f_{e,h}(E)}{\partial E}\, dE} = 2\mu_e k_B T \frac{F_{1/2}\left[E_F/k_B T\right]}{F_{-1/2}\left[E_F/k_B T\right]}. \tag{2.54}$$

Here, $g_e(E)$ is the density of states (the lowest energy in the conduction band is chosen to be zero), and $f_e(E)$ is the distribution function. $F_{1/2}\left[E_F/k_B T\right]$ is the Fermi-Dirac integral $F_n(\xi)\int_\infty^0 x^n \left[exp\left(x-\xi\right)+1\right]^{-1}$ which does not have an analytical solution. In case of a nondegenerate semiconductor (small doping densities and high temperatures), the distribution function is a Boltzmann distribution and equation 2.54 reduces to:

$$D_e = \mu_e \frac{k_B T}{e}. \tag{2.55}$$

[52] Diffusion does not depend on the electrical charge of the particle. The electrical (harge current has to be then: $j = -eJ$.

This expression is known as the Einstein relation [Ein05; Gru06]. It may be derived in the frame of the Drude model as well. On the contrary, for a degenerate semiconductor in equilibrium, equation 2.54 may be approximated as [Fab07]:

$$D_e = \frac{\mu_e}{e} \frac{n_e}{g\left(E_F\right)} \approx \frac{\mu_e}{e} E_F. \tag{2.56}$$

Here, $g\left(E_F\right) \approx k_F^3/E_F$ (3D) or $g\left(E_F\right) \approx k_F^2/E_F$ (2D) was used. This implicates that even at $T = 0$ the finite Fermi velocity causes diffusion. Equations 2.55 and 2.56 may also be derived with the simple consideration that $eD_e/\mu_e = 1/2mv_F^2$ has the dimension of an energy, which is in the case of a nondegenerate semiconductor k_BT and in the case of a degenerate semiconductor E_F [53] [Fab07]. Since the number of particles must be conserved, a continuity equation is valid:

$$\frac{\partial n}{\partial t} + \nabla J_F = 0, \tag{2.57}$$

with equation 2.53 and the condition of charge neutrality ($\nabla \cdot \boldsymbol{\mathcal{E}} = 0$), a drift-diffusion equation is deduced:

$$\frac{\partial n_e}{\partial t} = \mu_e \mathcal{E} \nabla n_e + D_e \nabla^2 n_e. \tag{2.58}$$

Spin drift and diffusion

A charge current described by the drift diffusion equation 2.58 includes electrons with both spin orientations, with a total electron density given by the sum of spin up and down $n_e = n_\uparrow + n_\downarrow$. A spin density in contrast is defined by $S = n_\uparrow - n_\downarrow$ (equation 2.7), and a general transport equation for such a spin polarization $\boldsymbol{S}$ in an uniform electric field $\boldsymbol{\mathcal{E}}$ and an magnetic field $\boldsymbol{B}$ may be derived analogue to equation 2.58 and is given by [Yu02a; Yu02b; Fur07; Fab07]:

$$\frac{\partial \boldsymbol{S}}{\partial t} = D_s \nabla_{\boldsymbol{r}}^2 S + \mu_s \left(\boldsymbol{\mathcal{E}} \cdot \nabla_{\boldsymbol{r}}\right) \boldsymbol{S} + g\mu_B \hbar^{-1} (\boldsymbol{B} \times \boldsymbol{S}) - \frac{\boldsymbol{S}}{\tau_s} + \boldsymbol{G}(\boldsymbol{r}). \tag{2.59}$$

The time evolution of a spin polarization then depends on a diffusion term, a drift term, a term describing the Larmor precession and finally the spin relaxation and the generation rate $\boldsymbol{G}(\boldsymbol{r})$. Spin diffusion may be caused by a gradient of spin density, at a constant carrier density, but also by a carrier gradient, provided a spin polarization is present.

Flatté et al. developed the model of ambipolar spin diffusion [Fla00; Yu02b]. Here, spin or charge packets, propagating through the material, are considered (see figure 2.20). Considering a not highly-doped semiconductor, in which screening is not as effective as in metals, a nonequilibrium electron packet, created in the CB, evokes a propagating hole packet, due to local charge neutrality $\Delta n_e(x) \sim \Delta n_h(x)$ (figure 2.20 (a)). Here the ambipolar diffusion constant, describing the spatial distribution can be expressed as:

$$D_a = \frac{n_e \mu_e D_h + n_h \mu_h D_e}{n_e \mu_e + n_h \mu_h}, \qquad \mu_a = \frac{\left(n_e - n_h\right) \mu_e \mu_h}{n_e \mu_e + n_h \mu_h}. \tag{2.60}$$

Obviously the hole mobility dominates the ambipolar mobility for n doped semiconductors at low temperatures. Similarly a spin packet may be treated in an undoped

[53] The diffusion constant may be defined by the mean free path $l = \tau v_F$. $D = l^2/2\tau = v_F^2\tau/2$ [Fab07]. In case of a degenerate electron gas $v_F = \sqrt{2E_F/m^*}$, and in case of a nondegenerate gas the thermal velocity replaces the Fermi velocity. With the approximation of v_{th} as the most probable speed follows in 3D $v_{th} = \sqrt{2k_BT/m^*}$. Hence, equations 2.55 and 2.56 may be derived simply by using the appropriate velocities.

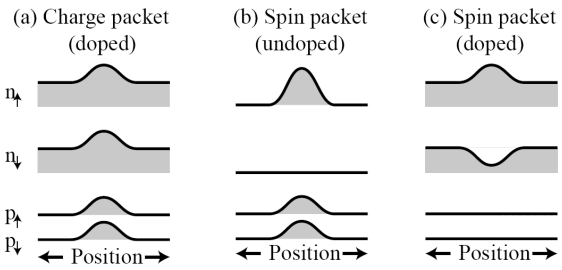

Figure 2.20: *(a) An electron packet drags a hole imbalance.* ***(b)*** *A spin packet in an undoped semiconductor invokes a hole imbalance as well.* ***(c)*** *In a doped semiconductor, the other spin species may be reduced so that the local charge neutrality does not require a drag of a hole imbalance. Taken from [Fla00].*

sample, see figure 2.20 (b). In this case, the generation of a nonequilibrium spin packet implies a nonequilibrium of the total electron density, and again a hole density packet is satisfying the charge neutrality. In doped semiconductors, however, the population of the other spin species may be reduced so that the total electron density is unchanged $\Delta n_e(x) = 0 = \Delta n_h(x)$ [Kik98]. Consequently, such a spin packet does not give rise to a local hole inhomogeneity. Similar to equation 2.60, diffusion constant and mobility may be defined as:

$$D_s = \frac{\tilde{\sigma}_\uparrow D_\downarrow + \tilde{\sigma}_\downarrow D_\uparrow}{\tilde{\sigma}_\uparrow + \tilde{\sigma}_\downarrow}, \qquad \mu_s = \frac{\tilde{\sigma}_\uparrow \mu_\downarrow + \tilde{\sigma}_\downarrow \mu_\uparrow}{\tilde{\sigma}_\uparrow + \tilde{\sigma}_\downarrow}. \tag{2.61}$$

Here $\tilde{\sigma} = e n_e \mu_e$ is the conductivity. In non magnetic semiconductors where the degree of spin polarization is small ($n_\uparrow - n_\downarrow \ll n_\uparrow + n_\downarrow$), the spin mobility and the spin diffusion constant are equal to the electron mobility and diffusion constant under the condition that many-body effects are neglected (e.g. Spin Coulomb drag effect) This means that $D_e = D_s$, $\mu_e = \mu_s$. Concerning the movement caused by an electric field, it has been shown for intrinsic samples that an applied electric field causes a spatial separation of electrons and holes, and that the spin-polarized electrons dominate the drift [Häg98; San02].

Assuming a spatially extended source like the ferromagnetic electrode considered in chapter 4, one can assume that a spin polarization in 2.59 decays exponentially $S(x) = S_0 \exp\left[-x/L(\boldsymbol{\mathcal{E}})\right]$ for one dimension and under the condition that the source is at $x = 0$. $L(\boldsymbol{\mathcal{E}})$ is the spin injection length. Without an applied external electric field, the spin injection length is the spin diffusion length $L_s = \sqrt{D_s \tau_s}$ [Aro76]. An applied electric field either increases the spin injection length, if the spin diffusion is opposite to the field (electrons move downstream), or decreases the spin injection length, if the spin diffusion is along the field (electrons move upstream). The spin injection length is then defined as downstream or upstream injection length L_d, L_u [Yu02b; Yu02a]:

$$L_{d,(u)} = \left[-(+)\frac{|e\mathcal{E}|}{2}\frac{\mu_e}{eD_s} + \sqrt{\left(\frac{|e\mathcal{E}|}{e}\frac{\mu_e}{eD_s}\right)^2 + \frac{1}{L_s^2}} \right]^{-1}, \tag{2.62}$$

$$L_{d,(u)} = L_s \left[-(+)\frac{\mathcal{E}}{2\mathcal{E}_c} + \sqrt{\left(\frac{\mathcal{E}}{2\mathcal{E}_c}\right)^2 + 1} \right]^{-1}. \tag{2.63}$$

$\mathcal{E}_c = D_s / (\mu_e L_s) = \mu_e^{-1} \sqrt{D_s/\tau_s}$ is the critical field. The spin injection length is dominated by the spin diffusion for $\mathcal{E} < \mathcal{E}_c$, and for $\mathcal{E} > \mathcal{E}_c$ the drift is dominating. The drift length is given by $L_D = |e\mu_e \mathcal{E}|\, \tau_s = |v_D|\, \tau_s$. Hence, the one-dimensional evolution of a

spin packet at $x = 0$, with an amplitude S_0 is given by [Wu10; Fab07]:

$$S(x,t) = \frac{S_0}{\sqrt{2\pi D_s t}} \exp\left[-\frac{t}{\tau_s} - \frac{(x - v_D t)^2}{4 D_s t}\right]. \tag{2.64}$$

The width of this Gaussian function is given by the diffusion length L_s and the displacement of the center is given by the drift length L_d [Wu10].

Optical spin injection (see chapter 2.2.1) creates spin-polarized electron-hole pairs. The electrons and holes will diffuse or drift according to equation 2.59. In the n-doped systems this work investigates, the hole spin lifetime is much shorter than the recombination time (GaAs bulk ~ 110 fs [Hil02]). Thus, the holes will recombine with both spin kinds equally leaving a spin polarization moving with the electron mobility. Unlike the case of a spatially extended electrode, the source here must be considered as a point source. Hence, the spin diffusion may be considered ideally as a radial movement away from the source, and the generation term in equation 2.59 $\boldsymbol{G}(\boldsymbol{r})$ becomes $G_z(\boldsymbol{r})$. For the case $\boldsymbol{B} = \boldsymbol{\mathcal{E}} = 0$ equation 2.59 reduces to:

$$S_z(\boldsymbol{r}) - \tau_z \nabla \cdot [D_z \nabla S_z(\boldsymbol{r})] = G_z(\boldsymbol{r})\, \tau_z, \tag{2.65}$$

where $\boldsymbol{r}$ is the in plane coordinate. D_z is the diffusion coefficient for the z-component of the electron spin. For a degenerate 2DES D_z is given by:

$$D_z = \frac{E_F \tau}{m^*}, \tag{2.66}$$

where equations 2.49 and 2.56 were used. τ is the microscopic scattering time (see equation 2.48) Due to electron-electron collisions this diffusion coefficient is significantly smaller than the carrier diffusion coefficient given by equation 2.56. This is described in detail in chapter 2.3.2. In the case $G_z(\boldsymbol{r})$ is a point source at the origin, the Green's function solution for this equation is [Fur07]:

$$S_z(\boldsymbol{r}) = C K_0(r/L_z), \tag{2.67}$$

with $C = G_z/2\pi D_z$, r the distance from the point like injection spot, and K_0 is the modified Bessel function of the second kind. Unlike the ordinary Bessel functions, which are oscillating as functions of a real argument, K_0 are exponentially decaying functions diverging at $r = 0$. These functions, also called MacDonald functions [Mac99], have far from the excitation spot ($r \gg L_z$) the asymptotic behavior:

$$S_z(\boldsymbol{r}) \propto \frac{\exp(-r/L_z)}{\sqrt{r/L_z}}, \tag{2.68}$$

For small enough diffusion length $K_0(r/L_s)$, a nearly exponential decay may be assumed ($r > L_s$) with an $1/e$ constant of $\sim 0.9 L_s$ as for example used by Furis et al. [Fur07].

In the literature it is often distinguished between a pure spin current and a spin polarized charge current, in which the spin transport is caused by a gradient in the electron density or in the spin density. In the latter, spin transport always includes charge transport. If the two spin species travel with opposite velocities $j_\uparrow = -j_\downarrow$, however, there is no net charge current $j = j_\uparrow + j_\downarrow = 0$, and the spin current would be $j_s = j_\uparrow - j_\downarrow = 2j_\uparrow$. Such a spin current is called pure spin current. The situation figure 2.20 (c) describes could be considered as such a case. The absence of a spin kind, required by charge neutrality, traveling in the same direction as the spin packet, may also be considered as a spin packet of opposite spin traveling in the opposite direction. A pure spin current is invariant under time reversal, which indicates low dissipation. Whether a pure spin current is dissipation less or not is still not fully resolved [Shi06; She08]. Such a pure spin current was realized by quantum interference of one and two photon absorption [Ste03; Bha00]. The most prominent example of course is the spin hall effect [Dya71b; Dya71a; Hir99; Kat04b].

Many-body effects on spin diffusion (Spin Coulomb drag)

So far the expressions for mobility and diffusion are derived without considering many-body effects. D'Amico et al. showed that the diffusion constant is reduced for interacting electrons [D'A00; D'A01; D'A02; D'A03; D'A06; Fle01], due to not only the spin Coulomb drag effect (SCD) but also a reduction in the spin stiffness (energy cost of spin-density fluctuations). The spin stiffness is the inverse spin susceptibility which is reduced primarily by exchange interaction, whereas the spin coulomb drag is essentially a friction for the relative motion of the two spin species. Although the total momentum of the electron gas is conserved, the momentum of the individual spin kinds is not conserved. Hence a momentum transfer from the majority spins to the minority spins causes a drag of the latter. This is similar to the Coulomb drag effect [Gra91; Roj99]. Here moving electrons in a thin layer drag along electrons in an isolated layer due to Coulomb interaction. Thus, a force on one spin kind generates a current in the other kind. From this, it follows that a spin trans-resistivity $\rho_{\uparrow\downarrow}$ is induced in the resistivity tensor:

$$\begin{pmatrix} \boldsymbol{\mathcal{E}}_{\uparrow} \\ \boldsymbol{\mathcal{E}}_{\downarrow} \end{pmatrix} = \begin{pmatrix} \rho_{\uparrow\uparrow} & \rho_{\uparrow\downarrow} \\ \rho_{\downarrow\uparrow} & \rho_{\downarrow\downarrow} \end{pmatrix} \begin{pmatrix} \boldsymbol{j}_{\uparrow} \\ \boldsymbol{j}_{\downarrow} \end{pmatrix}. \tag{2.69}$$

Likewise, off diagonal elements are induced in the spin stiffness tensor so that the chemical potential of one spin species depends on the density of the other species. D'Amico et al. introduced a generalized Einstein equation $e^2 D_{\alpha\beta} = \sum_{\beta} \sigma_{\alpha\gamma} S_{\gamma\beta}$ and derived an expression for the reduced diffusion constant D_s^{SCD}:

$$\frac{D_s^{SCD}}{D_s} = \frac{\tilde{S}}{\tilde{S}_C} \frac{1}{1 - \rho_{\uparrow\downarrow}/\rho_D}. \tag{2.70}$$

Here $\tilde{S}$ is the spin stiffness, $S_C = k_B T n/(4n\uparrow) n_{\downarrow}$ is the Curie spin stiffness of an ideal gas and $\rho_D = m^*/ne^2\tau_D$ is the Drude resistivity. The influence of the SCD varies depending on temperature and doping densities. It was shown that the effects of the reduced spin stiffness dominate at low temperatures whereas the Coulomb drag dominates at high temperatures [D'A01]. Weber et al. observed the SCD in a GaAs QW using spin-grating technique [Web05]. Additionally, Zhao et al. derived a diffusion equation considering the spin Coulomb drag and the induced hole diffusion for optical spin injection without an external magnetic field [Zha09]:

$$\frac{\partial S}{\partial t} = \nabla \cdot \left[(D_a - D_s)\, S\, \nabla \ln n + \nabla S \right] - \frac{S}{\tau_s} + G, \tag{2.71}$$

here $n = n_{\uparrow} + n_{\downarrow}$ is the total electron density, D_a is the ambipolar diffusion constant from equation 2.60, and D_s is the reduced diffusion constant due to SCD, which is expressed in this publication as: $D_s = D/\left(1 + \hat{\gamma}\tau_s\right)$ ($\hat{\gamma}$ is a friction coefficient).

2.4 Dynamic nuclear polarization (DNP)

Since all the stable isotopes in GaAs/AlGaAs (^{69}Ga, ^{71}Ga, ^{75}As) carry a nuclear spin of $I_n = 3/2$ [Mei84], it is necessary to consider an interaction of such a nuclear spin with the electron spin. The dominant interaction of the electron magnetic moment with the magnetic moment of the nuclei, is the Fermi contact hyperfine interaction, whose Hamiltonian is given by [Fer30; Pag77; Mei84; Sch03a]:

$$\hat{H}_{HF} = \frac{8\pi}{3} \frac{\mu_0}{4\pi} g_0 \mu_B \gamma_N \hbar\, \hat{\boldsymbol{I}}_{\boldsymbol{n}} \cdot \hat{\boldsymbol{S}}\, \delta(\boldsymbol{r}) = \frac{2}{3} \mu_0 g_0 \mu_B \gamma_N \hbar\, \hat{\boldsymbol{I}}_{\boldsymbol{n}} \cdot \hat{\boldsymbol{S}}\, |\psi(0)|^2 . \tag{2.72}$$

Here $\hat{\boldsymbol{S}}$ is the electron spin, $\hat{\boldsymbol{I}}_n$ is the nuclear spin, μ_B is the Bohr magneton, $\gamma_N = g_N/(\bar{\mu}_N \hbar)$ is the gyromagnetic ratio of the nucleus, $\bar{\mu}_N$ is the magnetic moment of the

nucleus which is about three orders of magnitude smaller than the electron magnetic moment (approximately a factor of 2000), and g_0 is the g-factor of the free electron. The contact type of the interaction implicates the delta function, which is replaced by $|\psi(0)|^2$ after averaging over the orbital coordinates of the electron. Hence, the degree of the overlap between the electron and the nuclear wave function determines the strength of the interaction. Moreover, it follows that localized electrons dominate the influence on the nuclei [Pag77]. The probability density of such a localized electron is usually spread over $10^4 - 10^6$ lattice sites [Žut04], and it was shown that itinerant electrons polarize localized electrons within a timescale of 10^{-11} s because of the spin exchange interaction [Pag82]. Equation 2.72 also makes clear that the interaction with holes due to Fermi contact is weak due to their p-type character. Holes interact with nuclei via the weaker dipole-dipole interaction. The Fermi contact interaction may be divided into static and dynamical effects [Mei84]. The static effects follow from a hyperfine magnetic field created by polarized nuclei acting on the electrons (Overhauser field), or by a hyperfine magnetic field generated from an electron spin polarization acting on the nuclei (Knight field). These fields induce a Zeeman-like split, which may be observed in a shift of the resonances in NMR (nuclear magnetic resonance) or ESR (electron spin resonance) measurements. The electrons at the occupied states q generate a Knight field acting on a nucleus i at position r_i [Pag77]:

$$\boldsymbol{B}_e^i = \frac{2}{3}\mu_0 g_0 \mu_B \hbar \sum_q \gamma_i \boldsymbol{S}_q \left|\psi_q(r_i)\right|^2 . \tag{2.73}$$

W.D. Knight found shifts in the NMR in five metals because of this hyperfine field [Kni49]. Similarly an electron spin in an orbital state $|\psi_q|$ experiences an Overhauser field given by [Pag77]:

$$\boldsymbol{B}_N^q = \frac{2}{3}\mu_0 \frac{g}{g^*}\hbar \sum_i \gamma_i \boldsymbol{I}_i^n \left|\psi_q(r_i)\right|^2 , \tag{2.74}$$

with the nucleus i at position r_i. The shift in the NMR caused by this field is called Overhauser shift [Ove53b]. Assuming an uniform nuclear polarization the effective field, of an averaged nuclear spin $\langle \boldsymbol{I}_n \rangle$ (involving all nuclear species) is given by:

$$\boldsymbol{B}_N = b_N \frac{\langle \boldsymbol{I}_n \rangle}{I_n}. \tag{2.75}$$

Here b_N is the field given by a complete polarization of the nuclei, for GaAs it has been determined to $b_N = -5.3$ T (involving all isotopes of spin $I_n = 3/2$) [Pag77; Dya08; Mei84]. Additionally, electrons feel a fluctuating field B_{NF}, which is proportional to the square root of nuclei (N) in the area of localization of an electron $\left\langle B_{NF}^2 \right\rangle = B_N^2/N$. This field causes electron spin relaxation, see chapter 2.2.4.

The dynamic effect of the Fermi contact interaction causes a spin flip of electrons and nuclei. This becomes clear if the product $\hat{\boldsymbol{I}}_{\boldsymbol{n}} \cdot \hat{\boldsymbol{S}}$ is expressed with ladder operators ($\hat{\boldsymbol{X}}_\pm = \hat{X}_x \pm i\hat{X}_y$, $\hat{X} = \hat{I}_n, \hat{S}$):

$$A\hat{\boldsymbol{I}}_n \cdot \hat{\boldsymbol{S}} = A\left[I_z^n S_z + 0.5\left(I_+^n S_- + I_-^n S_+\right)\right]. \tag{2.76}$$

$I_\pm^n S_\mp$ reverses simultaneously the electron/nuclear spin. If the electron system is in equilibrium, a nuclear polarization may relax due to this interaction. A polarized electron system, otherwise, may transfer a polarization to the nuclear system, which is called dynamic nuclear polarization [Abr59; Lam68; Dya73; Dya74; Pag77]. Such a process happens on a timescale of seconds [Pag77; Str03; Col03].

The nuclear polarization diffuses, due to the dipole-dipole interaction between the neighboring nuclei [54] [Pag82; Mal00; Pan06; Kuh97], and the nuclear spin relaxes since the dipole-dipole interaction does not conserve the angular momentum [55]. In the case of continuous excitation, however, the whole sample may be polarized within minutes to hours [Kik00; Str03; Sal01a; VD05]. The total nuclear field may then reach values on the order of a few Tesla. The diffusion constant has been approximated for GaAs bulk to 10^{-3} cm^2/s by Paget [Pag82] and Kuhns [Kuh97]. Additionally, Malinowski et al. estimated for a GaAs / $Al_xGa_{1-x}As$ quantum well a nuclear diffusion constant of 10^{-4} cm^2/s [Mal01]. Further, the nuclear spin might relax through quadrupolar spin-lattice interaction [McN76; Mal00] [56], or precession in the Knight field, or in the field of nuclear spin fluctuation B_{NF} [Str03]. Huang et al. showed that in GaAs bulk, weakly donor-bound electrons are dominating the DNP process. They found DNP time constants of 10 min for itinerant electrons and for the localized electrons of less than 1 min.

In a QW, the localization of electrons is less because of remote modulation doping (chapter 2.1.1), and additionally the spin polarization is smaller because of lower spin lifetimes. Due to the geometric confinement, however, the overlap between the itinerant electrons and the nuclear system is enhanced, and an even higher DNP may be achieved than in bulk. A theoretical discussion of DNP in 2DES may be found in:[Ţif04; Ţif03; Ţif11]. Salis et al showed DNP in (110)-grown GaAs quantum wells [Sal01a; Sal01b], and Malinowski et al. studied nuclear dynamics in undoped (001) oriented GaAs QW [Mal01]. Besides the above mentioned NMR and ESR methods, there are various other methods to measure dynamic nuclear polarization, for example a change of the Larmor frequency which may be observed in time-resolved Faraday/Kerr rotation experiments [Kik00; Mal00]. The influence of a nuclear polarization is also found in an oblique magnetic field, the Hanle effect, which is shown in chapters 4.5, 5.5. A good overview over such experiments may be found in [Dya08; Mei84].

[54] The dipole-dipole interaction acts on the electron as well. Typically, it is neglected compared to the contact hyperfine interaction.

[55] The dipole-dipole interaction conserves the energy but not the angular momentum. The Hyperfine interaction on the contrary conserves both angular momentum and energy [Dya08; Ţif11].

[56] The quadrupole moment of the nuclear spin may couple the piezoelectric field of a phonon.

Chapter 3

Experimental methods

The purpose of this chapter is to introduce the applied measurement techniques this work uses. Here the Hanle-MOKE method is the main technique to detect spin dynamics and spin transport phenomena. To describe the Hanle-MOKE method this chapter firstly discusses the magneto-optical Kerr effect (MOKE) and then depicts the Hanle effect. Moreover, this work uses Photoluminescence (PL) measurements to determine electron temperature and carrier densities in the sample. By observing the PL time resolved, the recombination times of the carriers can be investigated. It is possible to yield the absolute degree of spin polarization as well, by conducting spin-resolved PL measurements. This chapter also discusses the method of optical (electrical) gating, a means to manipulate the carrier density in the sample. Finally, the different experimental setups are presented.

3.1 Magneto-optic Kerr/ Faraday effect

In 1845, Michael Faraday observed that linearly polarized light propagating through a medium interacts with an applied magnetic field [Far46]. Hereby, the polarization axis is rotated by an angle proportional to the applied magnetic field $\theta = \nu_v d_{opt} B$, where d_{opt} is the length of the optical path through the medium and ν_v is the Verdet constant, which is a material property determining the magnitude of the Faraday effect [1]. Is the light reflected on a material containing a magnetization instead of propagating though it, the same effect occurs [Ker77; Ker78]. Among several other technical applications these magneto-optic effects may be used to determine a magnetization or a spin polarization in a material. In this context, one speaks of the Faraday effect regarding to the transmission of the probe beam, as depicted in figure 3.1 (a), and the Kerr effect in the case of reflection displayed in figure 3.1 (b)-(d)). Furthermore, the magneto-optical Kerr effect (MOKE) needs to be differentiated regarding the orientation of the magnetization with respect to the sample plane. If the magnetization is oriented perpendicular to the sample surface, one speaks of the polar MOKE (p-MOKE, figure 3.1 (c)). Instead of a linear polarization, like the incident beam has, the reflected beam shows an elliptic polarization, and the main axis of the ellipse is rotated by the Kerr angle θ compared to the axis of the initial linear polarization. On the contrary, the longitudinal MOKE is present if the magnetization is oriented in the sample plane, parallel to the plane of incidence. Similar to the polar MOKE, the polarization changes to elliptic after the re-

[1] A positive Verdet constant implies a material where the polarization rotates counterclockwise, if the light propagation is along the magnetic field.

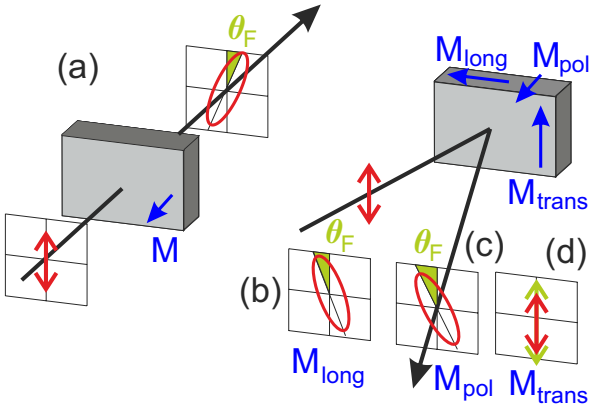

Figure 3.1: *(a) Linearly polarized light becomes elliptic passing through the sample due to the Faraday effect. The main axis of the ellipse is rotated by the Faraday angle θ_F to the incident polarization axis. Similarly these effects are observed at the longitudinal* ***(b)*** *and the polar* ***(c)*** *MOKE with the difference of dealing with reflected instead of transmitted light. The transversal MOKE* ***(d)*** *causes a modulation of the polarization vector instead of a rotation.*

flection and the main axis is rotated by the Kerr angle as well. The longitudinal MOKE, however, is an order of magnitude smaller than the polar MOKE. Finally, the transversal MOKE is present if the magnetization is oriented in the sample plane, perpendicular to the plane of incidence. Only the p-polarization (polarization vector is parallel to the plane of incidence) shows an effect though. On the contrary to the preceding effects the polarization does not rotate, the polarization vector is modulated instead (whether it is increased or decreased depends on the direction of the magnetic field). Under normal incidence only the polar MOKE is observable, making the p-MOKE the most widely used MOKE effect. A macroscopic explanation for the magneto-optic effects is based on antisymmetric off-diagonal terms in the dielectric tensor [Per67; Hun67] [2] [3]. Linearly polarized light consists of right and left circularly polarized components. In a medium these two components cause circular motion of electrons with equal radius. On these electrons, an additional Lorentz force is acting, induced by an external magnetic field, resulting in an elliptic motion of the electrons. Those elliptic orbits are different for left and right hand rotating electrons resulting in unequal dielectric constants and refractive indices. Hence, the complex rotation is given by [Qiu00]:

$$\theta = \frac{\pi\, d_{opt}}{\lambda}\,(\tilde{n}_{lcp} - \tilde{n}_{rcp}) = \frac{\pi\, \tilde{n}\, d_{opt}}{\lambda}\boldsymbol{Q}\cdot\boldsymbol{k}. \tag{3.1}$$

Here λ is the wavelength of the light, $\boldsymbol{Q}$ is the Voigt vector [4], $\tilde{n}_{lcp} = n - (0.5\,\boldsymbol{Q}\cdot\boldsymbol{k})$, $\tilde{n}_{rcp} = \tilde{n} + (0.5\,\boldsymbol{Q}\cdot\boldsymbol{k})$. are the refractive indices for right- and left-hand circularly polarized light, and $\tilde{n} = \sqrt{\varepsilon}$ the averaged refractive index. The real part of equation 3.1 gives the rotation angle, and the imaginary part the ellipticity. A simplified analytic expression for the magneto-optical effects may be found in [You96]. SO-coupling, which may be seen as an effective magnetic field, see chapter 2.2.2, enhances the Faraday rotation in ferromagnetic materials, and semiconductors with a spin imbalance [Qiu00].

As described in chapter 2.2.1, circularly polarized light generates a spin polarization according to the selection rules (in figure 3.2 (a)-(b) without loss of generality only the transition LH-CB for σ^+ light is shown, see figure 2.7). Because of VB mixing the hole

[2] $D_i = \varepsilon_0 \sum_j \varepsilon_{ij} E_j$; $i,j = x,y,z$ with D the electric displacement field, E the electric field, and ϵ_{ij} the dielectric tensor [Kli05].

[3] Under time reversal the electric field $\mathcal{E}/D$ remains unchanged, but the magnetic field H changes its sign. It can be shown that the antisymmetric part of the dielectric tensor arises from the magnetic field [Qiu00].

[4] A mathematical form where a tensor is represented by a vector with lower order.

spin relaxes fast, so that recombination may involve both electron spin kinds (figure 3.2 (c)). Eventually, a spin-polarized Fermi sea is present in the CB (figure 3.2 (d)).

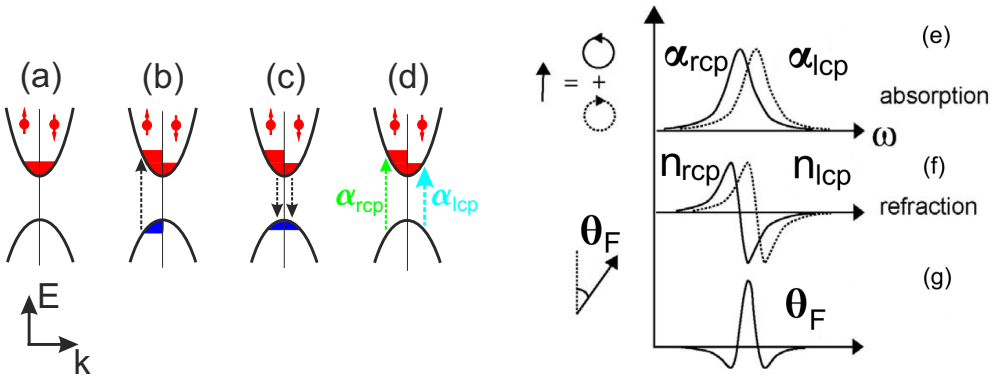

Figure 3.2: ***(a)*** *A doped semiconductor in equilibrium.* ***(b)*** *Spin pumping: A spin imbalance is created by right circular polarized light. According to the selection rules this would be a transition from LH to CB.* ***(c)*** *The hole spin relaxes fast due to VB mixing, therefore both electron spin orientations are involved in recombiantion..* ***(d)*** *A spin imbalance is left in steady state.* ***(e)*** *The simplified absorption function, assuming a Lorentzian line shape, differs for the two helicities. Therefore, the refraction indices differ as well* ***(f)****. This results in a Farady/ Kerr angle* $\theta \propto \tilde{n}_{rcp} - \tilde{n}_{lcp}$ ***(g)****.* ***(e)****,* ***(f)****,* ***(g)*** *taken from [Büg09].*

According to the Zeemann effect the two spin orientations are split in the energy, yielding two different Fermi energies [5], see figure 3.2 (b). Hence, the absorption resonances for the different helicities of light with energy $\hbar\omega$ are unequal. Figure 3.2 (e) shows the absorption assuming a Lorentzian line shape, although the Faraday/Kerr resonance also depends on the exact line shape of the absorption edges [Büg09]. Consequentially the two indices of refraction are split in energy, giving rise to the Kerr angle $\theta \propto (\tilde{n}_{lcp} - \tilde{n}_{rcp})$. This is also called circular birefringence. The difference of the refractive indices may be obtained using the Kramers-Kronig transformation [Bec05]:

$$\tilde{n}_{rcp} - \tilde{n}_{lcp} = \frac{c}{\pi\omega\tilde{n}} \mathcal{P} \int_0^\infty \frac{\omega' \left(\tilde{\alpha}_{rcp} - \tilde{\alpha}_{lcp}\right)}{\omega'^2 - \omega^2} \, d\omega'. \tag{3.2}$$

Here $\mathcal{P}$ is the principal value of the integral for $n_{rcp} - n_{lcp} \ll n$ and $\tilde{\alpha}_{rcp,lcp}$ are the absorption coefficients [6]. Under the assumption of a parabolic band, a spectral dependence of the Kerr/Farady rotation may be calculated. Figure 3.3 shows the calculation from M. Beck and a qualitative measurement by S. Crooker [Cro05a; Cro07] for bulk GaAs at liquid-helium temperature. Both results show at least one sign change of the Faraday/ Kerr signal. The position of the extrema depends on various parameters such as temperature and carrier density, yielding an important parameter for spin dynamics measurements. For the QW sample this work uses, figure 5.10 in chapter 5.2 presents an analog measurement. Altogether, a spin polarization may be probed with a linearly polarized laser, having a photon energy close to the Fermi energy, instead of using the circular polarization degree of the photoluminescence. The Kerr/ Faraday angle is then

[5] $E_{F,3D}^{\uparrow/\downarrow} = \hbar^2 (2m^*)^{-1} \left(3\pi^2 n^{\uparrow/\downarrow}\right)^{2/3}$, $E_{F,2D}^{\uparrow/\downarrow} = \hbar^2 \pi m^{*-1} n^{\uparrow/\downarrow}$.

[6] $\tilde{\alpha}_{rcp/lcp} = \tilde{\alpha}_0^{hh} \left(1 - \left(1 + \exp\left(\frac{\hbar\omega - E_g - (m/\mu_{hh}) E_F^{\uparrow/\downarrow}}{k_B T}\right)\right)^{-1}\right)$

$\tilde{\alpha}_0^{lh} \left(1 - \left(1 + \exp\left(\frac{\hbar\omega - E_g - (m/\mu_{lh}) E_F^{\uparrow/\downarrow}}{k_B T}\right)\right)^{-1}\right)$ with $\mu_{hh,lh} = \left(m^{-1} + m_{hh,lh}^{-1}\right)$ [Bec05].

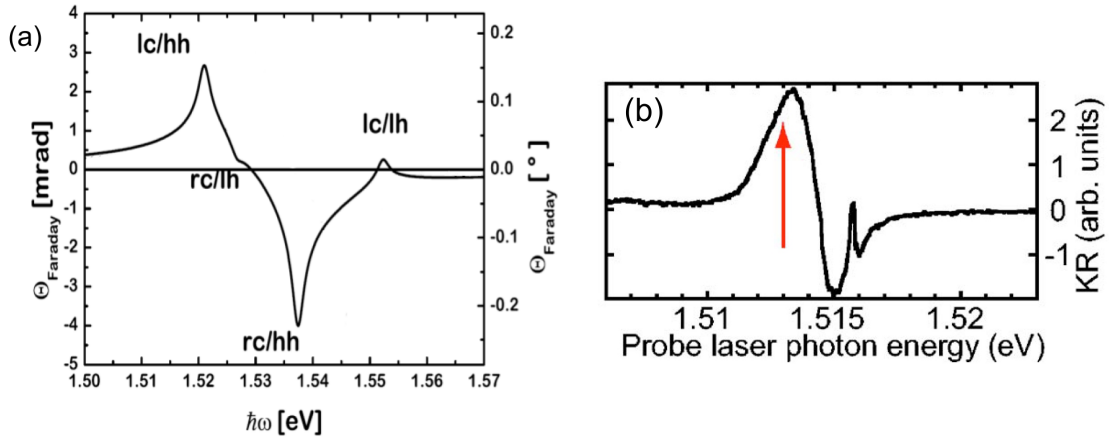

Figure 3.3: ***(a)*** *Calculated spectral dependence of the Faraday/Kerr angle in n-GaAs bulk at liquid-helium temperature, by M. Beck ($n^{\uparrow} = 1.5 \cdot 10^{17}$ cm^{-3}, $n^{\downarrow} = 0.5 \cdot 10^{17}$ cm^{-3})[Bec05].* ***(b)*** *Experimentally determined spectral dependence for n-GaAs bulk ($n = 10^{16}$ cm^{-3}). The red arrow indicates the laser energy used for excitation. Taken from [Cro07].*

proportional to the spin polarization per area (equation 2.7). Spin imbalances with a degree higher then 20% require the consideration of nonlinear effects though [Bec05]. A widely used method to observe spin dynamics is the time-resolved Faraday or Kerr rotation (TRFR/ TRKR), which may be utilized to measure spin lifetimes from 100 fs to a few ns [Aws85; Bau94]. In this work, the polar MOKE is employed, in association with the Hanle-MOKE technique described in the following chapter.

3.2 Hanle-MOKE technique

In 1924 R.W. Wood and A. Ellett found a reduced degree of polarization in the resonance fluorescence of mercury, when a small magnetic field is applied [Woo24]. W. Hanle presented a semiclassical explanation for this effect [7] [Han91]. Later a quantum mechanical explanation based on the concept of level crossing was presented [Bre33]. Here an atomic state, split because of fine or hyperfine interaction, is coherently excited by linearly polarized light (assuming the excitation is spectrally broad enough). In an external magnetic field these levels may cross by the induced Zeeman splitting. Similar to Youngs double slit experiment, this level crossing yields an interference of the emitted resonance fluorescence [8]. From this interference, the lifetimes of atomic states may be determined [Fra61; Dem03]. Parsons et al. used the Hanle method to determine the spin lifetimes in semiconductors first [Par69]. In all-optical measurements the depolarization of a spin ensemble may be measured either by polarization-resolved photoluminescence [Par69; Dzh02; Ave06] or using the polar MOKE (chapter 3.1) [Fur07; Cro05a; Cro07; Völ11]. The all-optical measurements presented in this work contain a spin polarization, which is oriented along the growth direction (z-direction), and is generated by a continuous-wave (cw) laser. An applied magnetic field in y-direction

[7] The incident linearly polarized light excites valence electrons to oscillate in the polarization direction, yielding a emission of dipole radiation. Due to the dipole nature the observed intensity along the polarization direction is zero. Is an magnetic field applied, the electrons precess allowing a detection. Hence, the observed intensity may be modulated with the magnetic field [Dem03].

[8] The total intensity of the resonance light is proportional to $|A_{b,a}|^2 + |A_{c,a}|^2$ in the case of not crossed levels b,c, where A is the amplitude of the emitted wave, and a the ground state. A total intensity proportional to $|A_{b,a} + A_{c,a}|^2$ is found for crossed levels [Fra61].

invokes the electrons to precess with the Larmor frequency $\omega_L = g\mu_B B/\hbar$. The average projection of the electron spin on the z-direction, detected by the p-MOKE, is derived as a solution from equation 2.30 or 2.59, neglecting drift and diffusion terms:

$$S_z = \exp\left(-t/\tau_s\right)\cos\left(\omega_L t\right). \tag{3.3}$$

In order to justify this neglect of the diffusion term, the laser spot size needs to be about the spin diffusion length. The degree of the depolarization for a certain magnetic field is then determined by the spin lifetime τ_s (figure 3.4), and the average steady-state spin polarization for continuous excitation, may be expressed by [Fur07]:

$$S_z = \int_0^\infty S_0 e^{-t/T_s}\cos(\omega_L t)\, dt. \tag{3.4}$$

This integral has an analytical solution in the form of a Lorentzian function:

$$S_z = \frac{S_0 T_s}{1+(\omega_L T_s)^2}. \tag{3.5}$$

Hence, the spin polarization S_0 may be extracted from the amplitude $S_z(B=0) = S_0 T_s$ of the Hanle curve. This value is a time averaged spin polarization, on the contrary to Spin resolved PL measurements where the absolute degree of spin polarization is determined. According to the definition of a Lorentzian, the factor $\omega_L T_s$ is the half width at half maximum (HWHM). This value can be used to determine the spin lifetime ($g\mu_B B_{1/2} T_s = 1$), which contains the spin dephasing time τ_s and the recombination time τ_r:

$$T_s = \frac{\hbar}{g\mu_B B_{\frac{1}{2}}}\ , \qquad \frac{1}{T_s} = \frac{1}{\tau_r} + \frac{1}{\tau_s}. \tag{3.6}$$

The probability ϖ that the electron-hole recombination involves spin-polarized electrons depends on the electron density of optically generated spin polarized electrons (holes) n_{opt} and the doping density n:

$$\varpi = \frac{n_{opt}}{n + n_{opt}}\ , \qquad \frac{1}{\tau_r} = \varpi \cdot \frac{1}{\tau_{r0}}. \tag{3.7}$$

For small excitation-densities and high n-doping the recombination time may be neglected so that $T_s \approx \tau_s$. Obviously Hanle measurements based on analyzing the depolarization of the PL are unsuitable for systems with long spin lifetimes, since the short carrier lifetime limits the depolarization in the applied field due to spin precession. This is discussed in more detail in chapter 5.2. Figure 3.4 (a) shows simulated Hanle curves with spin lifetimes of 10 ns and 50 ns (assuming GaAs bulk with a g-factor of $|g_{GaAs}| = 0.44$). The occurrence of such curves is explained by a spin vector, which represents the total ensemble spin, and precesses a certain angle within its lifetime, see figure 3.4 (b). So that a spin vector, corresponding to a spin ensemble with a shorter lifetime, may precess the same angle as a spin vector corresponding to a spin ensemble with a longer lifetime, it has to precess faster. Hence, a higher magnetic field is necessary, yielding a wider Hanle curve for shorter spin lifetimes. At the marked position 2 on the Hanle curve in figure 3.4 (a) the external magnetic field is zero, therefore the spin vector does not precess and the detected z-component is maximal. At positions 1 and 3 the precession is so fast that the time average is zero. In contrast to the previously mentioned TRKR measurements, which is appropriate for lifetimes from 100 fs to a few ns (limited by the length of the mechanical delay line and the laser repetition rate), the Hanle method is adequate for lifetimes from a few ns to a few hundred ns. Larger lifetimes require a very high resolution of the applied magnetic field, whereas smaller

lifetimes need large magnetic fields. Figure 3.4 (c) depicts the time-resolved evolution of a spin polarization, which may be measured e.g with the TRKR method. Without an applied magnetic field, the spin polarization decays exponentially with time. For a nonzero magnetic field, however, the spin polarization follows a damped cosine function. As above mentioned, the continuous excitation implies integration over all times, which results in a vanishing averaged total spin polarization for high magnetic fields.

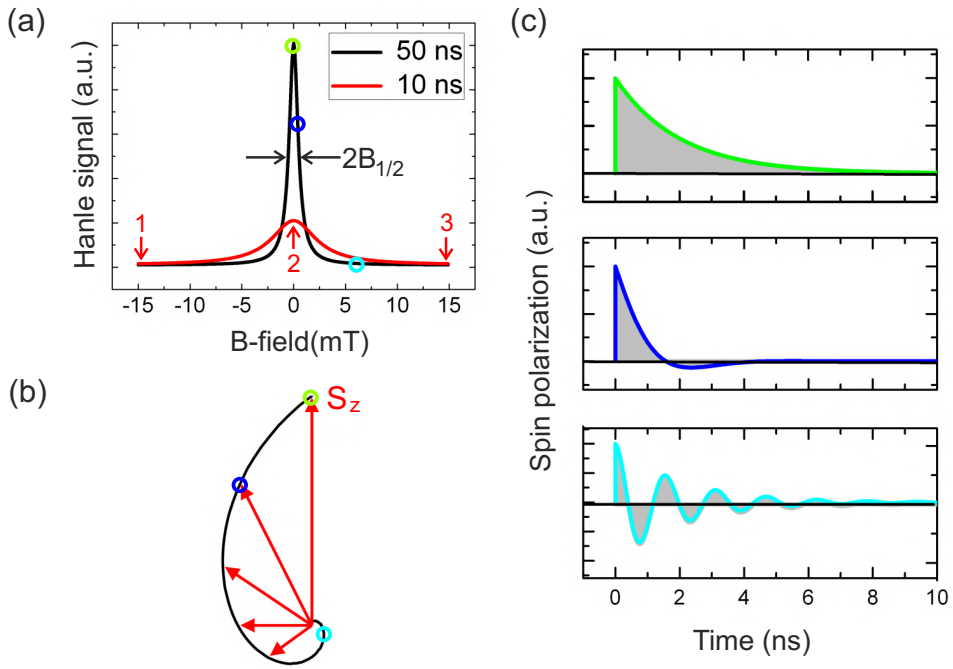

Figure 3.4: ***(a)*** *In case of optical spin injection, the Hanle curves have a Lorentzian line shape. From the HWHM the spin lifetime may be calculated.* ***(b)*** *The spin vector describing the spin ensemble precesses within the magnetic field. Simultaneously, the spin ensemble dephases, yielding a reduction of the length of the vector.* ***(c)*** *Without an applied magnetic field, the spin polarization decays exponentially, whereas a magnetic field induces a damped cosine behavior. Thus integrating the spin polarization over the time results in a reduction of the initial spin polarization.*

Up to now, the application of the Hanle-MOKE method on systems with isotropic spin dephasing was discussed. The spin lifetime in (110)-grown GaAs QW is, however, anisotropic in the spatial directions. Therefore, the spin lifetime obtained by the Hanle method is approximated with the geometric mean of out-of-plane spin lifetime τ_z and in-plane spin lifetime $\tau_\parallel$ [9]:

$$\tau_s = \sqrt{\tau_z \tau_\parallel}. \tag{3.8}$$

The dynamic polarized nuclei discussed in chapter 2.4 entails effective magnetic fields which influences the Hanle curve.

In the cases such a behavior is not of interest, utilizing a liquid crystal retarder suppresses the influence of nuclear effects on the Hanle curve effectively. The helicity of the pump laser is modulated between 0° and 90° here.

[9]The geometric mean is giving a more meaningful average in case that the two lifetimes differs significantly. In the arithmetic mean of two numbers, with a great difference in the value, for example the change of the larger number would alter the mean more effectively then the change of the smaller number.

So far transport properties have been neglected in the discussion. Henceforth, spin drift and diffusion along a 1D line within a 2D plane are considered. Now only a specific subset of the whole spin ensemble is measured. Electrons that travel from the point of origin require a certain time of flight to arrive at the detection point. This is approximated by a Gaussian distribution of the arrival times of a spin subset at position x. Under the condition that the spin drift length exceeds the spin diffusion length ($\mu\mathcal{E}\tau_s > \sqrt{D\tau_s}$) [10] a spin accumulation is found at a distance x depending on the external magnetic field B_y [Fur07]:

$$S_z(x, B_y) = \int_0^\infty \frac{S_0}{\sqrt{4\pi D t}} e^{-(x-v_d t)^2} e^{-t/T_s} \cos(\omega_L t)\, dt. \tag{3.9}$$

Here, the mentioned Gaussian distribution is simply added to the integrand in equation 3.4, and the point of spin injection is set to be at $x = 0$. An analytical solution for this integral is presented in [Fab07] (equation II.238):

$$S_z(x) = -\frac{j_{s0} L_s}{eD} e^{-\alpha_1 x/L_s} \left[\frac{2\kappa + \alpha_1}{(2\kappa + \alpha_1)^2 + \alpha_2^2} \sin\left(\frac{\alpha_2}{L_s} x\right) + \frac{\alpha_2}{(2\kappa + \alpha_1)^2 + \alpha_2^2} \cos\left(\frac{\alpha_2}{L_s} x\right) \right], \tag{3.10}$$

with

$$\alpha_1 = \frac{1}{\sqrt{2}} \sqrt{1 + \kappa^2 + \sqrt{(1+\kappa^2)^2 + (\omega_L T_s)^2} - \kappa}, \tag{3.11}$$

$$\alpha_2 = \frac{1}{\sqrt{2}} \sqrt{-1 - \kappa^2 + \sqrt{(1+\kappa^2)^2 + (\omega_L T_s)^2}}. \tag{3.12}$$

Here, L_s is the diffusion length (chapter 2.3.2), and j_{s0} is the magnitude of the spin current at $x = 0$. Parameter α_1 expresses the effective spin relaxation, and α_2 presents the effective spin precession. Moreover, the parameter $\kappa = v_d T_s / 2L_s$ becomes zero in the case of pure spin diffusion.

For measuring spin diffusion lengths with a high enough spatial resolution, taking a whole Hanle curve is not efficient. Here, a three-point Hanle measurement is employed instead. The magnetic field is ramped to values at each side of the Hanle curve, where the spin polarization is approximately zero (points 1 and 3 in figure 3.4 (a)), and then to zero magnetic field where the spin polarization is maximal (point 2 in figure 3.4 (a)). The difference of the measured maximum value and the mean of the values from points 1 and 3 yields a approximate magnitude of the amplitude, which is plotted as a function of the distance between pump and probe laser spot. As discussed in chapter 2.3.2 the spin diffusion is considered as a radial movement from a point source. The resulting spatial dependence has therefore the asymptotic behavior of a MacDonald function, equation 2.68.

3.2.1 Hanle-MOKE and electrical spin injection

The initial orientation of the spin polarization is the only feature the above discussed measurements differ from the Hanle-MOKE measurements, where the spin injection happens electrically, through a (Ga,Mn)As electrode (figure 3.5 (a)), as presented in chapter 4. The spins are injected into the GaAs under the contact and diffuse or drift away laterally, where next to the electrodes a detection is possible. Since the magnetization of the electrode lies in the sample plane (y-direction), and the p-MOKE is only sensitive to an out-of-plane magnetization, there is no Kerr rotation observed at

[10] This is true for the downstream case, see chapter 2.3.2 and of course in the all-optical experiments.

zero field. Whereas an applied magnetic field causes a spin precession, which enables a detection of the out-of-plane component. The Hanle signal is then a point-symmetric function. Figure 3.5 (b) depicts simulated, normalized Hanle curves for this geometry with spin lifetimes from 10 ns to 100 ns (assuming GaAs bulk with a g-factor of $|g_{GaAs}| = 0.44$).

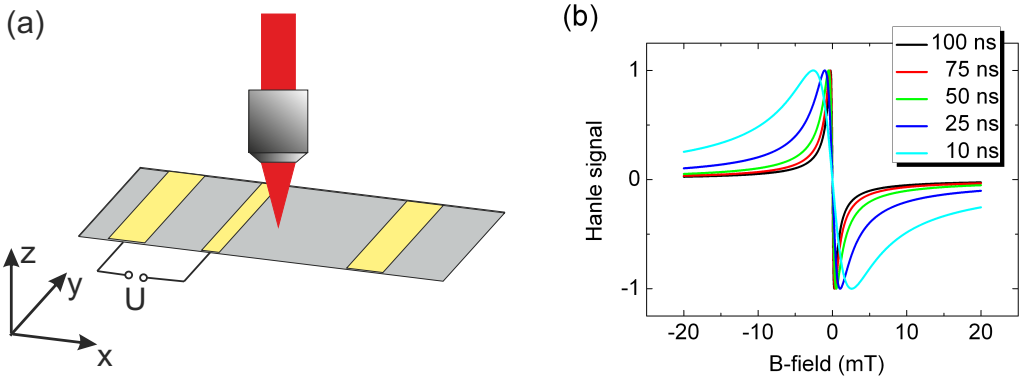

Figure 3.5: ***(a)*** *Schematic illustration of the sample structure used for electrical spin injection. Microstructured (Ga,Mn)As electrodes inject a spin polarization (Esaki diode) which is initially oriented in the sample plane along the y-direction. For the Hanle measurement, a magnetic field along the x-direction is applied.* ***(b)*** *Simulated, normalized Hanle curves for different spin lifetimes in GaAs bulk.*

Consequently, equations 3.9 and 3.10 need to be modified to:

$$S_z(x, B_y) = \int_0^\infty \frac{S_0}{\sqrt{4\pi D t}} e^{-(x-v_d t)^2} e^{-t/T_s} \sin(\omega_L t)\, dt, \tag{3.13}$$

$$S_z(x) = -\frac{j_{s0} L_s}{eD} e^{-\alpha_1 x/L_s} \left[\frac{2\kappa + \alpha_1}{(2\kappa+\alpha_1)^2 + \alpha_2^2} \cos\left(\frac{\alpha_2}{L_s} x\right) - \frac{\alpha_2}{(2\kappa+\alpha_1)^2 + \alpha_2^2} \sin\left(\frac{\alpha_2}{L_s} x\right) \right] \tag{3.14}$$

In this case it is more complex to determine the spin lifetime, since spin drift and diffusion need to be considered. The obtained Hanle curves may be fitted with function 3.14, and providing the spin diffusion length is known and drift is absent, a spin lifetime can be extracted. One needs to take into account, however, the extent of the electrode and integrate over all possible distances. Similarly to the optical injection case, measuring diffusion length in an adequate time with reasonable spatial resolution does not allow taking full Hanle curves. Instead, a two-point scheme is used here. The spin polarization is proportional to the amplitude of the Hanle signal. Thus, two values of the signal are taken for a magnetic field at, or close to the extrema and the difference of those is plotted against the distance to the electrode. The decay is fitted with an exponential function ($\exp(-r/L_s)$).

Measuring the spin polarization injected from a ferromagnetic electrode has also been done using another ferromagnetic contact to detect the spin polarization. In this all-electrical injection and detection setup, the Hanle effect is often used as well. The voltage on the detector electrode is measured as a function on an out-of-plane magnetic field, yielding a Lorentzian-shaped curve [Lou06; Lou07; Cio09].

3.3 Photoluminescence spectroscopy

Photoluminescence spectroscopy (PL) is based on the evaluation of the luminescence of the sample after excitation with monochromatic light, whereas with photoluminescence excitation spectroscopy (PLE), the absorption is investigated. Here, the detection is fixed at a certain wavelength and the excitation is ramped over various wavelengths. In this work, PL spectroscopy is employed to determine sample parameters such as the carrier density and electron temperature. By time resolved observation of the photoluminescence, the carrier recombination time can be determined. Finally, by applying spin-resolved PL, the degree of spin polarization is obtained.

For the determination of the carrier density and the electron temperature, first of all electron-hole pairs are generated with nonresonant laser light (laser energy above band gap), as depicted in figure 3.6 (a). The generated electrons and holes relax towards the band minimum and maximum, respectively, through intra-subband scattering, for example, with phonons. This process is also called thermalization. The emission of photons because of recombination is called luminescence, which is detected by a spectrometer. For emission and absorption of light, energy and momentum conservation is valid, and due to the negligible photon k-vector, transitions occur vertically in the $E(\boldsymbol{k})$ graph, see chapter 2.2.1. The emission starting from the highest occupied state at the Fermi energy E_F to the lowest energy E_0, which is the bandgap energy in case of a bulk material, and the subband minimum in case of a quantum well, results in a shark-fin-shaped function depicted in figure 3.6 (b) [11]. The second peak at the lower-energy side is presumably caused by carbon impurities [Str81; Teh88; Teh90]. Because of the large effective mass of the heavy holes the curvature of the HH band is neglected in the region of the luminescence. Therefore, the spectral width ΔE in the PL curve is approximately given by the conduction band dispersion.

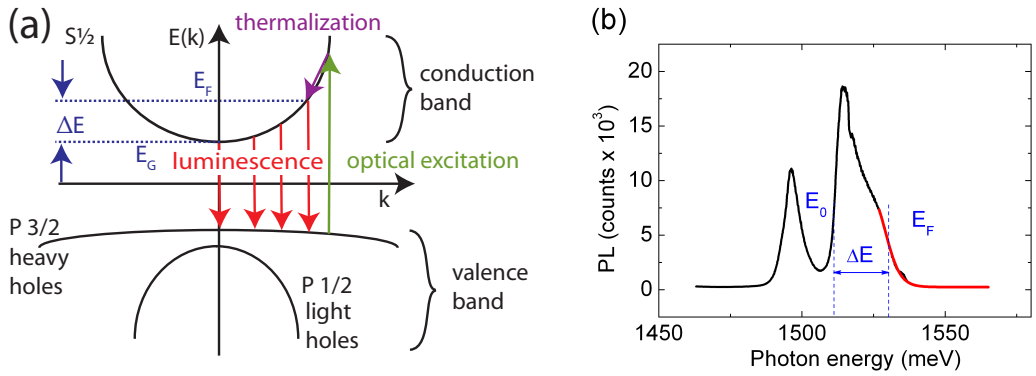

Figure 3.6: ***(a)*** *Schematic process of photoluminescence measurements. After nonresonant excitation carriers thermalize and recombine under emission of a photon. Taken from [Gri12b].* ***(b)*** *PL spectra obtained for sample QWA at 18 K. From the spectral width the electron density is obtained, and from fitting the high-energy tail the electron temperature can be extracted. The second peak on the low-energy side is caused by carbon impurities.*

The width of the PL trace $\Delta E = E_F - E_0$ is a measure for the carrier density. With the expression of the Fermi energy in a 2DES the carrier density may be approximated by [Gri12b]:

$$n = \frac{E_F\, m^*}{\pi\hbar^2} \approx \frac{\Delta E\,[\mathrm{meV}]}{3.57} 10^{11}\mathrm{cm}^{-2}. \tag{3.15}$$

[11] The Amplitude of the PL spectra depends also on the absorption of the 2DES.

The approximation contains the parameter $E_0 \approx E_G$ and the effective mass for conduction electrons in bulk GaAs $m^* = 0.067m_0$ [Sti69; Sti71; Law71; Bla82]. Determining the carrier density with this method is not accurate for densities in the excitonic regime [12].

Besides the carrier density the electron temperature may be deducted from the PL spectra as well. As described in chapter 2.1.1, the electrons in the conduction band follow the Fermi-Dirac distribution:

$$f_e(E,T) = \frac{1}{\exp\left[(E - E_F/k_BT)\right] + 1}. \tag{3.16}$$

The high-energy tail of a PL trace can be approximated with this function since the energy distribution smears out around the Fermi energy $E_F \pm k_BT_e$ for $T_e > 0$ K. On this grounds, the electron temperature, and the Fermi energy can be extracted. In some cases, a second PL peak is visible at higher temperatures, corresponding to the occupation of higher subbands. Thus, the fitting function 3.16 has to be expanded simply by adding a Lorentzian function to obtain more accurate results.

The photoluminescence can be monitored time resolved by employing pulsed excitation and a streak camera instead of the CCD camera after the spectrometer, see experimental setup in chapter 3.5, figure 3.11. From the exponential decay of the time resolved PL (TRPL) the carrier lifetime can be extracted [Rya84]. A description of the functionality of the utilized streak camera and the setup can be found in [Sch10].

The selection rules discussed in chapter 2.2.1 are of course also valid for the emission of light. Threfore an evaluation of the emitted light in regard to the degree of circular polarization makes it possible to determine the degree of spin polarization in a sample. This is an absolute value, in contrast to the value of spin polarization obtained by the Hanle-MOKE method, where the Kerr rotation is proportional to the time-averaged spin polarization. For the extraction of the spin information, two measurements are conducted with different excitation helicities (left/ right circularly polarized). Each time the PL intensity is detected with a fixed polarization direction. One speaks of co- or contra-circular polarization in the case that excitation and emission have the same or the contrary polarization direction. The degree of circular polarization is then defined by [Kor10]:

$$P_{circ} = \frac{I_{co} - I_{contra}}{I_{co} + I_{contra}}. \tag{3.17}$$

Here $I_{co,contra}$ represents the PL intensities for co or contra setups. Pfalz et al. have shown that the fast thermalization of electrons is spin-conserving [Pfa05]. In the utilized QW the obtained PL is mostly caused by transitions involving HH states. The circular polarization from transitions at $\boldsymbol{k} \neq \boldsymbol{0}$ could alternate the measured circular polarization, because of the present VB-mixing [Pfa05]. Similar to the Hanle method (section 3.2) a magnetic field is then applied which causes a dephasing of the electron spins. The determination of the absolute degree of spin polarization requires conducting the same procedure, as described before, again, now with an applied magnetic filed, whose value is high enough to ensure a total depolarization. By subtracting the circular polarization with magnetic field P^B_{circ} from the value without an existing offset is removed [13]:

$$P = P_{circ} - P^B_{circ}. \tag{3.18}$$

[12] At low electron densities, screening effects are not sufficient to prevent the formation of excitons [Kle85a; Shi95].

[13] Under the assumption of excitation from the Γ-point the degree of spin polarization is often directly extracted from P_{circ}. Considering the transition probabilities, e.g., for GaAs bulk, described in chapter 2.2.1, figure 2.7, a degree of spin polarization of 50% is achieved according to equation 2.6. In case LH and HH states are equally occupied the photoluminescence intensities is given by $I_{co} \propto n_\downarrow + 3n_\uparrow$ and $I_{contra} \propto 3n_\downarrow + 1n_\uparrow$. P_{circ} is then $0.25 = -P/2$ (equation 2.6).

Typically the circular polarization degree is averaged over the spectral linewidth of the PL emission in the spectral regions with strong PL emission. This degree of spin polarization is of course already reduced due to the loss of polarization on the optical components in the experiment, such as beam splitter etc. Time resolved monitoring of the degree of circular polarization, may be employed to extract spin lifetimes [Döh04]. This method, however, is limited if systems with long spin lifetimes compared to the carrier lifetimes are involved, see the discussion in chapter 5.2

3.4 Gating

The spin dynamics depend strongly on the carrier density n in the sample. Usually, this parameter depends on the growth parameters, such as doping concentration or spacer width. A way to tune the carrier density of a given sample is gating. There is electrostatic gating where an electrostatic field is applied between the 2DES and a metallic top gate. The electric field influences the band structure and the carrier density. Depending on the initial band composition, a quantum well can be made more symmetric or asymmetric. Accordingly the structure inversion asymmetry (see chapter 2.2.2) changes, which impacts on the spin dephasing. Additionally, the electric field influences the band edge profile and therfore can lead to depletion or an increase of the electron density in the conduction band. This results in a change of the Fermi wave vector $k_{F,2D} = \sqrt{2\pi n}$, which in turn affects BIA (chapter 2.2.2) and SIA (chapter 2.2.2). A reduced carrier density also implies a lower electron-electron scattering time, according to equations 2.51 and 2.52. Moreover, the momentum scattering time τ_p decreases, due to less effective screening of impurities [Rös10].

Another method to modulate the electron density is optical gating and has been shown for GaAs modulation-doped heterostructures [Kuk89] and GaAs quantum wells [Cha86; Gri12a; Syp07]. The latter publication even showed a transition from a p-type structure to a n-type structure. This method, whose principle is shown in figure 3.7, is used in this work to modulate the carrier density of the (110)-grown quantum well structures. Low-intensity above-barrier illumination, which is realized in this work by a

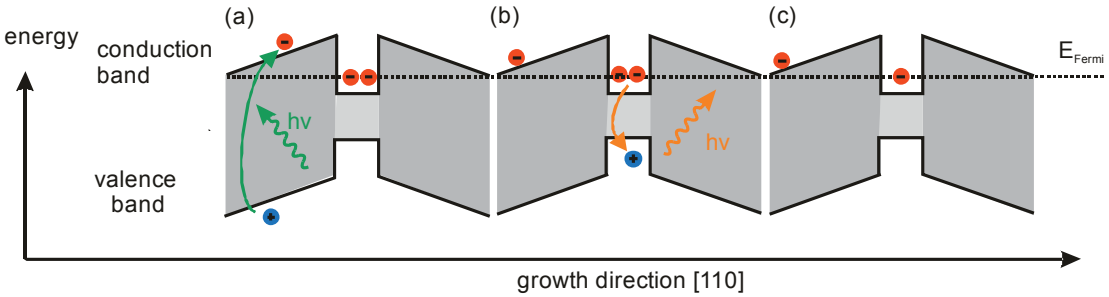

Figure 3.7: ***(a)*** *Creation of an electron-hole pair because of above barrier illumination.* ***(b)*** *According to the potential gradient they are moving towards the doping layer and the holes towards the quantum well. Resident electrons in the QW recombine with the additional holes.* ***(c)*** *In a steady state the electron density is modulated with the intensity of the above barrier illumination. Taken from [Gri12b].*

green laser ($\lambda = 532$ nm), generates electron-hole pairs in the barrier, see figure 3.7 (a). Under the condition of a potential structure depicted in figure 3.7, the electron moves towards the doping layer according to the gradient, yielding a reduction of the number of ionized doping atoms. The holes on the other hand move towards the quantum well, where they recombine with the resident electrons and accordingly reduce the electron density n in the quantum well, see figure 3.7 (b). Due to thermal or optical activation,

or tunnel processes, electrons get from the doping layer to the quantum well [Cha86]. As a consequence of the continuous excitation, a steady state arises, where the rate of electron-hole pairs created by the above-barrier illumination is proportional to the electron-hole recombination rate as well as the rate of electrons moving from the doping layer to the quantum well. For single-sided doped quantum wells, the laser intensity I_L can be expressed as a function of the adjusted steady state electron density n_s, by [Cha86; Car99]:

$$I_L = \iota\,(n_0 - n_s)\exp\left(-\upsilon\sqrt{n_s}\right). \tag{3.19}$$

Here $n_0 - n_s$ is the out-of-equilibrium electron density, and ι describes the tunneling attempt frequency. Tunneling through a triangular potential barrier with a height proportional to n_s leaves the factor $\exp\left(-\upsilon\sqrt{n_s}\right)$, where υ is a barrier parameter. The electron density in the quantum well may be conveniently modulated with the intensity of the above barrier illumination. In addition to the previously described effects of a reduced electron density on the BIA and SIA terms in the electrical case, one must consider in the optical case an increased spin dephasing rate because of contributions of the BAP mechanism, which the increased hole density invokes.

3.5 Experimental setup

The Hanle measurements were conducted with an experimental setup which is sketched in figure 3.8.

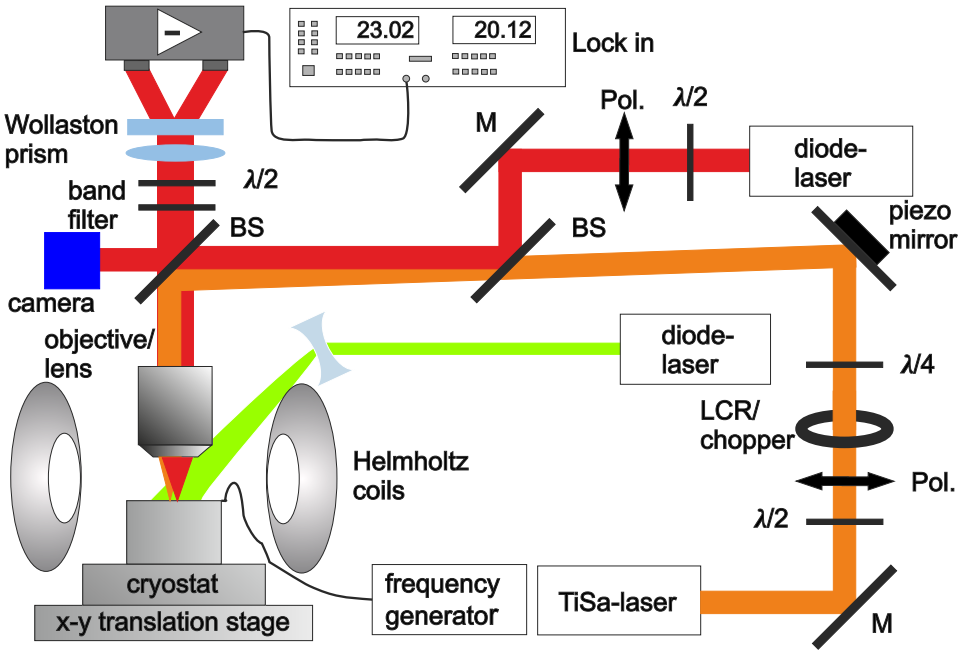

Figure 3.8: *Experimental setup for Hanle measurements. A Linearly polarized probe beam and a circularly polarized pump beam are focused through an objective on the sample sitting in a cryostat. After passing through an band filter, the reflected light is evaluated by a detection stage and a Lock in amplifier, whose reference frequency is provided by and LCR a chopper wheel or a frequency generator.*

Hereby, the sample is mounted in an Oxford Microstat HiRes II (pillared version) continuous-flow cryostat. Liquid helium provided through a low-loss transfer tube is evaporating at the base of a 10 cm long cold finger and herby cooling it down to liquid

helium temperatures of about 4 K. Measured with a heat sensor at the base of the pillar, the temperature can be adjusted from 4 K to room temperature using an electrical heating system. Since a good thermal contact between the cold finger and the sample is very crucial for all the measurements, the sample is mounted with conductive silver on a copper plate, which is fixed on the cold finger with vacuum grease. After several cooling cycles, however, the mounting has to be renewed since the conductive silver becomes porous because of mechanical strain during the cooling cycles. Assuming a good thermal contact, a sample temperature of 8-10 K is expected (compare with [Qua09]). In the cases, where an electrical voltage needs to be applied a sample holder as depicted in figure 3.9 is used. Thin Au wires connect the sample with the pads on the sample holder. Those pads are again connected with the electrical access of the cryostat.

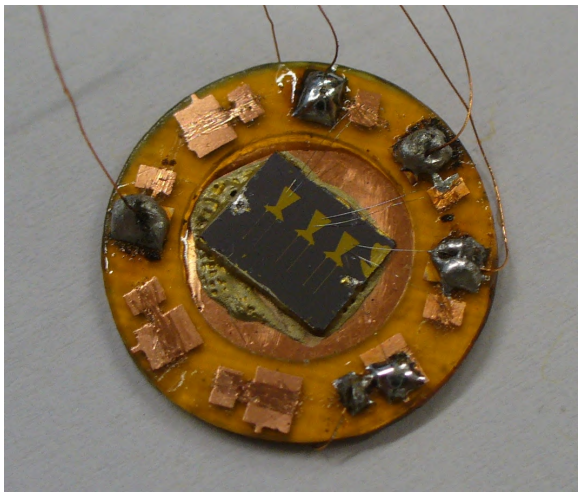

Figure 3.9: *Typical sample holder used in the experiments. The sample is mounted with conductive silver to the copper base plate of the holder. Thin Au wires connect the sample with the contact pads.*

A pair of Helmholtz coils provides the necessary magnetic fields. These can be ramped in 0.05 mT steps. Controlled via a voltage given by the lock-in amplifier, an analog bipolar Kepco BOP 72-6M power supply powers the coils. The obtained in-plane field can be tuned up to 26.5 mT. Additionally, the system may be expanded by another set of smaller Helmholtz coils (7.8 mT) on the perpendicular axis. Subsequently, a magnetic field along each in-plane direction is generated from the sum of the two fields. In order to control the position of the fixed probe beam on the sample, the cryostat is mounted on high resolution x-y stage with a stepping motor (Linos x.act XY 100-1ST). This model has a travel range of 100 mm, a spatial resolution of 0.5 μm and a unidirectional reproducibility of 0.5 μm.

To generate a spin polarization a continuous wave (cw) Titanium-Sapphire laser (Spectra 3900) with a tuning range of 700 - 1000 nm is used in combination with a $\lambda/4$ waveplate. The TiSa laser is pumped by a diode-pumped solid state laser (DPSS) system (Spectra Millenia). This system consists of a Nd:YVO_4 (Neodymium-doped yttrium orthovanadate) laser head, which is pumped by a diode bar (20 W) emitting at a wavelength of 1024 nm. After a frequency doubling (SHG), laser light of 532 nm with a power of 6 W is emitted. For probing the spin polarization, a very stable (very low amplitude noise, and no spectral drift of the laser wavelength) diode Laser (Toptica DL 100/ pro design) is employed. It is tunable through a motorized grating in a range of 800 to 830 nm, with a power of 50 mW at the central wavelength of 827 nm. The laser wavelength is detected by an Ocean optics USB 2000 fiber optic spectrometer. Both lasers are focused on the samples either by an microscope objective or a 50 mm lens, and their power is tuned by a combination of a Glan-Thomson polarizer and a $\lambda/2$ waveplate. The objectives are Nikon CFI Plan Fluor ELWD with magnifications 10x and 20x, and Nikon CFI LU Plan EPI SLWD 100x.

In order to determine the size of the focused laser spot on the sample, the intensity of the reflected laser beam is monitored while scanning over a sharp edge (lithographically made gold pad) [Riz08]. Mathematically, the measured intensity profile (figure 3.10) is a convolution of a step function and a Gaussian function [14] (assuming the laser has a Gaussian profile). Hence, taking the derivative of the measured signal gives the beam

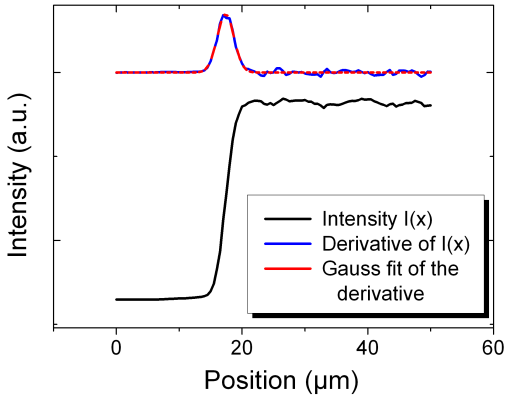

Figure 3.10: *The intensity of the reflected laser spot is monitored while scanning over a sharp edge. The derivative correlates to the laser profile. The FWHM from this Gaussian function is the minimal spot size.*

profile (figure 3.10). The full width at half maximum (FWHM) of a Gaussian fit is then the minimal spot size of the laser [15]. Approximate values for the utilized optics are: 8 μm (10x), 4 μm (20x) 1 μm (100x) and 40 μm (lens). These magnitudes are valid for both lasers in the used wavelength range for the smallest focus.

The spot of the pump laser can be moved on the sample through a piezo-motor-actuated mirror mount (CONEX-AG-M100D). This mirror mount has an exact absolute position sensor. It has a travel range of $\pm 0.75°$, a bidirectional repeatability of $0.01°$ and a minimum incremental motion of $0.001°$. The position of the laser spot on the sample is monitored by a CMOS camera (mvBlueFox 102C). This camera is IR sensitive. The laser spot on the camera picture, however, appears larger than its actual size because of pixel overflow. Furthermore, this laser is modulated either by a chopper wheel or by a liquid crystal retarder (LCR) from Meadowlark optics, if nuclear effects need to be suppressed. This device switches the axis of the linear polarized beam between $0°$ and $90°$ in front of the $\lambda/4$ waveplate with a frequency of ≈ 20 Hz, so that the modulation of the excitation is between σ^+ and σ^- light. Compared to the modulation with a chopper wheel, where the modulation is between zero and full, the Hanle curves have twice the amplitude with modulation by an LCR. The reflected light needs to travel through a bandpass to filter out the laser light from the pump beam. Depending on the sample the central wavelength of the bandpass is chosen (820 ± 5 nm / 810 ± 5 nm). The Kerr rotation of the probe beam is then evaluated by a detection stage. The essential part here is a Wollaston prism. This birefringent crystal splits the polarization of a linearly polarized beam into a parallel and a perpendicular component. These two beams are focused on two photodiodes. The signals from these diodes are differentiated by a differential amplifier. With a $\lambda/2$ waveplate, this differential signal is adjusted to zero (the polarization axis is rotated to $45°$, where both components are equal) in the absence of the pump beam. The difference signal is then evaluated by a lock-in amplifier (Scientific instruments SR830 DSP) with a reference frequency given by the modulation of the spin injection.

For optical injection experiments, this reference is supplied by the chopper wheel or the LCR as described, in the case of electrical injection and the CISP experiments, the

[14] $I(x) = \int_{-\infty}^{\infty} g(y)\theta(x-y)\,dy$, with $g(y)$ the Gaussian beam profile and $\theta(x-y)$ the step function.

[15] As a rule of thumb, one can assume that the laser intensity is within the spot diameter over 60% and outside under 40%.

reference frequency is given by a square wave generator. The spin injection is driven by a rectangular signal with offset, so that the two voltages are zero and V_{inj}. For the optical gating experiments described in section 3.4, a green DPSS laser is used (532 nm).

Figure 3.11 depicts the experimental setup for the photoluminescence measurements. The TiSa-laser is utilized again, for excitation. The emitted light is focused on the en-

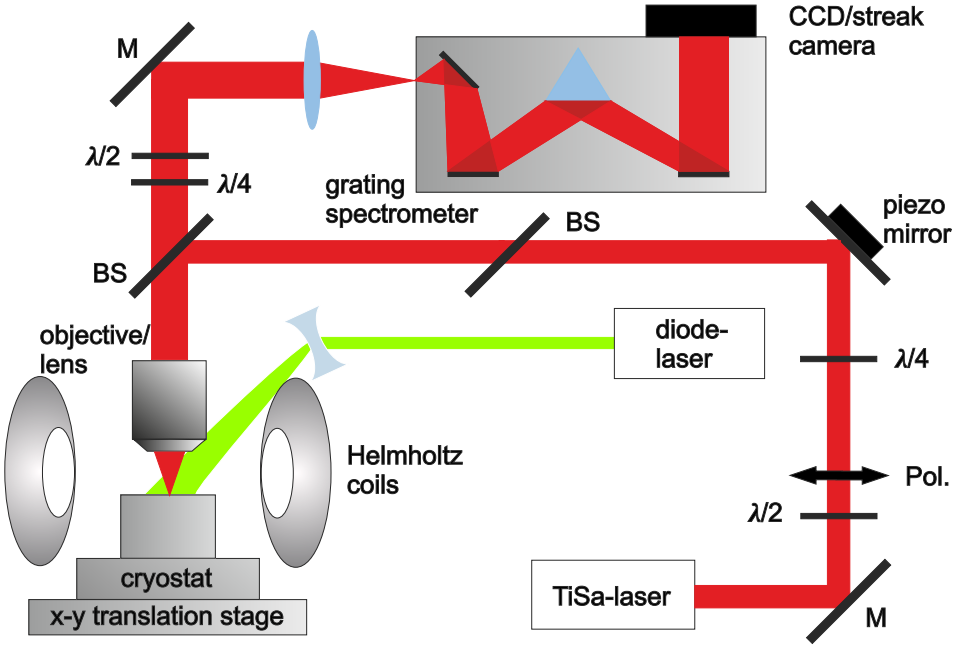

Figure 3.11: *Setup for photoluminescence experiments. For excitation the TiSa-Laser is used. The emission is evaluated by a grating spectrometer.*

trance slit of a grating spectrometer. Here, the third stage of a triple Raman spectrometer with a liquid nitrogen cooled CCD detector (S&I TriVista, Princeton Instruments) is used.

Chapter 4

Electrical Spin-injection into GaAs bulk from (Ga,Mn)As contacts

Motivated by the original concept of a spin transistor by Datta and Das, spin injection into semiconductors from ferromagnetic contacts has become a subject of research interest [Dat90]. Chapter 2.2.1 introduces the theoretical basics of this concept. In order to generate a spin imbalance, a p^+ (Ga,Mn)As/ n^+ GaAs Esaki Zener diode structure is employed. Spin polarized electrons are injected in the area below the contact and then diffuse or drift laterally. Samples fabricated from the same wafer as the examined samples were already subject of investigation, with different detection methods and geometries: Ciorga et al. demonstrated an all-electrical spin injection and detection method [Ein09; Cio09; Cio10; Cio11; Cio13], and Endres et al. used Kerr rotation technique to investigate the spin polarization on the cleaved edge of the GaAs channel [End11; End12]. The latter technique allows monitoring the spin distribution starting directly below the injecting electrode, whereas the method used in this work monitors a spin polarization from the top side of the sample. The results presented here confirm several findings and provide a more complete picture of the spin dynamics and transport. After introducing the sample structure and discussing characteristics of the electrodes and the samples, this chapter investigates the spin dynamics, in particular the spin lifetime and the bias dependence of the spin polarization, as well as spin diffusion and spin drift. Finally, this chapter closes with a discussion of the effect of dynamic nuclear polarization.

4.1 The sample structure

The following section introduces the utilized samples, describing the sample growth, and the preparation of the sample structure. Three different samples are used in this chapter, where two are fabricated from the same wafer with the internal number C080903A (samples ElA and ElB) and the other is from a similar wafer with the internal number C101129B (sample ElC). The wafers were grown by M. Utz from the group of Prof. D. Bougeard, employing the MBE technique (see chapter 2.1.1).

In the first fabrication step, the growth temperature was about 620° C, ensuring pure GaAs crystal growth. A schematic sample structure is depicted in figure 4.1. On top of a semi-insulating undoped (001) GaAs substrate, a 300 nm GaAs buffer layer followed by a 500 nm (Al,Ga) As/GaAs superlattice are deposited, for the sake of canceling roughness and impurities on the substrate surface. The subsequent layer is

the 1 μm thick GaAs layer, where the spin imbalance is created. This layer is doped with Si, yielding an electron density of $n = 2.7 \cdot 10^{16}$ cm^{-3} for samples ElA and ElB and $n = 6.7 \cdot 10^{16}$ cm^{-3} for sample ElC. According to chapter 2.2.5, figure 2.17 (a) these density values imply metallic behavior close to the MIT ($n = 2 \cdot 10^{16}$ cm^{-3}), where high spin lifetimes are expected. In the following 15 nm wide $n \rightarrow n^+$ transition layer, the doping density gradually rises. Eventually, a highly n-doped GaAs film is grown with an electron density of $n^+ = 4 - 5 \cdot 10^{18}$ cm^{-3} (ElA, ElB) and $n^+ = 6 \cdot 10^{18}$ cm^{-3} (ElC). Such high densities are necessary for the formation of the p$^+$ (Ga,Mn)As/ n$^+$ GaAs Esaki Zener diode. As discussed in chapter 2.1.2, the growth of (Ga,Mn)As requires low temperatures compared to the GaAs growth. Thus, the last growth steps are conducted at 240° C in the same MBE chamber. Below the previously mentioned (Ga,Mn)As layer a 2.2 nm $Al_xGa_{1-x}As$ layer ($x = 0.36$ for the samples ElA and ElB, and $x = 0.32$ for the sample ElC) is incorporated. The purpose of this layer is to prevent back-diffusion of manganese atoms into the GaAs [Sch08]. Finally, a 50 nm layer of Ga_{1-x} Mn_x As is grown. For a manganese content of $x = 5.5\%$ (ElA, ElB) and $x = 6.1\%$ (ElC) a Curie temperature of 65 K could be determined by magnetoresistance measurements [Cio09]. A detailed presentation of the employed MBE system and the growth can be found in [Utz12].

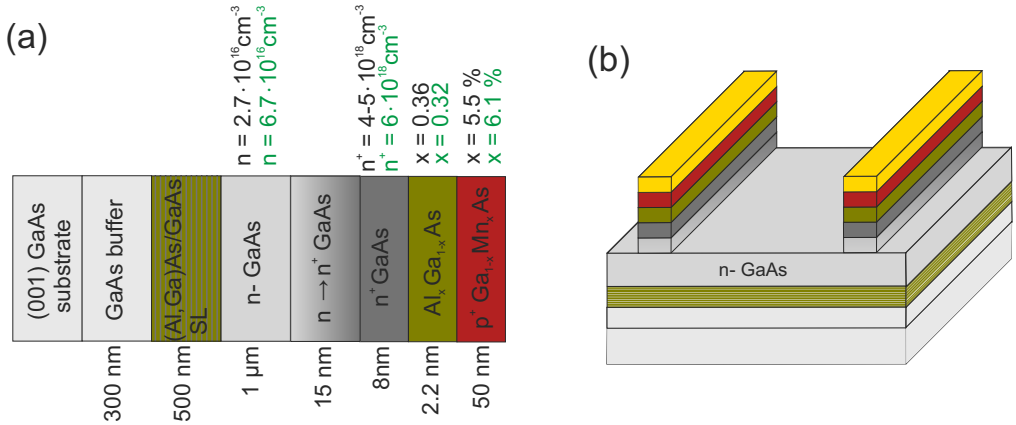

Figure 4.1: ***(a)*** *Growth scheme for both wafers utilized in the experiments. The structure and layer width is the same for both wafers. Doping concentrations and alloy concentrations, however, are different. Here the black values are valid for wafer C080903A (samples ElA and ElB), and the green values for wafer C101129B (sample ElC).* ***(b)*** *Scheme of the mesa structure with exposed n-GaAs channel.*

After the completion of the MBE growth several patterning procedures are necessary. A. Einwanger and M. Ciorga from the chair of Prof D. Weiss have conducted these procedures. The first step is defining a 50 μm wide mesa channel by optical lithography and removing the material around the channel down to the substrate by wet etching. Using electron beam lithography and the evaporation of 15 nm Ti and 110 nm Au the magnetic contacts and a mask for further etching is set. Then, the layers are gradually removed by wet etching, exposing eventually the n-GaAs channel, figure 4.1. In contrast to sample ElA, which has exclusively magnetic contacts, sample ElB and ElC contain nonmagnetic contacts as well. In this case, after removing the (Ga,Mn)As layer, 40 nm Pd and 111 nm Ge are deposited to form the contacts. After the exposure of the n-GaAs channel, the sample was annealed for 1 h at 225° C to alloy the PdGe contacts. It has been shown that PdGe contacts form a thermally stable, low-resistance ohmic contact ($\sim 10^{-6}$ Ωcm^2) with a smooth surface [Mar85; Kwa95; Lim00], and therefore

have better characteristics then formerly utilized AuGe contacts [Bra67] [1].

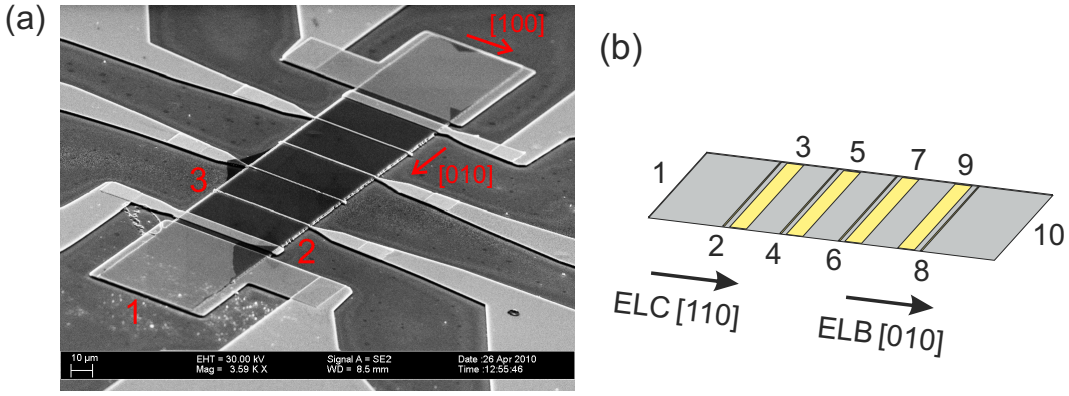

Figure 4.2: ***(a)*** *Scanning electron microscope (SEM) picture of the contact structure of sample ElA. Provided by A. Einwanger.* ***(b)*** *Contact structure of samples ElB and ElC. The distances between the electrodes and their width is displayed in table 4.1.*

Figure 4.2 displays the structures of sample ElA (a) and samples ElB, ElC (b). For both kinds of structures, the dimension of the channel is 350×50 μm. In contrast to samples ElA and ElB, where the channel is oriented along the crystallographic axis [010], the orientation of the channel for sample ElC is along the [110] direction [2]. Table 4.1 presents the dimensions (w) of the electrodes and the distances (d) between them. The first three columns display the electrode width according to the label depicted in figure 4.2, and the remaining columns show the distance between the specific electrodes. The non-itemized contacts are unused. The wide electrodes in samples ElB and ElC are nonmagnetic PdGe contacts, whereas the remaining and all contacts of sample ElA are magnetic ones.

electrode	1	2	3	1-2	2-3	3-4	3-5	5-9
	w(μm)	w(μm)	w(μm)	d(μm)	dμm)	d(μm)	d(μm)	d(μm)
sample ElA	75	10	0.5	5	35	35	-	-
sample ElB	75	0.6	5	30	7	17.4	25	50
sample ElC	75	0.5	4	30	2	17.4	20	40

Table 4.1: *The width (w) of the used contacts labeled according to figure 4.2, is shown in columns 1-3. The remaining columns display the distance (d) between the electrodes.*

[1] A contact, which has a linear I-V characteristic, is necessary for applying voltages on to a semiconductor. Usually, a metal-semiconductor contact forms a Schottky barrier because of the different electron affinities in both materials [Gru06], yielding a diode-like I-V characteristic. To obtain an ohmic behavior, a high surface doping concentration is needed to form a very thin Schottky barrier, which acts as a tunnel barrier. Hence, the contact will have small contact resistance in both current directions.

[2] The spin dynamics in GaAs are independent of the crystallographic axis. The reason for the difference in the orientation is that the [110]-oriented samples may also be employed in experiments measuring the Kerr rotation on a cleaved edge [End11; End12], since the directions [110] and $[1\bar{1}0]$ are the natural cleavage edges of GaAs.

4.2 Characterization of the sample

In order to characterize the contacts, first the I-V characteristic has been detected employing a Keithley 2400 SourceMeter. Figure 4.3 displays this exemplarily for a voltage applied to electrodes 9 and 1 at sample ElB at liquid helium temperature. The other samples and contact combinations show a similar behavior, however, with different slopes. The kink in the current behavior indicates the negative differential resistance (NDR) found in Esaki diode structures. The NDR of an idealized I-V characteristic is depicted in the inset of this figure. In the following experiments, the voltage is tuned in the linear regime between ±1 V.

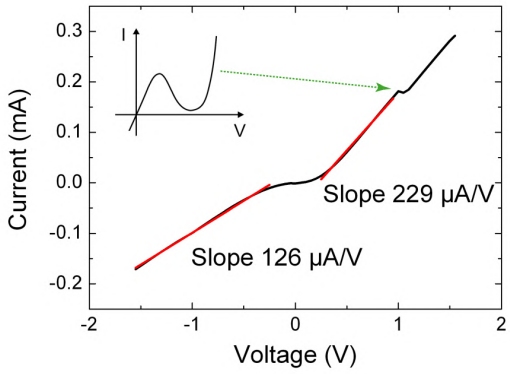

Figure 4.3: *I-V characteristic, with a voltage applied between contacts 9 and 1 at sample ElB. The inset depicts the NDR of an ideal Esaki diode.*

Knowledge about the orientation of the magnetization in the (Ga,Mn)As electrode is essential for spin injection experiments. The orientation depends on the existing magnetic anisotropies, i.e., on the orientation of easy and hard axis. After outlining the topic of magnetic anisotropies in (Ga,Mn)As, it is shown in the following section, how the Hanle measurements can be used to determine the magnetic field value, at which the magnetization switches parallel to an easy axis.

In principle, a bulk (Ga,Mn)As crystal would have easy axes along the crystal directions $\langle 100 \rangle$ $\langle 111 \rangle$, because of the T_d symmetry of the host crystal, see section 2.1.1, although an easy axis along the $\langle 111 \rangle$ direction has not been observed experimentally so far. (Ga,Mn)As grown on a GaAs substrate, however, has a lowered symmetry D_{2d} due to the strain, induced by the lattice mismatch [Gou07]. Considering a (001)-oriented GaAs substrate, the (Ga,Mn)As film is compressively strained [3]. Sawicki et al. showed that in this case, for low doping concentrations and low temperatures, the easy axis is oriented out of plane, and for temperatures close to T_C the easy axis is oriented in the plane. Then again, the out-of-plane axis becomes a hard axis for higher doping concentrations and the easy axis is oriented in the plane [Saw04]. The actual orientation of the easy axis in the plane is quite complex and depends on the temperature and magnetization (Mn concentration) [Pap07a; Gou07; Pap07a]. Three anisotropy components are found. For low temperatures and high magnetization, a biaxial component dominates, with easy axes along [100] and [010]. Close to T_c an uniaxial anisotropy with an easy axis along [110] or $[1\bar{1}0]$ dominates. The third contribution is small compared to the others, it is uniaxial and bears easy axis along [010] or [100] [4] [Pap07b; Wan05b; Pap07a].

It was shown by Wang et al., that macroscopically large (Ga,Mn)As films tend to align in a single-domain state [Wan05b]. In the case of the electrodes utilized here,

[3] It has also a tensile strained film been realized, using a (In,Ga)As buffer layer, showing an easy out-of-plane axis [Xia05].

[4] A good overview on this topic may be found for example in [Pap07c].

one has to consider the shape of the film as well. In a ferromagnetic thin film with a rectangular form, the shape anisotropy defines the easy axis along the long axis: the narrower the film, the more external field is needed to flip the magnetization in the axis. Such a behavior was found in (Ga,Mn)As as well [Ham06] and a shape anisotropy was assumed. Wenisch et al., however, showed that since the shape anisotropy depends on the magnetization, which is weak in (Ga,Mn)As compared to other ferromagnetic films, the shape anisotropy is not strong enough to dominate over the biaxial anisotropy. The effect that the magnetization in the (Ga,Mn)As electrode is oriented along the long axis of the electrode is explained by the fact that the strain relaxes along the narrow side of the electrode strongly, but only weakly along the long side. Hence, the external magnetic field to switch the magnetization parallel to the easy axis is higher for narrower electrodes [Wen07; Wen08]. In stripes with a width smaller than 1.5 μm this anisotropic strain relaxation induces a strong uniaxial anisotropy with an easy axis along the contact [Hof09; Cio13].

The Hanle method can be employed as a convenient way to determine the required magnetic fields to switch the magnetization in the electrode. First, a maximal magnetic field was applied along the electrode (y-direction) fixing the magnetization in this direction. Right afterwards, a Hanle measurement was conducted with the magnetic field oriented perpendicular to the electrode (x-direction), yielding a Hanle curve with a certain sign according to the direction of the injected electron spins. Following this, a magnetic field was applied in the minus y-direction, but this time a lower absolute value was chosen for the field, and another Hanle measurement was done. In case the field in minus y-direction was high enough that the magnetization switches, the sign of the Hanle signal switches, as shown in figure 4.4 (a). Therefore, by conducting this procedure several times, a successive approach to the value of the switching field is possible. In figure 4.4 (b), the values for several electrodes in the three samples are shown. The most narrow electrodes have the highest switching field of 11 mT, whereas the wide electrode switches its magnetization already at 6 mT. In samples ElA and ELB the

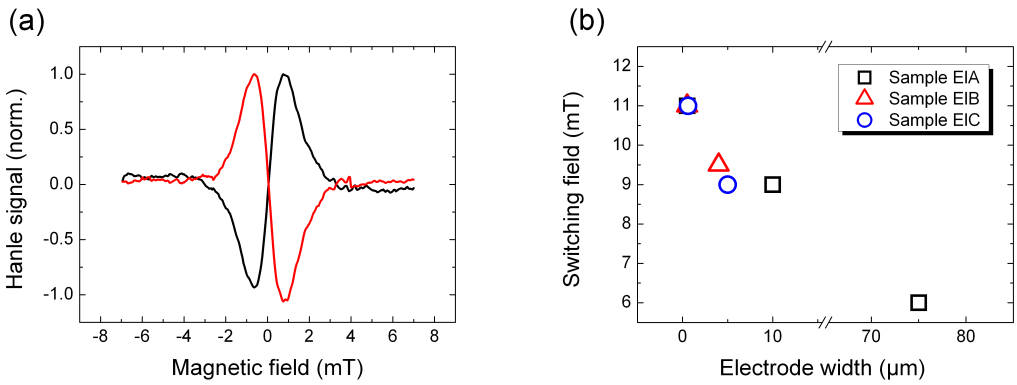

Figure 4.4: ***(a)*** *The Hanle signal changes its sign after a sufficiently high external magnetic field causes the magnetization in the electrode to flip.* ***(b)*** *Magnetic field values necessary to flip the magnetization in the easy axis, depending on the width of the contact.*

channel is oriented in a way that the orientation of the electrode is along [100] which is an easy axis according to the biaxial asymmetry of (Ga, Mn)As. In sample ElC the channel is oriented along [110], hence the electrode is oriented along [1$\bar{1}$0], which is a hard axis concerning the biaxial anisotropy, but an easy axis according to the weaker uniaxial anisotropy. A recent study by Ciorga et al. investigated the switching of the magnetization depending on the width and the orientation of the contact [Cio13]. They

found a clear single-switching pattern for narrow electrodes oriented along the [100] direction. Wider contacts oriented along the same direction showed a switching in two 90° steps during the reversal of the magnetic field. For contacts oriented along [1$\bar{1}$0] they concluded that the biaxial anisotropy is dominant and that the magnetization is oriented along the cubic [100] axis. Hence, the injected spins are in all configurations oriented along the [100] axis.

The magnetic field values to switch the electrodes were confirmed by an all-electrical type of measurement conducted only on sample ElA. A local spin valve measurement was employed using contacts 1 and 2. Typically, three types of all electrical measurements are distinguished, local- ,nonlocal- and three terminal-measurements (3T), depicted in figure 4.5 (b). The 3T method is based on the tunneling anisotropic magnetoresistance (TAMR), which was introduced by Gould et al. in a normal-metal-insulator-ferromagnetic-semiconductor tunneling device [5]. This effect was also found in a p^+ (Ga, Mn)As/ n^+ GaAs Esaki Zener diode structure [Cio07; Ein09]. The 3T measurement monitors a voltage drop across the FM/GaAs interface due to the TAMR effect. The resistance of the contact depends on the absolute magnetization orientation of the (Ga,Mn)As contact [Cio13].

The most common all-electrical technique to measure a spin polarization is the nonlocal method, where one electrode acts as a source of a pure spin current and a second contact as a detector. Hence, the measured magnetoresistance depends on the relative magnetizations of source and drain, and the difference between the magnetoresistance values for parallel and anti-parallel orientaion is proportional to the spin polarization [Lou07; Cio09; Ji07; Ino09].

In a local measurement, on the contrary, the injection voltage is applied between source and drain contact. Thus, instead of a pure spin current, a spin-polarized charge current flows between source and drain [Lou06; Cio11]. Figure 4.5 (a) shows the voltage measured by a Keithley 2400 SourceMeter with respect to the external magnetic field. Two sweep directions from negative to positive field and vice versa are displayed.

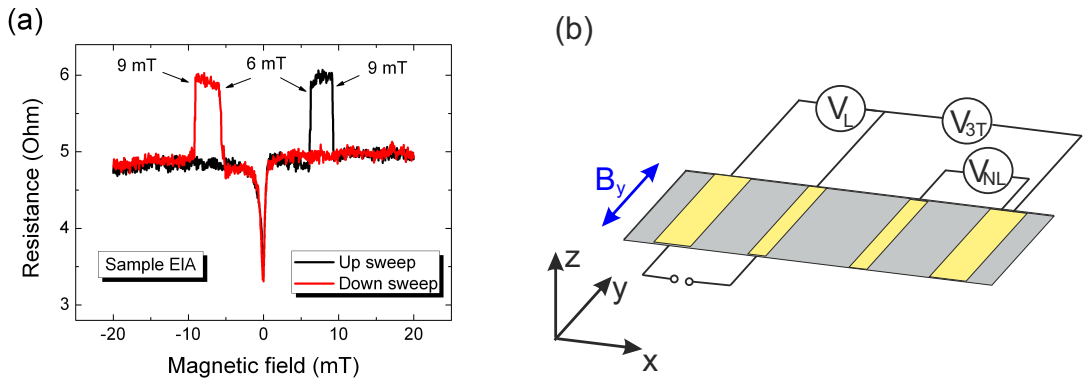

Figure 4.5: ***(a)*** *Local spin valve signal for contacts 1 and 2 in sample ElA. Two sweeps are shown, one from negative to positive magnetic field and vice versa.* ***(b)*** *Schematic measurement setup for all-electrical measurement methods.*

Starting, for example, from the negative maxima, the magnetizations of both contacts are oriented parallel. Because of the different widths, one electrode switches at a lower field than the other, yielding a change in the magnetoresistance. For higher fields both magnetizations are again parallel. The peak at zero field is attributed to the influence of

[5] They investigated the tunnel current from a gold contact into a single (Ga,Mn)As layer, which was separated from the metal layer by a Al_2O_2 tunnel barrier [Gou04]. The spin-split density of states in the (Ga,Mn)As causes a dependence of the magnetoresistance on the orientation of the magnetization.

dynamic nuclear polarization and is observed in local as well as nonlocal measurements [Lou07; Cio09; Cha09]. It has been investigated by Salis et al. in detail [Sal09]. They attributed the peak to a loss of average electron-spin-polarization due to dephasing caused by the perpendicular component of the nuclear Overhauser field. The switching fields match the values displayed in figure 4.4 (b) for contacts 1 and 2. Further investigations on spin information with this type of measurement are not presented here.

The applied magnetic field necessary for the Hanle measurements may also influence the magnetization in the electrode. Figure 4.6 depicts deformed Hanle curves caused by a tilted magnetization in the electrode because of the external field (red and blue curve). The desired Hanle signal (black curve) was obtained by applying the magnetic field perpendicular to the magnetization. Hence, before the measurement, with the set of the four Helmholtz coils, the external magnetic field is adjusted to be perpendicular to the initial spin orientation, in order to achieve a symmetric Hanle signal.

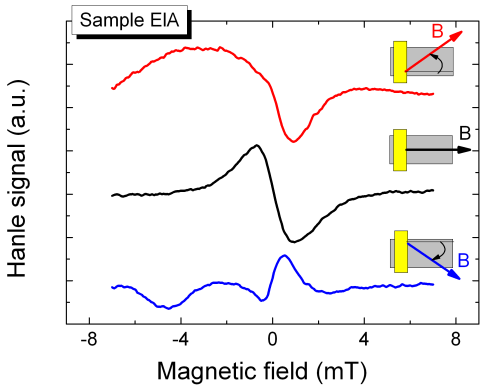

Figure 4.6: *Magnetic fields applied not perpendicular to the electrode cause a tilt in the magnetization of the contact, yielding a deformed Hanle curve.*

4.3 Spin dynamics

Regarding the interpretation of the results of spin dynamics and spin transport, it is important to clarify the circumstances concerning the measurement and the sample. The sample temperature in all the measurements was approximately 10 K, because of a limited thermal contact, see chapter 3.5. According to chapter 3.3 the Kerr sensitivity depends strongly on the temperature and the probe Laser wavelength. In the presented measurements, a maximum Kerr signal was achieved at a probe wavelength of 819.5 nm, in agreement with the dependence depicted in figure 3.1, and the power of the probe Laser was set to 1 mW. Constrained by the setup, the laser power could only be measured before the several beam splitters and the objective. A loss in the power by a factor 10 due to these optics was noticed, which implies an effective probe power at the sample of about 100 μW. In the following experiments, the 100$\times$ objective was employed with a spot size of 1.3 μm. Certainly, the probe beam should influence the system as little as possible. With equation 2.10 the number of additional electrons owing to the probe laser can be estimated. The absorption coefficient in this equation is calculated using the refractive index 3.5 for GaAs, at low temperatures [Bla82]. Using the Fresnel formula for normal incidence ($T = 1 - [(n_1 - n_2)\,/\,(n_1 + n_2)]$) yields an absorption of 60%. Assuming a penetration depth of 2 μm and a photocarrier lifetime of 100 ps a carrier density of $4 \cdot 10^{13}$ cm^{-3} is created in the region of the Laser, which may be neglected compared to the doping densities ($\sim 10^{16}$ cm^{-3}).

4.3.1 Spin lifetimes

In the following section, the spin dynamics are investigated employing Hanle-MOKE measurements described in chapter 3.2.1, where it is illustrated, that the extraction of the spin lifetime from the Hanle curves obtained by lateral spin injection is rather complicated and depends strongly on the relative position of the probe. Thus, for the purpose of comparison, a two-beam Hanle measurement, with optical orientation and detection, was conducted on the two wafers beforehand. In order to use equation 3.6, which neglects spin diffusion, for the determination of the spin lifetime, the laser spot size should be about the spin diffusion length. Owing to the dimensions of the sample an objective with a magnification not less then 20× has to be used [6]. The spot size of 4 μm is close enough to the measured spin diffusion length (6.9 μm) to determine the spin dephasing time. With a pump power of 50 μW, the Hanle curves depicted in figure 4.7 are obtained for sample ElA and ElC. From the HWHM a spin lifetime of 51 ns for sample ElA and 36 ns for sample ElC, which has a higher carrier density, is extracted. As discussed in chapter 2.2.5, the spin lifetime decreases with increasing carrier density. The obtained values, however, deviate from the expected ones. According to Dzhioev et al. ([Dzh02]), a spin lifetime of about 120 ns is expected for the carrier density of sample ElA, see figure 2.17 (a), which would drop to about 100 ns at the nominal sample temperature of 10 K. Several circumstances could explain the observed deviation. First, the actual sample temperature is not known, because of the unknown thermal contact efficiency between the sample and the cryostat. Secondly, the laser might induce local heating. Finally, the actual carrier density could deviate from the nominal value, since it was determined after the growth at a different piece of the wafer using Hall measurements.

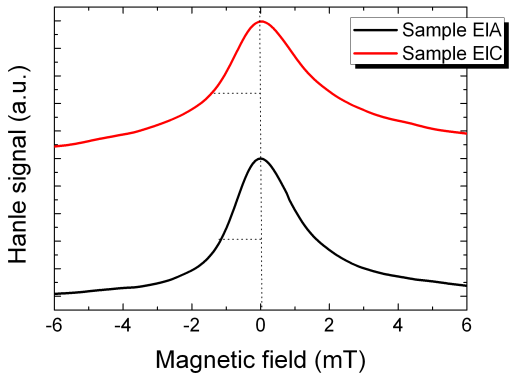

Figure 4.7: *Two-beam Hanle-MOKE signals for samples ElA and ElC. The Lorentzian line shape reveals different spin lifetimes of 51 ns and 36 ns, which may be extracted from the HWHM.*

In contrast to the Lorentzian line shape resulting from the all-optical measurement method, the electrical spin injection from the contact yields an asymmetric Hanle signal due to the initial in-plane orientation of the spin polarization. The extraction of the spin lifetime from these curves, however, is more complicated. The spin-polarized electrons are injected by the Esaki diode structure directly under the ferromagnetic contact, where the electron motion begins, including drift and diffusion processes. Thus, the accessible range to detect a spin polarization is either in the diffusive or the drift regime, and consequently only a subset of the spin polarization is detected according to equation 3.13. The detected spins have a well-defined average momentum and age, depending on the actual position of the probe beam relative to the contact. Several Hanle curves with increasing distance from the electrode have been obtained, with an applied voltage of 0.6 V (72 μA) between contacts 1 and 3 at sample ElA. The measurement was in

[6] As described in chapter 3.5 a USB CMOS camera is used for positioning. The laser spot appears in the camera picture larger than its actual size due to pixel overflow.

the diffusive regime, which means the detection spot is outside the current path. Some Hanle curves for increasing distance are displayed in figure 4.8 (a), whereas figure 4.8 (b) shows the position of the probe beam for the first measurement of this scan right next to contact 3 (taken by the CMOS camera). As expected, the peak to peak value, which is proportional to the spin polarization, decreases exponentially. A detailed discussion about the diffusive decay is included in chapter 4.4. Furthermore, the width of the Hanle signal decreases because of the time of flight between injection and detection, which can be clearly seen in figure 4.8 (a) and 4.9 (a).

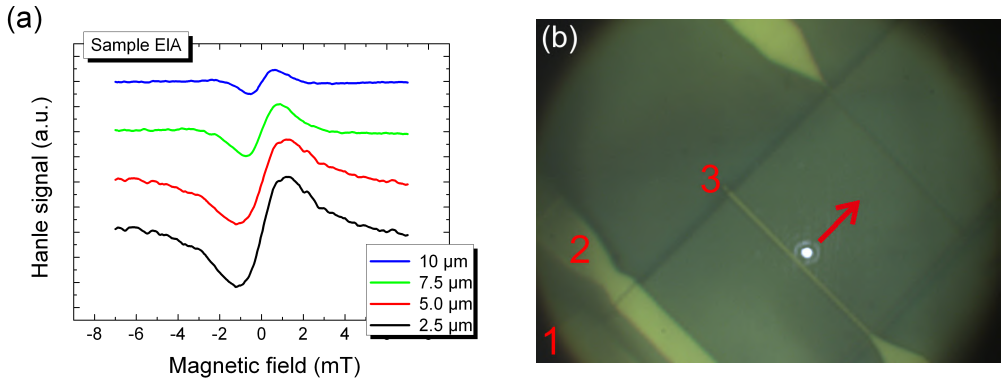

Figure 4.8: *(a) The peak to peak value of the Hanle curve decays exponentially with increasing distance between contact and detection. In addition, the width of the curve becomes smaller due to an increasing age of the spin polarized electrons.* ***(b)*** *The picture taken by the CMOS camera with white light illumination, depicts the starting position of the probe beam for the first Hanle measurement right next to contact 3 in sample ElA.*

In order to calculate the spin lifetime in this case, equation 3.14 has to be employed. Since only pure spin diffusion is present here, the terms concerning the drift may be neglected in this equation. Using the exact position of the detection, and the spin diffusion length of 6.9 μm, determined in chapter 4.4 for this sample, a numerical fit of the data using equation 3.14 (with the software Mathematica) could be conducted, as discussed in chapter 3.2.1. Figure 4.9 (b) depicts two exemplary fits for the Hanle curves taken at a distance of 2.5 μm and 10 μm.

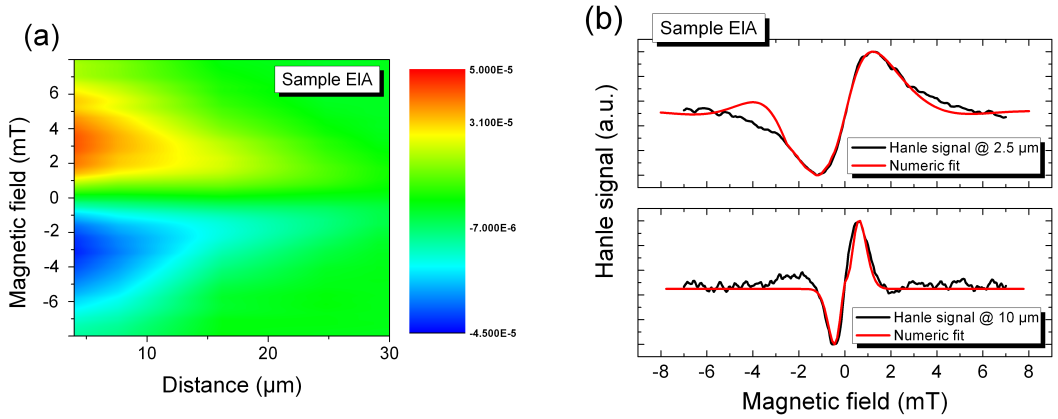

Figure 4.9: *(a) Color coded plot of the Hanle signal depending on the distance of the detection from the contact of sample ElA. A clear reduction of the width of the Hanle signal as well as the exponential decay of the peak to peak amplitude is observed.* ***(b)*** *A numerical fit using equation 3.14 for two particular distances.*

The Hanle curves for four distances have been evaluated as table 4.2 displays.

distance (μm)	2.5	5	7.5	10
spin lifetime (ns)	14.43	20.74	19.67	19.64

Table 4.2: *Spin lifetime extracted from the numerical fit on Hanle curves, detected at several distances from the contact.*

In some distance to the contact the obtained spin lifetimes are about 20 ns, closer to the electrode, however, the spin lifetimes deviate from this value. Since a uniform spin lifetime is expected throughout the sample, the most likely reason for this deviation is that the electric field of the electrode influences the spin dephasing. Such an impact on spin relaxation, caused by an electric field, has been investigated previously: Beck et al. proposed an increase of the electron temperature caused by the electric field, yielding a drop of the spin lifetime because of the DP-mechanism (as discussed in chapter 2.2.5) [Bec06]. Furthermore, Furis et al. suggested that the electric field induces an increase of the carrier density due to donor impact ionization, which as well reduces the spin lifetime according to the DP-mechanism (see chapter 2.2.5) [Fur06]. Finally, Endres et al. reported a nonuniform spin accumulation owing to the electric field around the electrode, which was detected on the cleaved edge starting directly from under the electrode, employing the Kerr effect [End12]. The reason for such a nonuniform spin accumulation, also presented in chapter 4.4, lies in the fact that the electric field under the electrode causes an electron drift, which shifts the peak of the spin polarization away from the electrode. On this grounds, Endres et al. argued that the assumption of a one-dimensional diffusion is not sufficient because of this nonuniformity, and developed a 2D simulation which yields higher spin lifetimes than the ones a one-dimensional fit obtains. The insufficiency of the 1D model might explain the discrepancy of the spin lifetimes, obtained by the two beam Hanle experiment and the electrical injection. The 2D simulation of Endres et al., involving samples from the same wafer as sample ELA, yielded a spin lifetime of about 50 ns which matches the obtained value of the all-optical measurement here, very well.

4.3.2 Bias dependence

For spin injection, an Esaki diode structure is typically operated under a small reverse bias, as explained in chapter 2.2.1 and depicted in figure 2.10. With increasing bias, the splitting of the quasi-Fermi levels rises, which results in an increasing tunnel current, since the spin-polarized electrons from the (Ga,Mn)As find more unoccupied states in the GaAs. Owing to the magnetization in the contact, more majority spins tunnel than minority spins, inducing an increased spin polarization in the GaAs. Eventually the spin polarization saturates, since the quasi-Fermi level of the (Ga,Mn)As hits the band gap. A small forward bias on the other side induces a tunneling current from the GaAs into the (Ga,Mn)As. Due to the magnetic orientation in the (Ga,Mn)As, mostly electrons with the same spin orientation as the majority spin in the contact are extracted from the semiconductor, see figure 4.10. Hence, a spin polarization is left with an orientation as the minority spins in the electrode. Therefore, the Hanle signal should change its sign if the sign of the bias is changed, which means changing from injection to extraction. Ideally the bias dependence of the spin accumulation should also be symmetric for both bias directions. This was, however, not the case for all investigated samples.

Figure 4.10 (b) shows the Hanle signals for various biases in sample ElA, using contacts 1 and 3. The detection point was in the diffusive regime at a distance of 5 μm away

from the contact. Extracting just the peak to peak amplitude from the Hanle curves, the bias dependencies are displayed in figure 4.11 for all three investigated samples. In

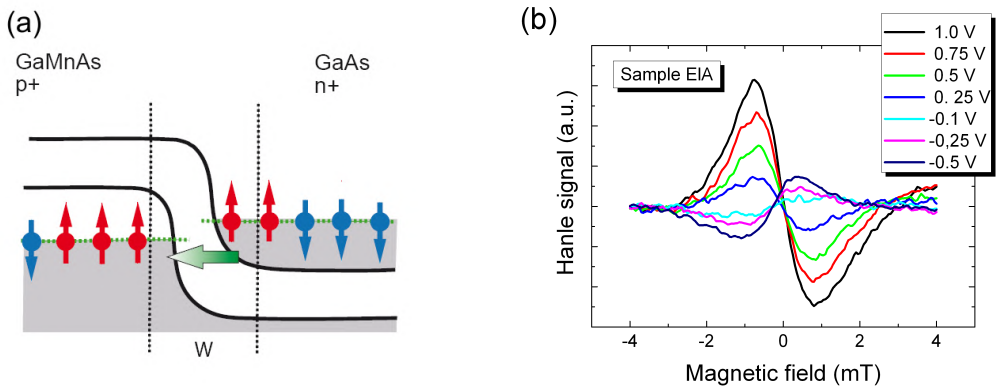

Figure 4.10: ***(a)*** *Spin extraction under small forward bias in a p^+ (Ga, Mn)As/ n^+ GaAs Esaki Zener diode structure. Electrons with a spin orientation according to the majority spin in the contact are extracted, leaving a spin accumulation oriented according to the minority spin orientation.* ***(b)*** *Hanle signal for various biases in sample ElA using contacts 1 and 3. The detection point was about 5 μm away from the contact. The signal change has a different sign for the case of injection and extraction.*

samples ElB and ElC the bias was applied at contacts 1 and 8 and detection was located again 5 μm away from the contact. Although with different slopes, all three samples show a linear increase for small reverse biases. The behavior at forward bias, however, is quite different, where a sign change is observed for samples ElA and ElB, but no sign change is noted for sample ElC [7].

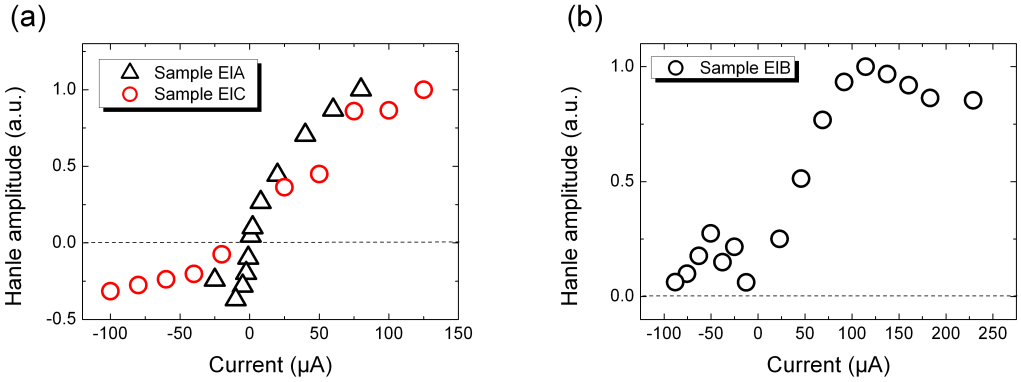

Figure 4.11: ***(a)****Bias dependence of the peak to peak amplitude for samples ElA and ElC. For forward bias spin extraction takes place, yielding a sign change of the Hanle signal.* ***(b)*** *Bias dependence of the peak to peak amplitude for sample ElB. For forward bias no sign change of the Hanle signal takes place, implying spin reflection.*

Previous studies have already reported both behaviors. Endres et al. showed a spin accumulation of majority spins in the case of injection and of minority spins in the case of extraction in GaAs, employing a (Ga,Mn)As Esaki diode structure and Fe / FeCo Schottky contacts [End11]. Kottisek et al. and Furis et al. also reported a

[7] Earlier works on a different wafer (internal wafer number C080605A) showed as well no sign change, presented in [Völ09].

sign change, utilizing FeCo and Fe Schottky contacts [Kot07; Fur07]. On the contrary, Crooker et al. and Lou et al. reported a spin accumulation of the same spin species for spin injection and extraction in GaAs, using Fe Schottky contacts [Cro05b; Lou06]. Ciuti et al. developed a theoretical model for tunnel/Schottky barriers. They suggested that owing to the exchange splitting of the assumed parabolic bands, different Fermi wave vectors for the two spin kinds need to be considered. Depending on the barrier shape, different matching conditions for the wave functions for incident electrons are found. Thus, spin dependent reflection and transmission coefficients, which influence the sign and magnitude of the spin accumulation, arise [Ciu02; McG03; Ste04]. This model, however, did not take into account the complex band structure of the barrier. In contrast, Dery et al. did consider the complex band structure of the barrier, they suggested that because of inhomogeneities in the doping of the semiconductor, a surface band arises at the interface, from which the extracted spin is opposite to that from the bulk conduction band [Der07]. The proposal of Chantis et al. involved a Fe/GaAs Schottky contact as well. They suggested that the reversal of the spin polarization is caused by minority-spin resonant states at the interface [Cha07a]. Such states reduce the tunnel conductance for the minority spins, yielding a spin accumulation of majority spins in the GaAs. To the authors best knowledge, so far no theoretical model has been developed for a (Ga,Mn)As interface. Altogether the bias behavior depends strongly on the exact conditions at the ferromagnet/ semiconductor interface. These interface conditions influence sign and magnitude of the spin accumulation.

Another feature of the bias dependencies in figure 4.11 is a saturation behavior and even a reduction of the spin polarization in sample ElB for high biases. This may be attributed to a reduced spin injection efficiency. As Ciorga et al. reported at a similar sample, an increased contribution of minority spins to the tunnel current reduces the spin injection efficiency [Cio09]. At the tunneling process, the energy and the transverse quasi-momentum are conserved, and the transmission coefficient depends on the mismatch of the group velocities between the two materials ((Ga,Mn)As and GaAs), the so called velocity mismatch [San07]. For increasing bias this mismatch may be rising for majority spins and decreasing for minority spins. Hence, the tunnel current consists of more minority carriers, which reduces the current polarization. Ciorga et al. could also determine a maximal spin injection efficiency of 50% at very low bias [Cio09]. Finally, for increasing bias a slight reduction of the spin lifetime was observed, see figure 4.10 (b), which may be attributed to a temperature increase of the electron gas due to the electric field as discussed earlier in chapter 4.3.1.

4.4 Spin drift and diffusion

4.4.1 Spin diffusion

The two-point Hanle measurements described in chapter 3.2.1 allow the investigation of the spatial properties of a spin polarization injected from the p^+ (Ga,Mn)As/ n^+ GaAs Esaki Zener diode structure into the n-GaAs channel. The results presented in the following section are nicely confirmed by Endres et al., using cross-sectional imaging of the spin polarization on the cleaved edge of the channel [End12]. The two works together reveal a complete picture of spin transport in these samples.

Figure 4.12 (a) displays the spatial decay of the two point Hanle signal, which is proportional to the spin polarization. Here the electrodes 1 and 2 of sample ElA were used, and a voltage of 0.4 V was applied resulting in a current of 80 μA (where the negative potential was on electrode 2). Thus, spin injection in the diffusive regime may be observed next to contact 2. The 100 μm long scan starts on top of the wide electrode 1 roughly in the middle of the channel. In order to identify the location of the electrodes

in the scan, a reflectivity scan along the same way is shown in figure 4.12 (a). Employing an exponential fit, a diffusion length of 6.9 ± 0.32 μm could be extracted, which agrees with the values Endres et al. found for the same wafer. The order of magnitude of the spin diffusion length accords with values obtained for GaAs as well, although with slightly different properties determined by various groups [Fur07; Kot07; Cro05b; Qua08; Qua09]. Usually one would expect the maximum of the spin polarization below the injecting electrode, and an exponential decay away from the electrode, considering a one-dimensional diffusion model. Here the maximum is, however, located about 3 μm away from the contact. Applying a scan on the edge of the channel starting below the electrode, Endres et al. observed the same feature [End12]. Moreover, they conducted a two-dimensional (the two dimensions are along the channel and the n-GaAs layer thickness) simulation of the spin density distribution, where they considered the electron current density influenced by various resistances and the spin diffusion. The electric field around the contact causes nonuniform local current directions below the electrode, depicted by the black lines in figure 4.12 (b) from the mentioned simulation. Naturally, below the electrode, this nonuniform electron drift shifts the polarization peak away from the center towards the diffusion side, shown in the color plot in figure 4.12 (b).

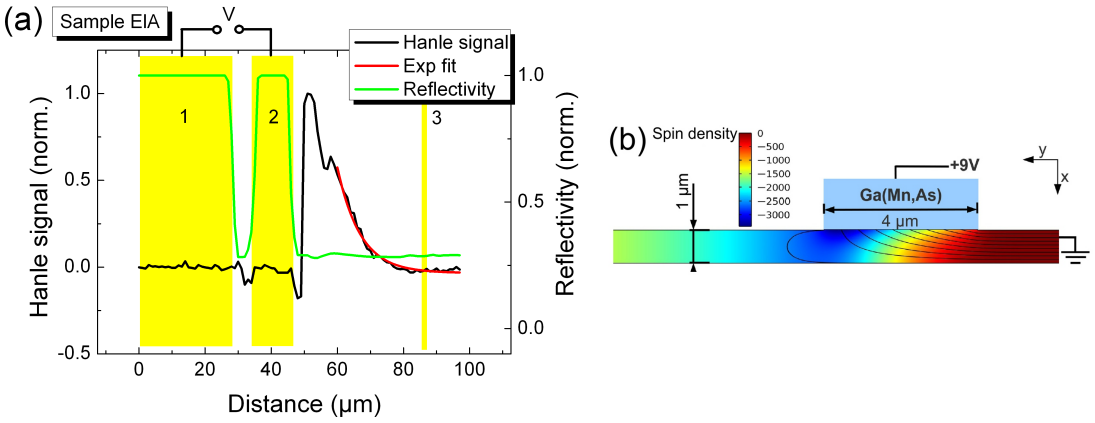

Figure 4.12: ***(a)*** *A two-point Hanle scan displays the decay of the spin polarization, yielding a spin diffusion length of* 6.9 ± 0.32 μm*. For the purpose of positioning, a reflection scan was conducted over the same scanning distance.* ***(b)*** *Spin density distribution under the electrode as a result of a two dimensional drift diffusion simulation. The black lines represent the local current direction. Taken from [End12].*

Since the peak position of the spin density distribution depends on the electric field under the contact, a series of line scans were taken at different voltages. This time, however, sample ElC was used, utilizing the contacts 10 and 8. Indeed, figure 4.13 depicts a slight shift of the peak away from the electrode for increasing voltage. The maximum observed shift at 1.5 V was about 4 μm. This is the case for rising negative voltage as well as for increasing positive voltage. As discussed in chapter 4.3, this sample shows the expected spin accumulation due to the extraction of carriers with spin according to the majority spin orientation in the electrode. Hence, the spin polarization observed for positive voltages is the result of minority spin accumulation.

Furthermore, the spin diffusion lengths for the different injection voltages were extracted. A rising voltage induces a small drop of the spin diffusion length, see figure 4.13 (b), since a higher bias yields a larger electric field under the electrode, which heats the electron gas. As discussed earlier in chapter 4.3 an increased electron temperature induces a reduction of the spin lifetime and therefore a reduction of the spin diffusion length ($L_s = \sqrt{D_s \tau_s}$). The larger field also accelerates the electrons, which affects the

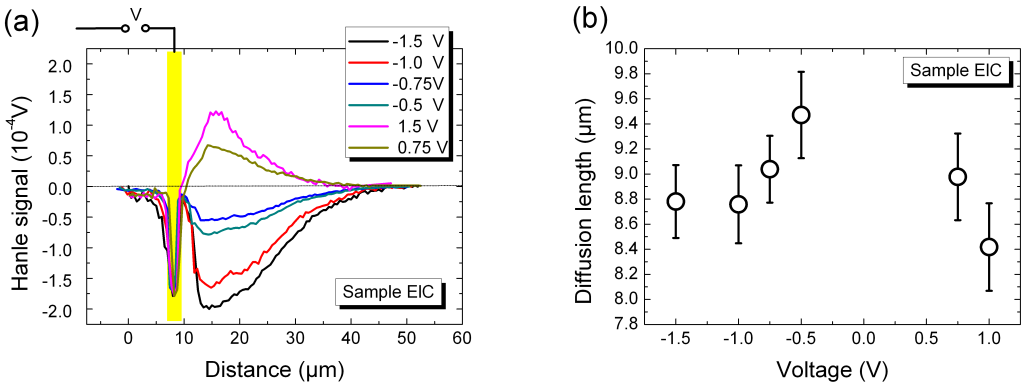

Figure 4.13: ***(a)*** *Spin diffusion depending on the applied voltage in sample ElC.* ***(b)*** *Bias dependence of the spin diffusion length in sample ElC.*

momentum scattering time, however in n-GaAs this effect is only important direct under the contact, since the mean free path is small. Additionally, in a DP dominated regime the spin diffusion length does not depend on the momentum scattering time [Fab07]:

$$L_s = \sqrt{D_s \tau_s} = \sqrt{\frac{v_F^2 \tau_p}{\bar{\Omega}^2 \tau_p}} = \frac{v_F}{\sqrt{\bar{\Omega}^2}}, \tag{4.1}$$

with equations 2.33 and 2.56. As expected, the spin diffusion length is the same for injection and extraction (see figure 4.13 (b)). Compared to samples ElA and ElB, sample ElC has a higher diffusion length (ElA: $\sim$ 7 μm, ElC: $\sim$ 9 μm) owing to the higher electron density.

The diffusion constant $D_s = L_s^2/\tau_s$ may be determined, with the extracted spin diffusion length for samples ElA, ElC, and the obtained spin lifetimes (ElA: 51 ns, ElC: 36 ns). For sample ElA a diffusivity of $D_s \approx 10$ cm^2/s, and for sample ElC $D_s \approx 23$ cm^2/s was calculated. Endres et al. determined for the wafer of sample ElA a mobility of 3500 cm^2/(V·s), by measuring a conductivity of 1500 S/m at 9 K. From the carrier density ($2.7 \cdot 10^{16}$ cm^{-3}) the Fermi energy can be approximated (4.89 meV) [8]. Using equation 2.56 for a degenerate semiconductor the carrier diffusion constant is calculated to $D_e = 17.11$ cm^2/s. The reduced spin diffusivity compared to the carrier diffusivity could indicate many-body effects on spin diffusion discussed in chapter 2.3.2.

So far there was only a one dimensional line scan presented, leaving the question open how the spin density distribution behaves along the electrode. Therefore, a two-dimensional scan has been conducted, mapping the spin polarization within the spin diffusion length along the whole contact. In order to correct for a possible deviation of a right-angle orientation of the electrode, the starting and the ending point in x direction are chosen manually. A third manual chosen point in y direction completes the definition of the scanned area. A 2D scan of the diffusive area next to contact 8 in sample ElB is shown in figure 4.14. A voltage of 1 V (74 μA) was applied between the contacts 1 and 8. The two false color coded plots of this scan show a uniform spin density distribution along the electrode, and the expected peak of the spin polarization a few micrometers away from the electrode.

4.4.2 Spin drift

The following section investigates spin drift. According to chapter 2.3.2, the critical electric field above which the spin drift dominates over spin diffusion can be approxi-

[8] $E_{F,3D} = \left[\hbar^2/\left(2m_e^*\right)\right]\left(3\pi^2 n_e\right)^{2/3}$, with n_e electron density.

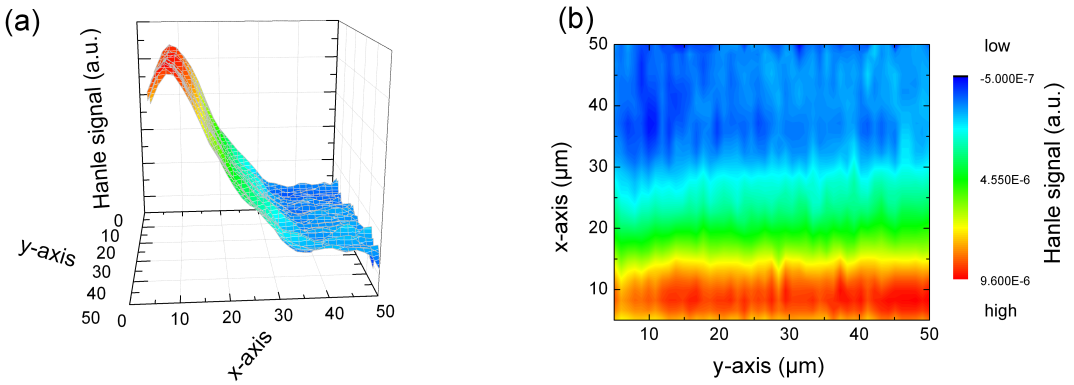

Figure 4.14: ***(a)*** *Two-dimensional spin diffusion behavior at electrode 8 in sample ElB.* ***(b)*** *False color-coded 2D spin diffusion at electrode 8 in sample ElB.*

mated as: $\mathcal{E}_c = D_s/(\mu_e L_s)$. For sample ElA/ElB, this field would be 4.08 V/cm. In addition to the diffusive case, in figure 4.15 the effect of drift is depicted for a voltage of 3.5 V applied between contacts 1 and 3. The voltage at contact 3 is hereby positive. A spin accumulation of minority-spin carriers owing to extraction of the majority spins occurs. Pure spin diffusion is observed on the right-hand side of the contact, where a spin diffusion length of 6.3 μm could be obtained. This value is slightly lower than in the spin injection case. On the left-hand side the spin diffusion is opposed by the carrier drift, resulting in a spin injection length of 1.4 μm. Using equation 2.63, the actual electric field on the channel is calculated to 19.2 V/cm. Figure 4.15 (b) shows the case where drift and diffusion are in the same direction. Here, spin injection in sample ElB was used. The black curve depicts the diffusion to the right of contact 8 (majority spins due to spin injection), where a voltage of 1 V was applied between contacts 1 and 8. As expected, a diffusion length, similar to sample ElA (samples ElA and ElB are from the same wafer) of 6.8 μm was obtained. The red curve, however, depicts the situation where spin drift dominates, the curve was measured in the current path (voltage between contacts 8 and 10). A spin injection length of 16.5 μm was obtained. Again the actual electric field could be calculated to 7.9 V/cm.

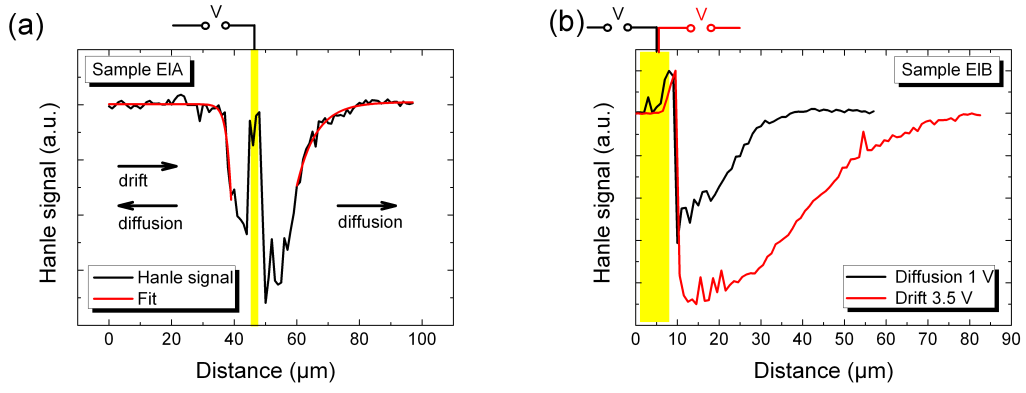

Figure 4.15: ***(a)*** *Spin drift and diffusion in sample ElA using contacts 1 and 3 (spin extraction). On the right-hand side of contact 3 pure spin diffusion is present. Whereas on the left-hand side the spin diffusion and spin drift oppose each other.* ***(b)*** *Spin diffusion and spin drift in sample ElB for spin injection. The observed spin injection length is larger than the pure spin diffusion length.*

4.5 Dynamical nuclear polarization detected via combined electrical and optical injection

Due to the small magnetic moment of the nuclei (2000 times smaller than electron magnetic moment), a nuclear polarization with an external field is quite ineffective, for example an external field of 100 T would only result in a nuclear polarization of 1% at 4 K [Dya08]. The polarization of nuclei through a spin-polarized electron ensemble, also called dynamic nuclear polarization (DNP), may, however, yield very high nuclear polarizations. As described in chapter 2.4, the dynamic effect of the Fermi contact hyperfine exchange interaction causes a spin flip between electrons and nuclei. In the case a spin-polarized electron ensemble is involved, this process transfers a polarization to the nuclear system. For n-doped bulk GaAs such a nuclear polarization has been shown several times, for example in [Kik00; Hua12]. DNP caused by electron spin injection with lateral transport has been investigated for example in [Str03; Joh00; Cha09; Sal09].

The following part presents a method with which the nuclear polarization can be observed using a combination of optical and electrical spin injection. Figure 4.16 displays a schematic description of the experiment, where sample ElA is used. Here itinerant

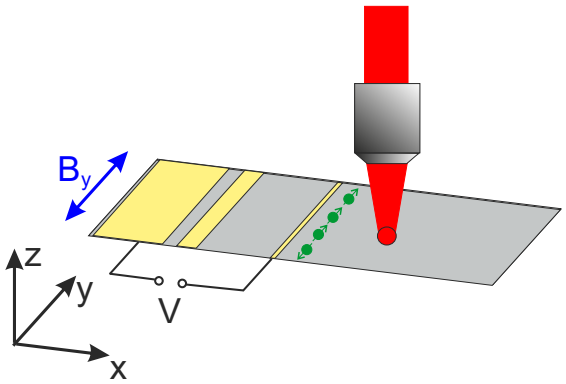

Figure 4.16: *The electrically injected electron spins cause a nuclear spin polarization. This has an impact on the precession of the optically generated spin polarization. These are measured with the Hanle MOKE method with an applied magnetic field parallel to the electrically injected spins. Hence, the electrically injected spins do not precess and do not contribute to the Hanle curve.*

electrons inside the n-doped GaAs layer polarize localized electrons (electrons bound to an Atom) on a timescale of 10^{-11} s because of the spin exchange interaction [Pag82], which then polarize the nuclei. Those itinerant electrons originating from the electrode are polarized in-plane and the optically generated electrons are oriented out-of-plane. Due to the applied external magnetic field for the Hanle measurement, only the optically injected electron spins precess. Thus, the time-average contribution to the nuclear field from the optically injected spins is zero, and the nuclear polarization depends only on the electrically injected electron spins. This argument, however, holds only under the assumption that the applied magnetic field is larger than the HWHM of the Hanle curves, which the optically injected spins would cause. For values around $B = 0$ the optically generated spins would polarize nuclear spin as well. This is observed in the following measurements. Another consequence of the fact that the electrically injected spins do not precess is that only the optically generated spins contribute to the Hanle signal, since the polar MOKE is only sensitive to out of plane magnetizations. The nuclear field is then given by [Pag77; Str03]:

$$\boldsymbol{B}_N = b_N \frac{(\hat{\boldsymbol{s}} \cdot \boldsymbol{B_{ext}})\, \boldsymbol{B_{ext}}}{B_{ext}^2 + B_0^2} \tag{4.2}$$

Here b_N is the value of the nuclear field, if all nuclear spins are polarized (determined

in GaAs to −5.3 T [Pag77; Dya08; Mei84]) [9], $\hat{\boldsymbol{s}}$ is a unit vector of the spin polarization, $\boldsymbol{B_{ext}}$ is the applied magnetic field, and B_0 is the nuclear dipole field (a typical value for the dipole field is about 0.2 mT [Str03]). The total field in which the optically generated spins precess is the sum of external and nuclear field $\boldsymbol{B} = \boldsymbol{B_{ext}} + \boldsymbol{B_N}$. Hence, the resulting Hanle curve is expected to have its maximum (at the total zero field) shifted along the magnetic field axis about the value of the nuclear field.

Such a detection of nuclear polarization has already been employed several times, however, mostly in an oblique magnetic field configuration. This means the applied magnetic field is not perpendicular to the optically induced electron spin polarization. Thus, because of the precession, there exists a non-vanishing projection of the electron spin vector on the external field, which induces a nuclear polarization. An overview over such experiments may be found in [Dya08; Mei84].

A closer look at the nuclear field shows that it is a vector sum of two opposed nuclear fields, since majority as well as minority electron spins are injected and both polarize nuclei [10]. The resulting field is therefore depending on the degree of polarization. In figure 4.17 (a) a Hanle curve is depicted, whose maximum is shifted by the nuclear field. Here the two collinear beams are focused with a 100× objective at the sample ElA in a

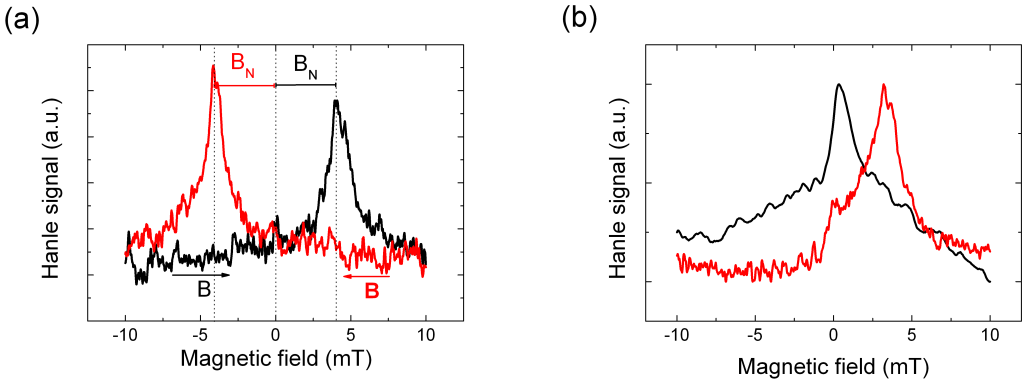

Figure 4.17: ***(a)*** *The maximum of the Hanle curve is shifted, and located at the magnetic field value where external field and nuclear field cancel each other. An immediate down sweep of the external field shows a sign change of the nuclear field, which indicates a switch in the magnetization direction in the contact.* ***(b)*** *In case the ramp speed is increased by a factor five, the nuclear effects may not be observed since the DNP is not an instant process.*

distance of about 7 μm from contact 3. The contact is biased in reverse direction, where a current of 50 μA is carried between contacts 3 and 1. A shift of about 4 mT is clearly observed. In this experiment, the magnetic field is ramped starting from −10 mT to 10 mT, and immediately ramped down again to −10 mT. In the up sweep the observed shift is positive, indicating a negative nuclear field, whereas in the down sweep, the observed shift is negative, indicating a positive nuclear field. This behavior is not fully understood, since the value of the magnetic field at which the electrode switches its magnetization is at 11 mT, and a switch due to the external field is not possible. The same experiment has been conducted with a maximal field value of 6 mT, so clearly below the switching field this behavior was still observed. A possible explanation might be that due to the external field, the probability that nuclear spins are oriented along the

[9] Whereas the Knight field is always antiparallel to the spin polarization the direction of the resulting nuclear field B_N depends on the signs of electron and nuclear g-factor [Dya08].

[10] Here and in the following, the term majority and minority spins mean that the electron spins in the semiconductor are oriented in the same direction as majority or minority spins in the ferromagnet.

minority spin orientation is higher. The resulting field as a sum of external and nuclear field might cause a switch of the magnetization in the contact. Among the nuclear spins an equilibrium is established, which is characterized by a nuclear spin temperature. This means that owing to interactions among the nuclear spins the population P_i of the energy levels E_i is given by a Boltzman exponential law ($P_i \sim \exp(E_i/k_B T_s)$). The existence of such a spin temperature favors the nuclear spins to lie along the external field [Mei84].

The process of dynamic nuclear polarization is not immediate, which becomes clear by changing the ramp speed of the external field. No nuclear effects were observed at a fast ramp speed, as displayed in figure 4.17 (b). Strand et al. investigated DNP due to lateral spin injection from a ferromagnet in a (Al,Ga)As quantum well with electroluminescence polarization. They found a steady state after $10 - 50$ sec and a saturation after 5 min [Str03]. Such a saturation process can be attributed to the long nuclear spin lifetime in semiconductors [Lam68; Str03].

The optically injected electron spins precess in the applied field with the Larmor frequency. Unless there is an angle deviating from 90° between the electron spin and the external field, no permanent nuclear polarization is caused. Because of the precession optically injected spins randomly polarize the nuclei, which cancel out over the time average. The only permanent nuclear polarization is induced by the non-precessing electron spins injected electrically. The optically oriented spins, however, do have an impact on the resulting value for the nuclear field. The more optically generated spins are present, the more nuclei are randomly oriented. Thus, an increased electron density created optically reduces the nuclear field. This is depicted in figure 4.18 (a) and the average peak position with respect to the pump power is shown in figure 4.18 (b). Clearly, the nuclear field reduces with increasing number of optically generated electron spins (where the electrode current stays fixed at 35 μA).

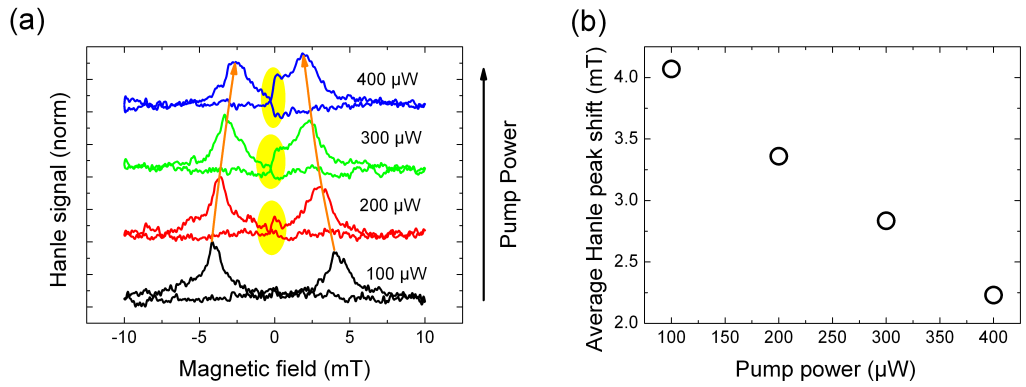

Figure 4.18: *(a) The nuclear field is reduced with increasing excitation density, due to rising impact of differently polarized electron spins canceling out over time. At zero magnetic field the optically generated spins do not precess and contribute to the nuclear field polarization, yielding a reduction of the total field and a step in the Hanle signal (highlighted in yellow)* ***(b)*** *Average between the peak positions from up and down sweep with respect to excitation power.*

An interesting feature is observed at zero external field, where a kink (highlighted in yellow in figure 4.18 (a)) arises for increasing excitation. At zero field the electron spins do not precess, so the resulting nuclear field is the vector sum of three orientations (z-direction, y-direction and minus y-direction), reducing the total field. The spin dephasing is caused here by the DP-mechanism. The out-of-plane oriented nuclear field B_N and the Dresselhaus field add up vectorial, which results in a slower spin dephas-

ing, see chapter 2.2.4. The higher spin lifetime at $B = 0$ leads then again to a higher Kerr-signal.

As previously mentioned, the resulting nuclear field depends on the vector sum of the fields due to the polarization of majority electron spins and minority electron spins. This means that the shift of the Hanle curve depends on the degree of spin polarization, which is proportional to the current controlled by the voltage on the electrode. Figure 4.19 (a) shows the Hanle curves for increasing bias and both sweep directions at a fixed excitation intensity (200 μW), and in figure 4.19 (b) are the peak positions of the Hanle curves depicted with respect to the electrode current. With the bias, the

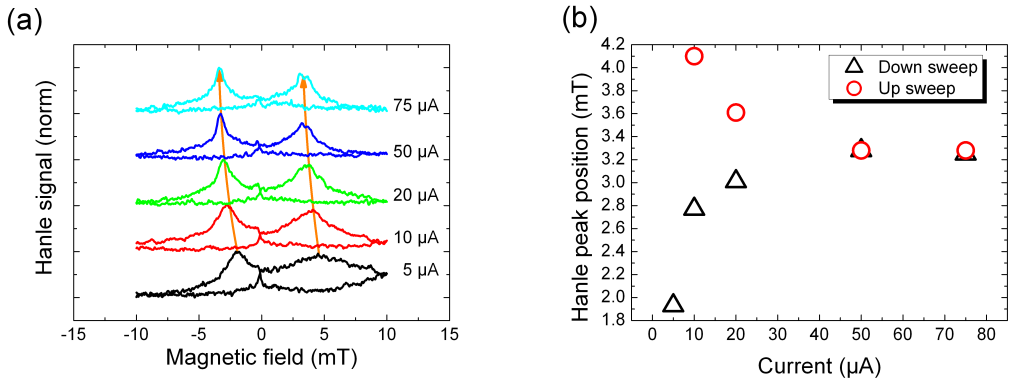

Figure 4.19: ***(a)*** *For low biases the DNP process is still ongoing during the up sweep and is saturated during the down sweep.* ***(b)*** *With rising current the spin polarization increases, yielding a higher nuclear field.*

number of spin polarized electrons in the semiconductor rises, yielding a more effective DNP. Starting from a low bias, the DNP is building up during the up sweep, and approaching the saturation at the down sweep. Therefore, the effect of the increasing nuclear field because of the rising spin polarization can only be observed there. At a current of 50 μA the number of electrons is high enough to reach a saturation of the DNP so that for up and down sweep the peak position has the same absolute value. Additionally, the spin polarization does not increase anymore owing to the reduction of the spin injection efficiency, see chapter 4.3.2. Another striking feature is that the Hanle curves at the low-bias up sweep are broader than at high bias or down sweep. A broader Hanle curve means a shorter spin lifetime. Since the DNP is still building up during the up sweep process, the nuclear field changes its value, yielding a fluctuation in the Larmor frequency of the electron spins and therefore cause an increased dephasing, see also chapter 2.2.4. One may reduce the spin polarization of the electrically injected electrons not only by reducing the current, but also by increasing the distance between the detection and the contact. As depicted in figure 4.20 the same behavior is observed. With increasing distance or decreasing spin polarization, the up sweep curve becomes wider, since the DNP is still building up. At the down sweep the DNP is saturated and a reduced nuclear field is observed. This argumentation holds obviously only if the diffusion of nuclear spin is neglected. This is valid since the nuclear spin diffusion constant in GaAs bulk is of the order $D_n = 10^{-3}$ cm^2/s by Paget [Pag82] and Kuhns [Kuh97], a factor 10000 smaller than the electron spin diffusion constant ($D_s = 10$ cm^2/s see chapter 4.4.1).

The rather small values of the nuclear field may be explained first by the influence of the optically generated electrons, and one needs to consider that the observed value is already the difference between nuclear fields generated by minority and majority spins. Kikkawa et al. showed that optical pumping induces nuclear fields up to 0.4 T in n-

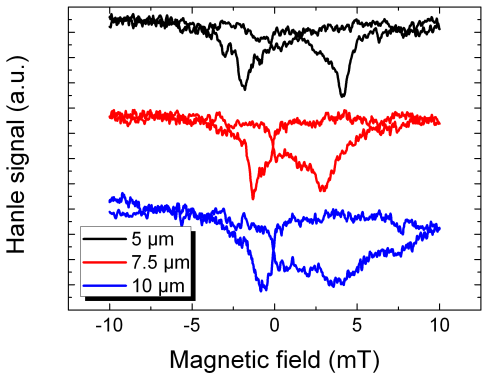

Figure 4.20: *Increasing the distance between electrode and the detection has the same effect as decreasing the current. Due to the lower spin polarization of electrically injected spins the nuclear field is smaller in the down sweep where the DNP is saturated. During the up sweep the DNP is still in progress. The current through the contact is* 50 μA*, and the excitation power* 100 μW*.*

GaAs, using NMR [Kik00]. Malinowski et al. also pumped optically and found a value of 0.7 T in a GaAs/AlGsAs quantum well. They observed electron Larmor beats in pump-probe reflectivity in an oblique field [Mal00; Mal01].

Chapter 5

Spin dynamics and spin transport phenomena in high-mobility (110)-grown quantum wells

This chapter focuses on high-mobility (110)-grown GaAs quantum wells. In these QWs, the anisotropy in the SO field allows very long spin lifetimes for optically generated electron spins (see chapter 2.2). Moreover, high mobilities are achieved by using a special growth scheme. After discussing the sample structure and a characterization of the samples, this chapter investigates the spin dynamics in regard to varying several parameters, such as excitation density, temperature and electron density. The next section examines spin diffusion and spin drift. Finally, this chapter shows the influence of dynamic nuclear polarization on spin dynamics. Most of the results are published in [Völ11; Völ13]. Similar samples were also used in several publications of M. Griesbeck et al. [Gri09; Gri12a; Gri12b]. Employing optical gating, an out-of-plane spin lifetime of 248 ns could be obtained with the resonant spin amplification method, there.

5.1 The sample structure of the high-mobility (110)-grown quantum wells

The samples used in this chapter were grown by Dieter Schuh and Christian Reichl from the group of Prof. Werner Wegscheider (formerly Regensburg University, now ETH Zürich), employing the Molecular-Beam Epitaxy (MBE) method (described in chapter 2.1.1). The growth scheme is comparable to the elaborate design of high-mobility growth by Umanski et al. [Uma09], and is illustrated in the following section. A similar description of the same samples can be found in the thesis of M. Griesbeck [Gri12b]. Umanski et al. achieved mobilities exceeding $30 \cdot 10^6 \mathrm{cm}^2/\mathrm{Vs}$ in a 2DES grown on a (100)-oriented substrate. The high growth temperature of $630° - 640°$ C ensures high purity. A (110) substrate, however, is nonpolar, yielding a reduced adhesion of As at these high temperatures [Pfe90b]. Thus, these substrates require lower growth temperatures ($\sim 480°$ C), which implicate a reduced purity and lower mobilities [1].

The basic idea of the growth scheme is the modulation doping, where the doping atoms are separated from the quantum well by a spacer layer, see chapter 2.1.1 for details. The

[1] Bel'kov et al. however showed that the increased temperature in the (001) growth leads to dopant migration, yielding an asymmetry and an increased SIA [Bel08].

remote doping is applied on both sides of the quantum well, resulting in a symmetric potential curve. This has an impact on not only the spin dephasing due to the structure inversion asymmetry (chapter 2.2.2), but also on the mobility. An asymmetric band profile yields a shift of the electron wave function towards the doped side, as depicted in figure 5.1 (a) (see also chapter 2.1.1), and therefore a higher penetration of the wave function into the barrier material. Caused by the random distribution of the alloy constituents, an additional scattering mechanism is present in the alloy $Al_xGa_{1-x}As$ [Har76; Cha80]. Thus, a deeper penetration of the wave function implies a reduced total mobility. Naturally, the alloy scattering is reduced by lowering the Al content. At the same time, however, the barrier height is decreased by reducing the Al content as well (see chapter 2.1.1), leading to a even deeper penetration of the wave function in the barrier. Hence, a careful optimization of the Al content (x) is necessary. Increased scattering due to the interface roughness is a further contribution to the lower mobility in the asymmetric case. In order to achieve a symmetric band profile, the Umansky scheme now proposes two Si-δ-doping layers [2] on each side of the quantum well, as depicted in figure 5.1 (b). The electron density in the quantum well consists of carriers

Figure 5.1: ***(a)*** *Single sided doping causes the wave function to penetrate into the barrier materials which reduces the total electron mobility.* ***(b)*** *Four δ-doping layers ensure a symmetric potential curve, yielding high mobility. Both taken from [Gri12b].*

from the two inner doping layers 2 and 3. By contrast, the two doping layers 1 and 4, with a high sheet density, far away from the QW, ensure flat-band conditions [3].

Ideally, the incorporation of the Si atom in the crystal is substitutional and forms a shallow donor level, i.e. the energy level is close below the CB minimum (in case of n-doping). The electron is smeared out over several lattice sites and is therefore only weakly bound [4]. After the electron is thermally activated, the ion is positively charged. The donor level, however may also lie deep in the bandgap [5]. An important case are the so called DX-centers. So far, no general agreement over a microscopic model has been achieved. It was suggested, that it is a complex formed by a substitutional atom (D) and a lattice defect (X). The donor atom is displaced to an interstitial lattice site leaving a vacancy at the substitutional site (X) [Moo90; Buk94]. Due to the high binding energy, the electron stays at the DX level, which leads to smaller carrier concentrations in $Al_xGa_{1-x}As$, compared to GaAs at room temperature, and a freeze-out of carriers for decreasing temperatures. Thus, at low temperatures, DX-centers dominate the transport in $Al_xGa_{1-x}As$, for $x > 0.22$ [6]. An ionization of the DX-centers by illumination

[2] δ-doping means that the doping atoms are confined to ideally one atomic layer. Diffusion, however, broadens that profile in reality.

[3] Doping layer 1 is, in contrast to the others, a bulk doping layer because of technical reasons [Gri12b].

[4] The extra electron is screened from the attractive Coulomb potential of the nucleus due to the incorporation. It can be described effectively as a hydrogen atom embedded in the crystal.

[5] The electron wave function for shallow donors is extended over many primitive cells and may therefore be described by a single Bloch function. Deep donors have localized wave functions, which involve Bloch functions over a large region in k-space [Yu05].

[6] For smaller Al concentration and in GaAs the DX level is degenerate with the CB. The energy level depends on the mole fraction, e.g., for $x \simeq 0.37$ it is close to the L band minimum, whereas for $x \simeq 0.8$ it corresponds to the X-band minimum.

is possible, resulting in an increased conductivity in the CB, which remains persistent because of poor transfer rates between CB and DX center [Moo90]. In a AlGaAs/GaAs heterostructures the mobility is reduced due to remote scattering on negatively charged DX-centers [Buk94]. In the Umanski scheme, a proposal by Baba et al. is developed further, reducing the effect of DX centers [Bab83]. The deep-level formation is effectively suppressed by introducing short-period superlattice (SPSL) δ-doping layers. Here, thin δ-doped GaAs layers are embedded in a GaAs/AlAs superlattice, see figure 5.2. The Si atoms are therefore separated from the AlAs layers, preventing the formation of DX-centers. Additionally, the confinement in a thin QW yields a quantization

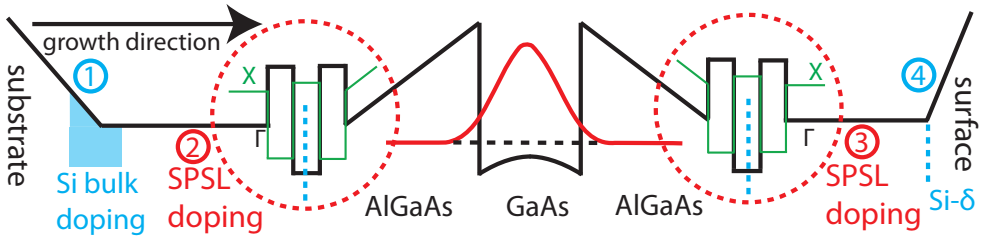

Figure 5.2: *The four δ-doping layers in the (110)-grown quantum wells. A Short period super lattice (SPSL) doping layers yield a further increase of the mobility. Layers 1 and 4 provide a flat band condition, whereas layers 2 and 3 are responsible for the carrier density in the quantum well. Taken from [Gri12b].*

and an increase of the electron energy, allowing a better charge transfer to the 2DES. Furthermore, a type-II superlattice [7] may be established by adjusting the parameters (width) of the individual layers [Guh98]. This means, that the ground state of the AlAs QW (minima in X-band) is lower than the minimum (Γ-point) in the GaAs, allowing a transfer of excess electrons. Those electrons in the AlAs wells have a higher effective mass (factor 3 more) and do not participate in the conduction process [Uma09], and screen the electric field of the ionized donors [Rös10].

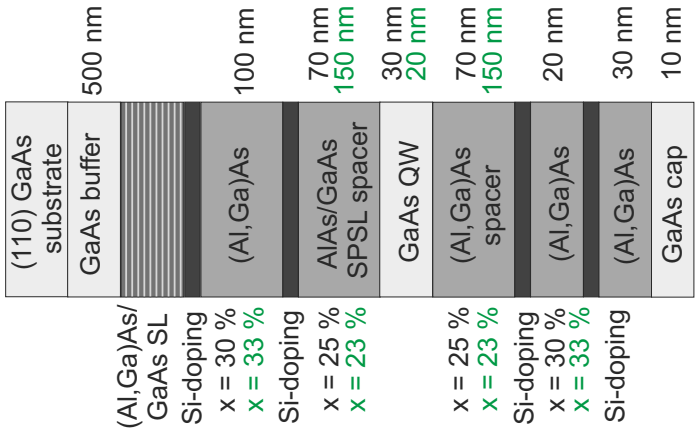

Figure 5.3: *Growth scheme of the high-mobility (110)-grown quantum well samples. Some values are different for sample QWC, these are marked in green.*

The complete growth scheme is outlined in figure 5.3. A buffer-layer and a (Al,Ga) As/GaAs superlattice are grown on top of the (110) substrate, in order to cancel roughness and impurities of the substrate surface. Then the first doping layer, a Si bulk doping follows (due to historical and technical reasons). In the subsequent $Al_xGa_{1-x}As$ layer, the Al portion is reduced during the growth from $x = 30\%$ to $x = 25\%$ ($x = 33\%$

[7] Type II in general means staggered subbands, often CB and VB are staggered in a way that holes and electrons are in different layers.

to $x = 23\%$). Then, there is a SPSL-doping layer, where a 2 nm wide δ-doped GaAs film is embedded by two 2 nm wide AlAs layers. Next, the GaAs quantum well (30 nm, 20 nm), surrounded by two spacer layers (70 nm, 150 nm) is grown. The Al fraction is kept here at $x = 25\%$ ($x = 23\%$). The spacer on top of the QW is an $Al_xGa_{1-x}As$ layer, however, the spacer below is again an AlAs/GaAs SPSL structure. The use of such a structure increases the quality of the interface to the QW. During the growth of $Al_xGa_{1-x}As$, impurity atoms usually accumulate and are eventually deposited at the interface. In the SPSL growth, the impurities are deposited on each SL interface. Moreover, the SPSL provides a smoother surface at the interface [Pet84]. After the active region, another SPSL-doping stack is grown, followed by a $Al_xGa_{1-x}As$ film where the Al portion is again raised to the initial values $x = 30\%$ ($x = 33\%$). After the fourth SPSL-doping layer a $Al_xGa_{1-x}As$ film follows, and finally a GaAs cap in order to prevent oxidation of the Al-containing layers is grown. A simplified band edge profile of the structure is depicted in figure 5.4, indicating the highly symmetric potential curve.

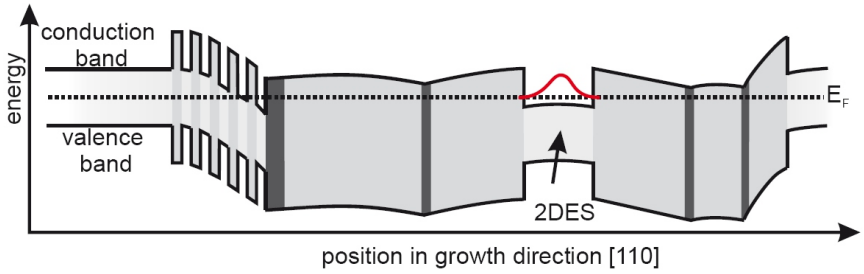

Figure 5.4: *Simplified band edge profile of the (110)-grown quantum well structures. Taken from [Gri12b].*

Table 5.1 lists the samples employed in this work. The carrier density and the mobility μ were determined by magnetotransport measurements at 4.2 K (without illumination) [8]. The Fermi energy is calculated with the expression for 2D systems: $E_F = n\pi\hbar^2/m_e^*$ (with $m_e^* = 0.067m_e$), and the diffusion constant D_e with the Einstein relation for degenerate electron systems (equation 2.56). The momentum scattering time is calculated from the mobility with equation 2.49, and the electron-electron scattering time with equation 2.51. All the values are valid for liquid-Helium temperature 4.2 K.

sample number	width (nm)	density n (10^{11} cm^{-2})	E_F (meV)	mobility μ (10^6 cm^2/Vs)	D_e (10^3 cm^{2}s^{-1})	τ_p (ps)	τ_{ee} (ps)
QWA	30	2.7	9.6	2.14	20.5	81.5	14.2
QWB	30	3.3	11.8	3.95	46.6	150.5	17.4
QWC	20	1.2	4.3	0.74	3.2	28.2	6.3

Table 5.1: *Various important parameters for the high-mobility (110)-grown quantum wells. All values are valid for liquid-Helium temperature 4.2 K. The internal wafer numbers are for sample QWA: D081104B, for sample QWB: D081205A, and for sample QWC: D111031B.*

[8] With Hall measurements, the carrier density is determined, from which the mobility can be derived with the sheet resistance. For the determination of the sheet resistance, typically the van-der-Pauw method is used. Here, four small contacts at the edges of the sample are used to determine the resistance, and cyclic permutation of the contacts minimizes the effects of contact resistance.

5.2 Spin dynamics in high-mobility (110)-grown quantum wells

This section discusses the spin dynamics for the three samples, described above. The Hanle-MOKE method is used, in order to examine the spin dephasing. This method measures the Kerr rotation, which is proportional to a time-averaged spin polarization. By contrast, the analysis of the spin resolved photoluminescence measurements provides an absolute value for the spin polarization. The spin dynamics are investigated under the influence of a variation of external parameters such as temperature, excitation density and carrier density. For a complete understanding of the spin dynamics, the carrier dynamics with respect to the temperature need to be investigated. Photoluminescence measurements have been conducted for that purpose.

5.2.1 Carrier dynamics of the (110)-grown quantum well samples

Photoluminescence measurements are a helpful tool to investigate carrier dynamics, see chapter 3.3. Figure 5.5 (a) depicts PL traces taken for sample QWC at different sample temperatures, whereas figure 5.5 (b) shows the temperature dependence of the photoluminescence in a false color plot. For the PL-intensity, a logarithmic scale is used. The photoluminescence of sample QWA is not shown here, since M. Griesbeck has already investigated it, see [Gri12b] page 48. Regarding the displayed sample temperatures, one has to consider, that these temperatures values are given by the temperature sensor at the bottom of the cold finger, as discussed in chapter 3.5. The actual sample temperature depends on the thermal contact and is at least $4-6$ K higher. For the measurement a nonresonant excitation with a wavelength of 760 nm was used. Because the recombination time is so long compared to the energy relaxation, the photoluminescence is mostly caused by thermalized carriers. A closer look at the PL-traces reveals a peak at low photon energies (about 1490 meV), vanishing at temperatures above $\sim$ 20 K. This peak may be attributed to carbon impurities [Str81; Teh88; Teh90], and is not investigated further.

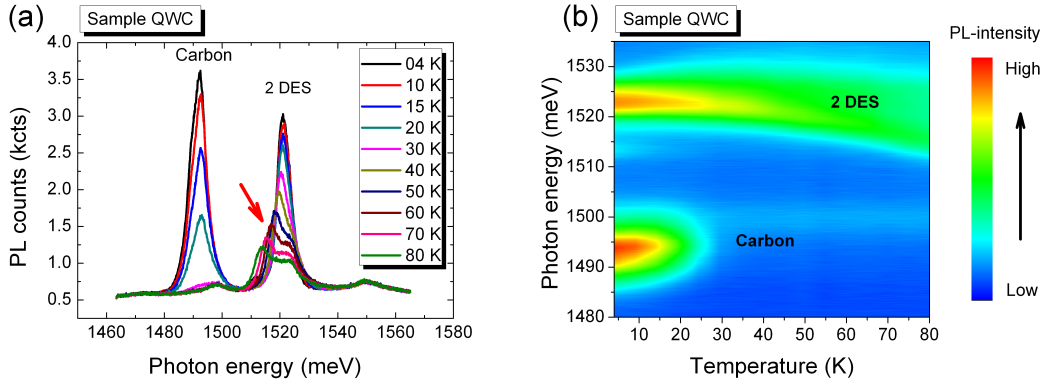

Figure 5.5: *(a) PL traces for increasing sample temperature. From the high energy tail the electron temperature may be determined, and from the spectral width the carrier density.* ***(b)*** *False color plot of the temperature dependence of the PL. The intensity is hereby on a logarithmic scale.*

The high energy tail of the main peak, which describes the photoluminescence from the first subband, may be fitted with a Fermi-Dirac distribution (equation 3.16), yielding the possibility to extract the electron temperature and the Fermi energy E_F, see chapter 3.3 for details. An exemplary PL trace from sample QWA with such a fit is displayed in figure 3.6 (b). Figure 5.6 shows the electron temperature with respect to the sample temperature for samples QWA (a) and QWC (b). The insets of both the

graphs depict the ratio between the obtained electron temperature and the provided sample temperature. The quite high ratios in the range 4 K $\lesssim$ T $\lesssim$ 25 K is most likely attributed to the already discussed difference of the measured sample temperature and the actual temperature (thermal contact to the cold finger), whereas in the range above 25 K these effects become less important. Here, sample QWA has a ratio $\sim$ 1.5 and sample QWC $\sim$ 1.0. A reason for the higher electron temperatures in sample QWA is the higher mobility, due to the larger carrier density. Caused by these high carrier densities, screening effects reduce the coupling between lattice and electron system, and the electron system is therefore not in thermal equilibrium with the lattice. Furthermore, a heating of the electron system caused by high excitation powers can be observed at temperatures below 25 K. The excitation densities are chosen in the same range as used in the Hanle experiments. Because of the different absorption in the samples, as discussed later in the chapter, the excitation densities at the 2DES are not alike.

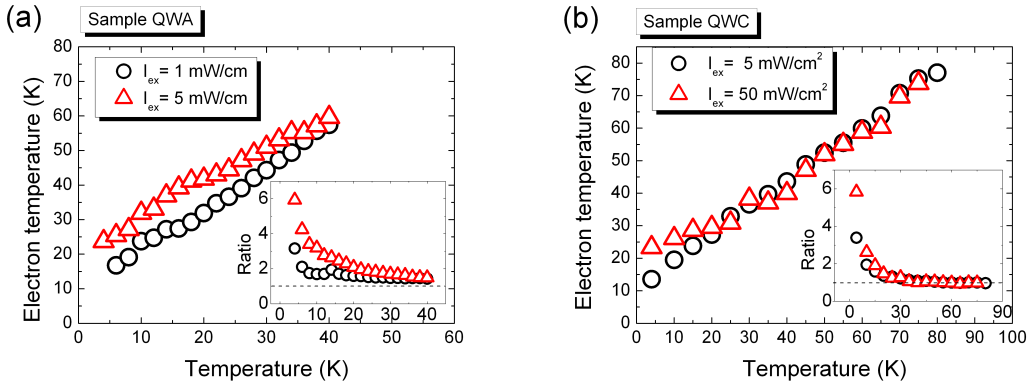

Figure 5.6: *Electron temperature versus sample temperature in sample QWA* ***(a)*** *and sample QWC* ***(b)****. The insets depict the ratio of the two with respect to the sample temperature.*

Besides the electron temperature, PL measurements provide information about the carrier density in the samples. The spectral width of the main peak $\Delta E = E_F - E_0$ (see figure 3.6 (b)), increases for rising temperature, indicating a growing carrier density. With increasing temperature, the Fermi distribution, which is a step function at zero temperature, smears out ($\delta E \propto k_B T$), leading to a carrier redistribution toward higher energies. Furthermore, for some wafers the remote donors are not fully ionized at low temperatures, resulting in an increase of the carrier density for rising temperature. According to the discussion in chapter 3.3, the carrier density may be calculated from the spectral width of the PL traces with equation 3.15. It turns out that the carrier density in sample QWA increases from $\sim 2 \cdot 10^{11}\,\mathrm{cm}^{-2}$ at 4 K to $\sim 3.5 \cdot 10^{11}\,\mathrm{cm}^{-2}$ above $\sim$ 30 K and in sample QWC from $\sim 1 \cdot 10^{11}\,\mathrm{cm}^{-2}$ at 4 K to $\sim 2 \cdot 10^{11}\,\mathrm{cm}^{-2}$ above $\sim$ 50 K, as depicted in figure 5.7 (a).

The low energy step, indicated by a red arrow in figure 5.5 (a), determines the band minimum E_0, see also figure 3.6 (b). For increasing temperatures a shift towards lower energies is observed. Such a redshift may be attributed to band gap renormalization effects as a consequence of changes in the carrier density, discussed in chapter 2.1.1. Besides the main peak, there is another one visible at higher photon energies (1550 meV in figure 5.5 (b)), which indicates an occupation of a higher subband due to the growing spectral width of the Fermi distribution $\delta E \propto k_B T$.

Time-resolved photoluminescence measurements (TRPL) are possible in a different setup employing a streak camera instead of a CCD camera and pulsed excitation, see chapter 3.3. Such a trace is depicted exemplarily for sample QWC at 4 K in fig-

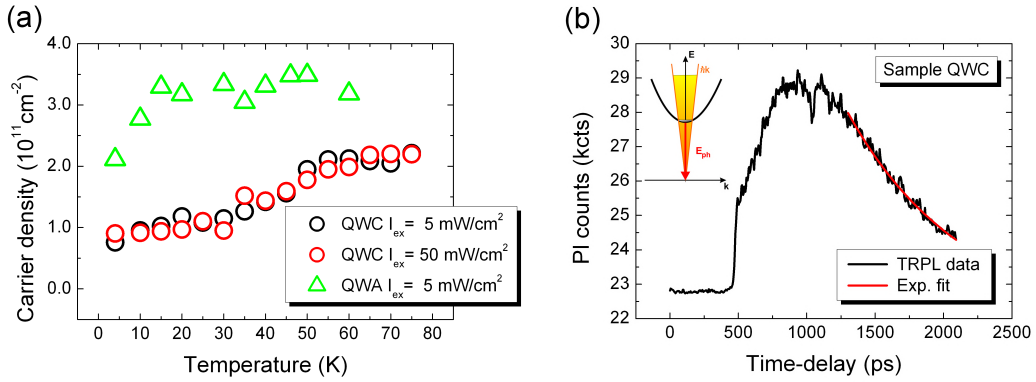

Figure 5.7: *(a) The carrier density dependence on the sample temperature for samples QWA and QWC. (b) Time-resolved photoluminescence trace with exponential fit from sample QWC at 4 K. The inset depicts the light cone, which is a result of the liner $E(\boldsymbol{k})$- dispersion of the photons.*

ure 5.7 (b). After the nonresonant excitation, electron and holes thermalize to their band extrema, where the recombination takes place. The PL consists mainly of transitions involving the HH band. For $\boldsymbol{k} \neq 0$, however, the LH/HH mixing causes transitions involving LH states as well [Pfa05]. In the recombination process energy as well as momentum conservation is valid. The increase in the PL intensity from 500 ps to 1000 ps is a result of momentum conservation. The fast electrons and holes need to reduce their momentum through scattering, until a momentum transfer with the photon is possible. When dealing with excitons, one usually speaks of a light cone, which is given by the linear photon dispersion $E(\boldsymbol{k})$, also shown in the inset of figure 5.7. Although no excitons are present in this case, the model of the light cone can be used as well to picture the momentum conservation requirement. A radiative recombination is then possible if electrons and holes are inside the light cone [Olb09]. The increase in the PL intensity after the excitation at position 500 ps to 1000 ps signifies an increase of the carrier density inside the light cone due to scattering processes, which yields more recombination and a higher PL intensity. Thereafter a monotonous decay of the PL is observed, from which the carrier lifetime can be determined using an exponential fit. At higher temperatures the carriers scatter more, and the carriers scatter out of the light cone, which leads to an increased PL lifetime [Olb09].

Figure 5.8 depicts the TRPL with respect to the sample temperature for the samples QWA and QWC. The results for sample QWA are taken from the thesis of M. Griesbeck

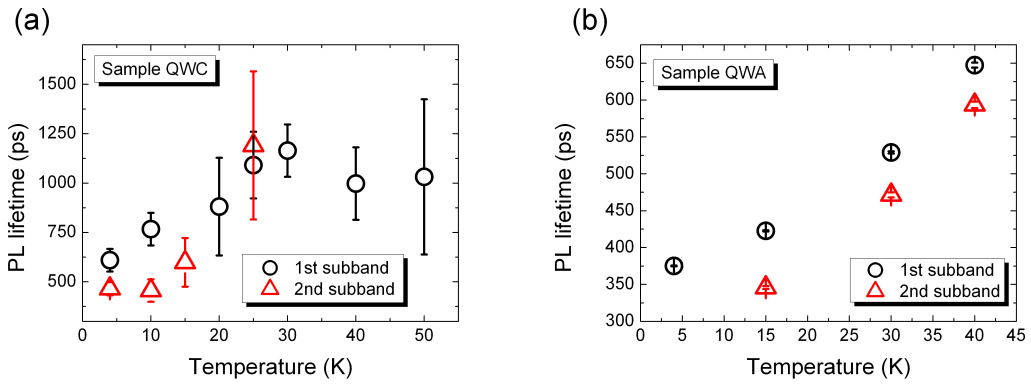

Figure 5.8: *Extracted PL lifetimes for samples QWC* ***(a)*** *and QWA (adapted from [Gri12b])* ***(b)****.*

[Gri12b]. The PL lifetimes for sample QWA start at 375 ps at 4 K and rise up to 650 ps at 40 K. Sample QWC, on the other side, has a PL lifetime of 600 ps at 4 K, above 25 K it saturates to a constant value of about 1 ns. Typically, one would expect a shorter carrier lifetime for narrower quantum wells, since the increased confinement yields a higher recombination probability because of an increased overlap of electron and hole wave functions [Hüb11]. However, since the scattering in and out of the light cone affects the PL lifetime, the explanation might be in the different mobilities of the two samples. The different carrier lifetimes are affecting the behavior of the spin lifetime, since an increased carrier lifetime yields a higher time averaged hole concentration which in turn affects the BAP spin dephasing mechanism.

The obtained values of the carrier lifetimes agree with the literature. Döhrmann et al. found in a (110)-grown modulation doped MQW (10×20 nm) sample a PL lifetime of 500 ps at 6 K and 9 ns at room temperature. Olbrich et al. measured 1.5 ns at 4 K up to 2.5 ns at 125 K in a (110)-grown MQW (20 nm)

5.2.2 Spin dephasing in (110)-grown quantum wells

The following section investigates the spin dephasing of the three (110)-grown quantum wells in terms of external parameters such as excitation intensity, temperature, and carrier density (varied by optical gating) using Hanle-MOKE measurements (see chapter 3.2). By doing so, the dominant spin dephasing mechanisms are revealed. Hereby, samples QWA and QWB show similar behavior, whereas sample QWC is often quite different. Hence, the discussion is many times restricted to the samples QWA and QWC.

After D'yakonov and Kachorovskiĭ stated, that the special symmetry of (110)-grown quantum wells implies an absence of DP spin relaxation due to BIA (in its k-linear approximation) [Dya86], Ohno et al. did the first measurements on undoped and directly doped GaAs MQW (60×7.5 nm wide QW) grown on a (110) substrate [Ohn99b]. They applied a pump-probe transmission measurement [9] at room temperature (RT), and found spin lifetimes of up to 2.1 ns (undoped), which they compared with lifetimes of 70 ps found in an (100)-oriented structure. Adachi et al. found a spin lifetime up to 10 ns (at RT) using the same technique in a MQW ($60 \times 4.4 - 8.3$ nm wide QW) [Ada01]. Adachi et al. and Ohno et al. only investigated the out-of-plane component of the spin polarization. Döhrmann et al., in contrast, showed an anisotropy in the spin dephasing for in- and out-of-plane spin orientations. They examined polarized luminescence of a symmetrical modulation doped MQW (10×20 nm wide QW), spectrally and temporally (by using a streak camera) after creating a spin polarization with circularly polarized light (TRPL technique). For the out-of-plane component they could confirm the value of the spin lifetime at RT obtained by Ohno et al., and found even longer lifetimes up to 7 ns at lower temperatures.

Optical excitation has the disadvantage of introducing additional holes into the system causing BAP dephasing, and furthermore a heating of the electron system. Spin noise spectroscopy provides the possibility to examine the spin dynamics in an unperturbed system. Here, the statistical fluctuations of an electron spin polarization are mapped via Faraday rotation onto the light polarization of a linear polarized, continuous-wave laser. Using this technique, Müller et al. extracted a spin lifetime of about 25 ns at 20 K in a MQW (10×16.8 nm wide QW) [Mül08]. The longest spin lifetimes so far were obtained by Griesbeck et al.. By employing the RSA technique [10], they found a spin

[9] Here, a spin polarization is created by a circularly polarized pulse, thereafter the transmission intensities of a subsequent pulse is measured for the same helicity or the contrary. From the difference of the intensities a spin polarization can be determined, and the decay by varying the time delay.

[10] The resonant spin amplification technique (RSA) is based on the TRFR/TRKR method, which is limited by the length of the mechanical delay line and the laser repetition rate. The Kerr/Farady

lifetime for the out-of-plane component of about 100 ns at 4 K [Gri12a]. The sample they used is from the same wafer as sample QWA used in this work. By reducing the carrier density through optical gating, the out-of-plane spin lifetime increased up to 248 ns [Gri12b].

In the Hanle-MOKE experiments presented here, circularly-polarized light creates spin-polarized electron hole pairs. In an undoped sample, a spin polarization may exist only within the photocarrier lifetime, which would dominate the measured lifetime, e.g. in TRKR measurements, in the case that the spin lifetime is longer than the carrier lifetime. In n-doped samples, the hole spin, however, relaxes towards thermal equilibrium, typically on a timescale of the momentum relaxation time ($\sim$ 100 fs [Hil02]), because of strong spin orbit coupling and VB mixing. Hence, the electron-hole recombination also involves unpolarized electrons in the CB, leaving a resident electron spin polarization after the recombination process.

In the case of a perpendicular incidence of the excitation, the electron spin polarization is oriented parallel to the sample normal, owing to angular momentum conservation. As described earlier, the effective magnetic field in a symmetric quantum well grown on a (110) substrate is oriented along the same direction (see figure 2.13), yielding no DP-spin dephasing invoked by BIA. Furthermore, a symmetric structure implies an absence of SIA, resulting in an suppression of the DP spin dephasing. This was experimentally shown by Bel'kov et al. employing the magnetophotogalvanic effect (MPGE)[11] and TRKR [Bel08; Olb09; Kor10]. Thus, the spin relaxation is dominated by BAP dephasing and the carrier recombination. Using surface acoustic waves, electrons and holes are trapped in the maxima and minima of the piezoelectric potential respectively. Hence, they are spatially separated, which results in a reduction of the BAP. Employing this, spin lifetimes up to 20 ns and the transport of a spin packet over 60 μm have been reported for temperatures up to 60 K [Cou07; Cou08; HM10].

Dependencies of the g-factor and the Kerr signal

Before discussing the spin dynamics, influences on the g-factor and the Kerr signal are revealed in this section. Spin lifetimes are calculated using equation 3.6, which includes the g-factor. The g-factor depends on the Fermi level in the conduction band, the penetration of the electron wave function into the barrier, as well as the nonparabolicity of the conduction band. In the discussion of the spin dephasing times, the influence of carrier density and temperature on the g-factor needs to be considered. Hübner et al. have shown, that due to the reduced symmetry in (110)-grown quantum wells (C_{2v} symmetry, see chapters 2.2.2 and 2.2.6) higher-order effects implicate off-diagonal terms in the g-factor tensor, which results in an anisotropy of the g-factor in the in-plane crystal directions [Hüb11]. They investigated several undoped (110) quantum wells with different widths using quantum beat spectroscopy [12]. It was reported that the anisotropy decreases with increasing well width. Their broadest QW was 19 nm, showing a negligible variation of the g-factor in the crystal direction. Thus, the g-factor is assumed to be isotropic in the crystal directions. The g-factors for the samples used in this work, displayed in figure 5.9, were determined by employing the resonant spin amplification (RSA) method (for details see [Kik98; Gri12a; Gri12b]), showing a weak

rotation is measured depending on a small applied external magnetic field at a fixed time delay between pump and probe pulse. A spin polarization created by subsequent laser pulses interfere constructively or destructively, depending on the precession angle. With this method in- and out-of-plane spin lifetimes as well as the g-factor may be extracted.

[11] Due to the higher C_{2v} symmetry in an symmetric QW the MPGE is absent.

[12] Quantum beat spectroscopy is polarization-resolved time evolution of the PL of an optically excited spin polarization in a perpendicular external field. Detecting only one component of the circularly polarized PL, the g-factor may be extracted from the Larmor oscillation of the PL intensity.

dependence on the temperature. M. Griesbeck conducted the measurements for sample QWA and QWB and C.Gradl for sample QWC.

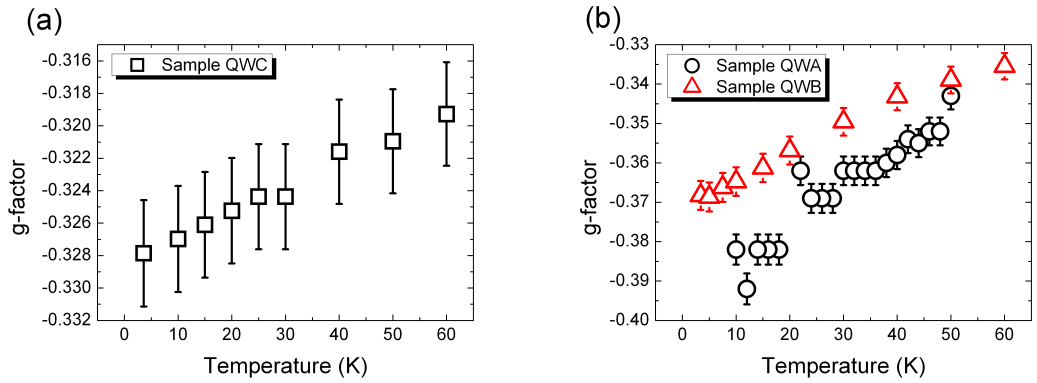

Figure 5.9: *(a) Temperature dependence of the g-factor in sample QWC measured by C. Gradl using RSA. (b) Temperature dependence of the g-factor in samples QWA and QWB measured by M. Griesbeck using RSA.*

The change in electron density as well as the band gap with the temperature (equation 2.1) yield a change in the sensitivity of the Kerr signal. In order to examine the dependence on the probe wavelength, a Hanle signal was taken for different probe wavelengths and different temperatures. As explained earlier (chapter 3.2), the amplitude of the Hanle curve is proportional to the Kerr rotation. In figure 5.10 these dependencies are depicted for sample QWC. Similar to figure 3.3, which shows the spectral depen-

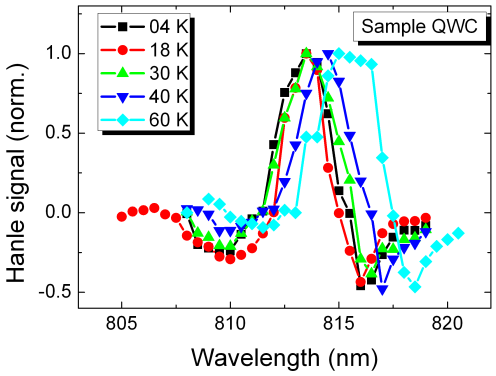

Figure 5.10: *Spectral dependence of the Kerr signal. The maximum shifts for temperatures above 40 K towards higher wavelengths.*

dence in n-GaAs bulk, several maxima are observed. The maximum at a wavelength of 813.5 nm is the most prominent one, and is therefore used in the following measurements. At temperatures above 40 K, the peak shifts towards higher wavelengths i.e. smaller energies, which is considered in the temperature-dependent measurements. The reason for the shift in the energy is a decrease in the bandgap energy according to equation 2.1. Since the amplitude is also proportional to the spin polarization and the spin lifetime, which change with the temperature, as described later, no statement about the relative change of the Kerr maximum with regard to the temperature change can be made, only the shift in the maximum may be considered. All the Hanle-MOKE measurements were taken using the Kerr wavelength yielding the maximal signal.

In samples QWA and QWB, it was not possible to obtain such a spectral dependence, since only for the maximum value of 818.5 nm a Hanle signal was obtained. Moreover a temperature dependence only up to 30 K was taken, where an adjustment of the Kerr wavelength to 819.5 nm was necessary. In order to suppress pump laser light in

the detection, pump and probe laser light need to be spectrally separated, yielding the necessity for non-resonant excitation. For all experiments, the excitation wavelength is chosen to be at 760 nm. Thus, the electron-hole pairs have an excess energy of about 100 meV, depending on the QW width and the sample temperature.

Excitation-density dependence of the spin lifetime

The following section discusses the dependence of the spin lifetime on the excitation density. First, the theoretical model developed by S.A. Tarasenko is introduced. The Hanle-MOKE method requires an external magnetic field, yielding an in-plane spin component, which experiences the DP-relaxation. The measured spin lifetime is therefore the geometric mean of in- and out-of-plane component $\tau_s = \sqrt{\tau_z \tau_\parallel}$ (equation 3.8). The two components can be expressed according to equation 2.42. For the out-of-plane component τ_z then follows:

$$\frac{1}{\tau_z} = \frac{1}{\tau_z^{lim}} + \gamma_z^{BAP} N_h + \gamma^r N_h, \tag{5.1}$$

where $1/\tau_z^{lim}$ is the spin dephasing rate in the limit of zero excitation. Even in the absence of a global Rashba field, there may exist small residual Rashba fields in any modulation-doped structure. Such residual Rashba fields may include regular Rashba fields, which arise from incomplete and asymmetric ionization of remote dopants. A further contribution to the residual Rashba field comes from the fact that the concentration of the dopant ions is not homogeneously distributed, which results in a grainy structure of the dopant layer. Additionally, the screening in the SPSL structure may vary locally. Such fluctuations arise locally different electric fields and therefore random Rashba fields [She03; Gla05; Gla10; Zho10; Pos13] (these Rashba fields are discussed in more details below within the description of the temperature dependence of the spin lifetimes). Thus, the limiting spin dephasing rate consists of the DP dephasing because of such residual Rashba fields as well as a contribution from the EY mechanism. The term $\gamma_z^{BAP} N_h$ describes the spin decay due to the BAP mechanism (chapter 2.2.4) which is proportional to the steady-state hole density N_h. The term $\gamma_z^r N_h$ defines the photocarrier recombination. It is valid to assume, that for a nondegenerate hole gas and in the absence of recombination centers [13], the recombination probability is proportional to the excitation densities $N_h \propto I$ for $N_{h,e} \ll n_e$. In the limit of very high excitation $N_{h,e} \gg n_e$, almost all of the optically oriented electrons would recombine with the holes, similar to the undoped case, and the photocarrier lifetime limits the spin lifetime. Assuming that the recombination rate is proportional to $N_h N_e \approx N_h^2$, the hole density would be proportional to the square root of the intensity $N_h = \sqrt{I}$. For the in-plane component follows according to equation 2.42:

$$\frac{1}{\tau_\parallel} = \frac{1}{\tau_\parallel^{lim}} + \gamma_\parallel^{BAP} N_h + \gamma^r N_h, \tag{5.2}$$

and therefore the total measured spin dephasing rate is given by (using equation 3.8):

$$\frac{1}{\tau_s} = \sqrt{\left[\frac{1}{\tau_z^{lim}} + \left(\gamma_z^{BAP} + \gamma^r\right) N_h\right] \left[\frac{1}{\tau_\parallel^{lim}} + \left(\gamma_\parallel^{BAP} + \gamma^r\right) N_h\right]}. \tag{5.3}$$

Here, $1/\tau_\parallel^{lim}$ is determined by the conventional DP mechanism since the effective spin-orbit field (BIA) is not parallel to the spin vector anymore. Hence, $1/\tau_\parallel^{lim} \gg 1/\tau_z^{lim}$

[13] A recombination center is an impurity or a charged point defect, in which a minority carrier (hole) is captured. A majority carrier (electron) may recombine with the captured one.

while γ_z^{BAP} and $\gamma_\parallel^{BAP}$ are comparable. Evaluating the spin polarization, that is proportional to the amplitude of the Hanle signal, as presented in the next chapter (5.2.3), shows that $1/\tau_z^{lim}$ and $\left(\gamma_z^{BAP}+\gamma^r\right)N_h$ are comparable for very low excitation densities see equation 5.17. For symmetrical quantum wells grown on a (110) oriented substrate, $\tau_z^{lim}/\tau_\parallel^{lim}\approx 7$ has been reported [Mül08]. Moreover, using RSA measurements, Griesbeck et al. found a value of up to 50 for this ratio [Gri12a]. Thus, the effects of BAP and recombination $\left(\gamma_\parallel^{BAP}+\gamma^r\right)N_h$ may be neglected, compared to $1/\tau_\parallel^{lim}$, in the in-plane spin dephasing rate. The spin lifetime obtained by the Hanle measurements is then given by:

$$\frac{1}{\tau_s}=\sqrt{\frac{1}{\tau_\parallel^{lim}}}\sqrt{\frac{1}{\tau_z^{lim}}+\left(\gamma_z^{BAP}+\gamma^r\right)N_h}. \tag{5.4}$$

Thus, the behavior of the extracted spin dephasing rates with respect to the excitation density, with $N_h\propto I$, and assuming $1/\tau_\parallel^{lim}$ depends negligibly on N_h, may be expressed by:

$$\frac{1}{\tau_s}(I)=\frac{1}{\tau_s}(0)\sqrt{1+\frac{I}{I_0}}. \tag{5.5}$$

For the DP-mechanism in the collision dominated regime an expression for $\tau_\parallel^{lim}$ can be found. The spin-orbit Hamiltonian in the case of a (110)-oriented symmetric QW is given by (using equations 2.18, 2.22, and with $\bar{\Omega}_k$ the Larmor precession in equation 2.32):

$$\hat{H}_{SO} = \beta\sigma_z k_x=\frac{1}{2}\hbar\bar{\Omega}_k\hat{\boldsymbol{\sigma}} \tag{5.6}$$

$$\Rightarrow\bar{\Omega}_k = \frac{2\beta}{\hbar}(0,0,k_x)=\underbrace{\frac{\gamma\left\langle k_z^2\right\rangle k_F}{\hbar}}_{\Omega_D^{`}}(0,0,k_x/k_F) \tag{5.7}$$

$$1/\tau_\parallel^{lim} = \tau\bar{\Omega}_k^2=\frac{1}{2}\tau\Omega_D^{`2} \tag{5.8}$$

$$\Rightarrow\tau_\parallel^{lim} = \frac{2}{\Omega_D^{`2}\tau} \tag{5.9}$$

$\Omega_D^{`}=\gamma\left\langle k_z^2\right\rangle k_F/\hbar$ is the frequency corresponding to the maximum Dresselhaus field (see also [Pos13]) at the Fermi circle, and $k_F=\sqrt{2\pi n}$ is the Fermi wave vector. The Dresselhaus parameter in equation 5.8 was defined in equation 2.23. The factor 1/2 in equation 5.8 comes from averaging $\Omega_D^{`2}$ over all angles (average of $\cos^2$ over 1 period).

At higher temperatures the 2DES is not perfectly degenerate and a characteristic energy is introduced: $\tilde{\epsilon}=E_F/\left[1-\exp\left(-E_F/k_BT\right)\right]$, so that the expression is valid for arbitrary statistics. With equation 5.9 $1/\tau_\parallel^{lim}$ is then given by:

$$1/\tau_\parallel^{lim}=\frac{\gamma^2\left\langle k_z^2\right\rangle^2 m^*\tau\tilde{\epsilon}}{\hbar^4} \tag{5.10}$$

The relative magnitude of γ_z^{BAP} and γ^r can not be determined from the excitation-density dependence. Moreover, this model does not take spin diffusion into consideration. In the following measurements, the 50 mm lens with a spot size of 40 μm is therefore used (with full overlap of pump and probe laser beam), in order to suppress effects of spin diffusion out of the laser spot.

Figures 5.11 (a) and 5.12 (a) depict measured Hanle curves for different excitation densities, in samples QWA and QWB. The traces were taken at nominal 4 K, however, as discussed earlier (chapter 3.5) the actual sample temperature may be up to 6 K

higher. For those two samples, a considerable increase of the line width of the Hanle curves with increasing excitation density is visible. Hence, the spin lifetime decreases with growing excitation density. The extracted spin lifetimes and spin dephasing rates depending on the excitation density are displayed in figures 5.11 (b) and 5.12 (b). They exhibit the square root characteristics according to equation 5.4.

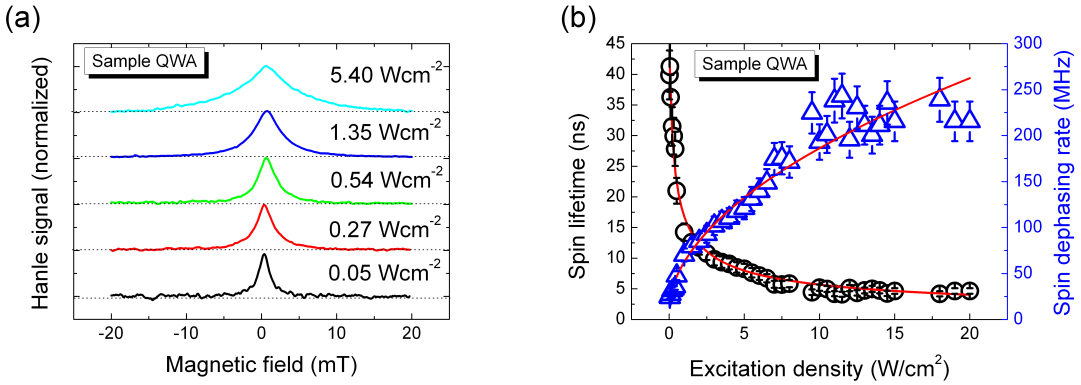

Figure 5.11: *Sample QWA at nominal 4 K:* ***(a)*** *The line width of the Hanle curves increases with growing excitation density.* ***(b)*** *Due to the rising hole density the spin lifetime decreases significantly.*

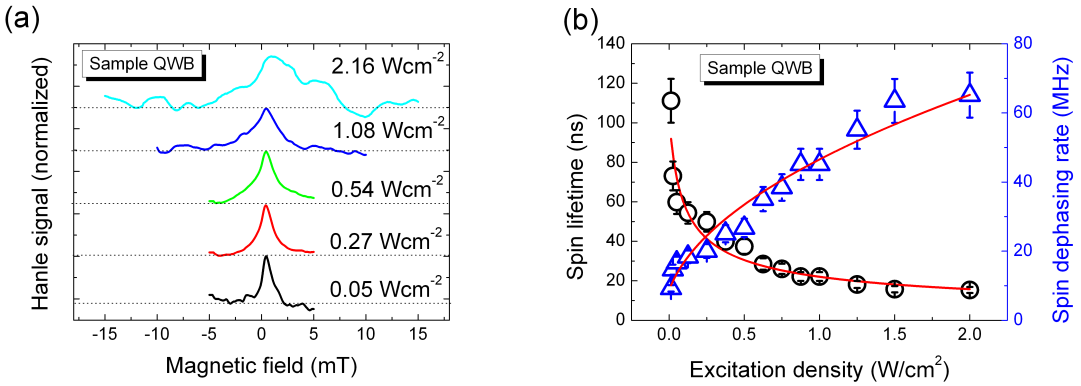

Figure 5.12: *Sample QWB at nominal 4 K:* ***(a)*** *The line width of the Hanle curves increases with growing excitation density.* ***(b)*** *Due to the rising hole density the spin lifetime decreases significantly.*

The continuous-wave excitation in this kind of experiment and the long carrier lifetime, see figure 5.8, yield that the spin dephasing is dominated by the BAP mechanism and the carrier recombination, according to the model described above. By increasing the excitation density, the hole density rises, resulting in more spin dephasing and recombination according to the factor $\left(\gamma_z^{BAP} + \gamma^r\right) N_h$ in equation 5.4.

Using the function in equation 5.5, the excitation-density dependence of the spin dephasing rate in samples QWA and QWC could be fitted with the values $I_0 = 52 \pm 16$ mW/cm^2 (QWA) and $I_0 = 257 \pm 98$ mW/cm^2 (QWB). From the fits, a spin lifetime at zero excitation of $\tau_s(0) = 46.9$ in sample QWA, and $\tau_s(0) = 110.27$ ns in sample QWB was extracted. Since the actual ratio of $\tau_z/\tau_\parallel$ is unknown, the actual value for the out-of-plane spin lifetime can not be determined. For an estimate, the smallest and the highest ratio of $\tau_z/\tau_\parallel$ of 5 and 50 are used, found in [Gri12a] for a sample of the same wafer as QWA at low temperatures, with $\tau_s = \sqrt{\tau_z \tau_\parallel}$. For sample QWA this gives in-plane lifetimes of $21 - 7$ ns, and out-of-plane spin lifetimes of $105 - 332$ ns.

A similar behavior of the spin lifetime with respect to the excitation density was reported by Lombez et al. [Lom07]. They investigated a MQW (20×8 nm wide QW) at room temperature using time-resolved optical orientation photoluminescence. Adachi et al. also showed a drop of the spin lifetime for increasing pump beam power at room temperature [Ada01].

Although both samples show the same behavior in the excitation density dependence, they differ in the maximum value of the spin lifetime τ_s, which is reached at low excitation, and in the range of excitation density in which the spin lifetime drops. For sample QWA, a maximum spin lifetime of 41 ns was obtained and for sample QWB 110 ns. The striking difference between the two numbers is most likely explained by the higher carrier density in sample QWB (see table 5.1). A higher carrier density implies a reduced electron-hole scattering rate. Since in the BAP mechanism, the spin dephasing rate is directly proportional to the e-h scattering rate, longer spin lifetimes are expected for larger carrier densities. The Pauli blocking, which suppresses the scattering, also weakens for lower electron density [Zho09], see also the discussion on the dependence of the spin lifetime on above-barrier illumination. Additionally, a different thermal contact or a local variation in the quantum well width might contribute to the difference. For increasing temperatures, the Pauli blocking is reduced allowing more scattering and therefore yielding lower spin lifetimes.

The excitation density dependence of the spin lifetime in sample QWC, on the other hand, is quite different at low temperatures, see figure 5.13. Here, the spin lifetime rises

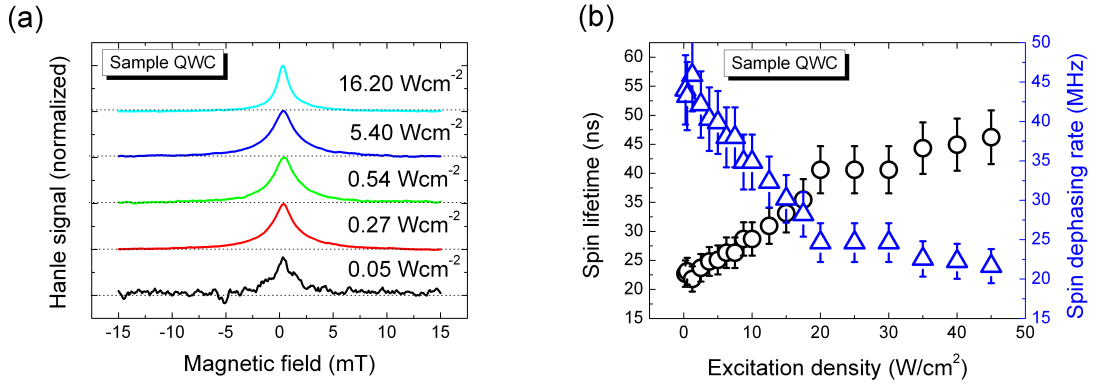

Figure 5.13: *Sample QWC at nominal 4 K:* ***(a)*** *The line width of the Hanle curves decreases slightly with growing excitation density.* ***(b)*** *The spin lifetime increases with the excitation-density since the DP mechanism dominates in this regime.*

with growing excitation linearly up to 20 W/cm^2 and stays constant for even higher excitations. This characteristics imply that the BAP mechanism is not dominating the spin dephasing in this temperature and excitation density regime, rather it is the DP mechanism. This mechanism is always present for the in-plane component because of the symmetry of the Dresselhaus field. Owing to a Rashba contribution resulting from incomplete donor ionization, which is discussed below in the section of the temperature dependence of the spin lifetime, the DP mechanism dominates the dephasing of the out-of-plane component as well. The increase in the spin lifetime with rising excitation density may be explained as follows. In the motional narrowing regime, the spin lifetime depends on the microscopic scattering time and the spin-orbit field according to equation 2.32:

$$\frac{1}{\tau_s} = \bar{\Omega}(\boldsymbol{k}_F)^2 \tau. \tag{5.11}$$

With the excitation density the density of the optically generated holes rises. Those serve as additional scattering centers, and reducing therefore the momentum relaxation

time and the microscopic scattering time τ. Furthermore, the rising excitation density induces local heating, yielding a rising spin lifetime as well, since the local heating aids the ionization of remote dopants. Additionally, a higher temperature influences the electron-electron scattering time, which in turn affects the spin lifetime. The following section discusses this in details. The change in the slope of the spin lifetime dependence, for excitation densities above 20 W/cm^2 in figure 5.13 (b) is attributed to a locally complete ionization of the remote dopants.

Temperature dependence of the spin lifetime

Obviously, the temperature dependence of the spin lifetime is quite important. Thus, the spin lifetime of the three samples are examined regarding to the temperature, see figure 5.14. Whereas in the BAP-dominated samples QWA and QWB the spin lifetime drops with the temperature, the temperature dependence of the spin lifetime in sample QWC shows a pronounced maximum at about 20 K, see figure 5.14 (b).

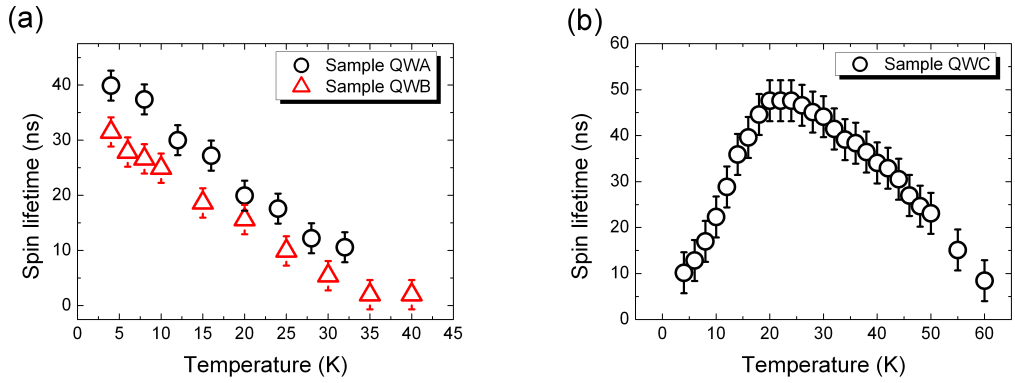

Figure 5.14: *(a) Temperature dependence of the spin lifetime measured with an excitation density of* 0.27 *W/cm*^{2} *for sample QWA and* 0.54 *W/cm*^{2} *for sample QWB.* ***(b)*** *Temperature dependence of the spin lifetime in sample QWC, measured with an excitation density of* 0.27 *W/cm*^{2}*.*

Using RSA measurements, Griesbeck et al. found such a behavior, as in sample QWC, in similar samples as well [Gri12a]. They reported an increase of the out-of-plane spin lifetime, whereas the in-plane spin lifetime stayed constant with the temperature. The experiments presented here, on the contrary, use cw excitation, which yields the presence of holes, and therefore different spin dephasing mechanisms.

The complex growth structure of the samples is responsible for the increase of the spin lifetime for rising temperature in the range between 4 K and 20 K displayed in figure 5.14 (b). The sample design is optimized to yield a highly symmetrical modulation doping, resulting in a vanishing Rashba spin-orbit field. Nevertheless, some wafers show, at low temperatures, an incomplete asymmetric ionization of the remote donors, also called a frozen asymmetry. Thus, this incomplete electron transfer into the QW yields a partial asymmetric electron density distribution δn, located either in the X-band of the AlAs layer of the SPSL or in the spacer, see figure 5.15. Naturally, this results in a built-in electric field $\mathcal{E}_z = e\delta n/\varepsilon$ (with e the elementary charge and ε the dielectric constant, which is in GaAs: $\varepsilon \approx 13$) and a Rashba spin orbit field $\alpha = 2\pi\alpha_0 e^2 \delta n/\varepsilon$ (with $\alpha_0 = 5.2$ eÅ^2 the Rashba coefficient for GaAs [Win03; Gri12a]). Griesbeck et al. showed that the Rashba SO field is comparable to the Dresselhaus SO field at low temperatures [Gri12a].

Moreover, besides the mentioned regular Rashba field, there might exist a random Rashba field, which is caused by spatially fluctuating electric fields of the donor ions.

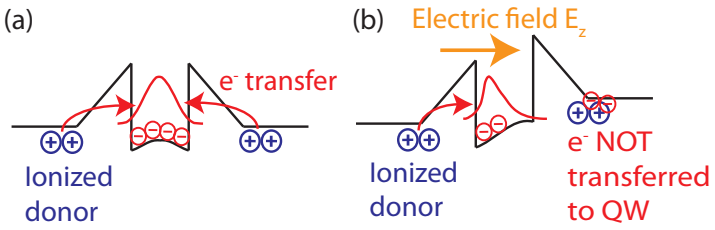

Figure 5.15: *(a) A symmetric band edge profile results from a complete ionization of the donors. (b) An incomplete transfer of the electrons to the QW yields a asymmetric potential curve, and a built-in electric field E_z. Taken from [Gri12b].*

The granular structure of the doping and an incomplete screening in the SPSL are causing this fluctuations. The spin dephasing rate due to such a random Rashba field is given by [She03; Gla10; Gri12a]:

$$\Gamma = \frac{16\pi}{\hbar^3} \frac{m^* e^2 \alpha_0^2 n_d k_F}{\varepsilon^2 R_d}. \tag{5.12}$$

Here, n_d is the donor density, and R_d is the distance from the 2DES to the dopant layer (see figure 5.3 for an estimate).

With increasing temperature, as the dopant layers become fully ionized, the frozen asymmetry disappears, leading to a vanishing regular Rashba field. Furthermore there occurs, with increasing temperature, a charge redistribution of itinerant electrons as well as electrons in the vicinity of the dopants, which results in a reduction of the random Rashba fields [Rös10; Gri12a]. Hence, the spin lifetime increases with rising temperature.

According to equations 2.32, 5.11 the microscopic scattering time and the effective SO field determine the spin dephasing in the DP-mechanism. These values depend also on the temperature. Although the temperature depicted in figure 5.14 is the value given by the temperature sensor in the cryostat, in the discussion the electron temperature is important. As shown in the PL measurements, this temperature may exceed the lattice temperature owing to the weak electron-lattice coupling in the high-mobility samples. In such high-mobility quantum wells, the electron-electron scattering, which depends on the temperature and the electron-density, limits the microscopic scattering time. This scattering mechanism is discussed in chapter 2.3.1 and given by equation 2.51:

$$\frac{1}{\tau_{ee}} \approx 3.4 \frac{E_F}{\hbar} \left(\frac{k_B T}{E_F} \right)^2 \propto T^2 n_e^{-1}. \tag{5.13}$$

Thus, $1/\tau_{ee}$ increases with the temperature ($E_F \propto n$ increases merely by a factor 2, see figure 5.7) [14]. The scattering on remote ionized impurities (AlGaAs), the scattering on residual ionized impurities (background impurities, GaAs), and the scattering on the interfaces are temperature-independent in the limit of low temperatures < 50 K [Wal84]. They do, however, depend on the carrier density, which rises at increasing temperature, see figure 5.7, yielding a reduced momentum scattering time. Additionally, the Fermi wave vector $k_F = \sqrt{2\pi n_e}$ increases with the carrier density. Since both, the Rashba as well as the Dresselhaus spin-orbit field, are linear in k (within the k-linear approximation), the change in the microscopic scattering time may be balanced, especially for the in-plane component, where both SO fields are effective. Another effect to consider is the so-called Thomas-Fermi or Coulomb screening. Here, a high electron

[14] A means to determine the electron-electron scattering rate is by four wave mixing [Kim92], or by transport measurements [Slu96].

density reduces the Coulomb scattering potential seen by an individual carrier, and therefore the momentum as well as the electron-electron scattering times increase for rising electron density.

These facts may also contribute to the explanation of the increase of the spin lifetime for rising excitation-density displayed in figure 5.13. Besides the increased scattering owing to photogenerated holes, a local increase of the electron gas temperature due to rising excitation-density was stated as a reason for the rising spin lifetime.

For sample QWC, the observed values, at 4 K and a excitation density of 0.27 W/cm^2, differ in the measurements displayed in figures 5.13 (b) and 5.14 (b). This is attributed to a less efficient thermal contact in the excitation-density measurement (figure 5.13 (b)), which yields a higher spin lifetime.

Above 30 K, the BAP mechanism dominates again in sample QWC, resulting in a decrease of the spin lifetime for rising temperature, figure 5.14 (b). This is just as in samples QWA and QWB, see figure 5.14 (a), where the spin lifetime reduces to only a few ns in a range up to 40 K.

The experimental results here confirm the theoretical predictions of Zhou et al. concerning the BAP [Zho08; Zho09; Wu10]. The authors approach is the fully microscopic kinetic spin Bloch equation (KSBE), which gives more accurate results, especially at low temperatures, compared to previous calculations e.g. of Maialle et al. who used Fermis golden rule with an elastic scattering approximation to calculate spin dephasing [Mai96]. The KSBE were constructed using the nonequilibrium Green function method:

$$\partial_t \hat{\varrho}_{\boldsymbol{k}} = \partial_t \hat{\varrho}_{\boldsymbol{k}}|_{coh} + \partial_t \hat{\varrho}_{\boldsymbol{k}}|_{scat}. \tag{5.14}$$

$\hat{\varrho}_{\boldsymbol{k}}$ represent the electron single-particle density matrix with a two dimensional momentum $\boldsymbol{k} = k_x, k_y$, whose diagonal elements give the electron distribution function, and the off-diagonal terms the spin coherence. Those coherence terms describe the electron spin precession due to spin orbit fields and the Hartree-Fock-Coulomb interaction. The scattering term consists of electron-impurity, electron-phonon, electron-electron Coulomb, electron-hole Coulomb and electron-hole exchange scatterings. A numerical solution of the KSBEs then yields the dependencies on the parameters. According to the calculations of Zhou et al., the Pauli blocking is an important factor in the BAP dephasing for degenerate electron gases, because it suppresses scattering at low temperatures. The scattering takes place around the Fermi disc. Since the Pauli principle prevents multiple occupation of electron states (Pauli blocking), and the smearing out of the Fermi energy is small at low temperatures, fewer states are available for scattering. Thus, scattering is suppressed at low temperatures. For nondegenerate systems (high T or small carrier densities) the Pauli blocking is weak and a Fermi golden rule approach is valid.

By solving equation 5.14 numerically, Zhou et al. showed that the spin lifetime in a BAP-dominated regime decreases with rising temperature [Zho08; Zho09; Wu10]. With rising temperature, the Pauli blocking is reduced, electrons and holes have also a higher momentum and therefore higher scattering rates. Thus, the spin lifetime reduces as depicted in figure 5.14 (a) for samples QWA and QWB and in sample QWC for temperatures above 30 K in figure 5.14 (b). For sample QWA, it was also shown that the carrier lifetime increases with the temperature, see figure 5.8. This implicates a larger hole density with growing temperature and more BAP dephasing.

The fact that in sample QWC, above 30 K, the BAP dominates may be substantiated by examining the excitation-density dependence at high temperatures. Indeed, the same behavior is found in sample QWC at 40 K, as in samples QWA and QWB at low temperatures, see figure 5.16 and compare to figures 5.11 (b) and 5.11 (b). Using the fitting function according to equation 5.5 yields $I_0 = 7.75 \pm 2.8$ W/cm^2. The quite high spin lifetimes of sample QWC in this temperature range compared to sample QWA may

be attributed due to the different electron temperatures. In sample QWA, the electron temperature is about a factor 1.5 higher than the lattice temperature, whereas in sample QWC, electron temperature and lattice temperature are about the same in this higher temperature range.

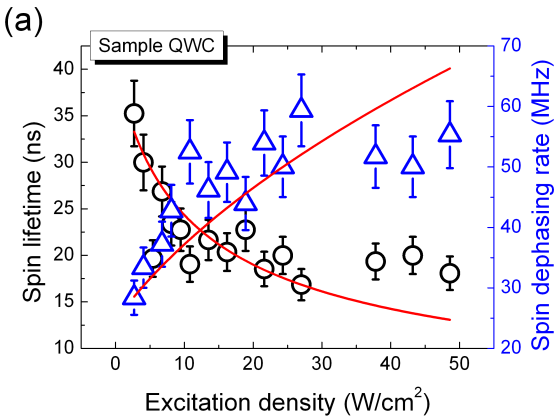

Figure 5.16: *For high temperatures (40 K), the BAP mechanism dominates the spin dephasing in sample QWC. The typical square-root like behavior is therefore found in the dependence of the spin dephasing rate and the spin lifetime.*

Concerning the temperature dependence in (110)-grown quantum wells, Döhrmann et al. reported an increase of the spin lifetime in a temperature range between 4 K and 100 K [Döh04]. They investigated a MQW structure (10×20 nm wide QW) with an electron density of $n = 1.1 \cdot 10^{11}$ cm^{-2}. As a reason for the increase with the temperature, they invoked a break of the spatial correlation between electron and hole wave function. At first glance this might contradict the results presented here. Owing to the lower electron density, in the work of Döhrmann et al., however, most likely excitonic spin relaxation due to BAP, described e.g. in [Mai96], is present, whereas in the samples here spin flip scattering of free electrons with unpolarized holes is present.

Further influences on the spin lifetime

A direct comparison of the spin lifetimes between the samples used here, having a well width of 30 nm and 20 nm, is impeded by the different carrier densities, carrier lifetimes [15], and the different effective dephasing mechanisms, because of the band symmetry.

Considering the dependence of the spin lifetime on the quantum well width, Zhou et al. stated that the electron-hole exchange strength is weakened by a form factor in the scattering matrix elements in the BAP mechanism for wider quantum wells [Zho08]. Interestingly, they compared the DP and the BAP mechanism in a (100)-grown quantum well. In this case, the DP mechanism is not suppressed in contrast to the (110)-grown QW discussed here. The Dresselhaus term also depends inversely on the well width. By increasing the QW width, the spin lifetimes become, therefore, larger due to BAP as well as DP mechanism. The variation of τ_{DP}, however, is larger than τ_{BAP}, yielding a more important influence of the BAP for wider QWs.

Next the excitation energy dependence of the spin lifetime is examined. Starting from high excitation energies or low excitation wavelengths, the spin lifetime drops if the excitation wavelength approaches 800 nm at a temperature of 4 K, see figure 5.17 (a). For samples QWA and QWB (not shown) the difference is more than a factor two. Whereas for sample QWC the spin lifetime changes only slightly with the excitation wavelength. This may be attributed to rising absorption in the substrate for these wavelengths, which may be seen more in samples with wider quantum well

[15] TRPL measurements show that the carrier lifetime in sample QWC (figure 5.8) is higher than in QWA, yielding a higher hole density and a stronger BAP.

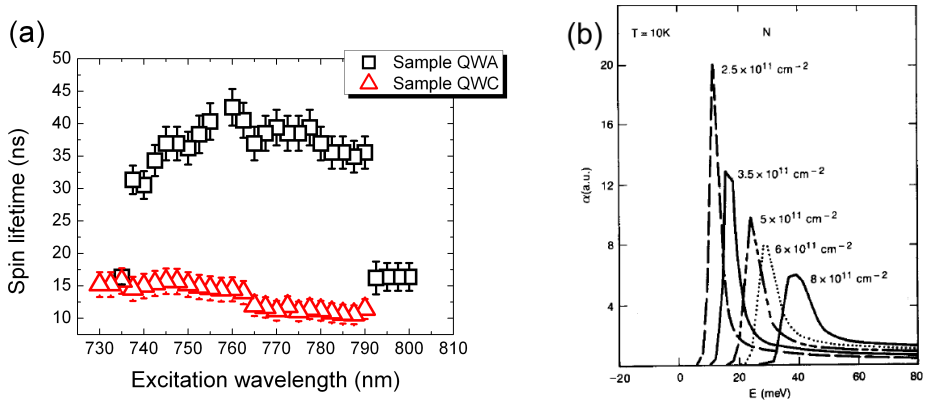

Figure 5.17: *(a) Dependence of the spin lifetimes on the excitation wavelength of samples QWA and QWC, measured with an excitation-density of* 0.27 *W/cm*^{2}*. (b) Calculated absorption coefficient in a n-GaAs/AlGaAs MQW (QW width* 12 *nm) as a function of the carrier concentration by Livescu et al. [Liv88].*

width, since the probing on the lowest subband is closer to the bulk. Because of the increased absorption, the sample heats up, which reduces the spin lifetime. Moreover, it is possible that a part of the detected Kerr signal originates from a spin orientation in the substrate.

As already stated, for all experiments, a wavelength of 760 nm is chosen, where high spin lifetimes are achieved. This nonresonant excitation creates spin-polarized electron hole pairs in the QW with an excess electron energy of about 100 meV, depending on the QW width and the sample temperature. The lower values for the spin lifetime in sample QWA, as previously published in [Völ11], are caused by the wavelength dependence of the spin lifetime. Here, only an excitation wavelength of about 799 nm was available, yielding an excess energy of the electron-hole pairs of about 25 meV.

So far, it is not clear why the range of the excitation density, in which spin dynamics is observed, differs for the samples, compare figures 5.11, 5.12, and 5.13. Obviously they do differ in the absorption. It seems that sample QWC has the lowest absorption, which could result from spatially indirect transitions due to the asymmetric potential at low temperatures. A comparison of the excitation density dependence in samples QWA and QWB shows a higher absorption in sample QWB. Since both samples have a symmetric band structure, the absorption should be higher in sample QWA, which has a smaller electron density. The absorption should be lower for larger electron densities, since with rising density the phase space occupation as well as exchange effects such as screening increase [SR89; Liv88]. Many-body calculations for modulation-doped MQW (QW width: 12 nm) by Livescu et al. showed such a behavior for resonant excitation displayed in figure 5.17 (b) [Liv88]. For higher excess energies, however, the absorption seems to be slightly lower for smaller carrier densities, and does not change with the temperature. But this was not discussed explicitly in this publication.

The matrix element of the allowed interband transitions is proportional to the joint density of states, which is constant within a subband in the 2D case [Gru06]. Thus, by varying the excess energy, the absorption should change when hitting the next subband. This could not be resolved in the wavelength-dependent Hanle measurements displayed in figure 5.17 (a).

Finally, the lower absorption in the sample has a positive effect on the Hanle signal. It allows operating with higher intensities, which means that the experiment is less susceptible to exterior influence. Hence, the lower absorption and the fact that the probing energy is further away from the bulk energy result in a higher Hanle signal for

sample QWC compared to samples QWA and QWB. A lock-in signal higher by two to three orders of magnitude was obtained in sample QWC.

Effect of above-barrier illumination on the spin lifetime

Another parameter that can be modified is the carrier density, by using above-barrier illumination, see chapter 3.4 for details. The behavior of the spin lifetime on the optical gating depends on the dominating spin dephasing mechanism. Due to the generation of electron-hole pairs in the barrier by above-barrier illumination, the donor electrons are redistributed. According to the potential structure formed by modulation doping, the optically created holes move towards the QW, whereas the electrons shift towards the doping layer, and eventually tunnel back into the QW, see figure 3.7. The surplus of holes in the QW results in a reduction of the carrier density due to recombination. In a steady state, the electron density in the QW may be modulated by the intensity of the above-barrier illumination according to equation 3.19. For this so-called optical gating a green diode pumped solid-state laser (532 nm) is used, in a way that the whole sample is illuminated. The photon energy of $E_{green} \approx 2.3$ eV exceeds the band gap energy of the AlGaAs barrier $E_{g,AlGaAs} \approx 1.83$ eV. Since the setup only allows a quite flat angle of the illumination, the actual intensity of the green light may not be determined. Hence, in the following only the laser power is stated. It is quite possible that the actual intensity in the various experiments differ. Similar to the excitation-dependence, a linear dependence of the hole density to green illumination is assumed.

PL measurements allow a direct observation of the reduction of the carrier density. In figure 5.18 (a), the change of the PL spectra under above-barrier illumination is depicted for sample QWA.

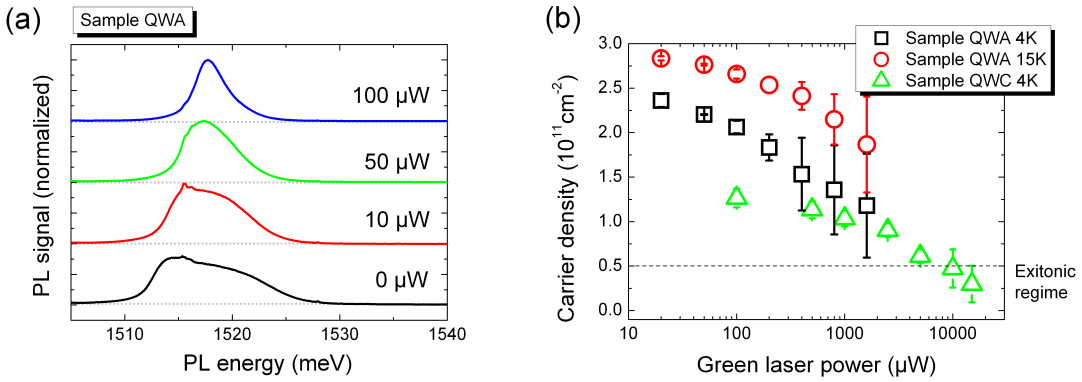

Figure 5.18: ***(a)*** *The PL spectra change from the typical shark-fin like shape at zero green illumination to a narrow peak at high illumination, implicating a reduced carrier density.* ***(b)*** *Dependence of the carrier density on the above-barrier illumination.*

Without the optical gating, the PL shows the typical shark-fin-like shape, and the PL width decreases with increasing green laser power. According to chapter 3.3, since the width of the PL peak corresponds to transitions from the conduction band minimum up to the Fermi energy of the 2DES, the carrier density may be determined from it. Figure 5.18 (b) displays the carrier densities with respect to the green laser power for samples QWA and QWC. The measurements of sample QWA have been conducted by S. Loibl, also found in [Gri12b]. In sample QWC, the carrier density approaches the excitonic regime for high green illumination. In this regime the values of the carrier density, obtained by the PL method, are not reliable anymore. In order to observe a noticeable effect in sample QWC higher green laser powers than in samples QWA and

QWB are necessary. The previously discussed difference in the absorption might be an explanation for this.

In order to study the effect of optical gating, Hanle measurements are conducted with a fixed excitation density and sample temperature, for varying green illumination. RSA measurements (not shown) demonstrate, that the electron g-factor changes up to 5% in the range of carrier densities that can be accessed by optical gating [16]. This change is neglected in the following measurements. In sample QWA, where the BAP mechanism dominates, the spin lifetime drops with rising above-barrier illumination, see figure 5.19 (a). Optical gating yields a more effective BAP mechanism due to increased electron-

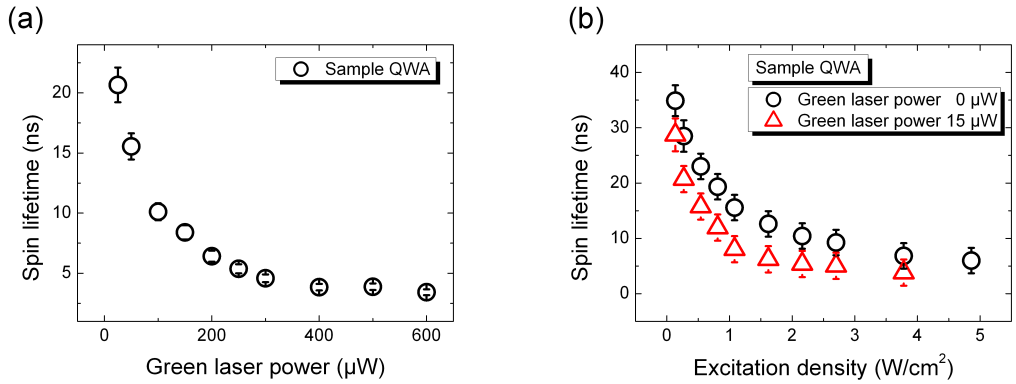

Figure 5.19: *(a) The spin lifetime drops with the green laser power in the BAP-dominated sample QWA. The measurement was taken at* 18 *K with an excitation density of* 0.27 *W/cm*^{2}*. (b) Due to the enhanced BAP mechanism, the spin lifetime drops faster with green illumination in an excitation density dependence measurement at* 10 *K for sample QWA.*

hole scattering. This is a result by the surplus of holes, analog to the discussion of the excitation-dependence (see equations 2.42, 5.2, 5.4), and because of the reduced electron density, which lowers the Coulomb screening of the photogenerated holes. Additionally, the Pauli blocking, which suppresses the scattering weakens for lower electron density [Zho09]. As described in chapter 5.2.3, the spin polarization first increases with rising green laser power, since resident unpolarized electrons recombine with the additional holes. At about 250 μW the spin polarization saturates and decreases slightly, see figure 5.29. This comes from more probable recombination of spin-polarized electrons with the photogenerated holes, which is attributed to the decreasing of the ratio of resident electrons to photogenerated holes. Concerning the spin lifetime, this effect is, however, negligible compared to the BAP mechanism. The increased BAP mechanism becomes visible as well, if the optical gating is combined with a variation of the excitation density. As depicted in figure 5.19 (b), a more effective decay of the spin lifetime is observed with an additional above-barrier illumination of 15 μW.

In contrast to sample QWA, in sample QWC, at low temperatures, where the DP mechanism dominates, the spin lifetime increases with rising green laser power, see figure 5.20 (a). As already discussed, regarding the temperature dependence, a reduction of the carrier density implies a change of the SO fields as well as the microscopic scattering time, which results in a modification of the spin lifetime according to equations 2.32 and 5.11. Reducing the carrier density results in a smaller Fermi energy and Fermi

[16] The nonparabolicity of the CB becomes more important the higher the Fermi energy lies in the CB. Moreover, a higher Fermi energy yields a stronger penetration of the wave function in the barrier material. Overall a decrease in the carrier density leads to an increase in the absolute value of the g-factor.

wave vektor $k_F = \sqrt{2\pi n_e}$. Thus, Rashba and Dresselhaus SO fields decrease, since they are linear in $\boldsymbol{k}$. The Thomas-Fermi screening decreases as well for lower electron densities, yielding reduced momentum scattering times. Furthermore, the electron-electron scattering also depends on the carrier density according to equation 2.51, 5.13, yielding shorter scattering times for lower densities [17].

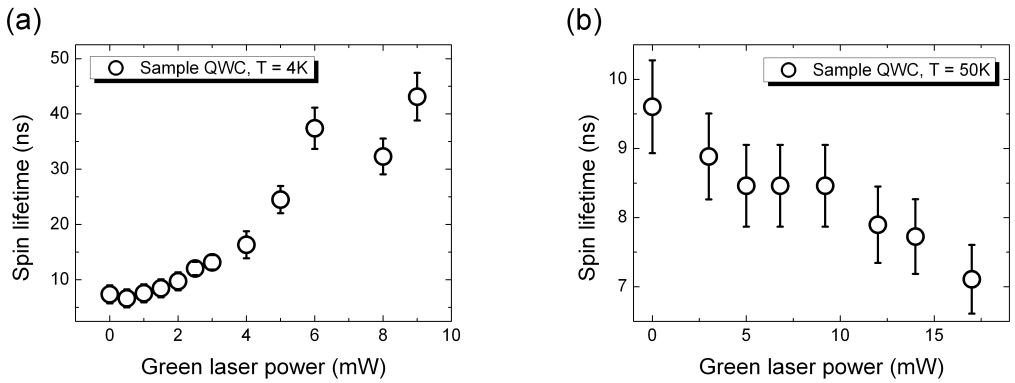

Figure 5.20: ***(a)*** *At low temperatures (4 K), the DP dephasing dominates in sample QWC, therefore the spin lifetime increases with the green illumination. The excitation density was* 0.54 W/cm^2. ***(b)*** *At high temperatures (50 K) the BAP dephasing dominates and the spin lifetime decreases for rising above-barrier illumination. The excitation density was also* 0.54 W/cm^2.

Griesbeck et al. found an increase in the spin lifetime for rising above-barrier illumination as well. A maximal out-of plane spin lifetime of 248 ns could be determined [Gri12a; Gri12b]. They also found an increase of the ratio between Dresselhaus and Rashba contribution, which implies an increase of the symmetry of the structure [Gri12b]. This can be understood as follows: the intensity of the above-barrier light decreases exponentially within the sample, according to the Lambert-Beer absorption law $I_{532nm}(z) \propto \exp(-\tilde{\alpha}_{ab} z)$ (z is the distance from the surface, $\tilde{\alpha}_{ab}$ is the absorption coefficient). Thus, the number of electron hole pairs created differ for the areas above and below the quantum well, yielding an asymmetric electron transfer and a change in the band symmetry. Assuming an initial asymmetry in the form as depicted in figure 5.21, the initial asymmetry may be canceled out partially with an increase of the green illumination power, which also implies a growth of the spin lifetime.

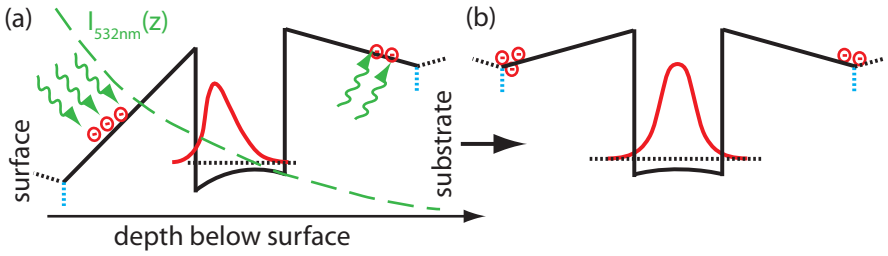

Figure 5.21: ***(a)*** *An initial asymmetry due to incomplete donor ionization may be canceled by above-barrier illumination because of unequal creation of electron-hole pairs above and below the quantum well. Resulting ideally in a symmetric band profile:* ***(b)***. *Taken from [Gri12b].*

[17] This may be understood as: In the scattering processes, only states around the Fermi disc are involved, and for rising electron density the circumference increases linearly whereas the area increases quadratically. Hence, comparatively less electrons may scatter for higher densities.

As already mentioned, the dominant spin dephasing mechanism changes in sample QWC from DP dephasing to BAP dephasing, at temperatures above 30 K. Thus, the spin lifetime should decrease at high temperatures with rising green laser power in sample QWC according to the BAP mechanism. Indeed, this behavior was found, as depicted in figure 5.20 (b), and a clear decrease of the spin dephasing time can be observed at a temperature of 50 K, when the intensity of the above-barrier illumination is increased.

5.2.3 Spin polarization in (110)-grown quantum wells

This section investigates the dependence of the spin polarization in regard to external parameters. Due to nonresonant excitation with circularly polarized light, spin-polarized electron-hole pairs are created. The holes usually lose their spin orientation during momentum relaxation, which results in an electron spin polarization in the CB, since the energy relaxation in the CB is spin-conserving [Pfa05]. Ideally in a QW, a spin polarization of 100% can be achieved, because of VB-mixing the spin polarization degree is, however, significantly lower. The degree of spin polarization in the sample is determined by investigating the circular polarization degree of the PL in backscattering geometry. This method gives a value for the absolute spin polarization degree, in contrast to the Hanle-MOKE measurements, which give a Kerr rotation angle proportional to the time-averaged spin polarization. Naturally, the spin polarization may change with the excitation wavelength, owing to the VB mixing. Hence, for the PL measurements the same fixed excitation wavelength of 760 nm as in the Hanle measurements is used.

At zero temperature and without an external magnetic field, in a 2DES all available states from $\boldsymbol{k} = 0$ up to $\boldsymbol{k_F}$ are occupied equally by spin-up and spin-down states. States above the Fermi energy are unoccupied. Additional spin-polarized electrons above the Fermi energy yield a spin polarization of the system. Finite temperatures cause a softening of the Fermi-Dirac function in the region around the Fermi energy. Thus, an occupation with a spin imbalance is also allowed below the Fermi energy. Such a behavior was observed in highly-doped n-bulk GaAs [Dzh02]. The helicity-resolved PL traces, at 4 K, depicted in figure 5.22 (a) for sample QWA and for sample QWC in figure 5.23 (a), clearly show differences for co- and contra-circular excitation. For co-circular excitation and detection the high-energy trail exposes a larger PL signal.

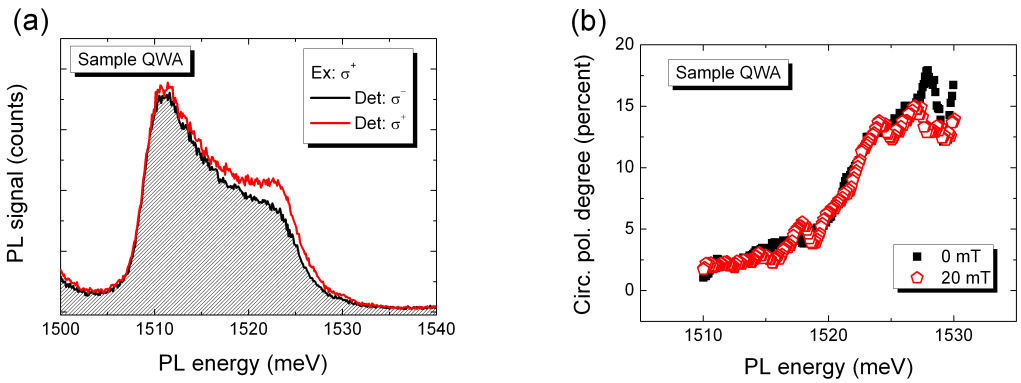

Figure 5.22: *(a) PL spectra of sample QWA measured for co- and contracircular helicity of excitation laser and detection.* ***(b)*** *Circular polarization degree, calculated from the high-energy tail of the PL traces, with respect to the PL energy $P(E)$, with and without an external magnetic field, in sample QWA. In order to reduce noise effects adjacent neighbor value averaging has been conducted.*

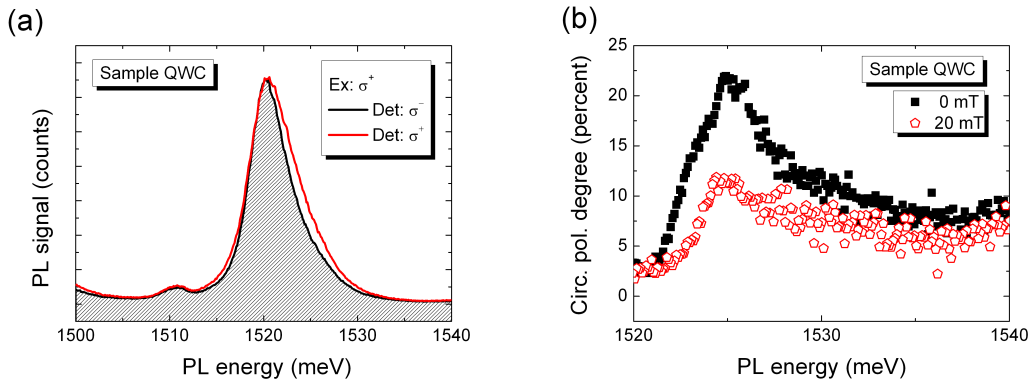

Figure 5.23: ***(a)*** *PL spectra of sample QWC measured for co- and contracircular helicity of excitation laser and detection.* ***(b)*** *Circular polarization degree, calculated from the high-energy trail of the PL traces, with respect to the PL energy $P(E)$, with and without an external magnetic field, in sample QWC.*

From these spectra, the circular polarization degree $P(E)$ may be calculated using equation 3.17. This is depicted in figures 5.22 (b) and 5.23 (b) for samples QWA and QWC, respectively. A maximal value for $P(E)$ of $\sim 22\%$ in sample QWC and $\sim 17.5\%$ in sample QWA was obtained. In comparison an initial spin polarization degree for optically oriented electrons of about 30 percent was observed in an undoped 20 nm wide QW, for similar excess energies [Pfa05]. This higher value is attributed to the absence of Pauli blockade in an undoped sample.

An external magnetic field causes precession of the electron spins and therefore a depolarization of the PL. The circular polarization degree in the case of an applied magnetic field of 20 mT is depicted in figures 5.22 (b) and 5.23 (b), as well. Only a slight change in the circular polarization is visible for this magnetic field. By contrast, in Hanle-MOKE measurements of the same samples, under comparable experimental conditions, no residual MOKE signal, corresponding to a time-averaged spin polarization, is observed for this magnetic field value. In these samples, the spin lifetime (chapter 5.2.2) exceeds the carrier lifetime (chapter 5.2.1, figure 5.8) significantly. The short effective carrier lifetime limits the depolarization due to the precession in the external field, yielding a high spin polarization. Inserting the carrier lifetimes at 4 K, determined in time-resolved PL measurements, as shown in figure 5.8, into equation 3.6 (with the g-factors from figure 5.9) the magnetic field corresponding to the HWHM of a Hanle curve can be calculated. In sample QWA, a carrier lifetime of 375 ps was observed, yielding a halfwidth of 80 mT, and in sample QWC a carrier lifetime of 619 ps was found, which gives a halfwidth of 55 mT. The impact of the longer carrier lifetime in sample QWC is a more noticeable change in the $P(E)$ for the same field, compare with figures 5.22 (b) and 5.23 (b). In conclusion, according to these observations, Hanle measurements based on analyzing the depolarization of the PL are unsuitable to accurately determine long spin lifetimes in samples such as presented here.

Analog to equations 2.28 - 2.30, the dynamics of an electron spin ensemble in an external magnetic field is described by a kinetic equation:

$$\frac{dS_\alpha}{dt} = G_\alpha - (\boldsymbol{S} \times \boldsymbol{\Omega})_\alpha - \sum_\beta S_\beta / \tau_{\alpha\beta}. \tag{5.15}$$

Here Ω is the Larmor frequency, and $\tau_{\alpha\beta}$ are the components of the spin-decay-rate tensor. The generation rate is proportional to the excitation density, $G \propto I$. As in the discussion in section 5.2.2, diffusion effects are neglected in the following. In the case

of zero magnetic field, and in steady-state equation 5.15 reduces, and the out-of-plane spin-density S_z is given by:

$$S_z = G_z \tau_z. \tag{5.16}$$

The out-of-plane spin lifetime is given by equation 5.1 in section 5.2.2, yielding:

$$S_z\left(0\right) = \frac{G_z}{1/\tau_z^{lim} + \left(\gamma_z^{BAP} + \gamma^r\right) N_h}. \tag{5.17}$$

The spin polarization at zero magnetic field $S_z(0)$ may be extracted from the amplitude of the Hanle curves at zero field and using equation 3.5. With the assumptions from section 5.2.2 follows $N_h \propto I$ and with $G_z \propto I$ the spin polarization obtained by the Hanle curves may be fitted with:

$$S_z\left(0\right) = \frac{I}{1 + I/I_0}. \tag{5.18}$$

The Hanle-MOKE measurements presented in chapter 5.2.2 are now evaluated concerning spin polarization. In figure 5.24 (a), Hanle curves are depicted from sample QWA at 4 K, for increasing excitation density. These were already used to extract spin lifetimes, depicted above in figure 5.11. From figures 5.24 (b) and 5.25 (a) the expected saturation of the spin polarization, according to the model introduced in equation 5.17, can be seen for the BAP-dominated samples QWA and QWB. Due to the linear behavior of the hole

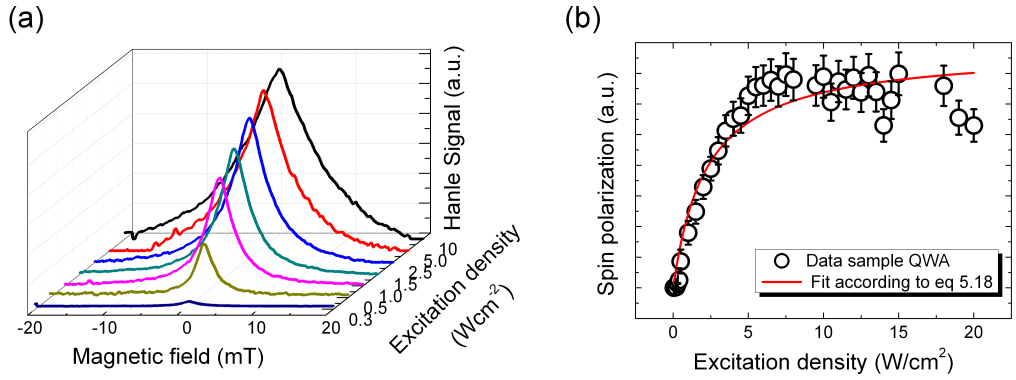

Figure 5.24: ***(a)*** *Hanle curves for increasing density at 4 K. Whereas the width behaves according to equations 5.4, 5.5 the spin polarization saturates according to equation 5.17 depicted in* ***(b)****. Using equation 5.18 the behavior could be fitted.*

density with the excitation-density, generation and dephasing are balanced, yielding a constant spin polarization. The behavior in figures 5.24 (b) and 5.25 (a) could be fitted using function 5.18 and the same I_0 values as used in chapter 5.2.2 in figures 5.11 (b), and 5.12 (b) for samples QWA and QWB, respectively.

In sample QWC in the DP-dominated regime, the spin polarization increases linearly up to $\sim$ 15 K. In this range the lifetime rises as well, due to increased scattering caused by the additional holes and local heating effects. A linear increase of the excitation density simply yields an increase in the number of spin-polarized electrons in the CB. The saturation observed for high excitation densities may be attributed to local heating, which aids the ionization of remote dopants. The additional unpolarized electrons balance the additional spin-polarized electrons (see equation 2.6) yielding a constant spin polarization, see figure 5.25 (b). For high temperatures, where the BAP dephasing dominates, the spin polarization saturates according to the described model, see figure 5.25 (b).

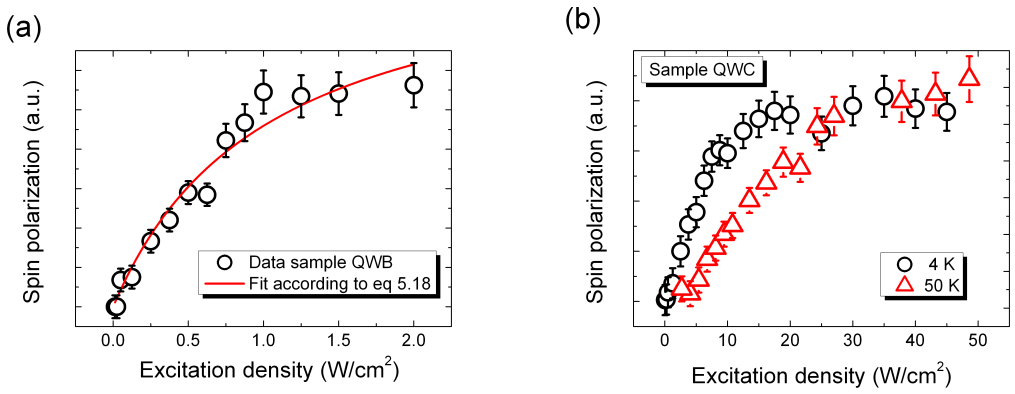

Figure 5.25: ***(a)*** *The spin polarization in sample QWB, at 4 K, saturates according to equations 5.17, 5.18* ***(b)*** *In sample QWC,in which the DP mechanism dominates at 4 K, the spin polarization rises at first due to additional spin-polarized electrons in the CB. Later, due to local heating the increase of spin polarized carriers is balanced by an increase of unpolarized carriers. At 50 K the spin polarization saturates as well due to the dominating BAP dephasing mechanism.*

By averaging the circular polarization degree in the PL measurements, (figures 5.22 (b), 5.23 (b)) over the spectral linewidth an averaged spin polarization degree may be obtained. In figure 5.26 (a) this degree is depicted as a function of the excitation energy. For sample QWA, a saturation of the spin polarization is visible similar to the results from the Hanle measurements in figure 5.24. Optical excitation with circularly polarized light allows a transfer of spin polarization from the photocarriers to the resident carriers. The MOKE signal is proportional to the time-averaged spin polarization of the resident electrons. The optically generated holes cause a reduction of the spin polarization due to BAP dephasing and the recombination of spin-polarized electrons according to equation 5.17. The saturation of the spin polarization in the PL measurement, however, occurs at considerably higher excitation densities. In principle the same behavior in the PL and the Hanle-MOKE measurement is expected. Since the recombination, however, occurs around the Γ-point where the electron polarization is small, the average spin polarization for weak excitation is too small to be observed. Figure 5.26 (b) shows a series of PL spectra of sample QWA measured for different excitation densities. Optically generated holes relax to the VB maximum during the photocarrier lifetime, and recombine with electrons close to the Γ-point, which are not spin polarized. Hence, for excitation densities the PL emission is dominated by the low-energy peak. For higher excitation-density values the optically generated holes also occupy VB-states with larger k-values and in the PL spectra a pronounced high energy shoulder appears. The electrons involved in the recombination at larger k-values carry a spin polarization. Thus, depending on the excitation density, different subsets of the 2DES are probed in PL experiments. The circular polarization degree, averaged over the spectral linewidth of the PL emission, which is displayed in figure 5.26, increases for rising excitation densities, where spin-polarized electrons start to contribute to the PL signal, and saturates for larger values of the excitation density. The fact that the PL-based measurements depends also on the hole distribution function indicates that these measurements are not suitable for a complete investigation of the spin dynamics in samples with long spin lifetimes. Furthermore, due to the lower carrier density the spin polarization degree in sample QWC is higher than in sample QWA, as depicted in figures 5.26 (b) and 5.27.

Figure 5.27 (b) shows the decrease of the averaged spin polarization degree for rising

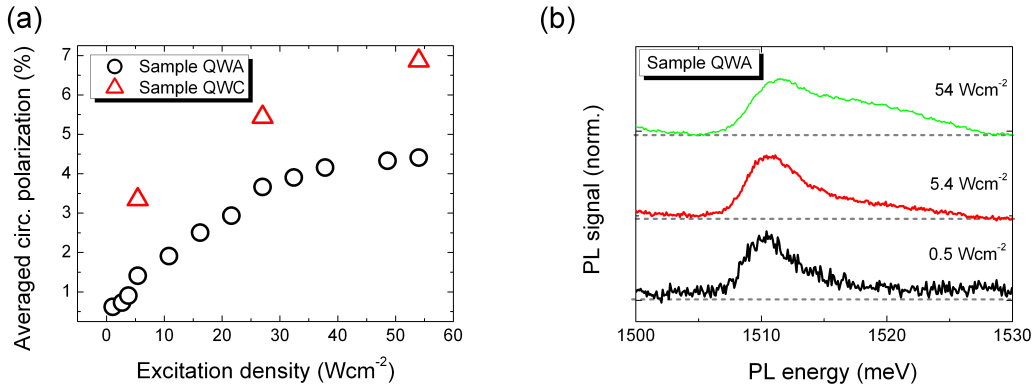

Figure 5.26: *(a) The averaged spin polarization degree saturates rises for increasing excitation density since more and more spin polarized electrons recombine. Given that only PL due to recombination of electrons close to the Fermi energy yields a circular polarization, higher excitation density values are necessary to observe the increase of the spin polarization, compared to the Hanle-MOKE measurements. The temperature was 4 K.* ***(b)*** *PL spectra as a function of the excitation density.*

temperature. For increasing temperature the carrier density increases, as depicted in figure 5.7. In k space, the area of the Fermi disc grows proportionally to the carrier density n, while the circumference of the Fermi disc, and the corresponding area around the Fermi energy, grows as $\sqrt{n}$. Hence, the average spin polarization degree, given by the area ratio of the Fermi disc and its edge region decreases with increasing n, according to equation 2.6.

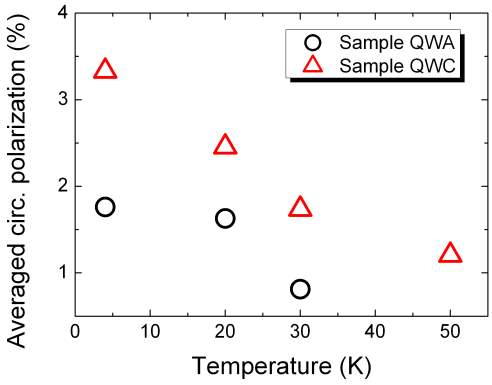

Figure 5.27: *The spin polarization drops with increasing temperature. Here the excitation density was 10 W/cm^2.*

The temperature dependence of the spin polarization obtained by the Hanle-MOKE technique is depicted in figure 5.28 (a) for samples QWA and QWB and in figure 5.28 (b) for sample QWC.

Since with MOKE only the "number" of spin polarized electrons is detected, not the ratio between spin polarized and unpolarized carriers as in the spin resolved PL measurements, the arguments stated before for the temperature dependence, concerning the ratio between the area of the Fermi disc and its circumferences are not valid here. In all samples the spin polarization drops with increasing temperature. In the BAP dominated regime present in samples QWA, QWB and in sample QWC above 20 K the observed reduction of the spin polarization with rising temperature has its reason in the reduction of the spin lifetime as displayed in figures 5.14 (a) and (b). The drop of the spin polarization in the DP dominated regime is puzzling and no explanation has been found so far. In this region the spin lifetime increases due to a more symmetric band profile

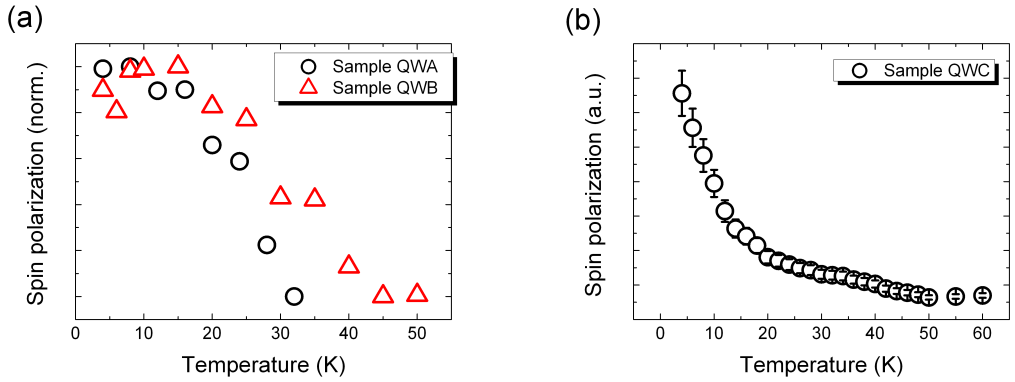

Figure 5.28: *(a) With rising temperature the spin lifetime drops and so does the spin polarization. The excitation density for sample QWA was* 0.27 *W/cm*^{2} *and for sample QWB* 0.54 *W/cm*^{2}*. (b) In the range above* 20 *K the BAP mechanism dominated and the drop in the spin polarization is explained by the reduced spin lifetime. For the drop of the spin polarization in the range between* 4 *K and* 20 *K no explanation exists so far. Here the excitation density was* 0.27 *W/cm*^{2}*.*

and therefore a decreasing Rashba SO-field with increasing temperature. A presumptive explanation would be a change in the absorption with higher temperature. Interestingly the spin-resolved PL measurement as well as the Hanle-MOKE measurement show a decrease of the spin polarization with rising temperature.

Effect of above-barrier illumination on the spin polarization

Finally, the dependence of the spin polarization, extracted from the Hanle curves, from above-barrier illumination is investigated. Figures 5.29 (a) and (b) depict these dependence for samples QWA (4 K) and QWC (4 K, 50 K). In sample QWA, the spin

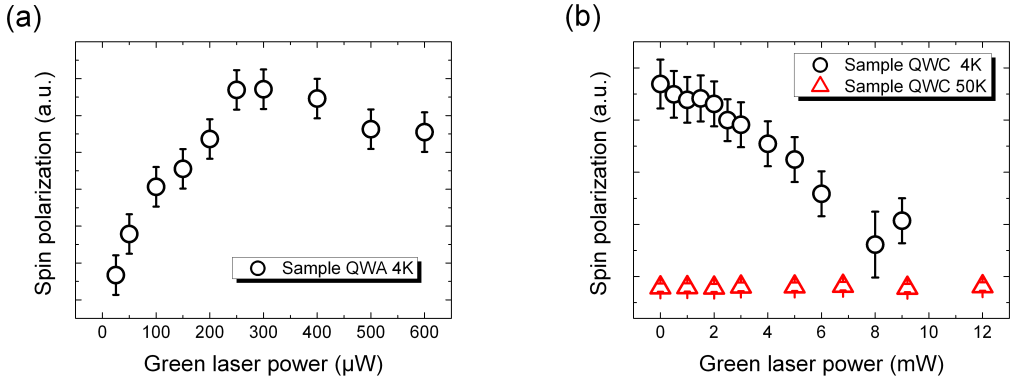

Figure 5.29: ***(a)****An increase of the spin polarization can be observed in sample QWA at* 4 *K, attributed to the decrease of the carrier density. For higher powers, recombination of spin polarized electrons is more probable, which results in a drop of the spin polarization. The excitation-density was* 0.27 *W/cm*^{2}*. (b) Recombination of spin polarized and unpolarized electrons reduces the spin polarization for rising green illumination in sample QWC at* 4 *K. At low temperatures no significant change of the spin polarization with the green illumination is visible. The excitation-density was* 0.54 *W/cm*^{2}*.*

polarization rises at first, since due to the additional holes mostly unpolarized electrons recombine, which results in a higher ratio of spin polarized to unpolarized electrons. For higher above-barrier illumination intensity the recombination of spin polarized elec-

trons becomes more probable yielding a decrease of the spin polarization. Due to the comparatively low carrier density in sample QWC at 4 K, the recombination involves unpolarized as well as spin polarized carriers, causing a reduction of the spin polarization for increasing above-barrier illumination. At high temperatures the carrier density increases because of thermal activation. At these temperatures the BAP mechanism is dominant, and the low spin lifetime results in a small spin polarization. The additional recombination caused by the green illumination, yields no visible effect on the already low spin polarization. The saturation behavior displayed in figure 5.24 can of course be modified by above-barrier illumination (not shown), similar to the dependence of the spin lifetime shown in figure 5.19.

5.3 Spin diffusion in (110)-grown quantum wells

In this section, spin diffusion as a function of experimental parameters is investigated. Spin transport in (110)-grown QW has been investigated by Hu et al.. They found at room temperature a spin diffusion length of 4 μm in MQW (20×8 nm wide QW) using transient spin grating technique [Hu11] [18]. Employing surface acoustic waves, a spin polarization was transported over 60 μm at low temperatures in (110)-grown QW [Cou07; Cou08; HM10]. Moreover, Sih et al. could observe the spin Hall effect in (110)-oriented quantum wells [Sih05].

The optically generated spin-polarized electron-hole pairs diffuse or drift according to equation 2.59. Since the hole spin lifetime is shorter than the recombination time, they also recombine with resident unpolarized electrons, leaving a spin polarization diffusing radially away from the pump spot. As described in chapter 3.2, a three-point Hanle measurement was used to map the spin diffusion for samples QWA and QWC. In order to achieve a spatial resolution, instead of a 50 mm achromatic lens, microscope objectives (10×, 20×) were utilized, yielding larger excitation densities. None of the samples showed an observable difference of the spin diffusion behavior, depending on the crystallographic axis. Provided the in-plane and the out-of-plane spin components relax independently, meaning there is no uniform Rashba field present, no anisotropy in the spin diffusion of the z-component is expected [Gri02]. Hence, in the following there is no distinction between the observed axes. As in the previous measurements, a excitation wavelength of 760 nm was used.

The excitation density dependence of the spin diffusion shows a monotonous decay of the spin polarization for increasing distance between pump and probe spot. By contrast, a local minimum becomes visible at the beam overlap, at higher excitation densities. This minimum becomes more pronounced as the excitation density is increased. In figure 5.30 (a) this behavior is depicted for sample QWA at 4 K, where the spin lifetime is maximal, according to chapter 5.2.2 figure 5.14 (a).

An explanation of such an anomalous spin distribution in the QW plane can be the different diffusion coefficients of electrons and heavy holes. The majority of the optically generated holes are most likely HH, since the average spacing between HH subbands is smaller in (110)-grown QW than in (001)-grown QW and valence-band relaxation is typically fast in comparison to photocarrier recombination. Thus, the two highest VB states at the Γ-point are HH bands followed by the first LH band, see chapter 2.2.6. Nonresonant excitation however, takes place at $\boldsymbol{k} \neq 0$ and due to VB mixing, light holes may be created as well. Compared to the majority HH, the electrons have a smaller

[18] Here, two laser beams with crossed linear polarizations interfere. The light intensity on the sample is uniform, however the polarization alternates between left-polarized, linear and right-polarized. In this way, a grating is created with alternating optical orientation of the electrons across the excitation region. Spin diffusion and spin lifetime can be obtained by analyzing the orientation decay [Cam96].

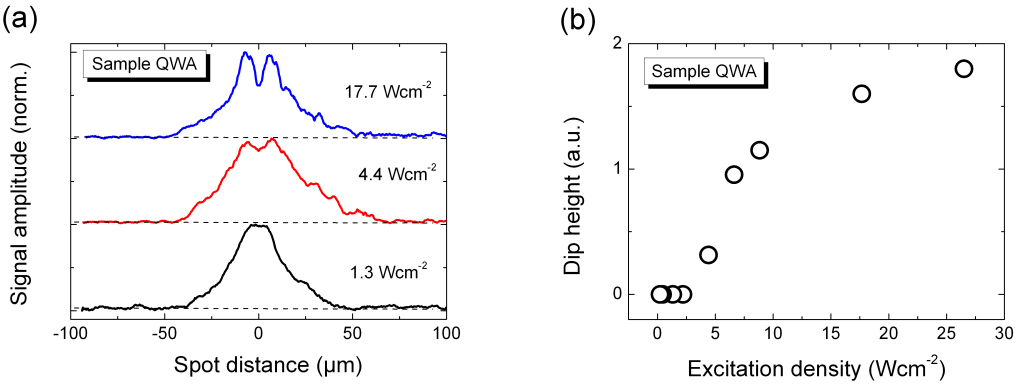

Figure 5.30: ***(a)*** *The spin diffusion profiles show a anomalous spin distribution for high excitation densities, for Sample QWA at a temperature of* 4 *K.* ***(b)*** *With increasing excitation density the difference between the minimum at beam overlap and the maxima on the side increases.*

effective mass, and may therefore diffuse away from the pump spot faster. In the overlap of pump and probe beam the spin dephasing rate is given by BAP dephasing and the recombination rate, see chapter 5.2.2. The electron diffusion is significantly faster in this high-mobility 2DES compared to bulk n-doped GaAs, due to the low concentration of momentum scattering sites and the large Fermi wave vector of the electrons. Hence, at some distance away from the pump spot the hole density is considerably reduced, as the hole diffusion is reduced by recombination with resident carriers and their large effective mass. Consequently, the hole-dependent spin dephasing and recombination processes are suppressed, resulting in an increased electron spin polarization at some distance and a dip in the diffusion profile. At the overlap position, the spin polarization saturates for high excitation densities, according to figure 5.24, due to the presence of optically generated holes. In figure 5.30 (b) the dip height is displayed as a function of the excitation density. The dip becomes visible at excitation densities of about 5 Wcm^{-2}. At this value, the saturation of the spin polarization was observed in figure 5.24. After a steep increase of the dip for rising excitation, the hole density becomes large enough to slow down the growth of the spin polarization in the maxima out side the pump spot, yielding a smaller slope in the increasing dip height.

To study the spatial dependence of the spin lifetime in more details, several Hanle-MOKE traces were taken at a high excitation density (5 Wcm^{-2}) as a function of the pump-probe distance, shown in figure 5.31 (a). The extracted amplitudes from the Hanle curves, depicted in figure 5.31 (b) show the same behavior as those obtained by the three-point Hanle method, displayed in figure 5.30. The effective spin lifetime increases from about 10 ns at the overlap position to a saturation value of about 24 ns in the area, where the increased spin polarization is observed. A spatially inhomogeneous spin lifetime due to optical pumping was observed in bulk n-GaAs as well by Quast et al. [Qua08; Qua09].

Diffusion traces were taken for sample QWC as well, at the temperature 18 K, where the highest spin lifetime was observed, according to figure 5.14 (b). Additionally, at this temperature the ionization of the remote donors most likely is complete and the BAP dephasing mechanism dominates. Four one-dimensional traces, two taken along the crystallographic axes and two along the angle bisector, have been used to extrapolate a 2D image displayed in figure 5.33 (a), and (b). Experimental difficulties do not allow an actual 2D scan so far.

Sample QWC also shows a pronounced minimum at the beam overlap, however at

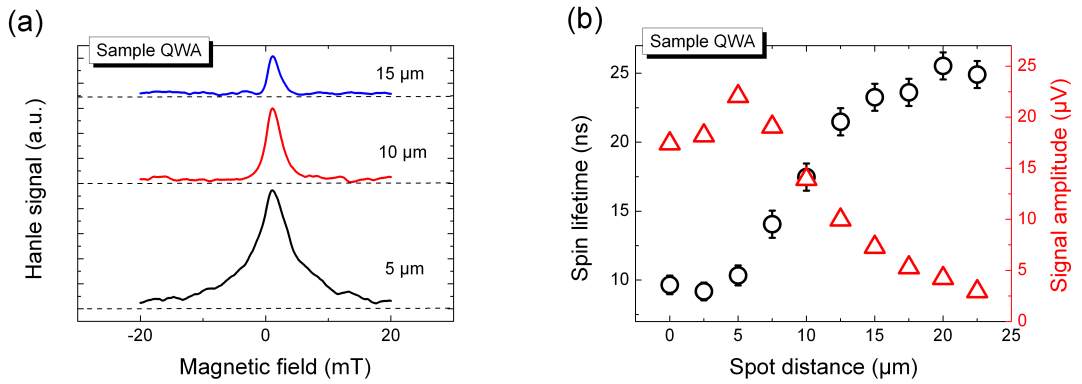

Figure 5.31: *(a) The Hanle MOKE traces for high excitation densities (5 Wcm^{-2}) become narrower for increasing distance between pump and probe spot. The temperature was 4 K.* ***(b)*** *The spin polarization extracted from the Hanle curves mimic the behavior of the three point Hanle measurements. The spin lifetime rises initially in the region where an increased spin polarization is observed and shows a saturating behavior afterward.*

significantly higher excitation densities, see figure 5.32. An explanation for this is probably the difference in the absorption of the two samples discussed in chapter 5.2.2. In this sample the spin polarization also saturates at higher excitation densities, as shown in figure 5.25 (b), where a saturation from about 30 Wcm^{-2} is visible. At these high excitation densities no Hanle signal is observed in sample QWA. The higher carrier mobility in sample QWA implies a less effective coupling to the lattice compared to sample QWC, see also the electron temperature obtained by PL measurements in figure 5.6. Thus, a too high electron temperature, due to high excitation densities, means a low spin lifetime (the spin lifetime drops in the BAP regime at rising temperature, see figure 5.14), which cannot be detected with this setup anymore. The low carrier mobility in sample QWC compared to sample QWA also means that the electrons move slower in sample QWC, which could be an additional factor in explaining the higher excitation densities necessary to observe the dip.

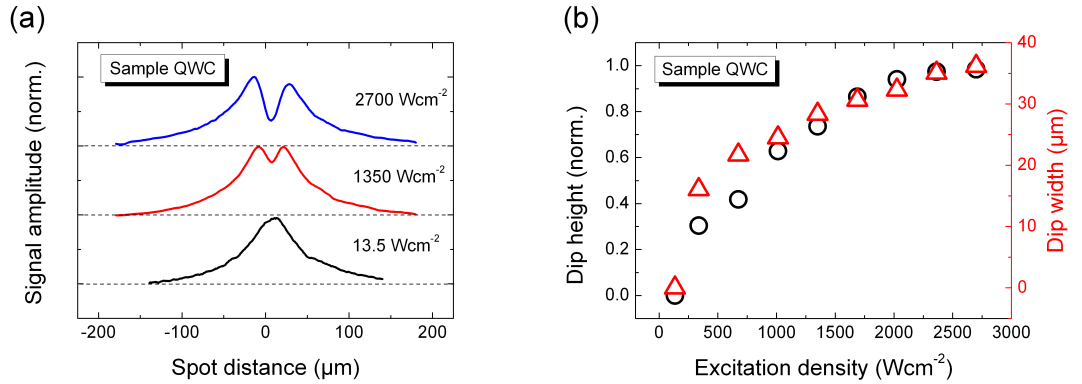

Figure 5.32: ***(a)*** *The spin diffusion profiles show an anomalous spin distribution for high excitation densities, for sample QWC at a temperature of 18 K, where the highest spin lifetimes are present.* ***(b)*** *With increasing excitation density the dip height and the dip width increase.*

Whereas, in sample QWA, the width of the dip increases slightly from about 8 μm to 13 μm in the observed excitation density range, in sample QWC an increase from $\sim$ 15 μm to 35 μm is observed (see figure 5.32 (b)). The reason for this difference is the

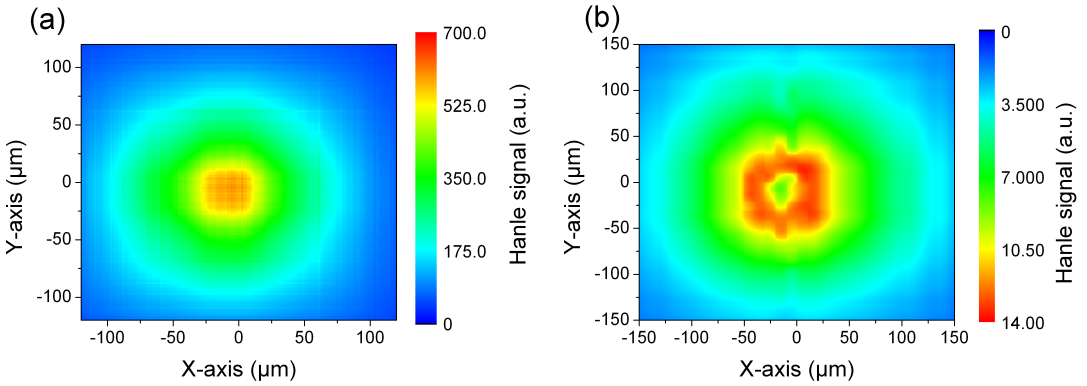

Figure 5.33: *Extrapolated 2D spin diffusion images for sample QWC for an excitation density of* 13.5 Wcm^{-2} ***(a)****, and an excitation density of* 2700 W/cm^2 ***(b)****. The sample temperature was* 18 K.

difference of the carrier lifetime in the two samples displayed in figure 5.8. The reduced recombination in sample QWC allows the holes to travel further, which results in a wider dip. According to figure 5.8 the carrier lifetime grows for rising temperature. Hence, the recombination becomes weaker at higher temperature, the hole diffusion rises, and the dip becomes weaker until at a temperature of 60 K no dip is observed anymore. This can be seen in the temperature dependent measurements of the dip displayed in figures 5.34 (a), (b). For the measurements an excitation density of 2.7 kWcm^{-2} was fixed.

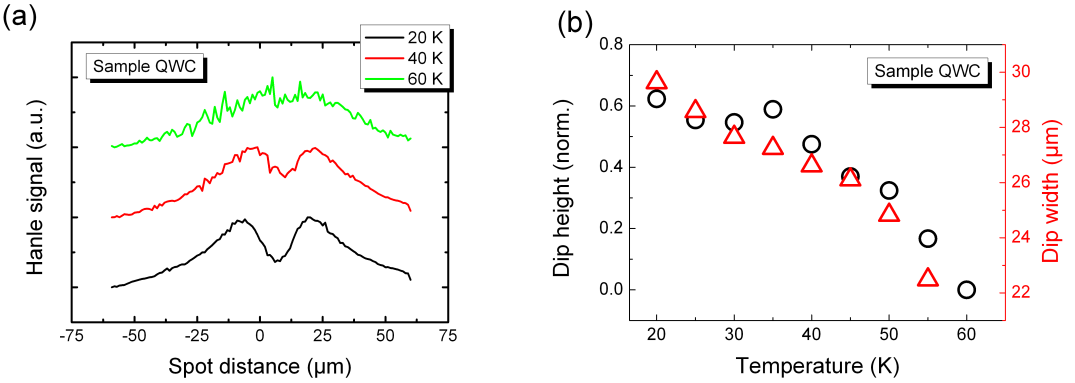

Figure 5.34: ***(a)*** *At increasing temperature the dip vanishes.* ***(b)*** *By rising the temperature, the hole density increases and the electron spin polarization decreases. Hence the dip width and dip height decrease. Here the excitation density was* 2.7 $kWcm^{-2}$.

From the diffusion traces, the diffusion length is extracted. The spatial dependence of the spin distribution is described by equation 2.65:

$$S_z(\boldsymbol{r}) - \tau_z \nabla \cdot [D_z \nabla S_z(\boldsymbol{r})] = G_z(\boldsymbol{r})\,\tau_z, \tag{5.19}$$

with a solution to this differential equation given by the modified Bessel function of the second kind (equation 2.67). These MacDonald functions have an asymptotic behavior given by equation 2.68:

$$S_z(\boldsymbol{r}) \propto \frac{\exp(-r/L_z)}{\sqrt{r/L_z}}. \tag{5.20}$$

In order to obtain the spin diffusion lengths (SDL) the spatial profile of the three-point Hanle signal is fitted with this formula. In figures 5.35 (a), (b) the SDL is depicted

with respect to the excitation density and in figures 5.36 (a), (b) depending on the temperature for samples QWA and QWC, respectively.

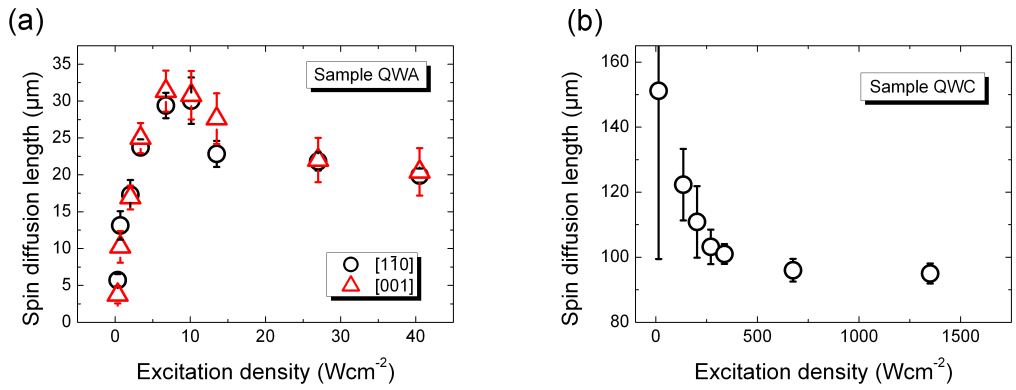

Figure 5.35: *Spin diffusion length depending on the excitation-density in sample QWA at 4 K* ***(a)****. and sample QWC at 18 K* ***(b)****.*

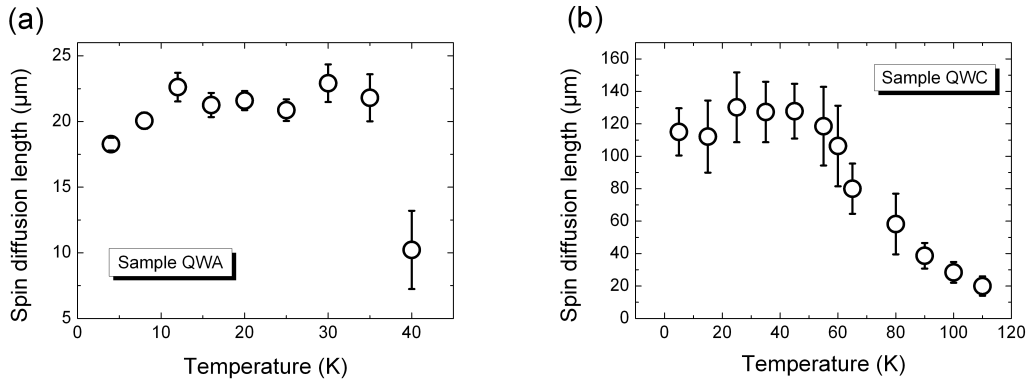

Figure 5.36: ***(a)*** *The spin diffusion length stays constant while increasing the lattice temperature due to overheating of the electron gas. The excitation-density was 5 W/cm^2.* ***(b)*** *Spin diffusion length with respect to the lattice temperature. Here the excitation density was 135 W/cm^2.*

The maximal obtained SDL in sample QWA is about 32 μm. Here, an exponential fit with the correction factor $1/e \sim 0.9L_s$ provided by Furis et al. [Fur07] would give the same results. This does not apply for the comparatively high SDL of up to 150 μm in sample QWC. In this case, a factor of up to 2.8 is found between an exponential fit and the MacDonald fit. The spin diffusion constant in equations 2.65 and 5.19 is given for a degenerate electron gas by equation 2.66:

$$D_z = E_F \tau / m^*. \tag{5.21}$$

This expression is derived from $D = \mu_e E_F / e$ and $\mu_e = \tau e / m^*$ (equations 2.56 and 2.49). Due to electron-electron collisions this diffusion coefficient is significantly smaller than the carrier diffusion coefficient given by equation 2.56. This is described in detail in chapter 2.3.2. With $L_z = \sqrt{D_z \tau_z}$ follows the spin diffusion length of the z-component:

$$L_z = \sqrt{\frac{E_F \tau \tau_z}{m^*}}. \tag{5.22}$$

Here τ is the microscopic scattering time. It includes the momentum scattering time due to not only scattering on static defects or phonons but also the electron-electron scattering. An increase of the SDL due to electron-electron scattering was shown by Kamra

et al. using Monte Carlo calculations [Kam11]. They showed, that e-e scattering leads to a narrower distribution in $\boldsymbol{k}$-space, yielding a reduced DP-dephasing. Moreover, they distinguished between the momentum relaxation time τ_p and the momentum redistribution time τ', which is basically the correlation time in equation 2.32 ($1/\tau_s = \bar{\Omega}^2\tau$), since electron-electron scattering does not influence the carrier mobility. The e-e influenced diffusion length may be expressed as: $L_s^{ee} = \sqrt{D\tau_s} = \sqrt{(v_F^2\tau_p)}/(\bar{\Omega}^2\tau') = \sqrt{\tau_p/\tau'}L_s$. Hence, the isotropization of the spin distribution in $\boldsymbol{k}$-space yields an increase in the SDL. τ may also be described as the decay of the first angular harmonic of the spin distribution in $\boldsymbol{k}$-space [Ley07a]. It determines the spin diffusion coefficient [D'A00] and the relaxation time of the pure spin current [Ivc08]. Although only the out-of-plane spin component is observed here, the DP-mechanism is important in this case, since far away from the pump spot only a small hole density is present and BAP dephasing is weak.

e-e scattering between majority spin and minority spin carriers causes a transfer of momentum from the majority spin carriers to the minority spin carriers. This Spin Coulomb drag effect described in chapter 2.3.2 may reduce the SDL as well. The consequence of the Spin Coulomb drag effect can be seen in the excitation-density dependence of sample QWA in figure 5.35 (a). By increasing the excitation density, the spin polarization grows, resulting in a lower probability of collisions between particles of opposite spin. Thus, the SDL rises while the Spin Coulomb drag becomes less important. Using "transmission-grating-photomasked transient spin grating" [19] Chen et al. found an increase of the spin ambipolar diffusion coefficient as well [Che12b]. For an excitation density of ~ 10 Wcm^{-2} the spin polarization saturates, see figure 5.24 and the SDL does not increase anymore, in fact it drops slightly and stays constant then (figure 5.35 (a)). This is most likely attributed to a local heating by the pump laser. By increasing the temperature the e-e scattering time decreases $\tau_{ee}^{-1} \propto T^2 n^{-1}$. Since in the high-mobility quantum wells the e-e-scattering dominates the microscopic scattering time, the spin diffusion length reduces according to equation 5.22. An increase of the SDL due to the Spin Coulomb drag is not observed in sample QWC, since the spin polarization is higher than in sample QWA, see figure 5.26. Collisions of carriers with opposite spin are therefore less probable. Again for increasing excitation density a drop of the SDL is observed, which is attributed once more to local heating and the reduction of the e-e-scattering time.

Comparing figures 5.35 (a), (b) and 5.36 (a), (b) shows that in sample QWC, the SDL is about five times larger than in sample QWA. The temperature dependence also displays that it is possible to observe a Hanle signal up to 110 K, whereas in sample QWA the signal is lost above 40 K. These SDL were taken with excitation densities, where the anomalous spin diffusion is not present. According to the PL measurements in figure 5.35, the electron temperature is higher in sample QWA than in sample QWC. At a lattice temperature of 40 K the spin lifetime is therefore too low to observe a Hanle signal.

Furthermore, both samples show a near-constant value of the spin diffusion length in a large temperature window. This is remarkable since the factors in equation 5.22 change with the temperature. E_F increases since the carrier density increases, see figure 5.7. The spin lifetime obtained with a large focal spot shows for sample QWC a maximum at

[19] Here, a typical setup of standard time-resolved pump-probe absorption spectroscopy with an optical delay line in probe path is extended by transmission grating placed on top of the sample. This one-dimensional binary opaque/transparent is fabricated by photolithography and has transparent slit width comparable to a diffusion length. Hence, the Gaussian profile of the pump and the probe laser are modulated into a periodic stripe profile, as they are transmitted to the grating. The change of the injected transient spin-polarized carrier grating is monitored by the absorption of the circularly polarized probe periodic stripe profile. See also [Che12a].

20 K and monotonously decreases in sample QWA for rising temperature. Moreover, as previously discussed, the e-e-scattering time decreases for rising temperature. Based on this, the Spin Coulomb drag effect should be increased, which hinders spin diffusion as well as the reduction of the microscopic scattering time in equation 5.22. From this, one can infer that the electron gas is significantly overheated below 30 K due to the large excitation densities resulting from the tightly focused excitation. Changes in the lattice temperature do not change τ_s or τ_{ee}. Such overheating effects were shown in low-doped bulk GaAs to be relevant below 25 K and distances of up to 30 μm [Qua13]. At low temperatures the coupling of the electron gas to the lattice is less efficient because of inefficient acoustical phonon scattering, whereas at higher temperatures the longitudinal optical phonon becomes energetically available. In the high-mobility samples used here, this effect can be even more pronounced also at higher temperatures, due to weaker coupling of lattice and electron gas. It can be estimated that the electron temperature during the diffusion measurement corresponds to the highest sample temperature for which the diffusion length is constant. For sample QWA this would be 35 K and for sample QWC 55 K. The associated spin lifetimes from figures 5.14 (a), (b) are 10 ns and 15.1 ns for sample QWA and QWC, respectively. Using these values and the spin diffusion length, in-and out-of-plane spin lifetimes, as well as the diffusion coefficients, may be calculated.

First, however, it is shown how to derive the utilized formulas, according to S.A. Tarasenko. The obtained spin lifetime with the Hanle-MOKE is the geometric mean of in- and out-of-plane spin lifetimes $\tau_s = \sqrt{\tau_z \tau_\parallel}$ (equation 3.8). Using the relation $\tau_\parallel = 2/\Omega_D^{`2}\tau$ (equation 5.9) it can be expressed as:

$$\tau_s = \sqrt{\frac{2\tau_z}{\Omega_D^{`2}\tau}}. \tag{5.23}$$

This expression in combination with equation 5.22 yields an expression for the microscopic scattering time τ:

$$\frac{L_z}{\tau_s} = \Omega_D^{`}\tau\sqrt{\frac{E_F}{2m^*}} = \Omega_D^{`}\tau v_F/2 \tag{5.24}$$

$$\Rightarrow \tau = \frac{2L_z}{\tau_s\Omega_D^{`}v_F} = \frac{2L_z m^*}{\tau_s\gamma\left\langle k_z^2\right\rangle k_F^2} \tag{5.25}$$

$$\tag{5.26}$$

Furthermore an expression for τ_z can be deduced:

$$L_z\tau_s = \frac{\tau_z}{\Omega_D^{`}}v_F \tag{5.27}$$

$$\Rightarrow \tau_z = \frac{L_z\tau_s\Omega_D^{`}}{v_F} = \frac{L_z\tau_s\gamma\left\langle k_z^2\right\rangle m^*}{\hbar^2} \tag{5.28}$$

$$\tag{5.29}$$

Finally, using equations 5.9, 5.25, and $v_F = \hbar k_F/m^* = \sqrt{2E_F/m^*}$, $\tau_\parallel$ is expressed by

$$\tau_\parallel = \frac{v_F\tau_s}{L_z\Omega_D^{`}} = \frac{\hbar^2\tau_s}{L_z\gamma\left\langle k_z^2\right\rangle m^*} \tag{5.30}$$

In the above derivations, a degenerate 2DES is assumed. The electron gas temperature, however, is high due to the already described overheating effect. Thus, a not perfectly degenerate 2DES has to be assumed, and the values of the Fermi energy needs to be replaced by the characteristic energy $\tilde{\epsilon} = E_F/\left[1-\exp\left(-E_F/k_BT\right)\right]$, so that the

expressions are valid for arbitrary statistics. Fermi wave vector and Fermi velocity are also replaced by values corresponding to $\tilde{\epsilon}$. The spin diffusion constant in equation 2.66/5.21 is therefore modified to:

$$D_z = \tilde{\epsilon}\tau/m^*, \tag{5.31}$$

In tables 5.2 and 5.3 several parameters are displayed at the temperature 35 K for sample QWA and 55 K for sample QWC. The Fermi energies were calculated for the observed carrier densities in the PL measurements (figure 5.7) at the used temperatures (sample QWA: $n = 3 \cdot 10^{11}\text{cm}^{-2}$ at 35 K, and sample QWC: $n = 2 \cdot 10^{11}\text{cm}^{-2}$ at 55 K. For the velocity $v_{\tilde{\epsilon}} = \hbar k_{\tilde{\epsilon}}/m^* = \sqrt{2\tilde{\epsilon}/m^*}$ was used. The expectation value of the z-component of the wave vector is given by: $\langle k_z^2 \rangle = (\pi/d)^2$ with d being the quantum well width. For sample QWC the confinement energy is ≈ 14 meV. For this confinement energy, a Dresselhaus coefficient of $\gamma \approx 12\text{eV}\mathring{\text{A}}^3$ has been found experimentally [Ley07b; Eld11], see also chapter 2.2.2. $\Omega_D^{'} = \gamma \langle k_z^2 \rangle \sqrt{2\tilde{\epsilon}m^*}/\hbar$ is the maximum effective Dresselhaus frequency (see also [Pos13]). The values for τ_s and L_z were extracted from the experimental data in figures 5.14 and 5.36. The values τ_z and $\tau_\parallel$ were calculated using equations 5.30 and 5.28. Equation 5.25 was used for τ and equation 2.51, 5.13 for τ_{ee}. From these parameters a spin diffusion constant can be calculated. D_z^1 is obtained by $D_z = L_z^2/\tau_z$, D_z^2 with the value of τ in table 5.3 and equation 5.31, finally D_z^3 was calculated using τ_{ee} in table 5.3 and equation 5.21. The carrier diffusion constant D_e was calculated with equation 2.56, using the mobility obtained by magnetotransport measurements at liquid-helium temperature. The change in the mobility due to the higher temperature is not considered here.

#	E_F (meV)	$\tilde{\epsilon}$ (meV)	$v_{\tilde{\epsilon}}$ ($10^5\,\text{ms}^{-1}$)	$\langle k_z^2 \rangle$ (10^{12}cm^{-2})	$\Omega_D^{'}$ ($10^{10}\,\text{s}^{-1}$)	L_z (μm)	τ_s (ns)	τ_z (ns)	$\tau_\parallel$ (ns)
QWA	10.7	11	2.4	1	2.5	22	10	23	4.4
QWC	7.1	9.2	2.2	2.5	5.7	120	15.1	486	0.47

Table 5.2: *Material parameters for sample QWA (at 35 K) and sample QWC (at 55 K).*

#	τ (ps)	τ_{ee} (ps)	D_e ($10^3\text{cm}^2\text{s}^{-1}$)	D_z^1 (cm^2s^{-1})	D_z^2 (cm^2s^{-1})	D_z^3 (cm^2s^{-1})
QWA	0.73	0.23	22.9	211	211	64
QWC	1.3	0.063	5.3	296	295	11.7

Table 5.3: *Material parameters for sample QWA (at 35 K) and sample QWC (at 55 K).*

In high-mobility 2DES τ_{ee} is the upper limit for the microscopic scattering time. The calculated values for τ displayed in table 5.3, are however larger than the values for τ_{ee}. Strictly speaking, equation 2.51, 5.13 is valid for $k_B T \gg E_F$, which adds some error. The spin diffusion coefficients D_z^1 and D_z^2 differ therefore from D_z^3. Furthermore, the spin diffusion length in sample QWC is about a factor 6 larger than in sample QWA, despite the higher carrier mobility in sample QWA. So far no solution for this inconsistencies exists. Further investigations are necessary to expand the employed model. The values for D_z are considerably lower than the values for the carrier diffusion D_e, indicating the influence of many-body effects, see chapter 2.3.2. While these low values of D_z limit the spin diffusion length, they may in fact be beneficial in spin transport in which an electric field is used to laterally drag packets of spin polarized carriers. In this case, spin diffusion leads to spatial dispersion of the spin packets.

Effect of above-barrier illumination on the spin diffusion

The SDL is strongly modified under weak above-barrier illumination, as depicted in figure 5.37. At a critical value of the green illumination power the large spin diffusion

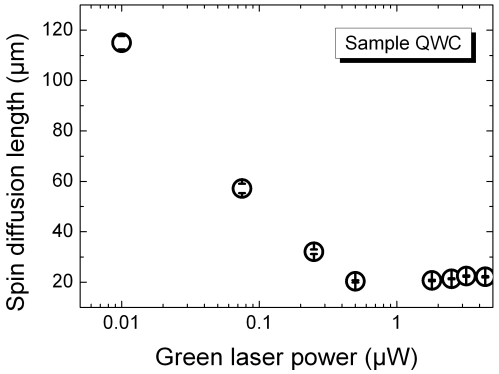

Figure 5.37: *The spin diffusion length drops drastically under weak above-barrier illumination. The trace was taken in sample QWC at* 18 *K with an excitation density of* 135 W/cm^2.

length drops significantly. The SDL can be reduced up to a factor of 6. This indicates that the reduced carrier density leads to a changeover from a degenerate to a nondegenerate regime in the 2DES, where Boltzmann statistics apply. The PL measurement in figure 5.18 (b) shows a drop of the carrier density down to $3 \cdot 10^{10}\text{cm}^{-2}$, corresponding to a Fermi temperature of 15 K. Spin-polarized electrons in a degenerate 2DES have a momentum given by the Fermi wave vector. In the nondegenerate regime, by contrast, they can be described by an average temperature, which may well be above the lattice temperature due to nonresonant excitation [Kie12]. Nevertheless it yields a lower average momentum than in the degenerate case.

5.3.1 Gate-controlled spin diffusion

By applying a gate voltage on the 2DES in a (110)-grown QW an in-plane Rashba field is induced, which causes a reduction of the spin lifetime. This was theoretically calculated for (110)-grown QW by Lau et al. [Lau02], and experimentally shown by Karimov et al. [Kar03]. They found a tenfold variation of the spin relaxation rate in undoped MQW (20×7.5 nm wide QW) at room temperature. In the following section, the spin diffusion depending on a gate voltage is investigated.

Usually, a thin semitransparent metallic top gate is deposited on the sample, which allows optical detection, see for example [Gri12b]. Here only a thin 5 μm wide metallic (Ti/Au) film is deposited on a piece from the same wafer as sample QWC. On the semiconductor surface 50 nm of Ti is evaporated followed by a 500 nm wide layer of Au [20]. The 2DES was contacted before the deposition in the following way. First, two scratches are made in the surface of the sample using a diamond tip scratcher, and some indium is deposited on the scratches with a clean soldering rod. The sample is then heated under forming gas atmosphere within 60 s to 350° C and kept at this temperature for another 60 s. This allows an alloying of the In into the sample, and provides an Ohmic contact after cooling out. The fabrication of the metallic gate was done by M. Ciorga from the chair of Prof. Weiss. Pump and probe beam were positioned in a way that the gate was in between them, with a distance of 50 μm between the two spots. Figure 5.38 shows an image taken with the CMOS camera, which shows the gate and the positioning of the two laser spots during the experiment.

The experiment was conducted at a sample temperature of 18 K, where the highest spin lifetimes are expected, and with an excitation density of 135 W/cm^2. For moderate

[20] The Ti layer increases the adhesion between the Au and the semiconductor.

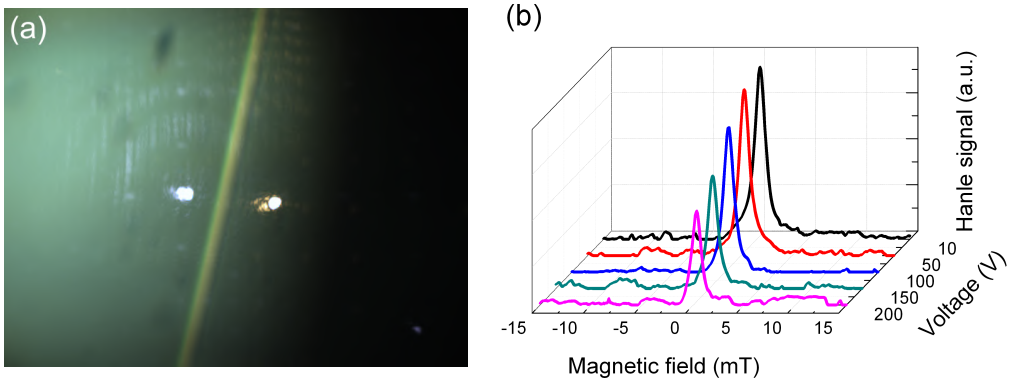

Figure 5.38: ***(a)*** *Microscopic image of the sample during the experiment. The distance of pump and probe spot was* 50 μm*, and the metallic gate was positioned right in between them.* ***(b)*** *The amplitude of the Hanle curves, measured at the probe spot, decreases whereas the width stays constant. The sample temperature was* 18 K*, and the excitation density was* 135 W/cm^2*.*

voltages, there is only a slight change in the Hanle signal observable. For very high voltages however, the amplitude of the Hanle signal decreases, see figure 5.38 (b). In figure 5.39 (a) the amplitude depending on the applied voltage is depicted. The extracted values are normalized with the value at zero voltage. By contrast the effective spin lifetime at the detection point also depicted in figure 5.39 (a), does not change with the voltage. Two reasons may be responsible for the modulation of the spin polarization. First, the induced Rashba field causes local dephasing, and therefore reduces the spin polarization in the area under the gate. Since at the detection point no Rashba SO-field is present the spin lifetime does not change there. The second possibility is, that the high voltage causes a depletion of the 2DES under the gate, and thus a reduction of the spin polarization at the probe spot. The Rashba parameter is given by $\alpha = 2\alpha_0\mathcal{E}_z$, see equation 2.27. Typically a few volt are necessary to achieve a observable change in the spin lifetimes, see [Kar03; Gri12b]. Since quite high voltages are necessary to observe a significant effect, it seems that the second possibility is more likely the reason. For the offset in spin lifetime and spin polarization in figure 5.39 (a) so far no explanation exists. The leakage current between the gate and the 2DES is minimal, as can be seen in figure 5.39 (b). It is only a few μA with an applied voltage of up to 200 V.

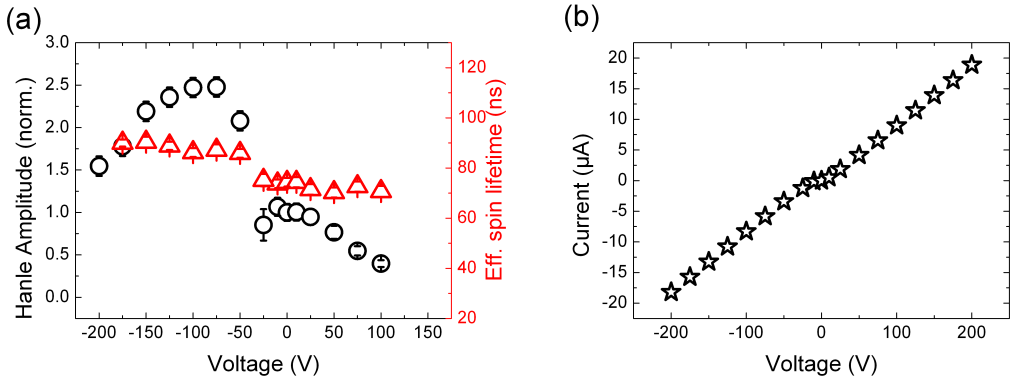

Figure 5.39: ***(a)****For increasing voltage the spin polarization decreases at the probe spot, whereas the spin lifetime stays constant. The sample temperature was* 18 K*, and the excitation density was* 135 W/cm^2*.* ***(b)*** *The I-V characteristic is linear, with a very small leakage current.*

The locally reduced carrier density yields a gradient, which is opposed to the diffusion direction induced by optical pumping. In order to investigate the dependence of the spin diffusion length three-point Hanle scans have been conducted under the same conditions as before. Hereby the probe spot stays fixed and the pump spot is moved. Figure 5.40 (a) depicts the reduction of the spin diffusion length for rising gate voltage respectively rising gradient against the spin diffusion. Even if the carriers do not need to pass the gate on their way from the generation to the detection point, the diffusion length drops by a factor 2, as depicted in figure 5.40. Hence, a detected diffusive Hanle signal may be "switched off" by an applied electric field. Further experiments are however necessary in order to fully understand the spin diffusion under the influence of a gate voltage. Future measurements involving time and spatially resolution are planned.

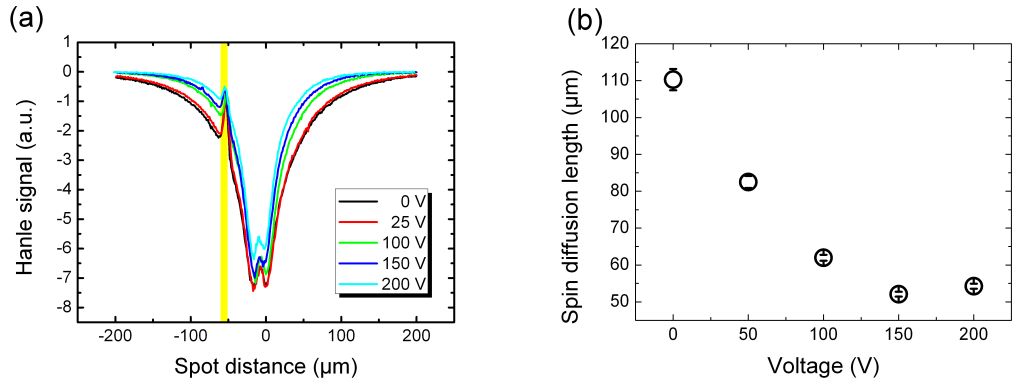

Figure 5.40: ***(a)*** *The depletion under the gate contact induces a gradient against the spin diffusion direction, yielding a reduction of the spin diffusion length.* ***(b)*** *Spin diffusion length with respect to the applied voltage. Here, the excitation density was* 135 W/cm^2 *and the temperature* 18 K.

5.4 Electric field dependent spin transport in (110)-grown quantum wells

So far spin transport was investigated only with regard to spin diffusion in this work. In the following section, the effects of an applied in-plane electric field on spin transport and spin polarization are discussed. On the first glance an electric field causes carrier drift, as discussed in chapter 2.3.2. It may however, also cause a spin polarization and an additional spin dephasing. First, the possibility of spin polarization due to an unpolarized electric current driven through a material, where SO-coupling is present, is discussed. Besides the spin-Hall effect [Dya71b; Dya71a; Kat04b], which is not considered in this work, the current-induced spin polarization (CISP), also called magneto-electric effect, yields a spin polarization in the material. Ivchenko et al. first suggested this effect [Ivc78], followed by a theoretical discussion by Edelstein et al. They showed, that a spin polarization arises in a 2DES due to an electric current in the presence of a SO field linear in $\boldsymbol{k}$, using linear response theory [Ede90]. Aronov et al. and Chaplik et al. did further calculations, in which they considered scattering in the calculations of the spin density matrix [Aro89; Aro91; Cha02]. Experimentally the CISP has been observed by Kato et al. in strained GaAs and InGaAs [Kat04a], and by Sih et al. in (110)-grown GaAs quantum wells [Sih05]. Stern et al. reported CISP in ZnSe epilayers at room temperature. Provided the spin polarization is large enough, this method could become an efficient tool to generate spin polarization in non magnetic semiconductors.

In a system with SO coupling, an electric field $\mathcal{E}$ causes a displacement of the two Fermi discs of [Sil04]:

$$\delta k_i = e\mathcal{E}\tau_i/\hbar, \tag{5.32}$$

where i stands for spin-up or spin-down, and τ is the microscopic scattering time. Such a displacement of the Fermi discs in k-space results in a correlated change of the charge current and a spin polarization in case SO-coupling is present. The subband contributions to the charge-current density and total spin density are given by [Sil04]:

$$j_i = \frac{e^2\mathcal{E}\tau_i v_F k_i}{4\pi\hbar}, \tag{5.33}$$

$$S_i = \pm\frac{1}{2}\frac{e\mathcal{E}\tau_i k_i}{4\pi\hbar}. \tag{5.34}$$

In thermal equilibrium, of course, no charge current and no spin polarization are present. The contributions from the spin-orbit field cancel each other. Due to the displacement only a partial cancellation is possible, yielding a total charge current given by equation 2.53 and a total spin polarization according to equation 2.6 [Sil04]:

$$P = \frac{e\tau\alpha_s}{\hbar E_F}\mathcal{E} \tag{5.35}$$

Here α_s is a general spin splitting parameter which depends on the present SO-fields. Thus, the spin polarization is proportional to the spin splitting energy and the applied electric field. Liu et al. proposed another way to understand the CISP [Liu08]. By applying equilibrium statistical mechanics they showed that unpolarized electrons, moving along $\boldsymbol{k}$, become polarized antiparallel to the effective magnetic field $\boldsymbol{B}_{eff}(\boldsymbol{k})$ induced by the SO-coupling. CISP is predicted here not only for SO terms linear in $\boldsymbol{k}$, but also for the cubic terms. The quantum statistical average of the spin distribution is then given by [Liu08]:

$$[\boldsymbol{S}]_{\boldsymbol{k}} = -\frac{\hbar}{2}\tanh\frac{\Delta E_{SO}}{4k_BT}\boldsymbol{B}_{eff}(\boldsymbol{k}) \tag{5.36}$$

Here $\Delta E_{SO} = 2\hbar\,|\boldsymbol{\Omega}(\boldsymbol{k})|$ represents the spin splitting energy. The hyperbolic function predicts an increase of CISP with the spin splitting energy and a decrease with the temperature. Due to the orientation of the Dresselhaus field in (110)-grown QW, shown in figure 2.13 a current along $[1\bar{1}0]$ direction yields an out of plane oriented spin polarization. A current along [001] on the contrary shows no spin polarization.

Due to the out-of-plane orientation of the spin polarization in (110)-grown QW, the Hanle-MOKE technique is suitable to observe the CISP in the samples used so far. A sample was prepared from the same wafer as sample QWA by scribing channels along the crystallographic axis, using a diamond tip, see inset in figure 5.41 (b). The channels were 1 mm wide and stretched along the whole sample piece. The 2DES was contacted in the same manner as described in section 5.3.1. The typical experimental setup was used, with the lock-in detection referenced to the frequency of a square wave alternating voltage with zero dc bias offset. An electric field applied in (001)-direction resulted in no visible Hanle signal whereas in $(1\bar{1}0)$-direction, a Hanle signal was observed displayed in figure 5.41 (a).

The amplitude increases linearly with the applied voltage up to 2 V according to equation 5.35, see figure 5.41 (b). The slope of the increase changes for voltages above 2 V slightly. This is attributed most likely to heating effects. The spin lifetime stays constant at ~ 42 ns. This value is in good agreement with the values obtained in chapter 5.2.2 for vanishing optical excitation in sample QWA, see figure 5.11.

Using the same frequency from the square-pulse generator to modulate an optical excitation via a chopper wheel, the observed Hanle signals from the two sources of spin

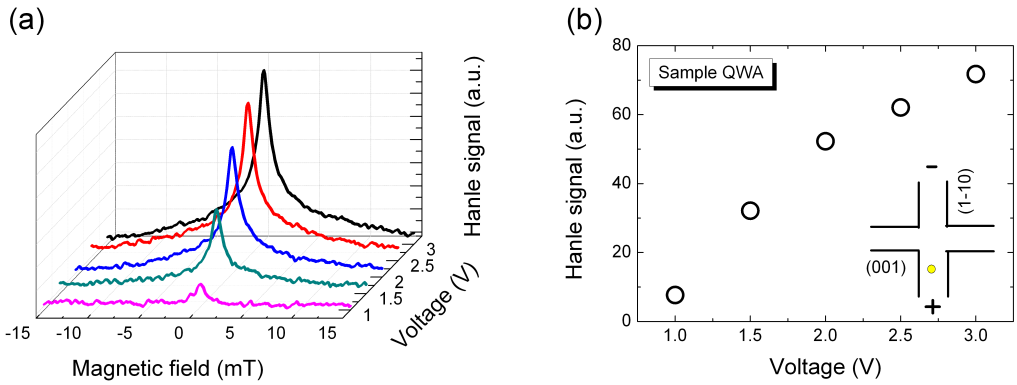

Figure 5.41: ***(a)*** *Hanle curves due to CISP, for increasing applied voltage.* ***(b)*** *The spin polarization increases with the applied voltage. The sample temperature was 4 K.*

polarization may add up or cancel each other out depending on the orientation of the two individual polarizations, see figures 5.42 (a), (b). In the case that the polarization is opposite, see figure 5.42 (a), the number of spin-up and spin-down carriers is comparable so that no net spin polarization is present, which may be detected by Kerr rotation. In the case that both spin polarizations are in the same direction, an increased spin polarization is detected, see figure 5.42 (b)

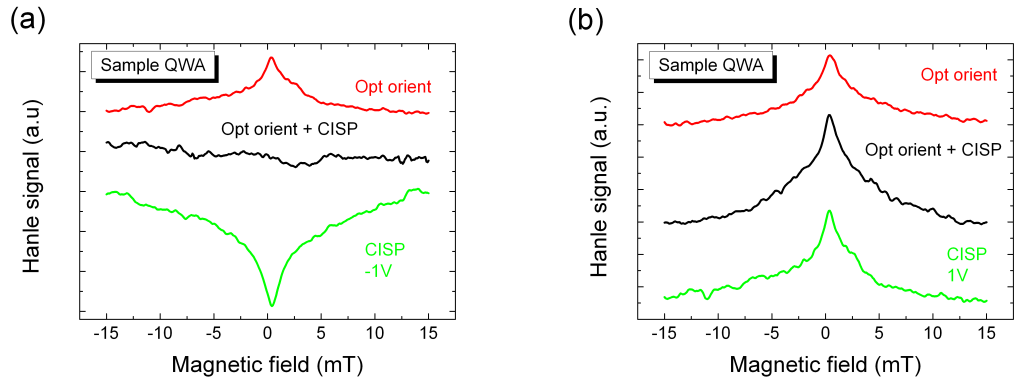

Figure 5.42: ***(a)*** *In case spin-polarized carriers generated by CISP are opposite to the optically generated ones, the net spin polarization cancels out.* ***(b)*** *In case spin-polarized carriers generated by CISP are oriented parallel to the optically generated ones, the net spin polarization adds up. The sample temperature was 4 K, and the excitation density 2 W/cm^2.*

The long spin lifetimes in the investigated samples here result in an effective nuclear polarization induced by the itinerant carriers, which is discussed in the next chapter 5.5. The effect of the DNP on the CISP is displayed in figure 5.43 (a). Here, continuous CISP is applied without an external magnetic field and after a certain time a Hanle curve is taken. The spin-polarized electrons transfer spin polarization to the nuclear system. Thus, the nuclear field is oriented out of plane and causes a spin polarization of further unpolarized electrons. This results in an increase of the observed spin polarization with lab time. After about 10 min only a slight decrease of the spin polarization is observed indicating a saturation of the nuclear system.

Next, a two-beam experiment is conducted, and the distance between pump and probe beam is about 20 μm. Here the spin dephasing due to photogenerated holes is not present, and the DP-mechanism dominates. The two laser spots are located in the

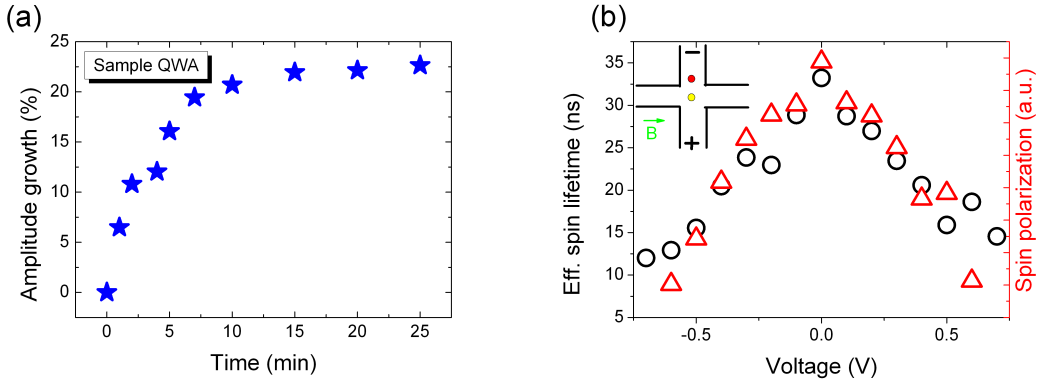

Figure 5.43: ***(a)*** *Nuclear spin polarization supports the spin polarization of electrons, yielding an increase of the observed spin polarization with time.* ***(b)*** *Spin dephasing due to the drift spin orbit field causes a reduction of spin lifetime and spin polarization with an applied electric field.*

channel along the (001)-direction, so that an electric current does not cause a CISP. The electric field has however a further consequence. Due to the drift, a regular effective magnetic field is present in addition to the fluctuating field $\Omega(k)$ caused by the change of the k-vector during scattering. This field accounts for the precession of the average spin of the drifting electrons and is proportional to the carrier mobility and the electric field ($\Omega_{drift} \propto \mathcal{E}\mu_e$) [Kal90]. In case the drift direction is oriented perpendicular to the applied field this yields a depolarization because of spin dephasing. This has been shown by Kalevich et al. by monitoring the circular polarization of the luminescence in (001)-oriented GaAs QW [Kal90]. Studer et al. could determine the Dresselhaus coefficient γ by observing the spin-precession frequency change due to the additional drift induced contribution [Stu10]. Figure 5.43 (b) displays clearly the reduction of the effective spin lifetime as well as a decay of the spin polarization. In case the drift direction is oriented along the applied field a shift of the maximum of the Hanle curve is expected due to superposition of the fields [Kal90]. Another sample prepared by M.Ciorga from the same

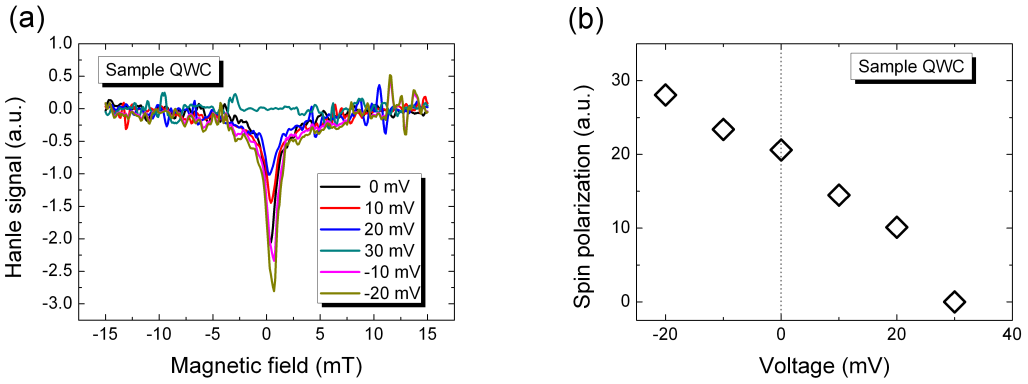

Figure 5.44: ***(a)*** *Hanle curves depending on the applied voltage.* ***(b)*** *Depending on the direction of the electric field spin polarized carriers are drawn towards the detection or away from it.*

wafer as sample QWC has channels along the crystallographic axes (50×300 μm). Here a current was applied along the channel oriented in (001)-direction with the magnetic field parallel to it, and the distance between pump and probe spot was 35 μm. Since the mobility in this sample is lower than in sample QWA, the depolarizing due to the

drift-SO-field is smaller and the effect of carrier drift may be seen at small voltages. A positive bias draws the electrons away from the detection point, yielding a lower spin polarization. Whereas a negative bias draws carriers towards the detection, yielding an increase of the spin polarization, see figure 5.44 (a), (b).

5.5 Dynamic nuclear polarization in (110)-grown quantum wells

Finally, this section presents a brief discussion of the influence of nuclear effects on the spin dynamics. The long spin lifetimes in the investigated samples allow for an efficient transfer of spin polarization from itinerant electrons to the nuclear system due to hyperfine interaction. Such a dynamic nuclear polarization (DNP) was introduced in chapter 2.4. DNP effects have already been found in (001)-grown QW [Mal00; Mal01] and in (110)-grown QW [Sal01a; Sal01b; Gri12b]. According to the calculations of Ţifrea et al., the nuclear spin polarization exceeds by far the electron spin polarization which causes the DNP. They estimated a few hundreds of gauss for the nuclear hyperfine field acting on the electrons and a few gauss [21] for induced nuclear dipolar fields, acting on electron as well as nuclear systems [Ţif11].

So far, nuclear effects have been suppressed in this work by using a liquid crystal retarder, which allows switching between the helicities (σ^+, σ^-) [22]. In the following, the effect of nuclear polarization on the Hanle curves is briefly shown for sample QWC. Thus, for the modulation of the pump beam, a chopper wheel is used. The itinerant electrons polarize nuclei via spin flip processes driven by contact hyperfine interaction. Since the electron spins precess in the external magnetic field, the spin polarization possesses an arbitrary phase. If the angle between field and spin is oblique, however, a nonzero time-averaged component of the electron spin is present, as depicted in figure 5.45, causing a nonzero time-averaged polarization of nuclei [Mal00]. A spin polarization of about 7% (see figure 5.26) yields an estimated $S_{\parallel} = S_0 \cos(90° - \alpha + \beta = 0.6\%)$ [23]. Due to the negative g-factor, this nuclear field $\boldsymbol{B}_N$ is opposite to the electron spin polarization.

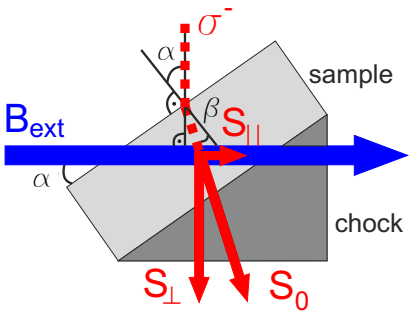

Figure 5.45: *Is the sample mounted on a copper chock, the magnetic field is oblique, yielding a non zero time averaged in plane component.*

RSA measurements by M. Griesbeck showed that small angles are already sufficient for an effective DNP in these samples [Gri12b]. Hence, by mounting the sample with conductive silver, which may already cause a small angle, a DNP could be present. In order to achieve a pronounced DNP, additional copper chocks, with small angles $(1°, 5°, 7°)$ are placed between sample and the cold finger of the cryostat, and the magnetic field is applied along the slope. In figure 5.46 (a), the Hanle curves under the influence of the nuclear field are displayed with respect to the excitation intensity. A copper chock with an angle of 7° is used here. For small excitation densities, the

[21] 1 gauss $= 10^{-4} T$.
[22] The LCR is positioned before the $\lambda/4$-plate and rotates the linear polarization between 0° and 90°.
[23] Here Snells law is used: $\frac{\sin\alpha}{n_{GaAs}} = \sin\beta$ with $n_{GaAs} = 3.5$ and $n_{vac} = 1$.

spin polarization is not high enough to introduce an observable nuclear polarization, and a typical Lorentzian-shaped Hanle curve is obtained. For higher excitations, the shape of the curves changes significantly. The reduction of the width of the curves indicates that the nuclear field and the external field have the same sign. This causes an increased Larmor frequency and a faster precession. The reason causing the undershoot for negative magnetic fields is not clear so far. Since it appears for quite small values of the external field, it could be influenced by local dipole fields which are expected to be of the order of a few gauss [Mei84; Ţif11]. In figure 5.46 (b) the Hanle signals for different chock angles are shown. Larger angles yield a bigger spin in-plane component, and a higher nuclear field. Thus, the curves become narrower for larger angles. Additionally the undershoot becomes more pronounced as well for larger angles. Compared to the Hanle curves in chapter 4.5, where a shift in the maxima has been observed as a result of the summation of nuclear field and external field, the maximum here is located at $B_{ext} = 0$. This is because for zero external field, there is no in-plane spin component and the nuclear field is oriented out of plane, whereas in chapter 4.5 there is a permanent in plane spin polarization due to the electrically injected spin polarization.

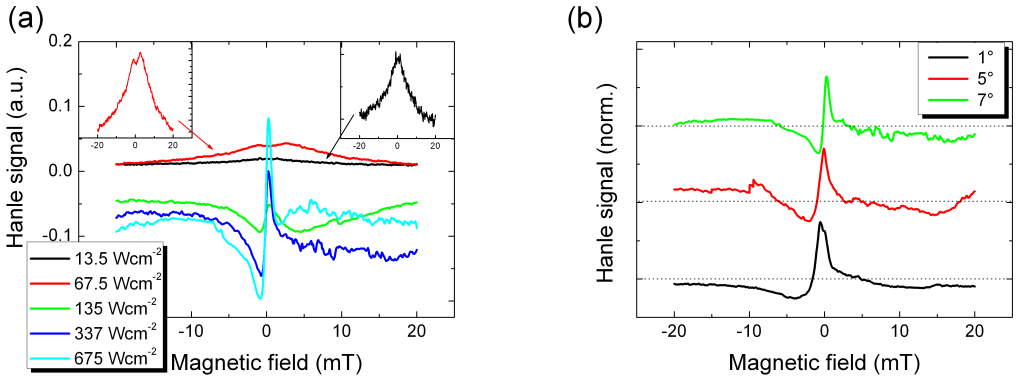

Figure 5.46: ***(a)*** *For small excitation density the spin polarization is not high enough to induce an observable nuclear polarization. For higher excitations a narrow Hanle curve with an asymmetric contribution is observed.* ***(b)*** *By increasing the angle of the chock the nuclear field rises. Hence the curves become narrower and the asymmetry more pronounced.*

By shining above-barrier illumination on the sample, the carrier density reduces drastically, see figure 5.18 (b). As already discussed, there is a transition from a degenerate 2DES to a nondegenerate 2DES. The lower momentum of an electron in the nondegenerate regime allows a more effective interaction with the nuclei. Furthermore, due to the lower electron density localization of electrons at impurities is more probable. The electron wave function overlaps with fewer nuclear wave functions which yields a stronger coupling. As displayed in figure 5.47 (a), for increasing green illumination the Hanle curve becomes narrower, due to a higher Larmor precession frequency, and an increased asymmetry in the curve is visible as well. The curve obtained for 6 mW (red curve) is exemplarily subdivided into an asymmetric and a symmetric part. The shape of the Hanle curves in the diffusive regime is similar as shown in figure 5.47 (b). Here, the distance between the spots was 26 μm. Again an undershoot is observed which becomes more pronounced for increasing green illumination. If the sweep direction of the magnetic field is changed from positive to negative, the position of the undershoot switches as well.

In the following, the nuclear polarization was induced by tilting the sample by 5°. The intention of the subsequent experiment was to determine the range in which nuclear

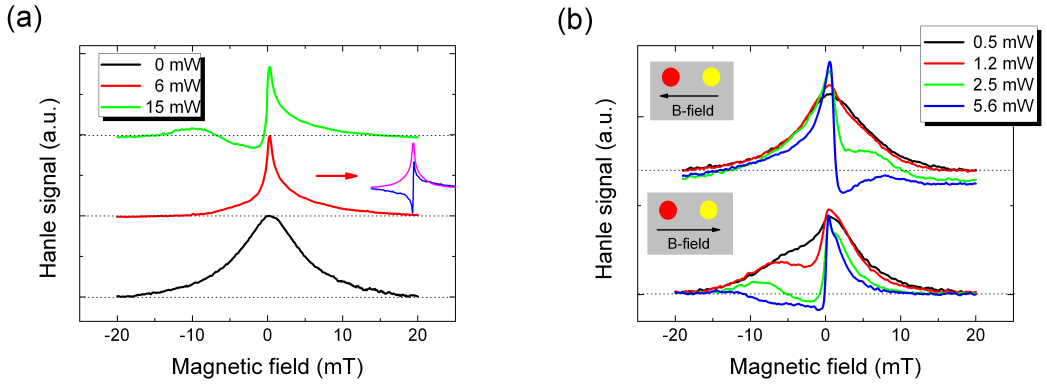

Figure 5.47: *(a) Above-barrier illumination reduces the carrier density, making electron nuclear interaction more likely. For rising green intensity nuclear effects become more pronounced. The inset shows the symmetric and the asymmetric part in which the curve can be subdivided. The sample temperature was* 10 *K and the excitation density* 67.5 Wcm^{-2}. ***(b)*** *In the diffusive regime the Hanle curves are deformed in the same manner for increasing green illumination. The distance between the two spots was* 26 μm^{-2}, *the sample temperature was* 10 *K and the excitation density* 67.5 Wcm^{-2}.

effects are observable. To begin with, a Hanle curve is measured with the LCR as a reference. This curve is depicted in figure 5.48 (a) as the black curve. Then circularly polarized light shines on the sample for 5 min, creating an electron spin polarization and polarizing nuclei. Afterwards another two-beam Hanle measurement is conducted using the LCR as modulation. The result is the red curve in figure 5.48 (a). A clear difference in the width of the curve is visible, since the influence of the nuclei causes additional electron spin dephasing due to hyperfine interaction, see chapter 2.2.4. After a waiting period of 5 min, again a spin polarization by circularly polarized light of 5 min starts. This time the next Hanle measurement is at a distance of 10 μm away from the initial spin injection point along the axis perpendicular to the slope of the chock. This procedure was applied several times, where the distance between the initial spin injection point and the measuring point is gradually increased. At a distance of

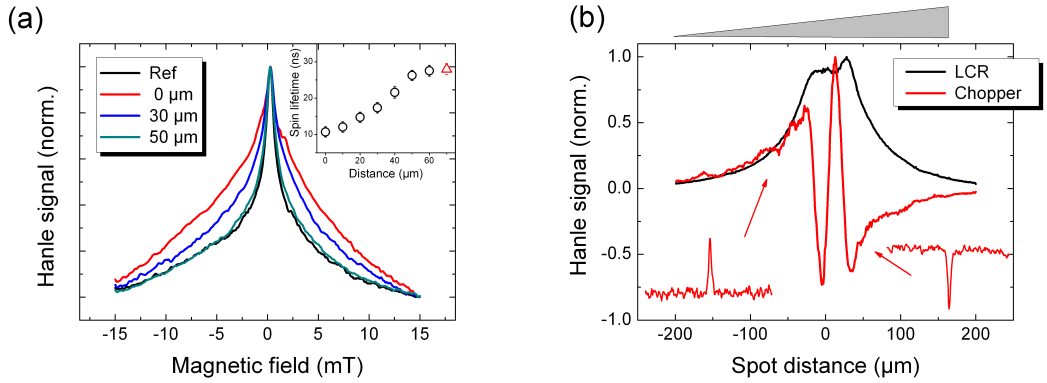

Figure 5.48: *(a) A nuclear polarization influences the spin dephasing via hyperfine interaction. A reduction of the spin lifetime by a factor 3 is observed due to nuclear spin polarization.* ***(b)*** *The diffusion profile under nuclear influence shows an monotonic decay above* 50 μm. *Within that range the curve can not be interpreted due to the non Lorentzian line shape of the Hanle signal. The inset shows the full Hanle curves taken at approximately the indicated position. Those curves have a Lorentzian shape due to the lack of nuclear influence.*

about 50 μm no significant change in the width of the Hanle curve is observed, compared to the reference curve. Hence, the influence of nuclear effects to the spin dephasing may be neglected. In the inset of figure 5.48 (a), the change of the effective spin lifetimes is depicted. The influence of the nuclear effects causes a reduction of the spin lifetime by a factor of 3. For increasing distance, the influence of the nuclear polarization becomes weaker and so does the spin dephasing via hyperfine interaction. The red triangle in the inset represents the spin lifetime of the reference curve.

The fact that at a distance of about 50 μm the nuclear effects are negligible, can also be seen comparing a three-point Hanle line scan once done with a LCR, which conveys the typical line shape, with a three-point measurement under the influence of DNP, see figure 5.48 (b). For distances above 50 μm, typical Lorentzian-shaped Hanle curves yield a monotonous decay of the spin polarization. Full Hanle curves taken at this positions are depicted in the insets in figure 5.48 (b). In this regime, neither the nuclear spin polarization originating from nuclear spin diffusion nor nuclear spin polarization from the reduced electron spin polarization is large enough to influence the electron spin. The behavior in between $\pm$50 μm is not interpretable due to the non-Lorentzian behavior. For the observed different signs for the two diffusion directions no explanation exists so far. Further experimental work is necessary for an exact description of the interaction between electron and nuclear system.

Chapter 6

Summary

For the development of new spintronics applications, substantial knowledge about the mechanisms which control the basic characteristics of a spin orientation in a material is necessary. Besides the task to create a spin polarization in a material, it is important to know how long a spin orientation exists until it relaxes to thermal equilibrium and which dephasing mechanisms are responsible for the decay. From the understanding of the spin dephasing mechanisms, the dependence of the spin lifetime on external parameters is deduced. Another crucial topic is to comprehend in which ways spin information can be transported in certain materials. This work addresses these topics by investigating two systems based on GaAs. The first system is a bulk n-GaAs sample, in which a p^+ (Ga, Mn)As/ n^+ GaAs Esaki Zener diode structure is used to inject a spin polarization. The second part of this dissertation studies spin dynamics and spin transport phenomena in high-mobility two-dimensional electron systems embedded in GaAs/AlGaAs quantum wells. The fact that GaAs is a direct semiconductor makes optical methods predestined tools to investigate the spin dynamics and the spin transport phenomena. The main technique employed in this work is the Hanle-MOKE method. Furthermore, PL and spin-resolved PL measurements are conducted.

The spin injection in the p^+ (Ga, Mn)As/ n^+ GaAs Esaki Zener diode structure takes place directly under the (Ga, Mn)As contact. The electric field around the electrode, however, causes nonuniform local current directions under the contact. This electron drift causes a shift of the polarization maximum away from directly under the electrode, which was observed by spatially resolved (1D and 2D) Hanle measurements. Depending on the detection position being inside or outside the current path, the measurement takes place either in the diffusive or the drift regime, and consequently only a subset of the spin polarization is detected. In order to determine the spin lifetime a 1D model is applied, which includes the distance between detection and injection and the spin diffusion length. The shift of the polarization maximum, however, yields an insufficiency of the 1D model to determine the spin lifetime. This became apparent by comparing the obtained spin lifetimes in the case of electrical spin injection (20 ns) and in the case of two-beam Hanle-MOKE measurements with optical orientation and detection (50 ns). Furthermore, the spin injection length could be increased or reduced in the case of electron drift against the diffusion or along it. Spin diffusion lengths of 7 μm and 9 μm were extracted from samples originating from two different wafers.

A combination of electrical and optical spin injection at the same time makes it possible to observe dynamic nuclear polarization effects. The electrically injected spins polarize the nuclei through the Fermi contact hyperfine exchange interaction. The

resulting Overhauser field causes a shift of the maxima of the Hanle curve with respect to the magnetic field axis. The nuclear field depends on the spin polarization of the electrically injected electrons, therefore by modulating the current through the electrode as well as by changing the distance between detection and the contact the nuclear field can be modulated. A buildup process of the DNP is visible, for low bias and large distances.

The second part of this work investigates spin dynamics and spin transport phenomena of two-dimensional electron systems embedded in GaAs/AlGaAs quantum wells. These single quantum wells were grown on a (110)-oriented substrate. According to D'yakonov and Kachorovskiĭ, this symmetry invokes no spin dephasing through the DP mechanism due to BIA (in its k-linear approximation). The special growth scheme further ensures a high symmetry of the quantum well structure. This implies on the one hand an absence of DP spin relaxation because of SIA, and on the other hand a high mobility of the 2DES. Three samples with a similar growth profile were investigated, however, with different carrier densities and quantum well widths. To begin with, electron temperature, carrier density, and carrier lifetime were determined using PL and time resolved PL measurements, respectively.

The spin dynamics of the three samples were investigated in regard to external parameters such as excitation density, sample temperature, and carrier density, which can be changed by optical gating. From those behaviors, the dominant spin dephasing mechanisms were inferred. Ideally, the normally dominant DP-mechanism is absent in these samples. The continuous optical excitation yields the presence of photogenerated holes, and may therefore lead to the domination of the BAP-mechanism, which is based on electron-hole scattering. Thus, the spin lifetime is limited by the BAP-mechanism and the carrier recombination. Since both scale with the hole density a corresponding excitation-density dependence of the spin lifetime was found, and a maximal spin lifetime of 110 ns was observed for small excitation densities and at low temperatures. At low temperatures an incomplete ionization of the remote donors may be present. In this case DP spin dephasing dominates due to regular and random Rashba fields. For increasing temperatures the remote donors ionize gradually. A maximum spin lifetime was observed at a temperature of 20 K, since both Rashba fields are minimal owing to a full ionization of the remote donors and a charge redistribution. By means of different excitation-density or carrier-density (modulated by above-barrier illumination) dependencies the dominant spin dephasing mechanism is identified in the corresponding temperature range. In the BAP regime, for example, the spin lifetime drops with rising above-barrier illumination, owing to a reduced coulomb screening, a weaker Pauli blocking and an increased hole density. By contrast, the spin lifetimes increase in the DP-regime with rising above-barrier illumination because of the influence of the reduced electron density on the SO field as well as the e-e scattering rates, and by a change of the asymmetry in the ionization of the remote donors.

From the Hanle curves, a relative spin polarization was extracted. By contrast, absolute values for the degree of spin polarization were obtained, by employing spin-resolved PL measurements. Maximal values of $\sim 22\%$ and $\sim 17.5\%$ were obtained. Because of a balanced generation and dephasing a saturation of the spin polarization for increasing excitation density is observed in the BAP dominated regime, whereas in the DP dominated regime, the spin polarization increases linearly owing to the rising density of spin polarized carriers. Above-barrier illumination also modulates the spin polarization. Depending on the initial carrier density and on the active dephasing mechanism, the spin polarization rises or drops, owing to the additional holes in the quantum well.

Spin diffusion profiles were obtained, depending on the distance between pump and probe laser spot, by evaluating the amplitude of the Hanle signal. From these profiles, spin diffusion lengths exceeding 100 μm were extracted. For low excitation densities

the time-averaged spin polarization decreases monotonously. A pronounced minimum develops, however, if the excitation density is increased. In the beam overlap the spin dephasing rate is given by BAP dephasing and the recombination rate. Due to the electron diffusion, that is significantly faster compared to the hole diffusion, a reduced dephasing exists at some distance away from the spot, which results in a larger spin polarization.

A dependence of the spin diffusion length on the excitation density is attributed to the spin Coulomb drag effect. By increasing the excitation-density, the spin polarization rises, resulting in a lower probability of collisions between particles of opposite spin and longer spin diffusion lengths. The sample with an already high degree of spin polarization showed therefore no such behavior. By contrast, a weak above-barrier illumination reduces the spin diffusion length significantly. This indicates that due to the reduced carrier density, a transition takes place from the degenerate to the non-degenerate regime, where the electrons have lower average momentum. The obtained spin diffusion lengths stayed constant in a wide temperature range, up to 50 K. It is inferred that the electron gas is significantly overheated at low temperatures owing to tightly focused excitation. This overheating influences the spin diffusion also far away from the pump spot. Moreover, the influence of a small metallic gate put in between pump and probe spot was investigated. An applied gate voltage causes a local depletion of the 2DES, which in turn induces a gradient against the spin diffusion direction, and therefore a reduction of the spin diffusion lengths.

An electric current along the $(1\bar{1}0)$-direction results in a out-of-plane spin polarization, as a result of the interplay of the displacement of the Fermi disc and the orientation of the SO-field (current induced spin polarization). A linear dependence of the spin polarization on the current has been shown. Additionally, spin orientations originating from CISP and from optical injection may cancel each other or add up depending on their relative orientations. The displacement of the Fermi disc also induces a regular effective field and therefore additional spin dephasing, which has been shown for a optically generated spin polarization.

Finally a strong effect of dynamic nuclear polarization was found in the case of an oblique magnetic field as well as by reducing the carrier density through optical gating. The Hanle curves showed an asymmetric behavior which could not be explained in detail so far. Spatially dependent measurements showed, however, that the range of the nuclear influence is about 50 μm in these samples.

Bibliography

[Abr59] M. Abraham, M. A. H. McCausland, and F. N. H. Robinson, *Dynamic Nuclear Polarization*, Phys. Rev. Lett. **2**, 449 (June 1959). (Cit. on p. 43).

[Ada01] T. Adachi, Y. Ohno, F. Matsukura, and H. Ohno, *Spin relaxation in n-modulation doped GaAs/AlGaAs (110) quantum wells*, Physica E: Low-dimensional Systems and Nanostructures **10**, 36 (2001). (Cit. on pp. 3, 33, 88, 94).

[Ada85] S. Adachi, *GaAs, AlAs, and $Al_xGa_{1-x}As$: Material parameters for use in research and device applications*, J. Appl. Phys. **58**, 1 (1985). (Cit. on pp. 8, 9).

[Ade05] C. Adelmann, X. Lou, J. Strand, C. J. Palmstrøm, and P. A. Crowell, *Spin injection and relaxation in ferromagnet-semiconductor heterostructures*, Phys. Rev. B **71**, 121301 (Mar. 2005). (Cit. on p. 18).

[Aha59] Y. Aharonov and D. Bohm, *Significance of Electromagnetic Potentials in the Quantum Theory*, Phys. Rev. **115**, 485 (Aug. 1959). (Cit. on p. 1).

[Alv92] S. F. Alvarado and P. Renaud, *Observation of spin-polarized-electron tunneling from a ferromagnet into GaAs*, Phys. Rev. Lett. **68**, 1387 (Mar. 1992). (Cit. on p. 18).

[Amo07] A. Amo, L. Viña, P. Lugli, C. Tejedor, A. I. Toropov, and K. S. Zhuravlev, *Pauli blockade of the electron spin flip in bulk GaAs*, Phys. Rev. B **75**, 085202 (Feb. 2007). (Cit. on p. 30).

[Aro76] A. G. Aronov, *Spin injection in metals and polarization of nuclei*, JETP Lett. **24**, 32 (1976). (Cit. on p. 40).

[Aro83] A. G. Aronov, G. E. Pikus, and A. N. Titkov, *Spin relaxation of conduction electrons in p-type III-V compounds*, JETP Lett. **57**, 680 (1983). (Cit. on pp. 29, 30).

[Aro89] A. G. Aronov and Y. B. Lyanda-Geller, *Nuclear electric resonance and orientation of carrier spins by an electric field*, JETP Lett. **50**, 431 (1989). (Cit. on p. 119).

[Aro91] A. G. Aronov, Y. B. Lyanda-Geller, and G. Pikus, *Spin polarization of electrons by an electric current*, JETP Lett. **73**, 537 (1991). (Cit. on pp. 2, 119).

[Art68] J. R. Arthur, *Interaction of Ga and As_2 Molecular Beams with GaAs Surfaces*, J. Appl. Phys. **39**, 4032 (1968). (Cit. on pp. 1, 6).

[Ash76] N. W. Ashcroft and M. N. D. *Solid State Physics*. Harcourt College Publishers, 1976 (cit. on pp. 6, 7, 36, 38).

[Ave02] N. S. Averkiev, L. E. Golub, and M. Willander, *Spin relaxation anisotropy in two-dimensional semiconductor systems*, Journal of Physics: Condensed Matter **14**, 271 (Mar. 2002). (Cit. on p. 26).

[Ave06] N. S. Averkiev, L. E. Golub, A. S. Gurevich, V. P. Evtikhiev, V. P. Kochereshko, A. V. Platonov, A. S. Shkolnik, and Y. P. Efimov, *Spin-relaxation anisotropy in asymmetrical (001) $Al_xGa_{1-x}As$ quantum wells from Hanle-effect measurements: Relative strengths of Rashba and Dresselhaus spin-orbit coupling*, Phys. Rev. B **74**, 033305 (July 2006). (Cit. on p. 48).

[Ave99] N. S. Averkiev and L. E. Golub, *Giant spin relaxation anisotropy in zinc-blende heterostructures*, Phys. Rev. B **60**, 15582 (Dec. 1999). (Cit. on pp. 2, 26).

[Aws85] D. D. Awschalom, J. M. Halbout, S. von Molnar, T. Siegrist, and F. Holtzberg, *Dynamic Spin Organization in Dilute Magnetic Systems*, Phys. Rev. Lett. **55**, 1128 (Sept. 1985). (Cit. on p. 48).

[Bab83] T. Baba, T. Mizutani, and M. Ogawa, *Elimination of Persistent Photoconductivity and Improvement in Si Activation Coefficient by Al Spatial Separation from Ga and Si in Al–Ga–As:Si Solid System —a Novel Short Period AlAs/n-GaAs Superlattice—*, Japanese Journal of Applied Physics **22**, L627 (1983). (Cit. on p. 83).

[Bai88] M. N. Baibich, J. M. Broto, A. Fert, F. N. Van Dau, F. Petroff, P. Etienne, G. Creuzet, A. Friederich, and J. Chazelas, *Giant Magnetoresistance of (001)Fe/(001)Cr Magnetic Superlattices*, Phys. Rev. Lett. **61**, 2472 (Nov. 1988). (Cit. on p. 1).

[Bal11] A. Balocchi, Q. H. Duong, P. Renucci, B. L. Liu, C. Fontaine, T. Amand, D. Lagarde, and X. Marie, *Full Electrical Control of the Electron Spin Relaxation in GaAs Quantum Wells*, Phys. Rev. Lett. **107**, 136604 (Sept. 2011). (Cit. on p. 26).

[Bar48] J. Bardeen and W. H. Brattain, *The Transistor, A Semi-Conductor Triode*, Phys. Rev. **74**, 230 (July 1948). (Cit. on p. 1).

[Bas81] G. Bastard, *Superlattice band structure in the envelope-function approximation*, Phys. Rev. B **24**, 5693 (Nov. 1981). (Cit. on p. 9).

[Bas85] G. Bastard, *Electronic energy levels in semiconductor quantum wells and superlattices*, Superlattices and Microstructures **1**, 265 (1985). (Cit. on p. 9).

[Bau83] R. S. Bauer, P. Zurcher, and H. W. Sang, *Inequality of semiconductor heterojunction conduction-band-edge discontinuity and electron affinity difference*, Appl. Phys. Lett. **43**, 663 (1983). (Cit. on p. 9).

[Bau94] J. J. Baumberg, D. D. Awschalom, N. Samarth, H. Luo, and J. K. Furdyna, *Spin beats and dynamical magnetization in quantum structures*, Phys. Rev. Lett. **72**, 717 (Jan. 1994). (Cit. on pp. 23, 48).

[Bec05] M. Beck. "Electron spin relaxation, transport and strain induced precession in n-GaAs". PhD thesis. Friedrich-Alexander-Universität Erlangen-Nürnberg, 2005 (cit. on pp. 47, 48).

[Bec06] M. Beck, C. Metzner, S. Malzer, and G. H. Döhler, *Spin lifetimes and strain-controlled spin precession of drifting electrons in GaAs*, Europhys. Lett. **75**, 597 (2006). (Cit. on p. 70).

[Bel08] V. V. Bel'kov, P. Olbrich, S. A. Tarasenko, D. Schuh, W. Wegscheider, T. Korn, C. Schüller, D. Weiss, W. Prettl, and S. D. Ganichev, *Symmetry and Spin Dephasing in (110)-Grown Quantum Wells*, Phys. Rev. Lett. **100**, 176806 (May 2008). (Cit. on pp. 2, 34, 81, 89).

[Ben00] C. H. Bennett and D. P. DiVincenzo, *Quantum information and computation*, Nature **404**, 247 (2000). (Cit. on p. 2).

[Ber06a] B. A. Bernevig, J. Orenstein, and S.-C. Zhang, *Exact SU(2) Symmetry and Persistent Spin Helix in a Spin-Orbit Coupled System*, Phys. Rev. Lett. **97**, 236601 (Dec. 2006). (Cit. on pp. 2, 26).

[Ber06b] B. A. Bernevig, T. L. Hughes, and S.-C. Zhang, *Quantum Spin Hall Effect and Topological Phase Transition in HgTe Quantum Wells*, Science **314**, 1757 (2006). (Cit. on p. 2).

[Ber06c] B. A. Bernevig and S.-C. Zhang, *Quantum Spin Hall Effect*, Phys. Rev. Lett. **96**, 106802 (Mar. 2006). (Cit. on p. 2).

[Ber07] E. Bernardes, J. Schliemann, M. Lee, J. C. Egues, and D. Loss, *Spin-Orbit Interaction in Symmetric Wells with Two Subbands*, Phys. Rev. Lett. **99**, 076603 (Aug. 2007). (Cit. on p. 25).

[Ber74] V. Berkovits, A. Ekimov, and V. Safarov, *Optical orientation in a system of electrons and lattice nuclei in semiconductors. Experiment*, JETP Lett. **38**, 169 (Jan. 1974). (Cit. on p. 31).

[Ber84a] G. Bergmann, *Weak localization in thin films*, Physics Reports **107**, 1 (1984). (Cit. on pp. 2, 27).

[Ber84b] M. V. Berry, *Quantal Phase Factors Accompanying Adiabatic Changes*, Proc. R. Soc. Lond. A **392**, 45 (Mar. 1984). (Cit. on p. 27).

[Bet12] C. Betthausen, T. Dollinger, H. Saarikoski, V. Kolkovsky, G. Karczewski, T. Wojtowicz, K. Richter, and D. Weiss, *Spin-Transistor Action via Tunable Landau-Zener Transitions*, Science **337**, 324 (July 2012). (Cit. on p. 2).

[Bha00] R. D. R. Bhat and J. E. Sipe, *Optically Injected Spin Currents in Semiconductors*, Phys. Rev. Lett. **85**, 5432 (Dec. 2000). (Cit. on p. 41).

[Bin89] G. Binasch, P. Grünberg, F. Saurenbach, and W. Zinn, *Enhanced magnetoresistance in layered magnetic structures with antiferromagnetic interlayer exchange*, Phys. Rev. B **39**, 4828 (Mar. 1989). (Cit. on p. 1).

[Bir74] G. L Bir and G. E. Pikus. *Symmetry and strain-induced effects in semiconductors*. Wiley New York, 1974 (cit. on p. 25).

[Bir75] G. L. Bir, A. G. Aronov, and G. E. Pikus, *Spin relaxation of electrons due to scattering by holes*, JETP Lett. **42**, 705 (1975). (Cit. on p. 29).

[Bla82] J. S. Blakemore, *Semiconducting and other major properties of gallium arsenide*, J. Appl. Phys. **53**, 123 (1982). (Cit. on pp. 37, 54, 67).

[Blo46] F. Bloch, *Nuclear Induction*, Phys. Rev. **70**, 460 (Oct. 1946). (Cit. on p. 26).

[Blu01] S. Blundell. *Magnetism in Condensed Matter*. Oxford University Press, 2001 (cit. on pp. 12, 13).

[Bog80] P. Boguslawski, *Electron-electron spin-flip scattering and spin relaxation in III-V and II-VI semiconductors*, Solid State Communications **33**, 389 (1980). (Cit. on p. 30).

[Bra67] N. Braslau, J. Gunn, and J. Staples, *Metal-semiconductor contacts for GaAs bulk effect devices*, Solid-State Electronics **10**, 381 (1967). (Cit. on p. 63).

[Bre33] G. Breit, *Quantum Theory of Dispersion (Continued). Parts VI and VII*, Rev. Mod. Phys. **5**, 91 (Apr. 1933). (Cit. on p. 48).

[Bro04] F. X. Bronold, A. Saxena, and D. L. Smith, *Semiclassical kinetic theory of electron spin relaxation in semiconductors*, Phys. Rev. B **70**, 245210 (Dec. 2004). (Cit. on p. 34).

[Buh11] H. Buhmann, *The quantum spin Hall effect*, Journal of Applied Physics **109**, 102409 (2011). (Cit. on p. 2).

[Buk94] E. Buks, M. Heiblum, Y. Levinson, and H. Shtrikman, *Scattering of a two-dimensional electron gas by a correlated system of ionized donors*, Semicond. Sci. Technol. **9**, 2031 (1994). (Cit. on pp. 82, 83).

[Bur54] E. Burstein, *Anomalous Optical Absorption Limit in InSb*, Phys. Rev. **93**, 632 (Feb. 1954). (Cit. on p. 10).

[Byc84a] Y. A. Bychkov and E. I. Rashba, *Properties of a 2D electron gas with lifted spectral degeneracy*, JETP Lett. **39**, 78 (1984). (Cit. on pp. 2, 25).

[Byc84b] Y. A. Bychkov and E. I. Rashba, *Oscillatory effects and the magnetic susceptibility of carriers in inversion layers*, J. Phys. C: Solid State Phys., **17**, 6039 (Nov. 1984). (Cit. on pp. 2, 25).

[Büg09] S. Bügel, D. Bürgler, M. Morgenstern, C. Schneider, and R. Waser, eds. *Spintronics - from GMR to Quantum Information. Lecture manuscripts of the Springschool 2009.* Forschungszentrum Jülich, 2009 (cit. on p. 47).

[Cam96] A. R. Cameron, P. Riblet, and A. Miller, *Spin Gratings and the Measurement of Electron Drift Mobility in Multiple Quantum Well Semiconductors*, Phys. Rev. Lett. **76**, 4793 (June 1996). (Cit. on p. 109).

[Car03] X. Cartoixà, D. Z.-Y. Ting, and Y.-C. Chang, *A resonant spin lifetime transistor*, Appl. Phys. Lett. **83**, 1462 (2003). (Cit. on p. 2).

[Car05] X. Cartoixa, D. Z.-Y. Ting, and Y.-C. Chang, *Suppression of the D'yakonov-Perel´ spin-relaxation mechanism for all spin components in [111] zincblende quantum wells*, Phys. Rev. B **71**, 045313 (Jan. 2005). (Cit. on pp. 24, 26).

[Car06] X. Cartoixa, L.-W. Wang, D.-Y. Ting, and Y.-C. Chang, *Higher-order contributions to Rashba and Dresselhaus effects*, Phys. Rev. B **73**, 205341 (May 2006). (Cit. on p. 33).

[Car88] M. Cardona, N. E. Christensen, and G. Fasol, *Relativistic band structure and spin-orbit splitting of zinc-blende-type semiconductors*, Phys. Rev. B **38**, 1806 (July 1988). (Cit. on p. 23).

[Car99] A. J. C. Cardoso, F. Qu, and P. C. Morais, *Optical control of the two-dimensional electron-gas density in single asymmetric quantum wells: Magnetic-field effect*, Phys. Rev. B **60**, 4501 (Aug. 1999). (Cit. on p. 56).

[Cha02] A. Chaplik, M. Entin, and L. Magarill, *Spin orientation of electrons by lateral electric field in 2D system without inversion symmetry*, Physica E: Low-dimensional Systems and Nanostructures **13**, 744 (2002). (Cit. on p. 119).

[Cha05] S.-W. Chang and S.-L. Chuang, *Strain-induced enhancement of spin relaxation times in [110] and [111] grown quantum wells*, Phys. Rev. B **72**, 115429 (Sept. 2005). (Cit. on p. 26).

[Cha06] A. N. Chantis, M. van Schilfgaarde, and T. Kotani, *Ab Initio Prediction of Conduction Band Spin Splitting in Zinc Blende Semiconductors*, Phys. Rev. Lett. **96**, 086405 (Mar. 2006). (Cit. on p. 23).

[Cha07a] A. N. Chantis, K. D. Belashchenko, D. L. Smith, E. Y. Tsymbal, M. van Schilfgaarde, and R. C. Albers, *Reversal of Spin Polarization in Fe/GaAs (001) Driven by Resonant Surface States: First-Principles Calculations*, Phys. Rev. Lett. **99**, 196603 (19 Nov. 2007). (Cit. on p. 72).

[Cha07b] C. Chappert, A. Fert, and F. N. Van Dau, *The emergence of spin electronics in data storage*, Nature Materials **6**, 813 (Nov. 2007). (Cit. on p. 17).

[Cha09] M. K. Chan, Q. O. Hu, J. Zhang, T. Kondo, C. J. Palmstrøm, and P. A. Crowell, *Hyperfine interactions and spin transport in ferromagnet- semiconductor heterostructures*, Phys. Rev. B **80**, 161206 (Oct. 2009). (Cit. on pp. 67, 76).

[Cha80] A. Chandra and L. F. Eastman, *A study of alloy scattering in $Ga_{1-x}A_xAs$*, J. Appl. Phys. **51**, 2669 (1980). (Cit. on p. 82).

[Cha81] D. Chattopadhyay and H. J. Queisser, *Electron scattering by ionized impurities in semiconductors*, Rev. Mod. Phys. **53**, 745 (Oct. 1981). (Cit. on p. 36).

[Cha86] A. Chaves, A. Penna, J. Worlock, G. Weimann, and W. Schlapp, *Optical control of two-dimensional electron density in a single asymmetric quantum well*, Surface Science **170**, 618 (Apr. 1986). (Cit. on pp. 55, 56).

[Che02] Y. H. Chen, X. L. Ye, J. Z. Wang, Z. G. Wang, and Z. Yang, *Interface-related in-plane optical anisotropy in GaAs / $Al_xGa_{1-x}As$ single-quantum-well structures studied by reflectance difference spectroscopy*, Phys. Rev. B **66**, 195321 (Nov. 2002). (Cit. on p. 34).

[Che11] L. Chen, X. Yang, F. Yang, J. Zhao, J. Misuraca, P. Xiong, and S. von Molnár, *Enhancing the Curie Temperature of Ferromagnetic Semiconductor (Ga,Mn)As to 200 K via Nanostructure Engineering*, Nano Letters **11**, 2584 (2011). (Cit. on p. 13).

[Che12a] K. Chen, W. Wang, J. Chen, J. Wen, and T. Lai, *A transmission-grating-modulated pump-probe absorption spectroscopy and demonstration of diffusion dynamics of photoexcited carriers in bulk intrinsic GaAs film*, Opt. Express **20**, 3580 (2012). (Cit. on p. 114).

[Che12b] K. Chen, W. Wang, J. Wu, D. Schuh, W. Wegscheider, T. Korn, and T. Lai, *Transmission-grating-photomasked transient spin grating and its application to measurement of electron-spin ambipolar diffusion in (110) GaAs quantum wells*, Opt. Express **20**, 8192 (Mar. 2012). (Cit. on p. 114).

[Cho71] A. Y. Cho, *GaAs Epitaxy by a Molecular Beam Method: Observations of Surface Structure on the (001) Face*, J. Appl. Phys. **42**, 2074 (1971). (Cit. on pp. 1, 6).

[Cho81] A. Y. Cho and K. Y. Cheng, *Growth of extremely uniform layers by rotating substrate holder with molecular beam epitaxy for applications to electro-optic and microwave devices*, Appl. Phys. Lett. **38**, 360 (1981). (Cit. on p. 6).

[Cio07] M Ciorga, M Schlapps, A Einwanger, S Geißler, J Sadowski, W Wegscheider, and D Weiss, *TAMR effect in (Ga,Mn)As-based tunnel structures*, New Journal of Physics **9**, 351 (2007). (Cit. on p. 66).

[Cio09] M. Ciorga, A. Einwanger, U. Wurstbauer, D. Schuh, W. Wegscheider, and D. Weiss, *Electrical spin injection and detection in lateral all-semiconductor devices*, Physical Review B (Condensed Matter and Materials Physics) **79**, 165321 (Apr. 2009). (Cit. on pp. 3, 19, 52, 61, 62, 66, 67, 72).

[Cio10] M. Ciorga, A. Einwanger, U. Wurstbauer, D. Schuh, W. Wegscheider, and D. Weiss, *In-plane anisotropy of tunneling magnetoresistance and spin polarization in lateral spin injection devices with (Ga,Mn)As/GaAs spin-Esaki diode contacts*, Physica E: Low-dimensional Systems and Nanostructures **42**, 2673 (Sept. 2010). (Cit. on pp. 3, 61).

[Cio11] M. Ciorga, C. Wolf, A. Einwanger, M. Utz, D. Schuh, and D. Weiss, *Local spin valve effect in lateral (Ga,Mn)As/GaAs spin Esaki diode devices*, AIP Advances **1**, 22113 (May 2011). (Cit. on pp. 3, 19, 61, 66).

[Cio13] M. Ciorga, M. Utz, D. Schuh, D. Bougeard, and D. Weiss, *Effect of contact geometry on spin-transport signals in nonlocal (Ga,Mn)As/GaAs devices*, Phys. Rev. B **88**, 155308 (Oct. 2013). (Cit. on pp. 19, 61, 65, 66).

[Ciu02] C. Ciuti, J. P. McGuire, and L. J. Sham, *Spin Polarization of Semiconductor Carriers by Reflection off a Ferromagnet*, Phys. Rev. Lett. **89**, 156601 (Sept. 2002). (Cit. on p. 72).

[Col03] J. S. Colton, T. A. Kennedy, A. S. Bracker, D. Gammon, and J. B. Miller, *Optically oriented and detected electron spin resonance in a lightly doped n-GaAs layer*, Phys. Rev. B **67**, 165315 (Apr. 2003). (Cit. on p. 43).

[Con50] E. Conwell and V. F. Weisskopf, *Theory of Impurity Scattering in Semiconductors*, Phys. Rev. **77**, 388 (Feb. 1950). (Cit. on p. 36).

[Cou07] O. D. D. Couto, F. Iikawa, J. Rudolph, R. Hey, and P. V. Santos, *Anisotropic Spin Transport in (110) GaAs Quantum Wells*, Phys. Rev. Lett. **98**, 036603 (Jan. 2007). (Cit. on pp. 89, 109).

[Cou08] O. D. D. Couto, R. Hey, and P. V. Santos, *Spin dynamics in (110) GaAs quantum wells under surface acoustic waves*, Phys. Rev. B **78**, 153305 (Oct. 2008). (Cit. on pp. 89, 109).

[Cro05a] S. A. Crooker and D. L. Smith, *Imaging Spin Flows in Semiconductors Subject to Electric, Magnetic, and Strain Fields*, Phys. Rev. Lett. **94**, 236601 (June 2005). (Cit. on pp. 19, 25, 47, 48).

[Cro05b] S. A. Crooker, M. Furis, X. Lou, C. Adelmann, D. L. Smith, C. J. Palmstrøm, and P. A. Crowell, *Imaging Spin Transport in Lateral Ferromagnet/Semiconductor Structures*, Science **309**, 2191 (2005). (Cit. on pp. 19, 72, 73).

[Cro07] S. A. Crooker, M. Furis, X. Lou, P. A. Crowell, D. Smith, C. Adelmann, and C. J. Palmstrøm, *Optical and electrical spin injection and spin transport in hybrid Fe/GaAs devices*, J. Appl. Phys. **101**, 081716 (2007). (Cit. on pp. 19, 47, 48).

[D'A00] I. D'Amico and G. Vignale, *Theory of spin Coulomb drag in spin-polarized transport*, Phys. Rev. B **62**, 4853 (Aug. 2000). (Cit. on pp. 42, 114).

[D'A01] I. D'Amico and G. Vignale, *Spin diffusion in doped semiconductors: The role of Coulomb interactions*, Europhys. Lett. **55**, 566 (2001). (Cit. on p. 42).

[D'A02] I. D'Amico and G. Vignale, *Coulomb interaction effects in spin-polarized transport*, Phys. Rev. B **65**, 085109 (Feb. 2002). (Cit. on p. 42).

[D'A03] I. D'Amico and G. Vignale, *Spin Coulomb drag in the two-dimensional electron liquid*, Phys. Rev. B **68**, 045307 (July 2003). (Cit. on p. 42).

[D'A06] I. D'Amico and C. A. Ullrich, *Spin Coulomb drag: an intrinsic dissipation mechanism in spintronics*, physica status solidi (b) **243**, 2285 (2006). (Cit. on p. 42).

[DC03] A. Di Carlo, *Microscopic theory of nanostructured semiconductor devices: beyond the envelope-function approximation*, Semiconductor Science and Technology **18**, 1 (Jan. 2003). (Cit. on p. 20).

[DS90] S. Das Sarma, R. Jalabert, and S.-R. E. Yang, *Band-gap renormalization in semiconductor quantum wells*, Phys. Rev. B **41**, 8288 (Apr. 1990). (Cit. on p. 10).

[Das90] B. Das, S. Datta, and R. Reifenberger, *Zero-field spin splitting in a two-dimensional electron gas*, Phys. Rev. B **41**, 8278 (Apr. 1990). (Cit. on p. 2).

[Dat90] S. Datta and B. Das, *Electronic analog of the electro-optic modulator*, Appl. Phys. Lett. **56**, 665 (1990). (Cit. on pp. 16, 61).

[Dem03] W. Demtroeder. *Laser Spectroscopy - Basic Concepts and Instrumentation.* Springer Berlin, 2003 (cit. on p. 48).

[Der07] H. Dery and L. J. Sham, *Spin Extraction Theory and Its Relevance to Spintronics*, Phys. Rev. Lett. **98**, 046602 (Jan. 2007). (Cit. on p. 72).

[DiV95] D. P. DiVincenzo, *Quantum Computation*, Science **270**, 255 (1995). (Cit. on p. 2).

[Die00] T. Dietl, H. Ohno, F. Matsukura, J. Cibert, and D. Ferrand, *Zener Model Description of Ferromagnetism in Zinc-Blende Magnetic Semiconductors*, Science **287**, 1019 (2000). (Cit. on p. 13).

[Die01] T. Dietl, H. Ohno, and F. Matsukura, *Hole-mediated ferromagnetism in tetrahedrally coordinated semiconductors*, Phys. Rev. B **63**, 195205 (Apr. 2001). (Cit. on pp. 13, 21).

[Din78] R. Dingle, H. L. Störmer, A. C. Gossard, and W. Wiegmann, *Electron mobilities in modulation-doped semiconductor heterojunction superlattices*, Appl. Phys. Lett. **33**, 665 (1978). (Cit. on p. 11).

[Dir28] P. A. M. Dirac, *The Quantum Theory of the Electron*, Proc. R. Soc. Lond. A **117**, 610 (1928). (Cit. on p. 21).

[Dre55] G. Dresselhaus, *Spin-Orbit Coupling Effects in Zinc Blende Structures*, Phys. Rev. **100**, 580 (Oct. 1955). (Cit. on pp. 2, 6, 22, 23).

[Dru00] P. Drude, *Zur Elektronentheorie der Metalle*, Annalen der Physik **306**, 566 (1900). (Cit. on p. 36).

[Dru81] T. J. Drummond, H. Morkoç, K. Hess, and A. Y. Cho, *Experimental and theoretical electron mobility of modulation doped Al[sub x]Ga[sub 1 - x]As/GaAs heterostructures grown by molecular beam epitaxy*, J. Appl. Phys. **52**, 5231 (1981). (Cit. on p. 11).

[Dya08] M. I. Dyakonov. *Spin Physics in Semiconductors.* Springer Berlin Heidelberg New York, 2008 (cit. on pp. 10, 21, 22, 31, 43, 44, 76, 77).

[Dya71a] M. I. Dyakonov and V. I. Perel', *Current-induced spin orientation of electrons in semiconductors*, Physics Letters A **35**, 459 (1971). (Cit. on pp. 2, 14, 41, 119).

[Dya71b] M. I. Dyakonov and V. I. Perel', *Possibility of orienting electron spins with current*, JETP Lett. **13**, 467 (1971). (Cit. on pp. 2, 14, 41, 119).

[Dya71c] M. I. Dyakonov and V. I. Perel', *Spin Orientation of electrons associated with the interband absorption of light in semiconductors*, JETP Lett. **33**, 1053 (1971). (Cit. on pp. 2, 23, 27).

[Dya73] M. I. Dyakonov and V. I. Perel', *Hyperfine interactions in optical orientation of electrons in semiconductors*, JETP Lett. **36**, 5 (1973). (Cit. on pp. 31, 43).

[Dya74] M. I. Dyakonov and V. I. Perel', *Optical orientation in a system of electrons and lattice nuclei in semiconductors. Theory*, JETP Lett. **38**, 177 (Jan. 1974). (Cit. on pp. 31, 43).

[Dya86] M. I. Dyakonov and V. Y. Kachorovskiĭ, *Spin relaxation of two dimensional electrons in noncentrosymmetric semiconductors*, Sov. Phys. Semicond. **20**, 110 (1986). (Cit. on pp. 2, 23, 24, 88).

[Dzh02] R. I. Dzhioev, K. V. Kavokin, V. L. Korenev, M. V. Lazarev, B. Y. Meltser, M. N. Stepanova, B. P. Zakharchenya, D. Gammon, and D. S. Katzer, *Low-temperature spin relaxation in n-type GaAs*, Phys. Rev. B **66**, 245204 (Dec. 2002). (Cit. on pp. 3, 31, 32, 48, 68, 103).

[Döh04] S. Döhrmann, D. Hägele, J. Rudolph, M. Bichler, D. Schuh, and M. Oestreich, *Anomalous Spin Dephasing in (110) GaAs Quantum Wells: Anisotropy and Intersubband Effects*, Phys. Rev. Lett. **93**, 147405 (Sept. 2004). (Cit. on pp. 3, 30, 31, 33, 34, 55, 98).

[Ede90] V. Edelstein, *Spin polarization of conduction electrons induced by electric current in two-dimensional asymmetric electron systems*, Solid State Communications **73**, 233 (1990). (Cit. on pp. 2, 119).

[Edm02] K. W. Edmonds, K. Y. Wang, R. P. Campion, A. C. Neumann, N. R. S. Farley, B. L. Gallagher, and C. T. Foxon, *High-Curie-temperature $Ga_{1-x}Mn_xAs$ obtained by resistance-monitored annealing*, Appl. Phys. Lett. **81**, 4991 (2002). (Cit. on p. 13).

[Ein05] A. Einstein, *Über die von der molekularkinetischen Theorie der Wärrme geforderte Bewegung von in ruhenden Flüssigkeiten suspendierten Teilchen*, Annalen der Physik **322**, 549 (1905). (Cit. on p. 39).

[Ein09] A. Einwanger, M. Ciorga, U. Wurstbauer, D. Schuh, W. Wegscheider, and D. Weiss, *Tunneling anisotropic spin polarization in lateral (Ga,Mn)As/GaAs spin Esaki diode devices*, Appl. Phys. Lett. **95**, 152101 (2009). (Cit. on pp. 3, 61, 66).

[Eis90] J. Eisenstein, H. Stormer, L. Pfeiffer, and K. West, *Spin-dependent properties of the fractional quantum Hall effect at odd denominators*, Surface Science **229**, 21 (1990). (Cit. on p. 2).

[Eld11] P. S. Eldridge, J. Hübner, S. Oertel, R. T. Harley, M. Henini, and M. Oestreich, *Spin-orbit fields in asymmetric (001)-oriented $GaAs/Al_xGa_{1-x}As$ quantum wells*, Phys. Rev. B **83**, 041301 (Jan. 2011). (Cit. on pp. 23, 26, 116).

[Ell54] R. J. Elliott, *Theory of the Effect of Spin-Orbit Coupling on Magnetic Resonance in Some Semiconductors*, Phys. Rev. **96**, 266 (Oct. 1954). (Cit. on pp. 21, 30).

[End11] B. Endres, F. Hoffmann, C. Wolf, A. Einwanger, M. Utz, D. Schuh, G. Woltersdorf, M. Ciorga, D. Weiss, C. H. Back, and G. Bayreuther, *Bias dependence of spin injection into GaAs from Fe, FeCo, and (Ga,Mn)As contacts*, J. Appl. Phys. **109**, 07C505 (2011). (Cit. on pp. 3, 61, 63, 71).

[End12] B. Endres, M. Ciorga, R. Wagner, S. Ringer, M. Utz, D. Bougeard, D. Weiss, C. H. Back, and G. Bayreuther, *Nonuniform current and spin accumulation in a 1 mu m thick n-GaAs channel*, Appl. Phys. Lett. **100**, 092405 (2012). (Cit. on pp. 3, 61, 63, 70, 72, 73).

[Esa58] L. Esaki, *New Phenomenon in Narrow Germanium $p-n$ Junctions*, Phys. Rev. **109**, 603 (Jan. 1958). (Cit. on p. 19).

[Fab07] J. Fabian, A. Matos-Abiaguea, C. Ertler, P. Stano, and I. Zutic. *Semiconductor Spintronics*. 2007 (cit. on pp. 18, 22, 23, 27, 31, 39, 41, 51, 74).

[Far46] M. Faraday, *Experimental Researches in Electricity. Nineteenth Series*, Philosophical Transactions of the Royal Society of London **136**, 1 (1846). (Cit. on p. 45).

[Fer01] A. Fert and H. Jaffrès, *Conditions for efficient spin injection from a ferromagnetic metal into a semiconductor*, Phys. Rev. B **64**, 184420 (Oct. 2001). (Cit. on pp. 17, 18).

[Fer30] E. Fermi, *Über die magnetischen Momente der Atomkerne*, Zeitschrift für Physik **60**, 320 (5-6 1930). (Cit. on p. 42).

[Fer68] A. Fert and I. A. Campbell, *Two-Current Conduction in Nickel*, Phys. Rev. Lett. **21**, 1190 (16 Oct. 1968). (Cit. on p. 16).

[Fil00] A. T. Filip, B. H. Hoving, F. J. Jedema, B. J. van Wees, B. Dutta, and S. Borghs, *Experimental search for the electrical spin injection in a semiconductor*, Phys. Rev. B **62**, 9996 (Oct. 2000). (Cit. on p. 18).

[Fis77] G. Fishman and G. Lampel, *Spin relaxation of photoelectrons in p-type gallium arsenide*, Phys. Rev. B **16**, 820 (July 1977). (Cit. on p. 30).

[Fla00] M. E. Flatté and J. M. Byers, *Spin Diffusion in Semiconductors*, Phys. Rev. Lett. **84**, 4220 (May 2000). (Cit. on pp. 38–40).

[Fle01] K. Flensberg, T. Stibius Jensen, and N. Asger Mortensen, *Diffusion equation and spin drag in spin-polarized transport*, Phys. Rev. B **64**, 245308 (Nov. 2001). (Cit. on p. 42).

[Fra61] P. A. Franken, *Interference Effects in the Resonance Fluorescence of "Crossed" Excited Atomic States*, Phys. Rev. **121**, 508 (Jan. 1961). (Cit. on p. 48).

[Fri54] J. Friedel, *Electronic structure of primary solid solutions in metals*, Advances in Physics **3**, 446 (1954). (Cit. on p. 13).

[Fur06] M. Furis, D. L. Smith, S. A. Crooker, and J. L. Reno, *Bias-dependent electron spin lifetimes in n-GaAs and the role of donor impact ionization*, Appl. Phys. Lett. **89**, 102102 (2006). (Cit. on p. 70).

[Fur07] M Furis, D. L. Smith, S Kos, E. S. Garlid, K. S. M. Reddy, C. J. Palmstrom, P. A. Crowell, and S. A. Crooker, *Local Hanle-effect studies of spin drift and diffusion in n:GaAs epilayers and spin-transport devices*, New Journal of Physics **9**, 347 (Sept. 2007). (Cit. on pp. 3, 19, 39, 41, 48, 49, 51, 72, 73, 113).

[Fur88] J. K. Furdyna, *Diluted magnetic semiconductors*, J. Appl. Phys. **64**, R29 (1988). (Cit. on p. 11).

[Gae06] T. Gaebel, M. Domhan, I. Popa, C. Wittmann, P. Neumann, F. Jelezko, J. R. Rabeau, N. Stavrias, A. D. Greentree, S. Prawer, J. Meijer, J. Twamley, P. R. Hemmer, and J. Wrachtrup, *Room-temperature coherent coupling of single spins in diamond*, Nat Phys **2**, 408 (2006). (Cit. on p. 3).

[Gan03] S. D. Ganichev and W Prettl, *Spin photocurrents in quantum wells*, Journal of Physics: Condensed Matter **15**, 935 (2003). (Cit. on p. 2).

[Gan04] S. D. Ganichev, V. V. Bel'kov, L. E. Golub, E. L. Ivchenko, P. Schneider, S. Giglberger, J. Eroms, J. De Boeck, G. Borghs, W. Wegscheider, D. Weiss, and W. Prettl, *Experimental Separation of Rashba and Dresselhaus Spin Splittings in Semiconductor Quantum Wells*, Phys. Rev. Lett. **92**, 256601 (June 2004). (Cit. on pp. 2, 26).

[Gan06] S. Ganichev, S. Danilov, P. Schneider, V. Bel'kov, L. Golub, W. Wegscheider, D. Weiss, and W. Prettl, *Electric current-induced spin orientation in quantum well structures*, Journal of Magnetism and Magnetic Materials **300**, 127 (2006). (Cit. on p. 2).

[Ger11] N. C. Gerhardt, M. Y. Li, H. Jähme, H. Höpfner, T. Ackemann, and M. R. Hofmann, *Ultrafast spin-induced polarization oscillations with tunable lifetime in vertical-cavity surface-emitting lasers*, Appl. Phys. Lett. **99**, 151107 (2011). (Cit. on p. 3).

[Gir12] R. Giri, S. Cronenberger, M. Vladimirova, D. Scalbert, K. V. Kavokin, M. M. Glazov, M. Nawrocki, A. Lemaître, and J. Bloch, *Giant photoinduced Faraday rotation due to the spin-polarized electron gas in an n-GaAs microcavity*, Phys. Rev. B **85**, 195313 (May 2012). (Cit. on p. 3).

[Gla02] M. Glazov and E. Ivchenko, *Precession spin relaxation mechanism caused by frequent electron-electron collisions*, JETP Lett. **75**, 403 (2002). (Cit. on p. 27).

[Gla03a] M. M. Glazov, *Mechanism of the D'yakonov-Perel' spin relaxation in frequent electron-electron collisions in a quantum well with a finite width*, Physics of the Solid State **45**, 1162 (2003). (Cit. on p. 38).

[Gla03b] M. M. Glazov and E. Ivchenko, *D'yakonov-Perel' Spin Relaxation Controlled by Electron-Electron Scattering*, Journal of Superconductivity **16**, 735 (2003). (Cit. on p. 27).

[Gla04] M. Glazov and E. Ivchenko, *Effect of electron-electron interaction on spin relaxation of charge carriers in semiconductors*, JETP Lett. **99**, 1279 (2004). (Cit. on pp. 27, 38).

[Gla05] M. M. Glazov and E. Y. Sherman, *Nonexponential spin relaxation in magnetic fields in quantum wells with random spin-orbit coupling*, Phys. Rev. B **71**, 241312 (June 2005). (Cit. on pp. 33, 91).

[Gla10] M. M. Glazov, M. A. Semina, and E. Y. Sherman, *Spin relaxation in multiple (110) quantum wells*, Phys. Rev. B **81**, 115332 (Mar. 2010). (Cit. on pp. 33, 91, 96).

[Gou04] C. Gould, C. Rüster, T. Jungwirth, E. Girgis, G. M. Schott, R. Giraud, K. Brunner, G. Schmidt, and L. W. Molenkamp, *Tunneling Anisotropic Magnetoresistance: A Spin-Valve-Like Tunnel Magnetoresistance Using a Single Magnetic Layer*, Phys. Rev. Lett. **93**, 117203 (Sept. 2004). (Cit. on p. 66).

[Gou07] C. Gould, K. Pappert, G. Schmidt, and L. Molenkamp, *Magnetic Anisotropies and (Ga,Mn)As-based Spintronic Devices*, Advanced Materials **19**, 323 (2007). (Cit. on p. 64).

[Gra91] T. J. Gramila, J. P. Eisenstein, A. H. MacDonald, L. N. Pfeiffer, and K. W. West, *Mutual friction between parallel two-dimensional electron systems*, Phys. Rev. Lett. **66**, 1216 (Mar. 1991). (Cit. on p. 42).

[Gri02] V. Gridnev, *Anisotropic spin diffusion in a semiconductor quantum well*, JETP Lett. **76**, 502 (2002). (Cit. on p. 109).

[Gri09] M. Griesbeck, M. M. Glazov, T. Korn, E. Y. Sherman, D. Waller, C. Reichl, D. Schuh, W. Wegscheider, and C. Schüller, *Cyclotron effect on coherent spin precession of two-dimensional electrons*, Phys. Rev. B **80**, 241314 (Dec. 2009). (Cit. on pp. 28, 81).

[Gri12a] M. Griesbeck, M. M. Glazov, E. Y. Sherman, D. Schuh, W. Wegscheider, C. Schüller, and T. Korn, *Strongly anisotropic spin relaxation revealed by resonant spin amplification in (110) GaAs quantum wells*, Phys. Rev. B **85**, 085313 (Feb. 2012). (Cit. on pp. 3, 55, 81, 89, 92, 93, 95, 96, 102).

[Gri12b] M. Griesbeck. "Spin dynamics in high-mobility two-dimensional electron systems embedded in GaAs/AlGaAs quantum wells". PhD thesis. Universität Regensburg, 2012 (cit. on pp. 3, 9, 16, 23–25, 28, 53, 55, 81–85, 87–89, 96, 100, 102, 117, 118, 123).

[Gru06] M. Grundmann. *The Physics of Semiconductors. An Introduction Including Devices and Nanophysics*. Springer Berlin Heidelberg New York, 2006 (cit. on pp. 7, 10, 18, 20, 36, 37, 39, 63, 99).

[Guh98] S. Guha, Q. Cai, M. Chandrasekhar, H. R. Chandrasekhar, H. Kim, A. D. Alvarenga, R. Vogelgesang, A. K. Ramdas, and M. R. Melloch, *Photoluminescence of short-period GaAs/AlAs superlattices: A hydrostatic pressure and temperature study*, Phys. Rev. B **58**, 7222 (Sept. 1998). (Cit. on p. 83).

[HM10] A. Hernández-Mínguez, K. Biermann, S. Lazić, R. Hey, and P. V. Santos, *Kerr detection of acoustic spin transport in GaAs (110) quantum wells*, Appl. Phys. Lett. **97**, 242110 (2010). (Cit. on pp. 89, 109).

[Hal03a] K. C. Hall, W. H. Lau, K. Gündogdu, M. E. Flatté, and T. F. Boggess, *Nonmagnetic semiconductor spin transistor*, Appl. Phys. Lett. **83**, 2937 (2003). (Cit. on p. 2).

[Hal03b] K. C. Hall, K. Gündoğdu, E. Altunkaya, W. H. Lau, M. E. Flatté, T. F. Boggess, J. J. Zinck, W. B. Barvosa-Carter, and S. L. Skeith, *Spin relaxation in (110) and (001) InAs/GaSb superlattices*, Phys. Rev. B **68**, 115311 (Sept. 2003). (Cit. on p. 22).

[Hal62] R. N. Hall, G. E. Fenner, J. D. Kingsley, T. J. Soltys, and R. O. Carlson, *Coherent Light Emission From GaAs Junctions*, Phys. Rev. Lett. **9**, 366 (Nov. 1962). (Cit. on p. 1).

[Ham06] K. Hamaya, T. Taniyama, T. Koike, and Y. Yamazaki, *Effect of the shape anisotropy on the magnetic configuration of (Ga,Mn)As and its evolution with temperature*, J. Appl. Phys. **99**, 123901 (2006). (Cit. on p. 65).

[Ham99] P. R. Hammar, B. R. Bennett, M. J. Yang, and M. Johnson, *Observation of Spin Injection at a Ferromagnet-Semiconductor Interface*, Phys. Rev. Lett. **83**, 203 (July 1999). (Cit. on p. 18).

[Han03] A. T. Hanbicki, O. M. J. van 't Erve, R. Magno, G. Kioseoglou, C. H. Li, B. T. Jonker, G. Itskos, R. Mallory, M. Yasar, and A. Petrou, *Analysis of the transport process providing spin injection through an Fe/AlGaAs Schottky barrier*, Appl. Phys. Lett. **82**, 4092 (2003). (Cit. on p. 18).

[Han91] W. Hanle, *Über magnetische Beeinflussung der Polarisation der Resonanzfluoreszenz*, Zeitschrift für Physik D Atoms, Molecules and Clusters **18**, 5 (1991). (Cit. on p. 48).

[Har76] J. W. Harrison and J. R. Hauser, *Alloy scattering in ternary III-V compounds*, Phys. Rev. B **13**, 5347 (June 1976). (Cit. on p. 82).

[Has10] M. Z. Hasan and C. L. Kane, *Colloquium : Topological insulators*, Rev. Mod. Phys. **82**, 3045 (Nov. 2010). (Cit. on p. 2).

[Has97] T. Hassenkam, S. Pedersen, K. Baklanov, A. Kristensen, C. B. Sorensen, P. E. Lindelof, F. G. Pikus, and G. E. Pikus, *Spin splitting and weak localization in (110) GaAs/$Al_xGa_{1-x}As$ quantum wells*, Phys. Rev. B **55**, 9298 (Apr. 1997). (Cit. on pp. 2, 24).

[Hay01] T. Hayashi, Y. Hashimoto, S. Katsumoto, and Y. Iye, *Effect of low-temperature annealing on transport and magnetism of diluted magnetic semiconductor (Ga, Mn)As*, Appl. Phys. Lett. **78**, 1691 (2001). (Cit. on p. 13).

[Hil02] D. J. Hilton and C. L. Tang, *Optical Orientation and Femtosecond Relaxation of Spin-Polarized Holes in GaAs*, Phys. Rev. Lett. **89**, 146601 (Sept. 2002). (Cit. on pp. 29, 41, 89).

[Hir99] J. E. Hirsch, *Spin Hall Effect*, Phys. Rev. Lett. **83**, 1834 (Aug. 1999). (Cit. on p. 41).

[Hof09] F. Hoffmann, G. Woltersdorf, W. Wegscheider, A. Einwanger, D. Weiss, and C. H. Back, *Mapping the magnetic anisotropy in (Ga,Mn)As nanostructures*, Phys. Rev. B **80**, 054417 (Aug. 2009). (Cit. on p. 65).

[Hoh06] P. E. Hohage, G. Bacher, D. Reuter, and A. D. Wieck, *Coherent spin oscillations in bulk GaAs at room temperature*, Appl. Phys. Lett. **89**, 231101 (2006). (Cit. on pp. 3, 33).

[Hol06] V. Holý, Z. Matăj, O. Pacherová, V. Novák, M. Cukr, K. Olejník, and T. Jungwirth, *Mn incorporation in as-grown and annealed (Ga,Mn)As layers studied by x-ray diffraction and standing-wave fluorescence*, Phys. Rev. B **74**, 245205 (Dec. 2006). (Cit. on p. 11).

[Hol07] M. Holub, J. Shin, D. Saha, and P. Bhattacharya, *Electrical Spin Injection and Threshold Reduction in a Semiconductor Laser*, Phys. Rev. Lett. **98**, 146603 (Apr. 2007). (Cit. on p. 3).

[Hu11] C. Hu, H. Ye, G. Wang, H. Tian, W. Wang, W. Wang, B. Liu, and X. Marie, *Room temperature spin diffusion in (110) GaAs/AlGaAs quantum wells*, Nanoscale Research Letters **6**, 149 (2011). (Cit. on p. 109).

[Hua12] J. Huang, Y. S. Chen, A. Ludwig, D. Reuter, A. D. Wieck, and G. Bacher, *Electron-nuclei spin coupling in GaAs—Free versus localized electrons*, Appl. Phys. Lett. **100**, 132103 (2012). (Cit. on p. 76).

[Hun67] R. P. Hunt, *Magneto-Optic Scattering from Thin Solid Films*, J. Appl. Phys. **38**, 1652 (1967). (Cit. on p. 46).

[Häg01] D Hägele, J Hübner, W. Rühle, and M Oestreich, *Coherent dynamics of coupled electron and hole spins in semiconductors*, Solid State Communications **120**, 73 (2001). (Cit. on p. 2).

[Häg98] D. Hägele, M. Oestreich, W. W. Rühle, N. Nestle, and K. Eberl, *Spin transport in GaAs*, Appl. Phys. Lett. **73**, 1580 (1998). (Cit. on pp. 3, 40).

[Hüb11] J. Hübner, S. Kunz, S. Oertel, D. Schuh, M. Pochwała, H. T. Duc, J. Förstner, T. Meier, and M. Oestreich, *Electron g-factor anisotropy in symmetric (110)-oriented GaAs quantum wells*, Phys. Rev. B **84**, 041301 (July 2011). (Cit. on pp. 23, 88, 89).

[Iba10] S. Iba, S. Koh, and H. Kawaguchi, *Room temperature gate modulation of electron spin relaxation time in (110)-oriented GaAs/AlGaAs quantum wells*, Appl. Phys. Lett. **97**, 202102 (Nov. 2010). (Cit. on p. 34).

[Ino09] T. Inokuchi, T. Marukame, M. Ishikawa, H. Sugiyama, and Y. Saito, *Electrical Spin Injection into n-GaAs Channels and Detection through MgO/CoFeB Electrodes*, Applied Physics Express **2**, 023006 (2009). (Cit. on p. 66).

[Ivc05] E. Ivchenko. *Optical Spectroscopy of Semiconductor Nanostructures.* Alpha Science International, Harrow, 2005 (cit. on p. 30).

[Ivc08] E. L. Ivchenko and S. A. Tarasenko, *Pure spin photocurrents*, Semiconductor Science and Technology **23**, 114007 (2008). (Cit. on p. 114).

[Ivc73] E. Ivchenko, *Spin relaxation of free carriers in noncentrosymmetric semiconductors in a longitudinal magnetic field*, Sov. Phys. Solid State **15**, 1048 (1973). (Cit. on p. 29).

[Ivc78] E. Ivchenko and G. Pikus, *New photogalvanic effect in gyrotropic crystals*, JETP Lett. **27**, 604 (1978). (Cit. on p. 119).

[Ivc96] E. L. Ivchenko, A. Y. Kaminski, and U. Rössler, *Heavy-light hole mixing at zinc-blende (001) interfaces under normal incidence*, Phys. Rev. B **54**, 5852 (Aug. 1996). (Cit. on p. 22).

[JH02] E. Johnston-Halperin, D. Lofgreen, R. K. Kawakami, D. K. Young, L. Coldren, A. C. Gossard, and D. D. Awschalom, *Spin-polarized Zener tunneling in (Ga,Mn)As*, Phys. Rev. B **65**, 041306 (Jan. 2002). (Cit. on pp. 3, 19).

[Jac99] J. D. Jackson. *Classical Electrodynamics.* New York: Wiley, 1999 (cit. on p. 21).

[Jaf02] H. Jaffrès and A. Fert, *Spin injection from a ferromagnetic metal into a semiconductor*, J. Appl. Phys. **91**, 8111 (2002). (Cit. on p. 17).

[Jeu97] P. L. Jeune, D Robart, X Marie, T Amand, M Brousseau, J Barrau, V Kalevich, and D Rodichev, *Anisotropy of the electron Landé g factor in quantum wells*, Semiconductor Science and Technology **12**, 380 (1997). (Cit. on p. 23).

[Ji07] Y Ji, A. Hoffmann, J. S. Jiang, J. B. Pearson, and S. Bader, *Non-local spin injection in lateral spin valves*, Journal of Physics D: Applied Physics **40, Number 5**, 1280 (2007). (Cit. on p. 66).

[Jia05] X. Jiang, R. Wang, R. M. Shelby, R. M. Macfarlane, S. R. Bank, J. S. Harris, and S. S. P. Parkin, *Highly Spin-Polarized Room-Temperature Tunnel Injector for Semiconductor Spintronics using MgO(100)*, Phys. Rev. Lett. **94**, 056601 (Feb. 2005). (Cit. on p. 19).

[Joh00] M. Johnson, *Dynamic nuclear polarization by spin injection*, Appl. Phys. Lett. **77**, 1680 (2000). (Cit. on p. 76).

[Joh85] M. Johnson and R. H. Silsbee, *Interfacial charge-spin coupling: Injection and detection of spin magnetization in metals*, Phys. Rev. Lett. **55**, 1790 (Oct. 1985). (Cit. on p. 2).

[Joh88] M. Johnson and R. H. Silsbee, *Electron spin injection and detection at a ferromagnetic-paramagnetic interface (invited)*, J. Appl. Phys. **63**, 3934 (1988). (Cit. on p. 2).

[Joh91] M. Johnson, *Analysis of anomalous multilayer magnetoresistance within the thermomagnetoelectric system*, Phys. Rev. Lett. **67**, 3594 (Dec. 1991). (Cit. on p. 18).

[Jul75] M. Julliere, *Tunneling between ferromagnetic films*, Physics Letters A **54**, 225 (1975). (Cit. on p. 18).

[Jun05] T. Jungwirth, K. Y. Wang, J. Ma šek, K. W. Edmonds, J. König, J. Sinova, M. Polini, N. A. Goncharuk, A. H. MacDonald, M. Sawicki, A. W. Rushforth, R. P. Campion, L. X. Zhao, C. T. Foxon, and B. L. Gallagher, *Prospects for high temperature ferromagnetism in (Ga,Mn)As semiconductors*, Phys. Rev. B **72**, 165204 (Oct. 2005). (Cit. on p. 13).

[Jun06] T. Jungwirth, J. Sinova, J. Ma šek, J. Ku čera, and A. H. MacDonald, *Theory of ferromagnetic (III,Mn)V semiconductors*, Rev. Mod. Phys. **78**, 809 (Aug. 2006). (Cit. on p. 13).

[Jus95] B. Jusserand, D. Richards, G. Allan, C. Priester, and B. Etienne, *Spin orientation at semiconductor heterointerfaces*, Phys. Rev. B **51**, 4707 (7 Feb. 1995). (Cit. on p. 23).

[Kai03] J. Kainz. "Theorie der Spinrelaxation und Intersubband Absorbtion in Halbleiter Quantenstrukturen". PhD thesis. Universität Regensburg, 2003 (cit. on p. 24).

[Kal90] V. K. Kalevich and V. L. Korenev, *Effect of electric field on the optical orientation of 2D electrons*, JETP Lett. **52**, 230 (1990). (Cit. on p. 122).

[Kam11] A. Kamra and B. Ghosh, *The role of electron-electron scattering in spin transport*, J. Appl. Phys. **109**, 024501 (2011). (Cit. on pp. 37, 114).

[Kan05] C. L. Kane and E. J. Mele, *Z_2 Topological Order and the Quantum Spin Hall Effect*, Phys. Rev. Lett. **95**, 146802 (Sept. 2005). (Cit. on p. 2).

[Kar03] O. Z. Karimov, G. H. John, R. T. Harley, W. H. Lau, M. E. Flatté, M. Henini, and R. Airey, *High Temperature Gate Control of Quantum Well Spin Memory*, Phys. Rev. Lett. **91**, 246601 (Dec. 2003). (Cit. on pp. 34, 117, 118).

[Kas06] S. Kasap and P. Capper, eds. *Springer Handbook of Electronic and Photonic Materials*. Springer Science, 2006 (cit. on pp. 6, 8).

[Kas59] T. Kasuya, *Effects of s-d Interaction on Transport Phenomena*, Progress of Theoretical Physics **22**, 227 (1959). (Cit. on p. 13).

[Kat04a] Y. K. Kato, R. C. Myers, A. C. Gossard, and D. D. Awschalom, *Current-Induced Spin Polarization in Strained Semiconductors*, Phys. Rev. Lett. **93**, 176601 (Oct. 2004). (Cit. on p. 119).

[Kat04b] Y. K. Kato, R. C. Myers, A. C. Gossard, and D. D. Awschalom, *Observation of the Spin Hall Effect in Semiconductors*, Science **306**, 1910 (2004). (Cit. on pp. 2, 14, 41, 119).

[Kav01] K. V. Kavokin, *Anisotropic exchange interaction of localized conduction-band electrons in semiconductors*, Phys. Rev. B **64**, 075305 (July 2001). (Cit. on p. 31).

[Ker77] J. Kerr, *On rotation of the plane of polarization by reflection from the pole of a magnet*, Philosophical Magazine Series **3**, 321 (1877). (Cit. on p. 45).

[Ker78] J. Kerr, *On reflection of polarized light from the equatorial surface of a magnet*, Philosophical Magazine Series **5**, 161 (1878). (Cit. on p. 45).

[Kie12] T. Kiessling, J.-H. Quast, A. Kreisel, T. Henn, W. Ossau, and L. W. Molenkamp, *Spatially resolved photocarrier energy relaxation in low-doped bulk GaAs*, Phys. Rev. B **86**, 161201 (Oct. 2012). (Cit. on p. 117).

[Kik00] J. M. Kikkawa and D. D. Awschalom, *All-Optical Magnetic Resonance in Semiconductors*, Science **287**, 473 (2000). (Cit. on pp. 44, 76, 80).

[Kik98] J. M. Kikkawa and D. D. Awschalom, *Resonant Spin Amplification in n-Type GaAs*, Phys. Rev. Lett. **80**, 4313 (May 1998). (Cit. on pp. 3, 32, 33, 40, 89).

[Kik99] J. M. Kikkawa and D. D. Awschalom, *Lateral drag of spin coherence in gallium arsenide*, Nature **397**, 139 (1999). (Cit. on p. 3).

[Kil63] J. S. Kilby. "Miniature Semiconductor Integrated Circuit". Pat. 3115581 A. 1963 (cit. on p. 1).

[Kil76] J. S. Kilby, *Invention of the integrated circuit*, IEEE Transactions on Electron Devices **23**, 648 (1976). (Cit. on p. 1).

[Kim01] A. V. Kimel, F. Bentivegna, V. N. Gridnev, V. V. Pavlov, R. V. Pisarev, and T. Rasing, *Room-temperature ultrafast carrier and spin dynamics in GaAs probed by the photoinduced magneto-optical Kerr effect*, Phys. Rev. B **63**, 235201 (May 2001). (Cit. on pp. 3, 33).

[Kim92] D.-S. Kim, J. Shah, J. E. Cunningham, T. C. Damen, S. Schmitt-Rink, and W. Schäfer, *Carrier-carrier scattering in a degenerate electron system: Strong inhibition of scattering near the Fermi edge*, Phys. Rev. Lett. **68**, 2838 (May 1992). (Cit. on p. 96).

[Kit96] C. Kittel. *Introduction to Solid State Physics*. Wiley, 1996 (cit. on pp. 6, 7).

[Kle85a] D. A. Kleinman, *Theory of excitons in semiconductor quantum wells containing degenerate electrons or holes*, Phys. Rev. B **32**, 3766 (Sept. 1985). (Cit. on p. 54).

[Kle85b] D. A. Kleinman and R. C. Miller, *Band-gap renormalization in semiconductor quantum wells containing carriers*, Phys. Rev. B **32**, 2266 (Aug. 1985). (Cit. on p. 10).

[Kli05] C. Klingshirn. *Semiconductor Optics*. Springer Berlin, 2005 (cit. on p. 46).

[Kli80] K. v. Klitzing, G. Dorda, and M. Pepper, *New Method for High-Accuracy Determination of the Fine-Structure Constant Based on Quantized Hall Resistance*, Phys. Rev. Lett. **45**, 494 (Aug. 1980). (Cit. on p. 1).

[Kni49] W. D. Knight, *Nuclear Magnetic Resonance Shift in Metals*, Phys. Rev. **76**, 1259 (Oct. 1949). (Cit. on p. 43).

[Koh01] M. Kohda, Y. Ohno, K. Takamura, F. Matsukura, and H. Ohno, *A Spin Esaki Diode*, Japanese Journal of Applied Physics **40**, L1274 (2001). (Cit. on pp. 3, 19).

[Koo09] H. C. Koo, J. H. Kwon, J. Eom, J. Chang, S. H. Han, and M. Johnson, *Control of Spin Precession in a Spin-Injected Field Effect Transistor*, Science **325**, 1515 (2009). (Cit. on p. 2).

[Kor09] J. D. Koralek, C. P. Weber, J. Orenstein, B. A. Bernevig, S.-C. Zhang, S. Mack, and D. D. Awschalom, *Emergence of the persistent spin helix in semiconductor quantum wells*, Nature **458**, 610 (2009). (Cit. on pp. 2, 23, 26).

[Kor10] T. Korn, *Time-resolved studies of electron and hole spin dynamics in modulation-doped GaAs/AlGaAs quantum wells*, Physics Reports **494**, 415 (Sept. 2010). (Cit. on pp. 15, 24, 54, 89).

[Kot07] P. Kotissek, M. Bailleu, M. Sperl, A. Spitzer, D. Schuh, W. Wegscheider, C. H. Back, and G. Bayreuther, *Cross-sectional imaging of spin injection into a semiconductor*, Nature Physics **3**, 872 (2007). (Cit. on pp. 72, 73).

[Kre96] O. Krebs and P. Voisin, *Giant Optical Anisotropy of Semiconductor Heterostructures with No Common Atom and the Quantum-Confined Pockels Effect*, Phys. Rev. Lett. **77**, 1829 (Aug. 1996). (Cit. on p. 22).

[Kri07] J. J. Krich and B. I. Halperin, *Cubic Dresselhaus Spin-Orbit Coupling in 2D Electron Quantum Dots*, Phys. Rev. Lett. **98**, 226802 (May 2007). (Cit. on p. 23).

[Kro01] H. Kroemer, *Nobel Lecture: Quasielectric fields and band offsets: teaching electrons new tricks*, Reviews of Modern Physics **73** (2001). (Cit. on pp. 1, 25).

[Kro63] H Kroemer, *A proposed class of hetero-junction injection lasers*, Proceedings of the IEEE **51**, 1782 (1963). (Cit. on p. 1).

[Kru11] V. Krueckl, M. Wimmer, I. Adagideli, J. Kuipers, and K. Richter, *Weak Localization in Mesoscopic Hole Transport: Berry Phases and Classical Correlations*, Phys. Rev. Lett. **106**, 146801 (Apr. 2011). (Cit. on p. 27).

[Kuh97] P. L. Kuhns, A. Kleinhammes, T. Schmiedel, W. G. Moulton, P. Chabrier, S. Sloan, E. Hughes, and C. R. Bowers, *Magnetic-field dependence of the optical Overhauser effect in GaAs*, Phys. Rev. B **55**, 7824 (Mar. 1997). (Cit. on pp. 44, 79).

[Kuk89] I. V. Kukushkin, K. von Klitzing, K. Ploog, V. E. Kirpichev, and B. N. Shepel, *Reduction of the electron density in GaAs-$Al_xGa_{1-x}As$ single heterojunctions by continuous photoexcitation*, Phys. Rev. B **40**, 4179 (Aug. 1989). (Cit. on p. 55).

[Kun12] Y. Kunihashi, M. Kohda, H. Sanada, H. Gotoh, T. Sogawa, and J. Nitta, *Proposal of spin complementary field effect transistor*, Appl. Phys. Lett. **100**, 113502 (2012). (Cit. on pp. 2, 26).

[Kwa95] J. S. Kwak, H. N. Kim, H. K. Baik, J.-L. Lee, H. Kim, H. M. Park, and S. K. Noh, *Thermally stable, low-resistance PdGe-based ohmic contacts to high–low doped n-GaAs*, Appl. Phys. Lett. **67**, 2465 (1995). (Cit. on p. 62).

[Lam68] G. Lampel, *Nuclear Dynamic Polarization by Optical Electronic Saturation and Optical Pumping in Semiconductors*, Phys. Rev. Lett. **20**, 491 (Mar. 1968). (Cit. on pp. 43, 78).

[Lan77] L. D. Landau and E. M. Lifshitz. *Quantum mechanics - Non relativistic theory.* Pergamon Press Oxford, 1977 (cit. on p. 11).

[Lar08] A. V. Larionov and L. E. Golub, *Electric-field control of spin-orbit splittings in $GaAs/Al_xGa_{1-x}As$ coupled quantum wells*, Phys. Rev. B **78**, 033302 (July 2008). (Cit. on p. 26).

[Lau02] W. H. Lau and M. E. Flatté, *Tunability of electron spin coherence in III-V quantum wells*, J. Appl. Phys. **91**, 8682 (2002). (Cit. on p. 117).

[Law71] P. Lawaetz, *Valence-Band Parameters in Cubic Semiconductors*, Phys. Rev. B **4**, 3460 (Nov. 1971). (Cit. on p. 54).

[Lee10] J. Lee, W. Falls, R. Oszwałdowski, and I. Žutić, *Spin modulation in semiconductor lasers*, Appl. Phys. Lett. **97**, 041116 (2010). (Cit. on p. 3).

[Lee99] W. Y. Lee, S. Gardelis, B.-C. Choi, Y. B. Xu, C. G. Smith, C. H. W. Barnes, D. A. Ritchie, E. H. Linfield, and J. A. C. Bland, *Magnetization reversal and magnetoresistance in a lateral spin-injection device*, J. Appl. Phys. **85**, 6682 (1999). (Cit. on p. 18).

[Lev99] M. Levinshtein, M. Shur, and S. Rumyantsev. *Handbook series on Semiconductor Parameters. Vol. 2.* World Scientific, 1999 (cit. on p. 8).

[Ley07a] W. J. H. Leyland, G. H. John, R. T. Harley, M. M. Glazov, E. L. Ivchenko, D. A. Ritchie, I. Farrer, A. J. Shields, and M. Henini, *Enhanced spin-relaxation time due to electron-electron scattering in semiconductor quantum wells*, Phys. Rev. B **75**, 165309 (Apr. 2007). (Cit. on pp. 28, 38, 114).

[Ley07b] W. J. H. Leyland, R. T. Harley, M. Henini, A. J. Shields, I. Farrer, and D. A. Ritchie, *Oscillatory Dyakonov-Perel spin dynamics in two-dimensional electron gases*, Phys. Rev. B **76**, 195305 (Nov. 2007). (Cit. on pp. 23, 28, 116).

[Lim00] J.-W. Lim, J.-K. Mun, S. Nam, M.-H. Kwak, H. Kim, M.-K. Song, and D. S. Ma, *PdGe-based ohmic contacts to high-low doped n-GaAs with and without undoped cap layer*, Journal of Physics D: Applied Physics **33**, 1611 (2000). (Cit. on p. 62).

[Liu08] M.-H. Liu, S.-H. Chen, and C.-R. Chang, *Current-induced spin polarization in spin-orbit-coupled electron systems*, Phys. Rev. B **78**, 165316 (Oct. 2008). (Cit. on p. 120).

[Liv88] G. Livescu, D. Miller, D. Chemla, M. Ramaswamy, T.-Y. Chang, N. Sauer, A. Gossard, and J. English, *Free carrier and many-body effects in absorption spectra of modulation-doped quantum wells*, Quantum Electronics, IEEE Journal of **24**, 1677 (1988). (Cit. on p. 99).

[Lom07] L. Lombez, D. Lagarde, P. Renucci, T. Amand, X. Marie, B. L. Liu, W. X. Wang, Q. K. Xue, and D. M. Chen, *Optical spin orientation in (110) GaAs quantum wells at room temperature*, physica status solidi (c) **4**, 475 (2007). (Cit. on p. 94).

[Los98] D. Loss and D. P. DiVincenzo, *Quantum computation with quantum dots*, Phys. Rev. A **57**, 120 (Jan. 1998). (Cit. on p. 2).

[Lou06] X. Lou, C. Adelmann, M. Furis, S. A. Crooker, C. J. Palmstrøm, and P. A. Crowell, *Electrical Detection of Spin Accumulation at a Ferromagnet-Semiconductor Interface*, Phys. Rev. Lett. **96**, 176603 (May 2006). (Cit. on pp. 52, 66, 72).

[Lou07] X. Lou, C. Adelmann, S. A. Crooker, E. S. Garlid, J. Zhang, K. S. Madhukar Reddy, S. D. Flexner, C. J. Palmstrøm, and P. A. Crowell, *Electrical detection of spin transport in lateral ferromagnet-semiconductor devices*, Nature Physics **3**, 197 (2007). (Cit. on pp. 52, 66, 67).

[Lü07] C. Lü, J. Cheng, M. Wu, and I. da Cunha Lima, *Spin relaxation time, spin dephasing time and ensemble spin dephasing time in n-type GaAs quantum wells*, Physics Letters A **365**, 501 (2007). (Cit. on p. 27).

[Mac05] A. H. MacDonald, P. Schiffer, and N. Samarth, *Ferromagnetic semiconductors: moving beyond (Ga,Mn)As*, Nature Materials **4**, 195 (2005). (Cit. on p. 12).

[Mac99] H. M. MacDonald, *Zeroes of the Spherical Hormonic $P_n^m(\mu)$ considerd as a Function of n*, Proceedings of the London Mathematical Society **s1-31**, 264 (1899). (Cit. on p. 41).

[Mai96] M. Z. Maialle, *Spin relaxation of electrons in p -doped quantum wells via the electron-hole exchange interaction*, Phys. Rev. B **54**, 1967 (July 1996). (Cit. on pp. 97, 98).

[Mal00] A Malinowski and R. Harley, *Dynamic nuclear Overhauser shifts in Larmor beats from a quantum well*, Solid State Communications **114**, 419 (2000). (Cit. on pp. 44, 80, 123).

[Mal01] A Malinowski, M. Brand, and R. Harley, *Nuclear effects in ultrafast quantum-well spin-dynamics*, Physica E: Low-dimensional Systems and Nanostructures **10**, 13 (2001). (Cit. on pp. 44, 80, 123).

[Man68] H. M. Manasevit, *SINGLE-CRYSTAL GALLIUM ARSENIDE ON INSULATING SUBSTRATES*, Applied Physics Letters **12**, 156 (1968). (Cit. on p. 1).

[Mar83] V. A. Marushchak, M. Stepanova, and A. Titkov, *Spin relaxation of conduction electrons in moderately doped gallium arsenide crystals*, Sov. Phys. Solid State **25**, 2035 (1983). (Cit. on p. 23).

[Mar85] E. D. Marshall, W. X. Chen, C. S. Wu, S. S. Lau, and T. F. Kuech, *Non-alloyed ohmic contact to n-GaAs by solid phase epitaxy*, Appl. Phys. Lett. **47**, 298 (1985). (Cit. on p. 62).

[Mat98] F. Matsukura, H. Ohno, A. Shen, and Y. Sugawara, *Transport properties and origin of ferromagnetism in (Ga,Mn)As*, Phys. Rev. B **57**, R2037 (Jan. 1998). (Cit. on p. 13).

[Mav00] P. Mavropoulos, N. Papanikolaou, and P. H. Dederichs, *Complex Band Structure and Tunneling through Ferromagnet / Insulator / Ferromagnet Junctions*, Phys. Rev. Lett. **85**, 1088 (July 2000). (Cit. on p. 20).

[Maŝ04] J. Maŝek and F. Máca, *Interstitial Mn in (Ga,Mn)As: Binding energy and exchange coupling*, Phys. Rev. B **69**, 165212 (Apr. 2004). (Cit. on p. 11).

[McG03] J. P. McGuire, C. Ciuti, and L. J. Sham, *Theory of Spin Orientation of Semiconductor Carriers at a Ferromagnetic Interface*, arXiv.org > cond-mat > arXiv:cond-mat/0302088v1 (2003). (Cit. on p. 72).

[McN76] J. A. McNeil and W. G. Clark, *Nuclear quadrupolar spin-lattice relaxation in some III-V compounds*, Phys. Rev. B **13**, 4705 (June 1976). (Cit. on p. 44).

[Mei07] L. Meier, G. Salis, I. Shorubalko, E. Gini, S. Schon, and K. Ensslin, *Measurement of Rashba and Dresselhaus spin-orbit magnetic fields*, Nature Physics **3**, 650 (2007). (Cit. on p. 26).

[Mei84] F. Meier and B. Zakharchenya. *Optical Orientation Vol. 8 Modern Problems in Condensed Matter Science*. North Holland, Amsterdam, 1984 (cit. on pp. 25, 42–44, 77, 78, 124).

[Mer02] I. A. Merkulov, A. L. Efros, and M. Rosen, *Electron spin relaxation by nuclei in semiconductor quantum dots*, Phys. Rev. B **65**, 205309 (Apr. 2002). (Cit. on p. 31).

[Mil84] D. A. B. Miller, D. S. Chemla, T. C. Damen, A. C. Gossard, W. Wiegmann, T. H. Wood, and C. A. Burrus, *Band-Edge Electroabsorption in Quantum Well Structures: The Quantum-Confined Stark Effect*, Phys. Rev. Lett. **53**, 2173 (Nov. 1984). (Cit. on p. 16).

[Mim80] T. Mimura, S. Hiyamizu, T. Fujii, and K. Nanbu, *A New Field-Effect Transistor with Selectively Doped GaAs/n-$Al_xGa_{1-x}As$ Heterojunctions*, Japanese Journal of Applied Physics **19**, L225 (1980). (Cit. on p. 1).

[Moo65] G. E. Moore, *Cramming More Components onto Integrated Circuits*, Electronics **38**, 114 (Apr. 1965). (Cit. on p. 1).

[Moo90] P. M. Mooney, *Deep donor levels (DX centers) in III-V semiconductors*, J. Appl. Phys. **67**, R1 (1990). (Cit. on pp. 82, 83).

[Mos54] T. S. Moss, *The Interpretation of the Properties of Indium Antimonide*, Proceedings of the Physical Society. Section B **67**, 775 (1954). (Cit. on p. 10).

[Mot02] V. F. Motsnyi, J. D. Boeck, J. Das, W. V. Roy, G. Borghs, E. Goovaerts, and V. I. Safarov, *Electrical spin injection in a ferromagnet/tunnel barrier/semiconductor heterostructure*, Appl. Phys. Lett. **81**, 265 (2002). (Cit. on p. 19).

[Mot64] N. Mott, *Electrons in transition metals*, Advances in Physics **13**, 325 (1964). (Cit. on p. 16).

[Mül08] G. M. Müller, M. Römer, D. Schuh, W. Wegscheider, J. Hübner, and M. Oestreich, *Spin Noise Spectroscopy in GaAs (110) Quantum Wells: Access to Intrinsic Spin Lifetimes and Equilibrium Electron Dynamics*, Phys. Rev. Lett. **101**, 206601 (Nov. 2008). (Cit. on pp. 3, 30, 33, 88, 92).

[Nit97] J. Nitta, T. Akazaki, H. Takayanagi, and T. Enoki, *Gate Control of Spin-Orbit Interaction in an Inverted $In_{0.53}Ga_{0.47}As/In_{0.52}Al_{0.48}As$ Heterostructure*, Phys. Rev. Lett. **78**, 1335 (Feb. 1997). (Cit. on p. 2).

[Odo06] B. Odom, D. Hanneke, B. D'Urso, and G. Gabrielse, *New Measurement of the Electron Magnetic Moment Using a One-Electron Quantum Cyclotron*, Phys. Rev. Lett. **97**, 030801 (July 2006). (Cit. on p. 14).

[Oes95] M. Oestreich and W. W. Rühle, *Temperature Dependence of the Electron Landé g Factor in GaAs*, Phys. Rev. Lett. **74**, 2315 (12 Mar. 1995). (Cit. on p. 22).

[Oes96] M. Oestreich, S. Hallstein, A. P. Heberle, K. Eberl, E. Bauser, and W. W. Rühle, *Temperature and density dependence of the electron Landé g factor in semiconductors*, Phys. Rev. B **53**, 7911 (Mar. 1996). (Cit. on p. 22).

[Ohn96] H. Ohno, A. Shen, F. Matsukura, A. Oiwa, A. Endo, S. Katsumoto, and Y. Iye, *(Ga,Mn)As: A new diluted magnetic semiconductor based on GaAs*, Applied Physics Letters **69**, 363 (1996). (Cit. on pp. 11, 13).

[Ohn98] H. Ohno, *Making Nonmagnetic Semiconductors Ferromagnetic*, Appl. Phys. Lett. **281**, 951 (1998). (Cit. on pp. 11–13).

[Ohn99a] Y. Ohno, D. K. Young, B. Beschoten, F. Matsukura, H. Ohno, and D. D. Awschalom, *Electrical spin injection in a ferromagnetic semiconductor heterostructure*, Nature Physics **402**, 790 (1999). (Cit. on pp. 3, 19).

[Ohn99b] Y. Ohno, R. Terauchi, T. Adachi, F. Matsukura, and H. Ohno, *Spin Relaxation in GaAs(110) Quantum Wells*, Phys. Rev. Lett. **83**, 4196 (Nov. 1999). (Cit. on pp. 3, 33, 88).

[Olb09] P. Olbrich, J. Allerdings, V. V. Bel'kov, S. A. Tarasenko, D. Schuh, W. Wegscheider, T. Korn, C. Schüller, D. Weiss, and S. D. Ganichev, *Magneto-gyrotropic photogalvanic effect and spin dephasing in (110)-grown $GaAs/Al_xGa_{1-x}As$ quantum well structures*, Physical Review B (Condensed Matter and Materials Physics) **79**, 245329 (June 2009). (Cit. on pp. 25, 34, 87, 89).

[Ove53a] A. W. Overhauser, *Paramagnetic Relaxation in Metals*, Phys. Rev. **89**, 689 (Feb. 1953). (Cit. on p. 31).

[Ove53b] A. W. Overhauser, *Polarization of Nuclei in Metals*, Phys. Rev. **92**, 411 (Oct. 1953). (Cit. on p. 43).

[Pag77] D. Paget, G. Lampel, B. Sapoval, and V. I. Safarov, *Low field electron-nuclear spin coupling in gallium arsenide under optical pumping conditions*, Phys. Rev. B **15**, 5780 (June 1977). (Cit. on pp. 42, 43, 76, 77).

[Pag82] D. Paget, *Optical detection of NMR in high-purity GaAs: Direct study of the relaxation of nuclei close to shallow donors*, Phys. Rev. B **25**, 4444 (Apr. 1982). (Cit. on pp. 43, 44, 76, 79).

[Pan06] A. M. Panich, C. L. Teske, and W. Bensch, *Nuclear spin diffusion in the semiconductor $TlTaS_3$*, Phys. Rev. B **73**, 115209 (Mar. 2006). (Cit. on p. 44).

[Pap07a] K Pappert, C Gould, M Sawicki, J Wenisch, K Brunner, G Schmidt, and L. W. Molenkamp, *Detailed transport investigation of the magnetic anisotropy of (Ga,Mn)As*, New Journal of Physics **9**, 354 (2007). (Cit. on p. 64).

[Pap07b] K. Pappert, S. Hümpfner, J. Wenisch, K. Brunner, C. Gould, G. Schmidt, and L. W. Molenkamp, *Transport characterization of the magnetic anisotropy of (Ga,Mn)As*, Appl. Phys. Lett. **90**, 062109 (2007). (Cit. on p. 64).

[Pap07c] K. Pappert. "Anisotropies in (Ga,Mn)As". PhD thesis. Universität Würzburg, 2007 (cit. on p. 64).

[Par69] R. R. Parsons, *Band-To-Band Optical Pumping in Solids and Polarized Photoluminescence*, Phys. Rev. Lett. **23**, 1152 (Nov. 1969). (Cit. on p. 48).

[Per67] P. S. Pershan, *Magneto-Optical Effects*, J. Appl. Phys. **38**, 1482 (1967). (Cit. on p. 46).

[Pet05] J. R. Petta, A. C. Johnson, J. M. Taylor, E. A. Laird, A. Yacoby, M. D. Lukin, C. M. Marcus, M. P. Hanson, and A. C. Gossard, *Coherent Manipulation of Coupled Electron Spins in Semiconductor Quantum Dots*, Science **309**, 2180 (2005). (Cit. on pp. 3, 31).

[Pet84] P. M. Petroff, R. C. Miller, A. C. Gossard, and W. Wiegmann, *Impurity trapping, interface structure, and luminescence of GaAs quantum wells grown by molecular beam epitaxy*, Appl. Phys. Lett. **44**, 217 (1984). (Cit. on p. 84).

[Pfa05] S. Pfalz, R. Winkler, T. Nowitzki, D. Reuter, A. D. Wieck, D. Hägele, and M. Oestreich, *Optical orientation of electron spins in GaAs quantum wells*, Phys. Rev. B **71**, 165305 (Apr. 2005). (Cit. on pp. 15, 54, 87, 103, 104).

[Pfe06] P. Pfeffer and W. Zawadzki, *Anisotropy of spin g factor in GaAs / $Al_xGa_{1-x}As$ symmetric quantum wells*, Phys. Rev. B **74**, 233303 (Dec. 2006). (Cit. on p. 23).

[Pfe90a] P. Pfeffer and W. Zawadzki, *Conduction electrons in GaAs: Five-level k·p theory and polaron effects*, Phys. Rev. B **41**, 1561 (Jan. 1990). (Cit. on p. 23).

[Pfe90b] L. Pfeiffer, K. W. West, H. L. Stormer, J. P. Eisenstein, K. W. Baldwin, D. Gershoni, and J. Spector, *Formation of a high quality two-dimensional electron gas on cleaved GaAs*, Appl. Phys. Lett. **56**, 1697 (1990). (Cit. on p. 81).

[Pos13] A. V. Poshakinskiy and S. A. Tarasenko, *Effect of Dresselhaus spin-orbit coupling on spin dephasing in asymmetric and macroscopically symmetric (110)-grown quantum wells*, Phys. Rev. B **87**, 235301 (June 2013). (Cit. on pp. 33, 91, 92, 116).

[Pot01] S. J. Potashnik, K. C. Ku, S. H. Chun, J. J. Berry, N. Samarth, and P. Schiffer, *Effects of annealing time on defect-controlled ferromagnetism in $Ga_{1-x}Mn_xAs$*, Appl. Phys. Lett. **79**, 1495 (2001). (Cit. on p. 13).

[Pri98] G. A. Prinz, *Magnetoelectronics*, Science **282**, 1660 (1998). (Cit. on p. 12).

[Put04] W. O. Putikka and R. Joynt, *Theory of optical orientation in n-type semiconductors*, Phys. Rev. B **70**, 113201 (Sept. 2004). (Cit. on p. 33).

[Qiu00] Z. Q. Qiu and S. D. Bader, *Surface magneto-optic Kerr effect*, Review of Scientific Instruments **71**, 1243 (2000). (Cit. on p. 46).

[Qua08] J.-H. Quast, G. V. Astakhov, W. Ossau, L. W. Molenkamp, and J. Heinrich, *Lateral Spin Diffusion Probed by Two-Color Hanle-MOKE Technique*, Acta Physica Polonica A **114**, 1311 (2008). (Cit. on pp. 73, 110).

[Qua09] J.-H. Quast, G. V. Astakhov, W. Ossau, L. W. Molenkamp, J. Heinrich, S. Höfling, and A. Forchel, *Influence of light on spin diffusion in weak magnetic fields*, Phys. Rev. B **79**, 245207 (June 2009). (Cit. on pp. 57, 73, 110).

[Qua13] J.-H. Quast, T. Henn, T. Kiessling, W. Ossau, L. W. Molenkamp, D. Reuter, and A. D. Wieck, *Hot carrier effects on lateral electron spin diffusion in n-type GaAs*, Phys. Rev. B **87**, 205203 (May 2013). (Cit. on p. 115).

[Ras00] E. I. Rashba, *Theory of electrical spin injection: Tunnel contacts as a solution of the conductivity mismatch problem*, Phys. Rev. B **62**, R16267 (Dec. 2000). (Cit. on p. 18).

[Ras06] E. I. Rashba, *Spin-orbit coupling and spin transport*, Physica E: Low-dimensional Systems and Nanostructures **34**, 31 (2006). (Cit. on p. 21).

[Riz08] P. J. Rizo, A. Pugžlys, J. Liu, D. Reuter, A. D. Wieck, C. H. van der Wal, and P. H. M. van Loosdrecht, *Compact cryogenic Kerr microscope for time-resolved studies of electron spin transport in microstructures*, Review of Scientific Instruments **79**, 123904 (2008). (Cit. on p. 58).

[Roj99] A. G. Rojo, *Electron-drag effects in coupled electron systems*, Journal of Physics: Condensed Matter **11(5)**, R31 (1999). (Cit. on p. 42).

[Ros83] T. F. Rosenbaum, R. F. Milligan, M. A. Paalanen, G. A. Thomas, R. N. Bhatt, and W. Lin, *Metal-insulator transition in a doped semiconductor*, Phys. Rev. B **27**, 7509 (June 1983). (Cit. on p. 32).

[Rot59] L. M. Roth, B. Lax, and S. Zwerdling, *Theory of Optical Magneto-Absorption Effects in Semiconductors*, Phys. Rev. **114**, 90 (Apr. 1959). (Cit. on p. 22).

[Rud03] J. Rudolph, D. Hägele, H. M. Gibbs, G. Khitrova, and M. Oestreich, *Laser threshold reduction in a spintronic device*, Appl. Phys. Lett. **82**, 4516 (2003). (Cit. on p. 3).

[Rud05] J. Rudolph, S. Döhrmann, D. Hägele, M. Oestreich, and W. Stolz, *Room-temperature threshold reduction in vertical-cavity surface-emitting lasers by injection of spin-polarized electrons*, Appl. Phys. Lett. **87**, 241117 (2005). (Cit. on p. 3).

[Rud54] M. A. Ruderman and C. Kittel, *Indirect Exchange Coupling of Nuclear Magnetic Moments by Conduction Electrons*, Phys. Rev. **96**, 99 (Oct. 1954). (Cit. on p. 13).

[Rya84] J. F. Ryan, R. A. Taylor, A. J. Turberfield, A. Maciel, J. M. Worlock, A. C. Gossard, and W. Wiegmann, *Time-Resolved Photoluminescence of Two-Dimensional Hot Carriers in GaAs-AlGaAs Heterostructures*, Phys. Rev. Lett. **53**, 1841 (Nov. 1984). (Cit. on pp. 38, 54).

[Röm10] M. Römer, H. Bernien, G. Müller, D. Schuh, J. Hübner, and M. Oestreich, *Electron-spin relaxation in bulk GaAs for doping densities close to the metal-to-insulator transition*, Phys. Rev. B **81**, 075216 (Feb. 2010). (Cit. on p. 33).

[Rös10] C. Rössler, T. Feil, P. Mensch, T. Ihn, K. Ensslin, D. Schuh, and W. Wegscheider, *Gating of high-mobility two-dimensional electron gases in GaAs/AlGaAs heterostructures*, New Journal of Physics **12**, 043007 (2010). (Cit. on pp. 55, 83, 96).

[SR89] S. Schmitt-Rink, D. Chemla, and D. Miller, *Linear and nonlinear optical properties of semiconductor quantum wells*, Advances in Physics **38**, 89 (1989). (Cit. on p. 99).

[Sal01a] G. Salis, D. T. Fuchs, J. M. Kikkawa, D. D. Awschalom, Y. Ohno, and H. Ohno, *Optical Manipulation of Nuclear Spin by a Two-Dimensional Electron Gas*, Phys. Rev. Lett. **86**, 2677 (Mar. 2001). (Cit. on pp. 44, 123).

[Sal01b] G. Salis, D. D. Awschalom, Y. Ohno, and H. Ohno, *Origin of enhanced dynamic nuclear polarization and all-optical nuclear magnetic resonance in GaAs quantum wells*, Phys. Rev. B **64**, 195304 (Oct. 2001). (Cit. on pp. 44, 123).

[Sal09] G. Salis, A. Fuhrer, and S. F. Alvarado, *Signatures of dynamically polarized nuclear spins in all-electrical lateral spin transport devices*, Phys. Rev. B **80**, 115332 (Sept. 2009). (Cit. on pp. 67, 76).

[San02] H. Sanada, I. Arata, Y. Ohno, Z. Chen, K. Kayanuma, Y. Oka, F. Matsukura, and H. Ohno, *Relaxation of photoinjected spins during drift transport in GaAs*, Appl. Phys. Lett. **81**, 2788 (2002). (Cit. on p. 40).

[San06] P. Sankowski, P. Kacman, J. Majewski, and T. Dietl, *Tight-binding model of spin-polarized tunnelling in (Ga,Mn)As-based structures*, Physica E: Low-dimensional Systems and Nanostructures **32**, 375 (2006). (Cit. on p. 21).

[San07] P. Sankowski, P. Kacman, J. A. Majewski, and T. Dietl, *Spin-dependent tunneling in modulated structures of (Ga,Mn)As*, Phys. Rev. B **75**, 045306 (Jan. 2007). (Cit. on pp. 20, 72).

[Sap92] V. F. Sapega, M. Cardona, K. Ploog, E. L. Ivchenko, and D. N. Mirlin, *Spin-flip Raman scattering in GaAs / $Al_xGa_{1-x}As$ multiple quantum wells*, Phys. Rev. B **45**, 4320 (8 Feb. 1992). (Cit. on p. 23).

[Saw04] M. Sawicki, F. Matsukura, A. Idziaszek, T. Dietl, G. M. Schott, C. Ruester, C. Gould, G. Karczewski, G. Schmidt, and L. W. Molenkamp, *Temperature dependent magnetic anisotropy in (Ga,Mn)As layers*, Phys. Rev. B **70**, 245325 (Dec. 2004). (Cit. on p. 64).

[Sch00a] G. Schmidt, D. Ferrand, L. W. Molenkamp, A. T. Filip, and B. J. van Wees, *Fundamental obstacle for electrical spin injection from a ferromagnetic metal into a diffusive semiconductor*, Phys. Rev. B **62**, R4790 (Aug. 2000). (Cit. on p. 18).

[Sch00b] F. Schwabl. *Advanced Quantum Mechanics*. Springer Berlin Heidelberg New York, 2000 (cit. on pp. 14, 21, 30).

[Sch03a] J. Schliemann, A. Khaetskii, and D. Loss, *Electron spin dynamics in quantum dots and related nanostructures due to hyperfine interaction with nuclei*, Journal of Physics: Condensed Matter **15**, R1809 (2003). (Cit. on p. 42).

[Sch03b] J. Schliemann, J. C. Egues, and D. Loss, *Nonballistic Spin-Field-Effect Transistor*, Phys. Rev. Lett. **90**, 146801 (Apr. 2003). (Cit. on pp. 2, 26).

[Sch08] R. Schulz, T. Korn, D. Stich, U. Wurstbauer, D. Schuh, W. Wegscheider, and C. Schüller, *Ultrafast optical studies of diffusion barriers between ferromagnetic Ga(Mn)As layers and non-magnetic quantum wells*, Physica E: Low-dimensional Systems and Nanostructures **40**, 2163 (2008). (Cit. on p. 62).

[Sch10] R. Schulz. "Optische Spektroskopie an zweidimensionalen Lochsystemen in GaAs/AlGaAs-Quantenwells und an GaAs/AlGaAs/GaMnAs- Schichtstrukturen". PhD thesis. University Regensburg, 2010 (cit. on p. 54).

[Sch48] J. Schwinger, *On Quantum-Electrodynamics and the Magnetic Moment of the Electron*, Phys. Rev. **73**, 416 (Feb. 1948). (Cit. on p. 14).

[She03] B. Sherman, *Random spin-orbit coupling and spin relaxation in symmetric quantum wells*, Appl. Phys. Lett. **82**, 209 (Jan. 2003). (Cit. on pp. 33, 91, 96).

[She08] S.-Q. Shen, *Spintronics and Spin Current*, AAPPS Bulletin, **18(5)**, 29 (Oct. 2008). (Cit. on p. 41).

[Shi06] J. Shi, P. Zhang, D. Xiao, and Q. Niu, *Proper Definition of Spin Current in Spin-Orbit Coupled Systems*, Phys. Rev. Lett. **96**, 076604 (Feb. 2006). (Cit. on p. 41).

[Shi95] A. Shields, M. Pepper, D. Ritchie, M. Simmons, and G. Jones, *Quenching of excitonic optical transitions by excess electrons in GaAs quantum wells*, Phys. Rev. B **51**, 18049 (June 1995). (Cit. on p. 54).

[Sho49] W Shockley, *The Theory of p-n Junctions in Semiconductors and p-n Junction Transistors*, Bell System Technical Journal **28**, 435 (July 1949). (Cit. on p. 20).

[Sho52] W Shockley, *Proceedings of the IRE*, A Unipolar "Field-Effect" Transisto **40**, 1365 (1952). (Cit. on p. 1).

[Sht88] H. Shtrikman, M. Heiblum, K. Seo, D. E. Galbi, and L. Osterling, *High-mobility inverted selectively doped heterojunctions*, Journal of Vacuum Science & Technology B: Microelectronics and Nanometer Structures **6**, 670 (1988). (Cit. on p. 11).

[Sih05] V. Sih, R. C. Myers, Y. K. Kato, W. H. Lau, A. C. Gossard, and D. D. Awschalom, *Spatial imaging of the spin Hall effect and current-induced polarization in two-dimensional electron gases*, Nature Physics **1**, 31 (Oct. 2005). (Cit. on pp. 2, 109, 119).

[Sil04] R. H. Silsbee, *Spin-orbit induced coupling of charge current and spin polarization*, Journal of Physics: Condensed Matter **16**, R179 (2004). (Cit. on p. 120).

[Sil94] E. A. de Andrada e Silva, G. C. La Rocca, and F. Bassani, *Spin-split subbands and magneto-oscillations in III-V asymmetric heterostructures*, Phys. Rev. B **50**, 8523 (Sept. 1994). (Cit. on p. 2).

[Slu96] M. Slutzky, O. Entin-Wohlman, Y. Berk, A. Palevski, and H. Shtrikman, *Electron-electron scattering in coupled quantum wells*, Phys. Rev. B **53**, 4065 (Feb. 1996). (Cit. on p. 96).

[Sne91] M. J. Snelling, G. P. Flinn, A. S. Plaut, R. T. Harley, A. C. Tropper, R. Eccleston, and C. C. Phillips, *Magnetic g factor of electrons in GaAs/*$\mathrm{Al}_x\mathrm{Ga}_{1-x}As$ *quantum wells*, Phys. Rev. B **44**, 11345 (Nov. 1991). (Cit. on p. 23).

[Son87] P. C. van Son, H. van Kempen, and P. Wyder, *Boundary Resistance of the Ferromagnetic-Nonferromagnetic Metal Interface*, Phys. Rev. Lett. **58**, 2271 (May 1987). (Cit. on p. 17).

[Ste03] M. J. Stevens, A. L. Smirl, R. D. R. Bhat, A. Najmaie, J. E. Sipe, and H. M. van Driel, *Quantum Interference Control of Ballistic Pure Spin Currents in Semiconductors*, Phys. Rev. Lett. **90**, 136603 (Apr. 2003). (Cit. on p. 41).

[Ste04] J. Stephens, J. Berezovsky, J. P. McGuire, L. J. Sham, A. C. Gossard, and D. D. Awschalom, *Spin Accumulation in Forward-Biased $MnAs/GaAs$ Schottky Diodes*, Phys. Rev. Lett. **93**, 097602 (Aug. 2004). (Cit. on p. 72).

[Ste06] N. P. Stern, S. Ghosh, G. Xiang, M. Zhu, N. Samarth, and D. D. Awschalom, *Current-Induced Polarization and the Spin Hall Effect at Room Temperature*, Phys. Rev. Lett. **97**, 126603 (Sept. 2006). (Cit. on pp. 2, 3).

[Sti07a] D. Stich, J. H. Jiang, T. Korn, R. Schulz, D. Schuh, W. Wegscheider, M. W. Wu, and C. Schüller, *Detection of large magnetoanisotropy of electron spin dephasing in a high-mobility two-dimensional electron system in a [001] $GaAs/Al_xGa_{1-x}As$ quantum well*, Physical Review B (Condensed Matter and Materials Physics) **76**, 073309 (Aug. 2007). (Cit. on p. 26).

[Sti07b] D. Stich, J. Zhou, T. Korn, R. Schulz, D. Schuh, W. Wegscheider, M. W. Wu, and C. Schüller, *Effect of Initial Spin Polarization on Spin Dephasing and the Electron g Factor in a High-Mobility Two-Dimensional Electron System*, Physical Review Letters **98**, 176401 (2007). (Cit. on p. 28).

[Sti69] G. Stillman, C. Wolfe, and J. Dimmock, *Magnetospectroscopy of shallow donors in GaAs*, Solid State Communications **7**, 921 (1969). (Cit. on p. 54).

[Sti71] G. Stillman, D. M. Larsen, C. Wolfe, and R. Brandt, *Precision verification of effective mass theory for shallow donors in GaAs*, Solid State Communications **9**, 2245 (1971). (Cit. on p. 54).

[Str03] J. Strand, B. D. Schultz, A. F. Isakovic, C. J. Palmstrøm, and P. A. Crowell, *Dynamic Nuclear Polarization by Electrical Spin Injection in Ferromagnet-Semiconductor Heterostructures*, Phys. Rev. Lett. **91**, 036602 (July 2003). (Cit. on pp. 43, 44, 76–78).

[Str81] G. B. Stringfellow, W. Koschel, F. Briones, J. Gladstone, and G. Patterson, *Photoluminescence of carbon-implanted GaAs*, Appl. Phys. Lett. **39**, 581 (1981). (Cit. on pp. 53, 85).

[Stu09] M. Studer, G. Salis, K. Ensslin, D. C. Driscoll, and A. C. Gossard, *Gate-Controlled Spin-Orbit Interaction in a Parabolic* GaAs/AlGaAs *Quantum Well*, Phys. Rev. Lett. **103**, 027201 (July 2009). (Cit. on p. 26).

[Stu10] M. Studer, M. P. Walser, S. Baer, H. Rusterholz, S. Schön, D. Schuh, W. Wegscheider, K. Ensslin, and G. Salis, *Role of linear and cubic terms for drift-induced Dresselhaus spin-orbit splitting in a two-dimensional electron gas*, Phys. Rev. B **82**, 235320 (Dec. 2010). (Cit. on pp. 23, 122).

[Stö06] J. Stöhr and H. Siegmann. *Magnetism From Fundamentals to Nanoscale Dynamics*. Springer, 2006 (cit. on pp. 12, 13, 17).

[Sun10] B. Y. Sun, P. Zhang, and M. W. Wu, *Spin relaxation in n-type (111) GaAs quantum wells*, J. Appl. Phys. **108**, 093709 (2010). (Cit. on p. 26).

[Syp07] M. Syperek, D. R. Yakovlev, A. Greilich, J. Misiewicz, M. Bayer, D. Reuter, and A. D. Wieck, *Spin Coherence of Holes in GaAs/(Al, Ga)As Quantum Wells*, Phys. Rev. Lett. **99**, 187401 (Oct. 2007). (Cit. on p. 55).

[Tac99] A. Tackeuchi, T. Kuroda, S. Muto, Y. Nishikawa, and O. Wada, *Electron Spin-relaxation Dynamics in GaAs/AlGaAs Quantum Wells and InGaAs/InP Quantum Wells*, Japanese Journal of Applied Physics **38**, 4680 (1999). (Cit. on p. 30).

[Tar09] S. A. Tarasenko, *Spin relaxation of conduction electrons in (110)-grown quantum wells: A microscopic theory*, Phys. Rev. B **80**, 165317 (Oct. 2009). (Cit. on pp. 29, 33–35).

[Teh88] C. Teh and F. Weichman, *Photoluminescence decay mechanism of the $\sim$ 1.49 eV emission in LEC-grown semi-insulating GaAs*, Journal of Luminescence **40 & 41**, 359 (1988). (Cit. on pp. 53, 85).

[Teh90] C. K. Teh, J. Tuszyński, and F. L. Weichman, *The decay of carbon, luminescence in liquid-encapsulated Czochralski-grown semi-insulating GaAs*, Journal of Materials Research **5**, 365 (02 Feb. 1990). (Cit. on pp. 53, 85).

[Tho06] S. E. Thompson and S. Parthasarathy, *Moore's law: the future of Si microelectronics*, Materials Today **9**, 20 (2006). (Cit. on pp. 1, 2).

[Tho26] L. H. Thomas, *The motion of spinning electrons*, Nature **117**, 514 (1926). (Cit. on p. 21).

[Tor56] H. C. Torrey, *Bloch Equations with Diffusion Terms*, Phys. Rev. **104**, 563 (Nov. 1956). (Cit. on p. 26).

[Uch08] K. Uchida, S. Takahashi, K. Harii, J. Ieda, K. Koshibae W. andAndo, S. Maekawa, and E. Saitoh, *Observation of the spin Seebeck effect*, Nature **455**, 778 (2008). (Cit. on p. 14).

[Uhl26] G. E. Uhlenbeck and S. Goudsmit, *Spinning Electrons and the Structure of Spectra*, Nature **117**, 264 (1926). (Cit. on p. 13).

[Uma09] V. Umansky, M. Heiblum, Y. Levinson, J. Smet, J. Nuebler, and M. Dolev, *MBE growth of ultra-low disorder 2DEG with mobility exceeding*, Journal of Crystal Growth **311**, 1658 (2009). (Cit. on pp. 3, 11, 37, 81, 83).

[Utz12] M. Utz. "Epitaxie von (Ga,Mn)As". PhD thesis. University Regensburg, Oct. 2012 (cit. on pp. 20, 62).

[VD04] P. Van Dorpe, Z. Liu, W. Van Roy, V. Motsnyi, M. Sawicki, G. Borghs, and J. De Boeck, *Very high spin polarization in GaAs by injection from a (Ga,Mn)As Zener diode*, Appl. Phys. Lett. **84**, 3495 (2004). (Cit. on pp. 3, 19).

[VD05] P. Van Dorpe, W. Van Roy, J. De Boeck, and G. Borghs, *Nuclear spin orientation by electrical spin injection in an $Al_xGa_{1-x}As/GaAs$ spin-polarized light-emitting diode*, Phys. Rev. B **72**, 035315 (July 2005). (Cit. on p. 44).

[Val93] T. Valet and A. Fert, *Theory of the perpendicular magnetoresistance in magnetic multilayers*, Phys. Rev. B **48**, 7099 (Sept. 1993). (Cit. on p. 17).

[Var67] Y. Varshni, *Temperature dependence of the energy gap in semiconductors*, Physica **34**, 149 (1967). (Cit. on p. 8).

[Völ09] R. Völkl. "Optische Detektion von Spindrift und Spindiffusion in GaAs-basierten Halbleiterstrukturen". MA thesis. Universität Regensburg, 2009 (cit. on pp. 29, 71).

[Völ11] R. Völkl, M. Griesbeck, S. A. Tarasenko, D. Schuh, W. Wegscheider, C. Schüller, and T. Korn, *Spin dephasing and photoinduced spin diffusion in a high-mobility two-dimensional electron system embedded in a GaAs-(Al,Ga)As quantum well grown in the [110] direction*, Phys. Rev. B **83**, 241306 (June 2011). (Cit. on pp. 30, 34, 35, 48, 81, 99).

[Völ13] R Völkl, M. Schwemmer, M. Griesbeck, S. A. Tarasenko, D. Schuh, W. Wegscheider, C. Schueller, and T. Korn, *Spin polarization, dephasing and photoinduced spin diffusion in (110)-grown two-dimensional electron systems*, arXiv:1310.7345 (2013). (Cit. on p. 81).

[Wal08] A. Walsh, J. L. F. Da Silva, and S.-H. Wei, *Origins of band-gap renormalization in degenerately doped semiconductors*, Phys. Rev. B **78**, 075211 (Aug. 2008). (Cit. on p. 10).

[Wal12] M. P. Walser, C. Reichl, W. Wegscheider, and G. Salis, *Direct mapping of the formation of a persistent spin helix*, Nature Physics **8**, 757 (2012). (Cit. on pp. 2, 26).

[Wal84] W. Walukiewicz, H. E. Ruda, J. Lagowski, and H. C. Gatos, *Electron mobility in modulation-doped heterostructures*, Phys. Rev. B **30**, 4571 (Oct. 1984). (Cit. on pp. 37, 96).

[Wan05a] K. Y. Wang, R. P. Campion, K. W. Edmonds, M. Sawicki, T. Dietl, C. T. Foxon, and B. L. Gallagher, *Magnetism in (Ga,Mn)As Thin Films With T_C Up To 173K*, AIP Conference Proceedings **772**, 333 (2005). (Cit. on p. 13).

[Wan05b] K.-Y. Wang, M. Sawicki, K. W. Edmonds, R. P. Campion, S. Maat, C. T. Foxon, B. L. Gallagher, and T. Dietl, *Spin Reorientation Transition in Single-Domain (Ga,Mn)As*, Phys. Rev. Lett. **95**, 217204 (Nov. 2005). (Cit. on p. 64).

[Web05] C. P. Weber, N. Gedik, J. E. Moore, J. Orenstein, J. Stephens, and D. D. Awschalom, *Observation of spin Coulomb drag in a two-dimensional electron gas*, Nature **437**, 1330 (2005/10/27/). (Cit. on p. 42).

[Web85] R. A. Webb, S. Washburn, C. P. Umbach, and R. B. Laibowitz, *Observation of $\frac{h}{e}$ Aharonov-Bohm Oscillations in Normal-Metal Rings*, Phys. Rev. Lett. **54**, 2696 (June 1985). (Cit. on p. 1).

[Wen03] M. Q. Weng and M. W. Wu, *Spin dephasing in n -type GaAs quantum wells*, Phys. Rev. B **68**, 075312 (Aug. 2003). (Cit. on p. 28).

[Wen07] J. Wenisch, C. Gould, L. Ebel, J. Storz, K. Pappert, M. J. Schmidt, C. Kumpf, G. Schmidt, K. Brunner, and L. W. Molenkamp, *Control of Magnetic Anisotropy in $(Ga, Mn)As$ by Lithography-Induced Strain Relaxation*, Phys. Rev. Lett. **99**, 077201 (Aug. 2007). (Cit. on p. 65).

[Wen08] J. Wenisch. "Ferromagnetic (Ga,Mn)As Layers and Nanostructures: Control of Magnetic Anisotropy by Strain Engineering". PhD thesis. Julius-Maximilians-Universität Würzburg, 2008 (cit. on p. 65).

[Win00] R. Winkler, *Rashba spin splitting in two-dimensional electron and hole systems*, Phys. Rev. B **62**, 4245 (Aug. 2000). (Cit. on p. 25).

[Win03] R. Winkler. *Spin-orbit Coupling Effects in Two-dimensional Electron and Hole System*. 2003 (cit. on pp. 7, 8, 10, 21, 23, 25, 34, 35, 95).

[Win04] R. Winkler, *Spin orientation and spin precession in inversion-asymmetric quasi-two-dimensional electron systems*, Phys. Rev. B **69**, 045317 (Jan. 2004). (Cit. on p. 24).

[Wol70] C. M. Wolfe, G. E. Stillman, and W. T. Lindley, *Electron Mobility in High-Purity GaAs*, J. Appl. Phys. **41**, 3088 (1970). (Cit. on p. 37).

[Woo24] R. W. Wood and A. Ellett, *Polarized Resonance Radiation in Weak Magnetic Fields*, Phys. Rev. **24**, 243 (Sept. 1924). (Cit. on p. 48).

[Wu00] M. Wu and C. Ning, *A novel mechanism for spin dephasing due to spin-conserving scatterings*, The European Physical Journal B - Condensed Matter and Complex Systems **18**, 373 (2000). (Cit. on p. 28).

[Wu02] M. Wu and M. Kuwata-Gonokami, *Can D'yakonov Perel' effect cause spin dephasing in GaAs(110) quantum wells?*, Solid State Communications **121**, 509 (2002). (Cit. on pp. 28, 34).

[Wu10] M. Wu, J. Jiang, and M. Weng, *Spin dynamics in semiconductors*, Physics Reports **493**, 61 (2010). (Cit. on pp. 25, 29–31, 33, 41, 97).

[Xia05] G. Xiang, A. W. Holleitner, B. L. Sheu, F. M. Mendoza, O. Maksimov, M. B. Stone, P. Schiffer, D. D. Awschalom, and N. Samarth, *Magnetoresistance anomalies in (Ga,Mn)As epilayers with perpendicular magnetic anisotropy*, Phys. Rev. B **71**, 241307 (June 2005). (Cit. on p. 64).

[Yaf63] Y. Yafet, *g Factors and Spin-Lattice Relaxation of Conduction Electrons.* Solid State Physics **14**, 1 (1963). (Cit. on p. 30).

[Yos57] K. Yosida, *Magnetic Properties of Cu-Mn Alloys*, Phys. Rev. **106**, 893 (June 1957). (Cit. on p. 13).

[You96] C.-Y. You and S.-C. Shin, *Derivation of simplified analytic formulae for magneto-optical Kerr effects*, Appl. Phys. Lett. **69**, 1315 (1996). (Cit. on p. 46).

[Yu02a] Z. G. Yu and M. E. Flatté, *Electric-field dependent spin diffusion and spin injection into semiconductors*, Phys. Rev. B **66**, 201202 (Nov. 2002). (Cit. on pp. 39, 40).

[Yu02b] Z. G. Yu and M. E. Flatté, *Spin diffusion and injection in semiconductor structures: Electric field effects*, Phys. Rev. B **66**, 235302 (Dec. 2002). (Cit. on pp. 17, 39, 40).

[Yu05] P. Yu and M Cardona. *Fundamentals of Semiconductors Physics and Materials Properties.* Springer Berlin Heidelberg New York, 2005 (cit. on pp. 6–10, 36, 38, 82).

[Yug07] I. A. Yugova, A. Greilich, D. R. Yakovlev, A. A. Kiselev, M. Bayer, V. V. Petrov, Y. K. Dolgikh, D. Reuter, and A. D. Wieck, *Universal behavior of the electron g factor in GaAs / $Al_xGa_{1-x}As$ quantum wells*, Phys. Rev. B **75**, 245302 (June 2007). (Cit. on p. 23).

[Zee97] P. Zeeman, *The Effect of Magnetisation on the Nature of Light Emitted by a Substance*, Nature **55**, 347 (1897). (Cit. on p. 22).

[Zha09] H. Zhao, M. Mower, and G. Vignale, *Ambipolar spin diffusion and D'yakonov-Perel' spin relaxation in GaAs quantum wells*, Phys. Rev. B **79**, 115321 (Mar. 2009). (Cit. on p. 42).

[Zho07] J. Zhou, J. L. Cheng, and M. W. Wu, *Spin relaxation in n-type GaAs quantum wells from a fully microscopic approach*, Phys. Rev. B **75**, 045305 (Jan. 2007). (Cit. on p. 28).

[Zho08] J. Zhou and M. W. Wu, *Spin relaxation due to the Bir-Aronov-Pikus mechanism in intrinsic and p-type GaAs quantum wells from a fully microscopic approach*, Phys. Rev. B **77**, 075318 (2008). (Cit. on pp. 30, 97, 98).

[Zho09] Y Zhou, J. H. Jiang, and M. W. Wu, *Electron spin relaxation in p-type GaAs quantum wells*, New Journal of Physics **11**, 113039 (2009). (Cit. on pp. 30, 94, 97, 101).

[Zho10] Y. Zhou and M. W. Wu, *Spin relaxation due to random Rashba spin-orbit coupling in GaAs (110) quantum wells*, EPL (Europhysics Letters) **89**, 57001 (2010). (Cit. on pp. 33, 91).

[Zhu01] H. J. Zhu, M. Ramsteiner, H. Kostial, M. Wassermeier, H.-P. Schönherr, and K. H. Ploog, *Room-Temperature Spin Injection from Fe into GaAs*, Phys. Rev. Lett. **87**, 016601 (June 2001). (Cit. on p. 18).

[Ţif03] I. Ţifrea and M. E. Flatté, *Electric Field Tunability of Nuclear and Electronic Spin Dynamics due to the Hyperfine Interaction in Semiconductor Nanostructures*, Phys. Rev. Lett. **90**, 237601 (June 2003). (Cit. on p. 44).

[Ţif04] I. Ţifrea and M. E. Flatté, *Nuclear spin dynamics in parabolic quantum wells*, Phys. Rev. B **69**, 115305 (Mar. 2004). (Cit. on p. 44).

[Ţif11] I. Ţifrea and M. E. Flatté, *Nonequilibrium nuclear polarization and induced hyperfine and dipolar magnetic fields in semiconductor nanostructures*, Phys. Rev. B **84**, 155319 (Oct. 2011). (Cit. on pp. 44, 123, 124).

[Žut04] I. Žutić, J. Fabian, and S. Das Sarma, *Spintronics: Fundamentals and applications*, Rev. Mod. Phys. **76**, 323 (Apr. 2004). (Cit. on pp. 17, 22–24, 27, 29–31, 33, 43).

Symbols and abbreviations

Abbreviation	Description	introduced on page
2DES	Two dimensional electron system	9
a	Lattice constant	6
A	Area	14
AEI	Anisotropic exchange interaction	32
A_x	Factor proportional to the matrix element of the Coulomb exchange interaction	29
B	Magnetic field [T]	21
B_e	Knight field	43
B_{eff}	Effective magnetic field	22
B_{ext}	External magnetic field	22
B_N	Overhauser field	43
b_N	Overhauser field at a complete polarization of the nuclei	43
BAP	Bir-Aronov-Pikus spin dephasing mechanism	29
$B_i(\boldsymbol{k})$	Intrinsic effective k-dependent magnetic field	22
CISP	Current induced spin polarization	119
BIA	Bulk inversion asymmetry	22
c	speed of light	21
CB	Conduction band	6
d	Quantum well width	9
d_{opt}	Length of the optical path through the medium	45
D	Diffusion constant, in particular $D_{e,h}$ denotes electron/hole diffusion constant	26
D_a	Ambipolar spin diffusion constant	40
D_s	Spin diffusion constant	40
D_z	Spin diffusion constant for the z-component of the electron spin	41
DMS	Diluted magnetic semiconductors	11
DOS	Density of states	16
DP	Dyakonov-Perel' spin dephasing mechanism	27
DPSS	Diode-pumped solid state laser	58
dsd	double-sided doping	11
e	Electron elementary charge $1.602176565(35) \cdot 10^{-19}$ [C]	14
e-e	Electron-electron	38
E_F	Fermi energy (chemical potential at $T = 0$ K)	7
E_g	Band gap energy	7
$E_{n'}$	Subband energy	9
ΔE	Spectral width of PL	54
δE	Spectral width of high energy tail in the PL $\delta E \propto= k_B T$	86

Abbreviation	Description	introduced on page
ΔE_{SO}	Spin splitting energy $2\hbar\left\|\boldsymbol{\Omega}\left(\boldsymbol{k}\right)\right\|$	22
$\boldsymbol{\mathcal{E}}$	Electric field $\left[\mathrm{V}\cdot\mathrm{m}^{-1}\right]$	11
EY	Elliot-Yafet spin dephasing mechanism	30
$f_e(E)$	Fermi-Dirac distribution	10
F/N	Ferromagnet/nonmagnet	17
FWHM	Full width at half maximum	58
$\boldsymbol{G}$	Spin generation rate with components G_α, $\alpha = x, y, z$	34
g	g-factor	14
$\hat{\boldsymbol{g}}$	g-factor tensor	23
g_0	g-factor for free electron $2\left(1+\alpha'/2\pi+...\right) \approx 2.0023$	14
$g_e(E)$	Density of states	38
$\hat{H}_H$	Heisenberg Hamiltonian	13
$\hat{H}_{BAP}$	BAP Hamiltonian	29
$\hat{H}_{HF}$	Hamiltonian of Fermi contact hyperfine interaction	42
$\hat{H}_{SO}$	Hamiltonian of spin-orbit interaction	21
$H(\tilde{q}$	Form factor describing ee interaction in ee scattering time	21
HH	Heavy hole	7
HFI	Hyperfine interaction	31
HWHM	Half width at half maximum	49
$\hbar$	Planck constant $h/(2\pi) = 1.054571726(47)\cdot 10^{-34}$ $[\mathrm{J}\cdot\mathrm{s}] = 6.58211928(15)\cdot 10^{-16}$ $[\mathrm{eV}\cdot s]$	9
I	Excitation density	92
$\hat{\boldsymbol{I}}_n$	Nuclear spin operator	42
I_n	Nuclear spin	42
$I_{co,contra}$	PL intensities for co or contra setups	54
I_L	Laser intensity	56
ISR	Intersubband spin relaxation mechanism	31
$\boldsymbol{J}$	Total angular momentum	21
J_F	Carrier diffusion flux	38
$\hat{\boldsymbol{J}}_h$	Operator of the total angular momentum of the hole	29
j	Current density, in particular $j_{e,h}$ denotes electron/hole current density	38
$\tilde{J}_{i,j}$	Exchange integral	13
k_B	Boltzmann constant $1.380648(13)\cdot 10^{-23}$ $\left[\mathrm{JK}^{-1}\right]$ $k_BT(300\ \mathrm{K}) \approx 25$ meV	7
$\boldsymbol{k}$	Wave vector with parallel $k_\parallel$ and perpendicular $k_\perp$ component	7
$\langle k_z\rangle$	Quantum mechanical expectation value of k_z	24
k_{SO}	Splitting in k due to SOI	22
k_F	Fermi wave vector	7
K_0	Modified Bessel function of the second kind	41
KSBE	Kinetic spin Bloch equation	97
l	Mean free path	36
$\boldsymbol{L}$	Orbital angular momentum	21
L_s	Spin diffusion length $L_s = \sqrt{D_s\tau_s}$	40
L	Spin injection length, in particular $L_{d,(u)}$ denotes downstream or upstream injection length	40
L_z	Spin diffusion length for the z-component of the electron spin	41
lc	Left-hand circularly polarized	47
LCR	Liquid crystal retarder	58

Abbreviation	Description	introduced on page
LH	Light hole	7
$\boldsymbol{M}$	Magnetization	12
$m^*_{e,h}$	Effective mass for electron or holes	8
m_0	Mass of free electron $9.10938291(40) \cdot 10^{-31}$ kg	21
MBE	Molecular-Beam Epitaxy	6
MIT	Metal-insulator transition	32
MOKE	Magneto optic Kerr effect	45
MPGE	Magnetophotogalvanic effect	25
MQW	Multiple quantum wells	33
n	Carrier density, in particular $n_{e,h}$ denotes electron/hole density	14
n^+	Highly n-doped	19
$n_{a,d}$	Acceptor/donator doping densities	20
$n_{\uparrow\downarrow}$	Carrier density for spin up$\uparrow$ or spin down$\downarrow$	14
n^{tot}_{opt}	Total optically created electron density	15
n_{opt}	Spin polarized portion of n^{tot}_{opt}	15
N_h	Hole density in the case of optical cw excitation	35
δn	Asymmetric electron density distribution in the barrier	95
n'	Subband index	9
$\tilde{n}$	Refractive index	46
$\tilde{n}_{rcp}$	Refractive index of right-hand circularly polarized light	46
$\tilde{n}_{lcp}$	Refractive index of left-hand circularly polarized light	46
NIA	Natural interface asymmetry	22
P	Degree of spin polarization	14
P_{red}	Reduced net spin polarization	15
P_S	Spin polarization	14
P_j	Current spin polarization	17
$\bar{P}$	Average laser power	16
$\hat{\boldsymbol{p}}$	Linear momentum operator $-i\hbar\nabla$	21
p^+	Highly p-doped	19
p-MOKE	Polar Magneto optic Kerr effect	45
PL	Photoluminescence	53
PLE	Photoluminescence excitation spectroscopy	53
QW	Quantum well	9
$\boldsymbol{r}$	Position vector	22
$r_{F,N}$	Effective resistance for spin polarized transport	18
r_b	Interface resistance	18
rc	Right-hand circularly polarized	47
R_d	Distance between dopant layer and 2DES	96
RSA	Resonant spin amplification technique	89
RT	Room temperature	89
$\boldsymbol{S}$	Spin vector with components S_x, S_y, S_z	26
$\boldsymbol{S_{i,j}}$	Nearest neighbor spins	13
$\tilde{S}$	Spin stiffness	42
$\tilde{S}_C$	Curie spin stiffness $S_C = k_B T n/(4n\uparrow)n_\downarrow$	42
SDL	Spin diffusion length	112
SIA	Structure inversion asymmetry	22
$\boldsymbol{S}$	Spin vector	21
SO	Spin-orbit	7
SOI	Spin-orbit-interaction	7
ssd	single sided doping	11
SPSL	Short period super lattice	83
t	Time	21

Abbreviation	Description	introduced on page
T	Temperature in [K]	7
T_C	Curie temperature in [K]	12
T_F	Fermi temperature $T_F = E_F/k_B$	7
$\tilde{T}_{i\to f}$	Transition probability between two states i and f	14
T_s	Spin temperature $T_F = E_F/k_B$	78
T_1	Longitudinal spin relaxation time	27
T_2	Transverse spin dephasing time	27
T_2^*	Transverse ensemble spin dephasing time	27
TRFR	Time-resolved Faraday rotation	48
TRKR	Time-resolved Kerr rotation	48
TRPL	Time-resolved photoluminescence	54
$\boldsymbol{v}$	Velocity in [m/s]	36
$\boldsymbol{v_D}$	Drift velocity in [m/s]	36
v_F	Fermi velocity in $v_F = \sqrt{2E_F/m^*}$	7
v_{th}	Thermal velocity	36
V_C	Confinement potential	25
$\tilde{V}$	Volume	14
V	Voltage	20
V_{bi}	Built-in voltage	20
VB	Valence band	7
W	Width of the depletion zone	20
x, y, z	Cartesian coordinates	9
α	Rashba parameter $2\langle\alpha_0\mathcal{E}_z\rangle$	25
α_0	Material parameter in Bychkov-Rashba field, for GaAs:$\alpha_0 = 5,2$ eÅ^2	25
$\tilde{\alpha}_{ab}$	Absorption coefficient	16
$\tilde{\alpha}_{rcp,lcp}$	Absorption coefficient for right-, left-hand circularly polarized light	47
α_D	Dimension less material parameter in spin splitting parameter γ	23
α_s	General spin splitting parameter which depends on the present SO-fields	120
α_v	Volume coefficient of thermal expansion in Varshni formula	8
α'	Fine structure constant $e^2/(4\pi\epsilon_0)\hbar c = 7.2973525698(24)\cdot 10^{-3}$	14
β	Dresselhaus parameter $\gamma(\pi/d)^2$	24
$\tilde{\beta}$	Dimensionless parameter indicating the asymmetry of the current in the two-current model	17
β_v	Volume compressibility in Varshni formula	8
χ	Electron affinity	9
Δ_0	Spin-orbit gap	7
Δ_{BM}	Burstein-Moss shift	10
Δ_{RN}	Band gap renormalization	10
ε	Permittivity $\varepsilon = \varepsilon_0\varepsilon_r$	20
ε_r	Relative permittivity of the material	20
ε_0	Vacuum permittivity or electric constant $\approx 8.854187817\cdot 10^{-12}$ $\left[\mathrm{F\cdot m^{-1}(C/V\cdot m)}\right]$	14
$\tilde{\epsilon}$	Characteristic energy $\tilde{\epsilon} = E_F/[1-\exp(-E_F/k_BT)]$	92
ϕ	Electrostatic potential [V]	11
γ	Spin splitting parameter in Dresselhaus field	23
γ_z^{BAP}	Spin-decay parameter for BAP-dephasing	35
γ^r	Spin-decay parameter due to recombination	35
γ_N	Gyromagnetic ratio of the nucleus	42
$\hat{\gamma}$	Friction coefficient	42

Abbreviation	Description	introduced on page
$\hat{\Gamma}$	Spin relaxation tensor with components $\Gamma_{\alpha\beta}$ $(\alpha, \beta = x, y, z)$	35
ι	Tunneling attempt frequency	56
λ	Laser wavelength	16
λ_{dB}	de Broglie wavelength $\lambda_{dB} = h/p$	1
μ	Mobility, in particular $\mu_{e,h}$ denotes electron/hole mobility $\mu_{e,h} = e\tau/m^*_{e,h}$	36
μ_a	Ambipolar mobility	39
μ_s	Electron spin mobility	40
μ_B	Bohr magneton $e\hbar/2m_0$ $9.27400968(20) \cdot 10^{-24}$ $\left[\mathrm{J} \cdot \mathrm{T}^{-1}\right]$	14
$\bar{\mu}_i$	Magnetic moment $\bar{\mu}_i = -g_0\mu_B s_i/\hbar$	13
$\bar{\mu}_N$	Magnetic moment of the nucleus	42
$\tilde{\mu}$	Electrochemical potential	17
ν_V	Verdet constant $\left[\mathrm{rad} \cdot \mathrm{m}^{-1} \cdot \mathrm{T}^{-1}\right]$	45
ϖ	Probability that the electron-hole recombination involves spin-polarized electrons	49
θ	Faraday/ Kerr angle	45
Θ_D	Debye temperature	8
ρ	Resistivity	18
ϱ	Electron single-particle density matrix	97
$\hat{\boldsymbol{\sigma}}$	Pauli matrices with components $\sigma_x, \sigma_y, \sigma_z$	14
$\tilde{\sigma}$	Conductivity $\tilde{\sigma} = e\left(n_e\mu_e + n_h\mu_h\right)$	37
$\sigma^{\pm}$	Left (σ^+) or right (σ^-) circular polarization of photons	15
τ	Microscopic scattering time	27
τ_{ee}	Electron-electron scattering time	28
τ_p	Momentum scattering time	28
τ_{ph}	Photocarrier lifetime	16
τ_s	Spin lifetime	27
$\tau_\parallel$	In-plane spin lifetime	50
τ_z	Out-of-plane spin lifetime	50
τ_z^{lim}	Dephasing rate in the limit of zero excitation	35
υ	Barrier parameter	56
$\boldsymbol{\Omega(k)}$	Larmor precession vector	14
$\boldsymbol{\Omega(k)}_D$	Dresselhaus SO-field	24
$\boldsymbol{\Omega(k)}_{BR}$	Bychkov-Rashba SO-field	25
$\boldsymbol{\Omega(k)}_{drift}$	Effective SO-field due to drift	122
ω_L	Larmor frequency $\omega_L = g\mu_B B/\hbar$	49
$\psi_{n,k}(\boldsymbol{r})$	Electron wave function	7
∇	Nabla operator $(\partial_x, \partial_y, \partial_z)$	11

Danksagung

Am Gelingen dieser Arbeit hatten viele Personen einen Anteil, bei denen ich mich im Folgenden besonders bedanken möchte:

- Prof. Dr. Christian Schüller möchte ich danken, der mir die Möglichkeit gab, diese Arbeit in seiner Arbeitsgruppe durchführen zu können. Die besonderen Rahmenbedingungen die er zur Verfügung gestellt hat und die freundliche Anleitung erleichterten mir die Durchführung der Arbeit.
- PD Dr. Tobias Korn stand mir immer zur Seite bei Problemen im Labor und bei der Interpretation der Messergebnisse.
- Dr. Michael Griesbeck für die vielen aufschlussreichen wissenschaftlichen Diskussionen. Ebenso für das zur Verfügung stehen bei den oft späten Laboraktivitäten. Besonderer Dank auch für die LaTeX-Vorlage.
- Markus Schwemmer für seinen Beitrag im Rahmen seiner Masterarbeit.
- Prof. Dr. Sergey A. Tarasenko für den theoretischen Support.
- Christian Reichl, Dr. Dieter Schuh, Prof. Dr. Werner Wegscheider für die großartigen Quantentrog Proben.
- Mariusz Ciorga, Andreas Einwanger, Prof. Dr. Dieter Weiss für die Proben zur elektrischen Spininjektion.
- der ganzen AG Schüller für die kollegiale Zusammenarbeit. Im Besonderen meinen Laborkollegen Stefanie Heydrich, Dr. Michael Hirmer, Christoph Schönhuber Markus Schwemmer für die reibungslose Zusammenarbeit im Labor.
- Dr. Michael Kugler, Christoph Ermer, Imke Gronwald für IT- und technischen Support.
- den Mitarbeitern der Heliumausgabe, der Mechanikwerkstatt und der Elektronikwerkstatt.
- für das Korrekturlesen: Dr. Michael Griesbeck, PD Dr. Tobias Korn, Dr. Mariusz Ciorga, Markus Schwemmer, Christian Gradl, Gerd Plechinger, Stefanie Heydrich, Tobias Völkl und Yuanyuan Völkl.
- der DFG und dem SFB 689 für die Finanzierung der Arbeit.
- meiner Mutter Maria Völkl und meinen Geschwistern Christina Hösl und Tobias Völkl für ihre Unterstützung.
- meiner Frau Yuanyuan Völkl für ihre Liebe und Unterstützung.